Stabilization and comparison of manufacturing technologies for production of nano-crystalline suspensions

Mostafa Nakach

To cite this version:

Mostafa Nakach. Stabilization and comparison of manufacturing technologies for production of nano-crystalline suspensions. Chemical and Process Engineering. Ecole des Mines d'Albi-Carmaux, 2016. English. NNT : 2016EMAC0007 . tel-01967624

HAL Id: tel-01967624
https://theses.hal.science/tel-01967624

Submitted on 1 Jan 2019

THÈSE

En vue de l'obtention du

DOCTORAT DE L'UNIVERSITÉ DE TOULOUSE

Délivré par :

École Nationale Supérieure des Mines d'Albi-Carmaux

Présentée et soutenue par :
Mostafa Nakach
le vendredi 23 septembre 2016

Titre :

Stabilization and comparison of manufacturing technologies for production of nano-crystalline suspensions

École doctorale et discipline ou spécialité :
ED MEGEP : Génie des procédés et de l'Environnement

Unité de recherche :
Centre RAPSODEE, CNRS - UMR 5302, Ecole des Mines d'Albi-Carmaux

Directeur/trice(s) de Thèse :
Dr. Laurence Galet Ecole des Mines d'Albi-Carmaux
Dr. Alain Chamayou Ecole des Mines d'Albi-Carmaux

Jury :
Pr. Dr. Concepción Soláns Spanish council for Scientific Research (CSIC) (examinatrice)
DR. Christine Frances INPT-ENSIACET (Laboratoire de Génie Chimique)(Présidente du Jury)
Pr.Dr. Arno Kwade Institut für Partikeltechnik Technische Universität (rapporteur)
Pr.Dr Rainer Helmut Müller Freie Universität Berlin Department of Pharmacy (rapporteur)
Pr.Dr Tharwat Tadros Independant consultant(membre invité)
Dr. Jean-René Authelin Director of pharmaceutical engineering at Sanofi (membre invité)

Dedications

This PhD thesis is dedicated to the dearest people of my life: my wife Laurence, my children (Sami, Maëlyss and Noa) and my mother. I’m sure that this PhD thesis is a reward for their patience.

If my father was still alive, he would have been proud of the work I have done. This achievement is dedicated to his memory

This PhD thesis is also dedicated to the memory of Noël Midoux Professor Emeritus at Ecole Nationale supérieur des Industries Chimiques de Nancy (France), who brought me a tremendous help during this work

Acknowledgments

I would like to thank very much a number of people for their help and advice all along this Thesis.

I am very grateful to Drs Françoise Hodac, Jean-Yves Pommier, Didier Pertuy, Jean Louis Laly and Ross Blundell ex VP global head of CMC, ex VP global head of analytical sciences, VP global head of drug-device integrated development, VP global head of pharmaceutical sciences operations and local head of Pharmaceutical sciences operations-Paris, respectively, who gave me the opportunity to work on this thesis and allowed me to run all the experimental part within the laboratories of Sanofi - Vitry-Alfortville research center.

I would also like to thank the supervision/advices I received from everyone - My friend and my mentor Dr Jean-René Authelin for his invaluable help and advice throughout all this work- Dr Laurence Galet and Dr Alain Chamayou who gave the opportunity to achieve this work within the frame of Ecole des Mines d'Albi and for deep discussion and review of my experimental results -Dr Tharwat Tadros and Dr Bernard Cabane for their appreciated help and advice in the field of physico-chemistry

My sincere gratitude to Pr Abdessadek Lachgar, Dr Charlotte Pellet, Dr Thomas Ballet, Dr Otmane Boussif and Dr Vasco Filipe who kindly reviewed my thesis.

Table of content

Table of content

Figures List

Figures list

Tables List

Tables list

Glossary

ABREVIATIONS

A.D.H.D : Attention deficit hyperactivity disorder
A.P.I : Active Pharmaceutical ingredient
C.C.C : Critical coagulation concentration
D.L.S : Dynamic light scattering
D.L.V.O : Derjagin Landau Verwey Overbeek
G.P.C : Gel permeation chromatography
I.V : Intravenous
L.C.D : Liquid crystal display
P.C.D : Polycrystalline diamond
P.C.S : Photon correlation spectroscopy
P.O.C : Proof of concept
Q.Ds : Quantum dots
q.s : Quantity sufficient for
S.E.M : Scanning electron microscopy
U.V : Ultra-violet
X.R.P.D : X-ray pattern diffraction

SYMBOLS

$(6/d_{50})_\infty$	: Infinite implicit specific surface area	[m^{-1}]
[P]	: Partition coefficient between octanol and water	[-]
$6/d_{50}$	: Implicit specific surface area	[m^{-1}]
A	: Hamaker constant	[J]
A_{11}	: Hamaker constant between particles in a vacuum	[J]
A_{22}	: Hamaker constant for equivalent volumes of the medium	[J]
b	: Adsorption constant	[mol^{-1} m^{3}]
B	: Constant function of maximum attainable solid volume	[m^{3} mol^{-1}]
B'	: Constant	[m^{3} mol^{-1}]
C_-	: Concentration of negative ions	[mol m-^{3}]
C	: Concentration of particles having free energy ΔG	[mol m-^{3}]
C_+	: Concentration of positive ions	[mol m-^{3}]
C_1	: Initial surfactant or polymer concentration	[mol m^{-3}]
C_2	: Surfactant or polymer concentration at the equilibrium	[mol m^{-3}]
C_a	: API volume fraction	[mol m^{-3}]
C_{cor}	: Correction factor	[-]
C_f	: Friction coefficient	[-]
C_{gf}	: Geometrical factor	[m^2]
C_l	: API loading	[%]
C_p	: Concentration of particles having free energy ΔG	[mol m^{-3}]
C_{p0}	: Concentration of particles having free energy ΔG=0	[mol m^{-3}]
C_{pv}	: Volume concentration of solid	[-]
d	: Particle diameter	[m]
D	: Rotor or stirrer diameter	[m]
$d_{[3,2]}$	: Sauter diameter	[m]
d_1	: Starting particle diameter	[m]
D_1	: Inlet diameter of the seat outlet (conical part of homogenization valve)	[m]
d_{10}	: Characteristic diameters of particle distribution referring to diameter of 10 % of particle population	[m]
d_2	: Final particle diameter	[m]
D_2	: Outlet diameter of the seat outlet (conical part of homogenization valve)	[m]
d_{50}	: Characteristic diameters of particle distribution referring to diameter of 50 % of particle population	[m]
d_{90}	: Characteristic diameter of particle distribution referring to diameter of 90 % of particle population	[m]
D_f	: Diffusion coefficient	[m^2 s^{-1}]
d_{gm}	: Diameter of the grinding media	[m]

d_{gm_app}	: Apparent density of beads	[kg m^{-3}]
d_h	: Hydraulic diameter	[m]
$D_{Labstar}$	: Rotor diameter of Labstar mill	[m]
D_{LMZ2}	: Rotor diameter of LMZ2 mill	[m]
dS/dt	: Dissolution rate	[mol s^{-1}]
D_v	: Vessel diameter	[m]
e	: Elementary (protonic) charge	[-]
E	: Energy	[J]
E_S	: Specific energy	[J kg^{-1}]
f_{gf}	: Geometrical factor	[m]
F_{hydro}	: Hydrodynamic force	[N]
F_{sol}	: Solvation or hydration force	[N]
G_A	: Attractive energy	[J]
G_{el}	: Elastic interaction energy	[J]
G_{mix}	: Mixing interaction energy	[J]
G_R	: Electrical repulsive energy	[J]
G^s	: Gibbs free energy	[J]
G_S	: Steric stabilization energy	[J]
G_T	: Total potential energy	[J]
h	: Distance	[m]
H	: Height	[m]
K’	: Constant	[J^{-1} kg].
K’’	: Constant	[s^{-1}]
k_1	: Constant	[-]
k_2	: Constant	[s]
k_3	: Constant	[s$^{-0.8}$ m$^{1.8}$]
k_4	: Constant	[s^{-1} m^{2}]
k_5	: Constant	[s]
k_6	: Constant	[s]
k_{an}	: Constant	[s$^{-0.8}$ m$^{1.8}$]
k_B	: Boltzmann constant	[J/k]
K_f	: Hydrophilic repulsion forces or hydrophobic attraction forces	[N]
k_{ij} (fast)	: Fast coagulation rate constant	[m^{-3} s^{-1}]
k_{ij} (slow)	: Slow coagulation rate constant	[m^{-3} s^{-1}]
k_{ij}	: Second-order coagulation rate constant	[m^{-3} s^{-1}]

k_{p1}	: Constant	$[s^{-1} m^2]$
k_{p2}	: Constant	[-]
k_{p3}	: Constant	[-]
K_r	: Ripening rate	$[s^{-1}]$
K_{wf}	: wet-ability factor	$[kg^2 m_{-3}]$
l_g	: Correlation length of the orientational ordering of water molecules	[m]
l_{gap}	: Width of the homogenization valve gap	[m]
m	: Masse	[Kg]
M	: Molecular weight	[kg]
M_{API}	: API molecular weight,	[kg]
M_{SDS}	: SDS molecular weight	[kg]
m_{sp}	: Mass of single particle	[kg]
m_{total}	: Total mass of particles	[kg]
N	: Number of revolutions of the stirrer or rotor	$[s^{-1}]$
n^*	: induction index	[-]
n_0	: Initial concentration of particles	$[m^{-3}]$
n_{0i}	: Number of ions per unit volume	$[m^{-3}]$
N_{ag}	: number of micelles aggregation	[-]
N_{API}	: number of API molecules per micelle	[-]
N_c	: Number of grinding media contact	[-]
N_d	: Number of defects within the initial particle	[-]
N_{gm}	: Number of grinding media in the chamber	[-]
n_k	: Particle concentration	$[m^{-3}]$
N_P	: Power number	[-]
N_{part}	: Number of product particles	[-]
n_{pc}	: Number of polymer chains per unit area.	$[m^{-2}]$
N_Q	: Pumping capacity	[-]
n_t	: Total number of particles	[-]
n_{total}	: Total concentration of particles in suspension	$[m^{-3}]$
o	: Constant	[-]
P	: Pressure,	[Pa]
P.I	: Polydispersity index	[-]

P_1	: Homogenization valve inlet pressure	[Pa]
P_2	: Homogenization valve outlet pressure	[Pa]
Pe	: Peclet number	[-]
P_{ref}	: Pressure at particular point	[Pa]
P_s	: Probability that a particle is sufficiently stressed at media contact	[-]
P_V	: Vapor pressure	[Pa]
P_w	: Power draw	[W]
$P_w(0)$	: No loaded power	[W]
$P_w(t)$	: Power at time t of milling	[W]
P_{wv}	: Power density	[W m^{-3}]
P_{wvmax}	: Maximum power density	[W m^{-3}]
Q	: flow rate	[m^3 s^{-1}]
q	: Number of atoms per unit volume in particles	[m^{-3}]
r	: Radius	[m]
R	: Ideal gas constant	[J mol^{-}1 K^{-1}]
r_η	: Energy transfer coefficient due to viscosity	[-]
Re	: Reynolds number	[-]
R_{eg}	: Geometric factor	[m]
R_{ei}	: Reynolds number within the gap of the homogenization valve	[-]
$R_{el}(h)$	: Geometric function which depends on the segment density.	
R_{ep}	: Reynolds number of particles	[-]
RN	: Recycling number	[-]
r_p	: Effective pore radius of particles	[m]
S	: Bulk solubility.	[mol m^{-3}]
S_0	: API solubility in water	[mol m^{-3}]
SA	: Surface area	[m²]
SA_c	: Cross-sectional area	[m²]
SE_{gm}	: Stress energy of grinding media	[J]
SI	: Stress intensity	[N]
SI_{gm}	: Stress intensity of grinding media	[N]
SN	: Stress number	[-]
S_r	: Solubility of a particle with radius r,	[mol m^{-3}]

S_{r0}	: Solubility of a particle with radius r_0	$[\mathrm{mol\ m^{-3}}]$
Ss	: Saturation solubility	$[\mathrm{mol\ m^{-3}}]$
SSA	: Specific surface area	$[\mathrm{m^2\ kg^{-1}}]$
$SSA_{(\infty)}$	: Specific surface area at equilibrium	$[\mathrm{m^2\ kg^{-1}}]$
$SSA_{(t)}$	: Specific surface area at time t	$[\mathrm{m^2\ kg^{-1}}]$
SSA_v	: Volume specific surface area	$[\mathrm{m^2\ m^{-3}}]$
T	: Temperature	[K]
t	: Time	[s]
t_c	: Recirculation time	[s]
t_{eff}	: Effective milling duration	[s]
t_{eff_r}	: Reduced effective milling duration	[s]
u	: Fluid velocity	$[\mathrm{m^3\ S^{-1}}]$
V	: volume	$[\mathrm{m^3}]$
V_1	: Molar volume of the solvent	$[\mathrm{m^3\ mol^{-1}}]$
V_2	: Molar volume of the polymer	$[\mathrm{m^3\ mol^{-1}}]$
V_{ch}	: Volume of the grinding chamber	$[\mathrm{m^3}]$
V_d	: Volume of a single defect	$[\mathrm{m^3}]$
V_m	: Molar volume of the dispersed phase	$[\mathrm{m^3}]$
V_p	: Total volume of the particles within the mill chamber	$[\mathrm{m^3}]$
v_t	: Beads tangential velocity	$[\mathrm{m\ S^{-1}}]$
V_t	: Tip speed	$[\mathrm{m\ s^{-1}}]$
$V_{t\_Labstar}$:	: Rotation speed of Labstar mill	$[\mathrm{s^{-1}}]$
V_{t_LMZ2}	: Rotation speed of LMZ2 mill	$[\mathrm{s^{-1}}]$
V_{ta}	: Rotation speed applied with stirred annular mill	$[\mathrm{m\ s^{-1}}]$
V_{tp}	: Rotation speed to be applied with stirred pin mill	$[\mathrm{m\ s^{-1}}]$
W	: Stability ratio	[-]
w’	: Constant	[-]
x	: Constant	[-]
x’	: Constant	[-]
y	: Constant	[-]
y’	: Constant	[-]
z_-	: Valency of the negative ion	[-]
z’	: Constant	[-]

z_+ : Valency of the positive ion [-]

GREEK SYMBOLS

$\Omega_{(\infty)}$	: Number of possible configurations of rod like molecule in elastic interaction	[-]
θ	: Contact angle,	[rd]
η	: Viscosity	[Pa s]
ε	: Porosity	[-]
α	: Collision efficiency factor	[-]
ϕ	: Defects density	[m^{-3}]
ν	: Kinematic viscosity	[m^{2} s^{-1}]
γ	: Surface tension	[N m^{-1}]
β	: London dispersion constant	[J m^{6}]
$\tau_{\Phi a}$	: Characteristic time as function of bead filling rtae for stirred annular mill	[s]
$\Omega(h)$	: Reduced number of configurations of molecule in elastic interaction	[-]
$\tau_{\Phi p}$	: Characteristic time as function of bead filling rtae for stirred pin mill	[s]
$\dot{\gamma}$	: Shear rate	[s^{-1}]
Γ	: Adsorbed surfactant or polymer per unit area	[mol m^{-2}]
τ	: Characteristic time	[s]
τ'	: constant with dimensions of time	[s]
ρ	: Density	[Kg/m^{3}]
ψ	: Electrical potential	[j]
Δ	: Shear strain	[-]
σ	: Shear stress	[Pa]
Γ_{∞}	: infinite adsorbed surfactant or polymer per unit area	[kg m^{-2}]
τ_{a}	: Global characteristic time of stirred annular mill	[s]
τ_{cp}	: Characteristic time as function of API loading for stirred annular mill	[s]

ϕ_{gm}	:Filling ratio of the grinding media	[-]
ε_{gm}	: porosity of the bulk of grinding media	[-]
μ_i^s	: Chemical potential per molecule,	[J mol^{-1}]
λ_k	: Kolgomoroff length	[m]
τ_{Na}	: Characteristic time as function of rotation speed for annular mil	[s]
τ_{Np}	: Characteristic time as function of rotation speed for stirred pin mill	[s]
τ_p	: Global characteristic time of stirred pin mill	[s]
ΔSSA	: Created specific surface area.	[m² kg^{-1}]
μ	: Electrophoretic mobility	[m^2 s^{-1} V^{-1}]
$1/\kappa$	:Thickness of double layer known as Debye length	[m]
γ_{LV}	: Liquid-vapor interfacial tensions	[N m^{-1}]
γ_{SL}	: Solid-liquid interfacial tensions	[N m^{-1}]
γ_{SV}	: Solid-vapor interfacial tensions	[N m^{-1}]
ΔG	: Free energy change	[J]
ΔG_A	: Free energy changes (per unit area) corresponding to adhesion	[J m^{-2}]
ΔG_L	: Free energy changes (per unit area) corresponding to immersion	[J m^{-2}]
ΔG_s	: Free energy changes (per unit area) corresponding to spreading	[J m^{-2}]
ΔP	: Capillary pressure	[Pa]
ε_0	: Permittivity of free space	[c²J^{-1}m^{-1}]
ε_r	: Permittivity (dielectric constant)	[F m^{-1}]
ζ	: Zeta potential	[v]
κ	: Decay length of potential	[m^{-1}]
ρ_{gm}	: Beads density	[kg m^{-3}]
ΔP_b	: Pressure loss at the inlet of the valve	[Pa]
ΔP_{bc}	: Pressure loss linked to the frictions in the annular gap	[Pa]
ΔP_{cd}	: pressure loss at the outlet of the valve	[Pa]
Λ	: Cavitation number	[-]
ξ	: singularity coefficient	[-]

ϖ	: Constant	[J mol]
ρ_{gm_PS}	: Polystyrene beads density	[kg m^{-3}]
ρ_{gm_Zr}	: Zirconium oxide density	[kg m^{-3}]
ι	: Gap thickness of the homogenization valve	[m]
λ	: Thickness of diffusion layer,	[m]
Π	: Constant with dimensions of length	[m]
δ	: Stabilizer layer thickness	[m]
χ	: Flory-Huggings parameter	[-]
ω	: pressure ratio	[-]
Ξ	: Constant	[-]
Υ	: Constant	[-]

Abstract

Stabilization and comparison of manufacturing technologies for production of nano-crystalline suspensions

The small particle size of nano-crystalline suspension increases the bioavailability of water insoluble drug and facilitates their direct injection into the systemic circulation as particles. However, this small particle size can be responsible for their physical instability during storage and/or administration. The main challenges related to the production of nano-crystalline suspensions are to select the best stabilizer agent to ensure process-ability and to stabilize the API. Moreover, it is necessary to select the suitable technology for the suspension manufacturing taken into account the industrial constraints (scale-down/scale-up, process robustness and equipment reliability). The present thesis is focused on the formulation and the process development of nano-crystalline suspension.

For the formulation part, we described a systematic approach to select optimum stabilizer for the preparation of nano-suspensions of given drug. The stabilizer can be either a dispersant or a combination of dispersant and wetting agents. The proposed screening method is a fast and efficient way to investigate a large number of stabilizers based on the principles of physical-chemistry and employs a stepwise approach. The methodology has been divided in two main parts; the first part focused on qualitative screening with the objective of selecting the appropriate candidate(s) for further investigations. The second part discussed quantitative screening with the objective of optimizing the ratio and the amount of wetting and dispersing agents. The results clearly showed that SDS/PVP as wetting/dispersing 40/60% (w/w) at a total concentration of 1.2% was the optimum stabilizer composition, at which the resulting nano-suspensions were stable at room temperature. Furthermore, the formulation robustness was assessed by measuring the rate of perikinetic, orthokinetic aggregation rate as a function of ionic strength (using NaCl), temperature and of pH variation. The results show that using the SDS/PVP mixture, the critical coagulation concentration is about five times higher than that observed in the literature for suspension colloidaly stable at high concentration. The nano-suspension was also found to be very stable at different pH conditions. Desorption test confirmed the high affinity between API and wetting/dispersing agent. However, the suspension undergoes aggregation at high temperature due to desorption of the wetting/dispersing agent and disaggregation of SDS micelles. Furthermore, aggregation occurs at very high shear rate by overcoming the energy barrier responsible for colloidal stability of the system.

With respect to process engineering, a technological comparison (high pressure homogenization (HPH) versus bead milling) for the manufacturing of nano-suspension was carried out in terms of impact of suspension formulation, process parameters and technological configuration on the physical quality of the produced suspension. In addition both technologies were compared in terms of their robustness and their compliance to pharmaceutical regulations. The main findings are that, insofar the formulation is sufficiently robust and stable, both technologies are suitable for processing nano-crystalline suspensions. Bead milling is more powerful than HPH. It leads to a limit of milling (d_{50}) lower than that obtained with HPH (100 vs 200 nm). In addition, for both technologies, one can observe that regardless, the process parameters used for milling and the scale, the relationship of d_{90} versus d_{50} could be described by a unique master curve (technology signature of milling pathway) outlining that the HPH leads to a tighten particle size distributions.

Finally, a modelling approach based on adapted Tanka and Chodakov's equation was proposed for modelling the milling kinetic. The generated model provides an accurate fit of milling kinetic, to predict and to simulate the milling manufacturing process.

Abstract in French (Résumé)

Stabilisation et comparaison des technologies de production des suspensions nanocristallines

La faible taille des nanoparticules permet d'améliorer significativement la biodisponibilité des médicaments et faciliter leur administration par voie parentérale sous forme de particules sans risque de bouchage des vaisseaux sanguins. Cependant, cette faible taille peut être un facteur d'instabilité physique pendant le stockage ou/et pendant l'administration. Le principal défi lié à la fabrication des nano-suspensions réside dans leur stabilisation ainsi que dans le choix de la technologie appropriée pour leur fabrication. La présente thèse est centrée sur la stabilisation et la fabrication des suspensions nano-cristallines. Pour la partie formulation, la thèse décrit une approche systématique pour le choix des stabilisants. Ceux-ci peuvent être soit des dispersants ou soit une combinaison de dispersants et d'agents mouillant. La méthode proposée pour le criblage des stabilisants est rapide et efficace. Elle permet d'investiguer un grand nombre de stabilisant en se basant sur des principes physico-chimiques et en utilisant une approche étape par étape. Cette méthodologie a été divisée en deux parties : la première partie a été centrée sur un criblage qualitatif dont l'objectif est de sélectionner une tête de série à investiguer dans la seconde partie. La seconde partie est centrée sur un criblage quantitatif qui a pour objectif d'optimiser le ratio et la quantité d'agent mouillant et de dispersant. Les résultats obtenus ont montré clairement que le système SDS/PVP 40/60 % (m/m) à la concentration de 1.2 % est le stabilisant optimum qui a permis de stabiliser la suspension à température ambiante. Par ailleurs, la robustesse de la formulation a été évaluée en mesurant l'agrégation sous cisaillement ainsi qu'en fonction de la force ionique, la température et du pH. Les résultats ont montré que la concentration critique de coagulation du système étudiée est cinq fois plus importante que celle décrite dans la littérature pour des nano-suspensions concentrées et stables. En revanche, l'agrégation des nanoparticules a été observée à haute température et à haut taux de cisaillement. Pour la partie développement du procédé de fabrication, la thèse est centrée sur la comparaison technologique de l'homogénéisation haute pression (HHP) par rapport au broyage à billes. L'impact de la formulation de la suspension, des paramètres du procédé et de la configuration technologique sur la qualité physique de la suspension produite par chacune des technologies ont été investigués. En outre, les deux technologies ont été comparées en termes de leur robustesse et de leur conformité à la réglementation pharmaceutique. Les conclusions principales de cette étude ont mis en évidence que le broyage à billes conduit à une suspension plus fine que celle obtenue par le HHP. De plus, il a été montré pour les 2 technologies que la relation d_{90} versus

d_{50} est décrite par une seule courbe maîtresse indépendamment des paramètres du procédé et de l'échelle utilisée. Ceci a clairement mis en évidence que la HPH conduit à une distribution granulométrique plus resserrée que celle obtenue par broyage à billes.

Finalement, nous avons modélisé le procédé de broyage à bille en adaptant les équations de Tanka et Chodakov. Le modèle conçu a permis un lissage précis des cinétiques de broyage ainsi que la simulation et la prédiction du procédé de broyage.

Key words in English and French

Key words in English

- Suspension;
- Nanocrystalline
- Milling;
- Stabilization;
- Formulation;
- Homogenisation;
- Solubility.

Key words in French

- Suspension
- nanocristallines;
- Broyage;
- Stabilisation;
- Formulation;
- Homogénéisation;
- Solubilité.

General introduction

1. Introduction

Over the years, the trend in materials and devices has increasingly focused on development toward smaller and smaller length scales. Nanotechnology (derived from the Greek word “nano”, meaning dwarf) is considered as a sudden transition from the micron/sub-micron regime to 1-100 nano-metre (nm) scale. It is the “science of the small” referring to "understanding and controlling matter" at dimensions of roughly 1 to 100 nm (1 nanometer = 1 nm = 10^{-9} m). It involves the manufacturing, imaging, measuring, modelling of the matter at this scale and the understanding of its properties and their interaction in particular with the living world. At the nano-scale, materials exhibit unique properties that are not shared at larger bulk sizes or smaller molecular scale, mostly due to the high proportion of atoms located at the surface of on a nanoparticle resulting in a more reactive agent (1). A wide variety of scientific fields and industries are taking advantage of these unique properties (size, boiling point, melting point, solubility, crystal structure, electronic structure, quantum confinement, light scattering, diffusion, etc.) to provide novel functions, attributes and products.

An overview of active applications of nanotechnologies is described below (2):

i) Medicine and biomedical devices for diagnosis, treatment, monitoring, and control of biological systems;
ii) Composites materials manufacturing using carbon nano-tubes that present both flexibility and significant tensile strength (about 100 times stronger than steel);
iii) Electronic circuits manufacturing by using carbon nano-tubes for cables and electronic connection miniaturization;
iv) Flat screens manufacturing (brighter and more energy effective than LCD and plasma screens) by using carbon nano-tubes;
v) Textile: nano-particles (metal oxides or carbon nanotubes or clay) can be mixed with polymers before extrusion, thus introducing new material functionality (improved mechanical properties, reduced shrinkage, anti-bacterial effect, flame retardants capacity, UV stability, conductivity, wear resistance, reduced creep, etc.);
vi) Energy: batteries in which components are made of nano-particles would be longer-lasting and would have a higher energy density than those we use nowadays. Metal

nanoparticle clusters could also have revolutionary applications for hydrogen storage; they could also produce extremely efficient fuel cells by acting as electro-catalysts for these devices. Nano-particles may also open the way for more practical and renewable energy. They have already demonstrated many times the ability to improve solar panel efficiency many times over. Furthermore, when nano-particles are used as catalysts in combustion engines, they have shown properties that render the engine more efficient and therefore more economic;

vii) Thermal: specifically engineered particles could improve the transfer of heat from collectors of solar energy to their storage tanks. They could also enhance the cooling system currently used by transformers in these types of processes;

viii) Mechanical: nano-particles could provide improved wear and tear resistance for almost any mechanical device. They could also give to these devices previously unseen anti-corrosion abilities, as well as creating entirely new composites and structural materials that are both lighter and stronger than nowadays ones;

ix) Optical: Nano-particles could be engineered and used for anti-reflection product coatings, producing a refractive index for various surfaces, and also providing light based sensors for use e.g. in diagnosing cancer;

x) Cosmetic: the best known and most widely used nanomaterial is titanium dioxide (TiO_2). This mineral is known for its ability to reflect, scatter and absorb ultra-violet (UV) and to protect against the deleterious effects caused by prolonged sun exposure. It has been used in sunscreen products in the form of nano titanium dioxide for nearly 20 years. Titanium dioxide in nano form has a double advantage: it is a more effective sunscreen and is more transparent than the micrometric form. Indeed, it is nice to apply a sunscreen that does not make the face or "all white" body.

The present thesis is focused on the application of nanotechnologies in pharmaceutical industry specifically when using nano-crystalline suspensions to overcome the low solubility of Active Pharmaceutical Ingredients (API). The main scope is the stabilization and the manufacturing of nano-crystalline suspensions by ultra-fine milling. The plan of this dissertation is as follows:

Firstly, a bibliographic review will be presented where the following topics will be presented:

(i) Applications of nanotechnologies in medicine and biomedical devices will be detailed;

(ii) Different manufacturing processes for the production of nano-crystalline suspensions will be described;

(iii) Formulation design and engineering for the production of nano-crystalline suspensions by ultrafine milling;

(iv) Process engineering for the production of nano-crystalline suspensions by ultrafine milling.

Afterwards, the results of experimental section related to formulation engineering and a systematic comparison of manufacturing technologies (high pressure homogenization versus bead milling) will be presented and discussed. The last part will be dedicated to bead milling modelling for process prediction and simulation.

Bibliography review

2. Bibliographic review

2.1. Application of nanotechnologies in medicine and biomedical

Applications of nanotechnology in this field refer to the diagnosis, treatment, monitoring, and control of biological systems. For diagnosis, colloidal gold, iron oxide crystals, and quantum dots (QDs) semiconductor nano-crystals are examples of nano-particles used in diagnostic applications in biology and medicine. For the diseases treatment, nanotechnologies are aimed at overcoming formulation and biopharmaceutical limitations in terms of solubility, absorption, and distribution. Nano-particles enhance the bioavailability of highly insoluble drugs since the submicron particles (radius < 200 nm) have higher solubility when compared to larger particles (radius > 1 μm). Biodegradable nano-particles that can be prepared using block copolymers such as polylactic polyglycolic acid offer a potential for targeted delivery of drugs. This is the particular case of anti-cancer drugs whereby the molecules can be directed specifically to the cancer cells, thus reducing the overall dosage applied and hence significantly reducing side effects. In medicine, a wide variety of nano-particles composed of a range of materials including lipids, polymers and inorganic materials have been developed, resulting in delivery systems that vary in their physicochemical properties and thus their applications (3–6). The Figure 1 shows an array of nano-particulate drug delivery systems that have been investigated.

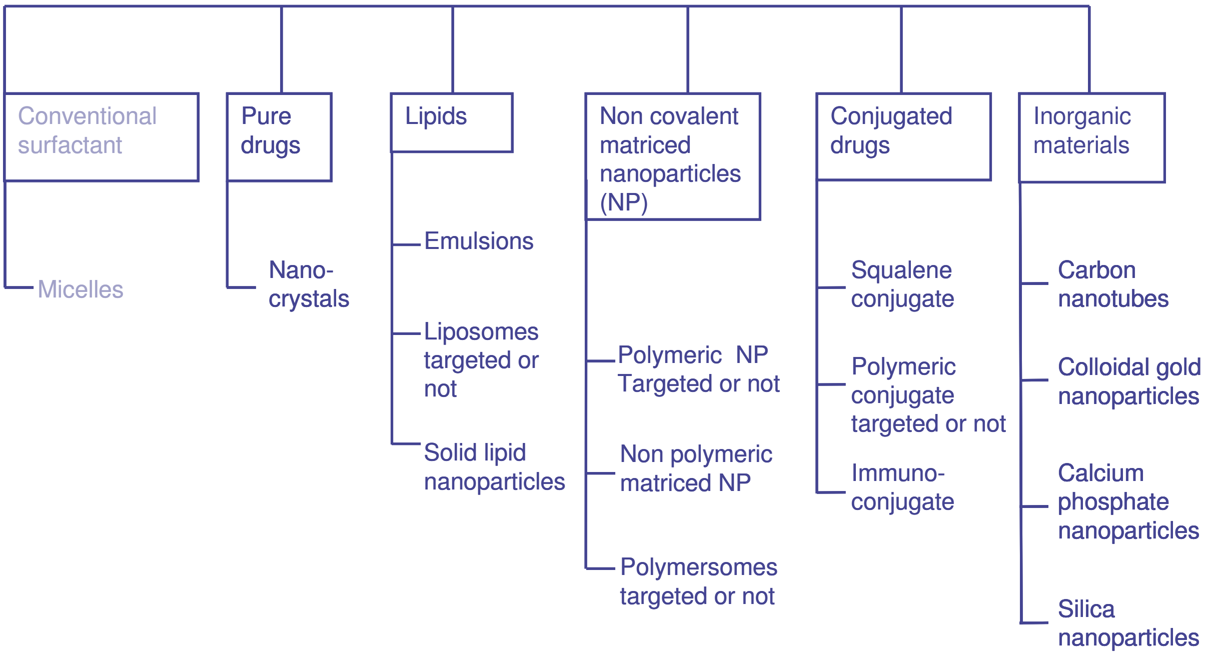

Figure 1 : different investigated drug delivery systems (7)**.**

2.1.1. Biopharmaceutical advantages of nano drug delivery systems

The biopharmaceutical advantages of different drug delivery systems are summarized in the Table 1.

Drug delivery system	**Biopharmaceutical advantages**
Micelles (8)	Enable the injection of poorly soluble drugs. Drug release quick after i.v. injection, and thus mimic the pharmacokinetics of the drug injected in the form of solution.
Crystalline nano-particles (9,10)	Enable the injection of poorly soluble drugs. Quick drug release after i.v. injection, and thus mimic the pharmacokinetics of drug injected in the form of solution.
Amorphous nano-particles (11)	Enable the injection of poorly soluble crystalline drugs, Enhance the drug dissolution in blood Quick drug release after i.v. injection, and thus mimic the pharmacokinetics of drug injected as solution.
Emulsions (12,13)	Enable the injection of poorly soluble drugs.

	Alter the pharmacokinetic profile of the encapsulated drugs
Liposomes (14,15)	Controlled drug release *in vivo* (allows delivery of drugs for both systemic and topical applications). Allow delivery of hydrophobic and hydrophilic drugs or their combination. Alter the pharmacokinetic profile of the encapsulated drugs. Accumulate in the organs with leaky/inflamed endothelium (eg. tumor, inflammation), and thus result in higher drug concentrations in these tissues. Improve efficacy and safety of the encapsulated drugs.
Targeted liposomes (16)	In addition to the benefits of the liposomes, the targeted liposomes allow targeting to a specific organ/tissue/cell, with the employment of homing device. Enhance the delivery of drugs through biological barriers (eg. cell membrane, blood brain barrier, blood intestinal barrier). Allow simultaneous therapy and imaging of the disease for monitoring of the response to therapy. Targeted liposomes loaded with imaging agents allow the diagnostic imaging of the pathological sites in the body.
Solid lipid nano-particles (17,18)	Controlled drug release *in vivo* (allows delivery of drugs for both systemic and topical applications). Alter the pharmacokinetic profile of the encapsulated drugs. Accumulate in organs with leaky/inflamed endothelium (eg. tumor, inflammation), and thus result in higher drug concentrations in these tissues.
Polymeric nano-particles (19)	Controlled drug release *in vivo* (allows delivery of drugs for both systemic and topical applications). Allow modulating drug release *in vivo* by optimizing the polymer material composition. Improve the efficacy and safety of the encapsulated drugs. Allow detoxification of blood contaminated with the toxic substances, owing to the nano-particles' high surface area.
Targeted polymeric nano-	In addition to the benefits of the polymeric nano-particles, the

particles (20)	targeted ones allow targeting of a specific organ/tissue/cell, with the employment of homing device. Allow simultaneous therapy and imaging of the disease for monitoring of the response to therapy. Targeted polymeric nano-particles loaded with imaging agents allow the diagnostic imaging of the pathological sites in the body. Enhances the delivery of drugs through biological barriers (eg. Cell membrane, blood brain barrier, blood intestinal barrier).
Polymersomes (21,22)	Allow delivery of hydrophobic and hydrophilic drugs or their combination. Alter the pharmacokinetic profile of the encapsulated drugs. Accumulate in organs with leaky/inflamed endothelium (e.g. tumor), and thus result in higher drug concentrations in these tissues. Enhance the efficacy and safety of the encapsulated drugs.
Targeted polymersomes (23)	In addition to the benefits of the polymersomes, the targeted polymersomes allow targeting of a specific organ/tissue/cell, with the employment of homing device. Allow simultaneous therapy and imaging of the disease for monitoring of the response to therapy. Targeted polymersomes loaded with imaging agents allow the diagnostic imaging of the pathological sites in the body.
Inorganic nano-particles (24,25)	Alter the pharmacokinetics of the associated drugs, allow stimuli-sensitive drug release at the disease site. Allow imaging of the organs/tissues/cells and pathological sites in the body (eg. iron oxide (magnetic field-responsive), gold nano-particles (optically-responsive), quantum dots (optically-responsive)). Plasmonic nano-particles (eg. gold) allows generating local heat at the sites of nanoparticle accumulation, and thus allows stimulus-mediated drug release or heat-induced cell kill/tissue damage.

	Some inorganic nano-particles (eg. cerium oxide) could be employed as biosensors.

Table 1 : Biopharmaceutical advantages of different drug delivery systems.

2.1.2. Context of using nano-crystalline suspensions in pharmaceutical industry

Nowadays, the discovery of drugs results lead to an increasing number of highly water insoluble active pharmaceutical ingredients (API). This low water solubility will result in poor bio-availability and/or food effect for oral administration. Consequently, in order to achieve the therapeutic drug concentration a dose escalation will be required which may leads to toxicity and reduction of patient convenience. For parenteral administration the poor water solubility issue will lead to a limitation of API formulation. The issue is even more intense for API belonging to class III (classified by Washington 1996), as they are poorly soluble in both aqueous and/or organic media, and for API having low log P value (26). Common strategies, such as micronization, solubilization using co-solvents, the use of permeation enhancers (27,28), oily solutions (27) and surfactant dispersions (29), have limited use. Although reasonable success has been achieved in formulating water-insoluble drugs using liposomes (30), emulsions (31), micro-emulsions (32), solid dispersion technology (33,34) and inclusion complexes employing cyclodextrins (35,36) (Figure 2), there is no universal approach applicable to all API. Consequently, there is a growing need for a universal strategy that can overcome the hurdles related to the challenges associated with the delivery of hydrophobic drugs in order to improve their clinical efficacy and optimize their therapy with respect to the biopharmaceutical requirements.

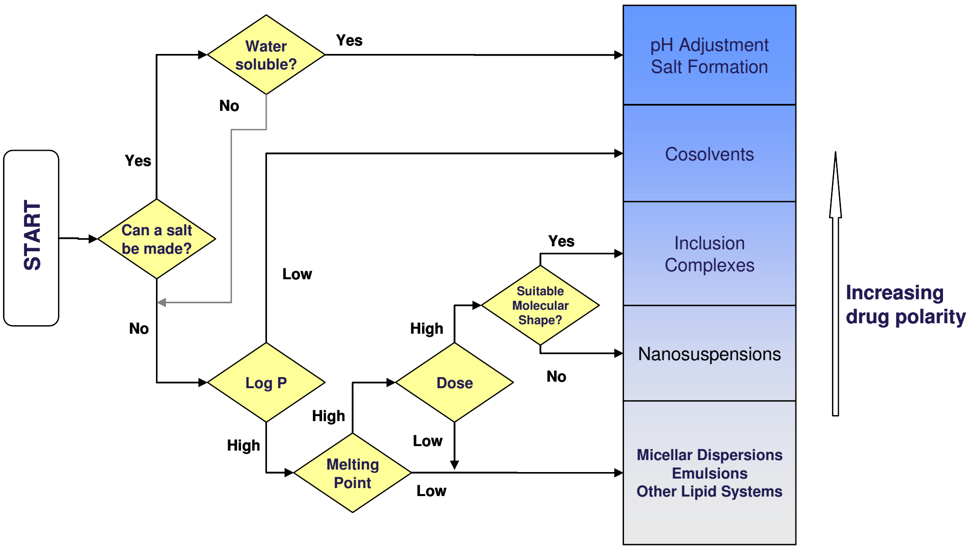

Figure 2 : Formulation strategies of insoluble APIs (37)**.**

Nano-suspensions have been applied for drug delivery of poorly water-soluble and poorly lipid-soluble APIs. They are unique because of their simplicity and have advantages improved over other strategies. Reduction of the particle size of the API will results in an improvement of bioavailability (38)(i.e. increasing exposure) by increasing dramatically the dissolution rate (ds/dt) due to the combination of specific surface area increase (SSA), saturation solubility increase (S_s) and reduction of thickness of the diffusion layer (λ). This is shown by Whitney equation (39,40) (see (Eq. 1))

$$\frac{\mathbf{dS}}{\mathbf{dt}} = \frac{\mathbf{D_f \times SA}}{\boldsymbol{\lambda}} \times (\mathbf{S_s - S}) \qquad \text{(Eq. 1)}$$

Where ds/dt is the dissolution rate, D_f is the diffusion coefficient, SA is the surface area, λ is thickness of diffusion layer, S_s is the saturation solubility and S is the bulk solubility. When the particle size is below 1-2 µm an increase on saturation solubility occurs (41) due to a high intrinsic dissolution pressure linked to much higher particle curvatures (see Figure 3).

Figure 3 : Increase of dissolution pressure as a function of the curvature of particles (42)

This can be understood from Ostwald–Freundlich equation (43) (see (Eq. 2)):

$$\ln\left(\frac{S_r}{S_{r0}}\right) = \frac{2 \times M \times \gamma}{\rho \times R \times T} \times \left(\frac{1}{r} - \frac{1}{r_0}\right) \quad \textbf{(Eq. 2)}$$

Where S_r is the solubility of a particle with radius r, S_{r0} is the solubility of a particle with radius r_0, ρ is the density, ɣ is the surface tension and M is the molecular weight of the dispersed phase. For a flat starting particle (r_0 approaches infinity) the increase in solubility ratio, S_r/S_{r0}, has been calculated to be larger than 2, as the particle size is reduced below 200 nm (44). This is the basis of production of nano-particles with r ≤ 100 nm (see Figure 4).

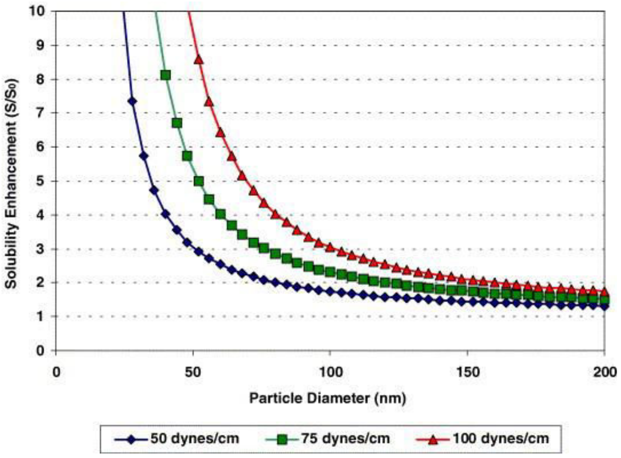

Figure 4 : Solubility as a function of particles radius (44).

The reduction of thickness of diffusional layer can be understood by the increasing of concentration gradient between the bulk and the diffusional layer (see Figure 5).

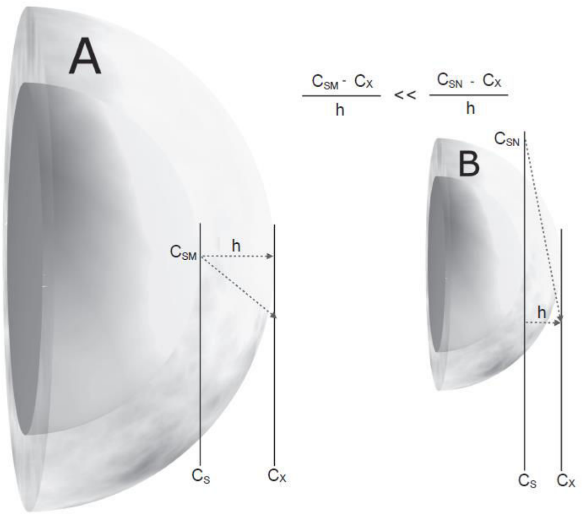

Figure 5: Increase in dissolution velocity due to the reduction of the diffusional layer (10)**.**

From the biopharmaceutical stand point, the intravenous administration of nano-crystalline suspension, could be comparable to the injection of solution (45). Indeed, if nano-particles cannot be solubilized quickly enough in the blood, they are rapidly opsonized and captured by the macrophages of the liver and spleen. As an additional advantage, the injectable dose can be increased for the parenteral administration as nano-particles are made essentially of pure drug and using a small amount of excipient. In contrast, the standard formulation using a solvent such as polysorbate leads to a limited amount of injected API due to the safety threshold of the excipient (46) (see Figure 6)

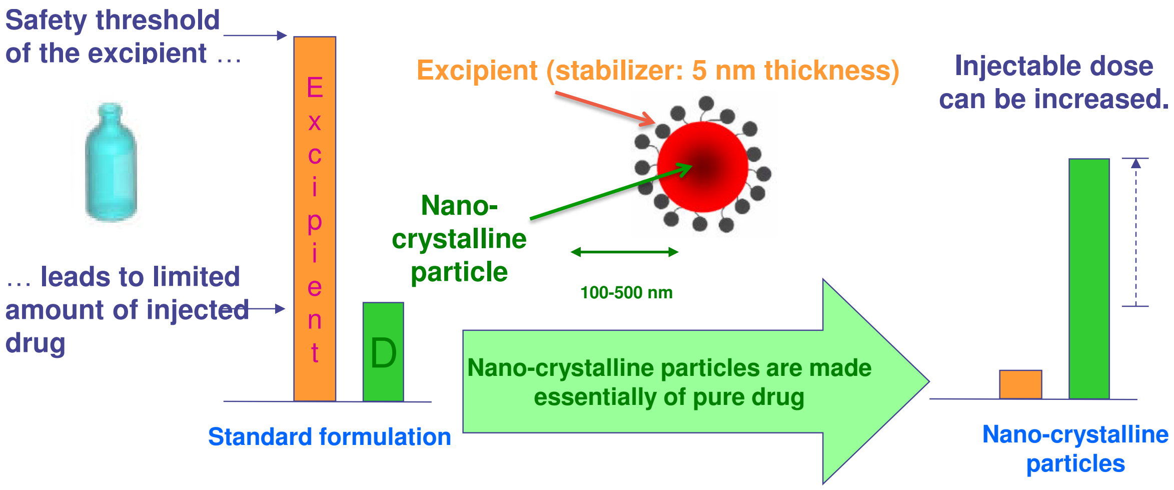

Figure 6 : Nano-crystalline particle advantage with regard to excipient safety (46)**.**

Nano-crystalline suspensions exhibit many advantages as discussed above. However, a risk assessment needs to be carried out regarding their deviation from the expected quality, as function of the route of administration.

For the oral administration of nano-crystalline suspension, a slight variation of the particle size may have no impact since the dissolution and the bioavailability may not be affected. At the same time, the safety profile, if related to the plasmatic exposure to the drug, is not considered to be different from standard solid dosage form.

For the parenteral route, the variation of the particle size may have significant impact. Indeed, the infusion rate should not go beyond the distribution and the solubilisation capacity of the body (47). A particular effort needs be done in order to reduce the particle size (to achieve mean diameter < 200 nm) and to control the particle size distribution in order to mitigate the risks of embolism of the thinnest capillaries (the lumen diameter is about 6 µm) (48,49). In addition it should be considered that activation of the complement and coagulation of nano-particles by nano stealth may lead to aggregation as bigger particles. Here, the adaptation of the infusion rate to the dispersing and solubilisation capacity of the blood needs to be taken into account.

2.1.3. Marketed product as nano-crystalline suspensions

The list of marketed product is described in the Table 2

It can be outlined that nano-crystalline suspension approach developed by Elan Nanosystems (Alkermess) was employed to produce the first three FDA-approved products: Rapamune®, Tricor®, and Emend®, and is expected to be broadly applicable to a range of drugs that suffer from solubility issues, which is an estimated 70–90% of potential drug compounds (38,50). It is noteworthy that the most of the marketed products are manufactured using Alkermess technology that involves a pearl/ball mill able to shear particles apart during agitation.

Product (broad name)	Used API	Indication	manufacturer	Year approved
Avinza®	Morphin sulphate	Psychostimulant	Alkermes/Pfizer	2002
Emend®	Aprepitant	Anti-emetic	Alkermes/Merck	2003
Focalin XR®	Dexmethylphenidate Hcl	Psychostimulant	Alkermes/Novartis	2005
Invega® Sustena®	Palperidone	Schizophrenia	Janssen Pharms	2009
Invega® Sustena®	Palperidone	Schizoaffective Disorder	Janssen Pharms	2014
Rapamune®	Sirolumis	Imunosuppressant	Alkermes/Wyeth	2000
Megace ES®	Megestrol Acetate	Anti-anorexic	Alkermes/Par/BMS	2001
Ritalin LA®	MethylPhenediate Hcl	psychostimulant	Elan/Novartis	2002
Tricor®	Fenofibrate	Lipid reduction	Alkermes/Abbott	2004
Triglide®	Fenofibrate	Lipid reduction	Skye Pharma/First Horizon Pharamceuticals/ Sciele Pharmla	2005
Zanaflex®	Tizanedine HCl	Muscle relaxant	Acorda	2002
Vitoss®	Calcium phosphate	Bone substitute	Stryker	2003
Ostim®	Hydroxyapatite	Bone substitute	Heraseus Kulzer	2004
OsSatura®	Hydroxyapatite	Bone substitute	Iso Tis Orthobiologics	2003
NanOss®	Hydroxyapatite	Bone substitute	Riti Surgical	2005
Equivabone®	Hydroxyapatite	Bone substitute	Zimmer Biomet	2009
Ryanodex®	Dantrolene sodium	Malignant hypothemia	Eagle Pharmaceuticals	2014

Table 2 : List of marketed product based on nano-crystalline particles (38,50).

2.1.4. Nano-crystalline products in clinical evaluation

The Overview of various drug candidates in clinical trials is given in the Table 3.

One can observe that the most of the products in clinical investigation are manufactured using Alkermess technology.

Trade name	Therapeutic use	Applied technology	Pharma company	Administration route	Status (Phase)
Fenofibrate	Lipid lowering	SkyePharma	Undisclosed	Oral	I
Insulin	Diabetes	BioSante	Self-developed	Oral	I
Busulfan	Anti-cancer	SkyePharma	Supergen	Intrathecal	I
Budesonide	Asthama	Elan Nanocrystal	Sheffield Pharmaceuticals	Pulmonary	I
Calcium phosphate	Mucosal vaccine	Biosante	Self-developed	Oral	I
Thymectacin	Anticancer	Elan Nanocrystal	NewBiotics/IIex oncology	Intravenous	I/II
Megesstol Acetate	AIDS related weight loss	Elan Nanocrystal	Par Pharmaceuticals Inc.	Oral	II
Panzem® NCD (2-methoxy estradiol)	Ovarian cancer	Elan Nanocrystal	EntreMed	Oral	II
Panzem® NCD	Recurrant glioblatoma multiform	Elan Nanocrystal	EntreMed	Oral	II
Panzem® NCD and Tamozolomide	Anti-cancer	Elan Nanocrystal	EntreMed	Oral	II
Panzem® NCD and Avastin (Bevacizumab)	Carcinoid tumor	Elan Nanocrystal	EntreMed	Panzem-Orally Bevacizumab-Intravenously	II
Panzem® NCD with and without Sanitinib Malate	Renal cell carcinoma	Elan Nanocrystal	EntreMed	Oral	II
Panzem® NCD Fenofibrate	Prostate cancer	Elan Nanocrystal	Solvay Pharmaceuticals	Oral	II

	Sleep apnea Syndrome				
Undisclosed	Antiinfective	Baxter NANOEDGE	Undisclosed	Oral/Intravenous	II
Cytokine inhibitor	Crohn’s disease	Elan Nanocrystal	Cytokine Pharmasciences	Oral	II
Guanylhydrazone (Semapimod®)	TNF-alpha inhibitor	Self-developed	Cytokine Pharmasciences	Intravenous	II
Themectacin (TheraluxTM)	Anticancer	Elan Nanocrystal	Celmed	Intravenous	II
Silver (Nucryst®)	Atopic dermatitis	Self-developed	Nucryst Pharmaceuticals		II
Paclitaxel (PaxceedTM)	Anti-inflammatory	Unknown	Angiotech	Intravenous	III
Paclitaxel	Anticancer	Unknown	American Pharmaceutical Partners	Intravenous	III

Table 3 : overview of various drug candidates in clinical trials (38).

2.2. Manufacturing of nano-crystalline suspensions

Nano-crystalline suspensions can generally be prepared by two methods: ‘bottom up’ and ‘top down’ processes. The bottom-up technologies involves controlled precipitation or crystallization. The top down technologies consist of particle size reduction. However, combination of techniques that involve a precipitation step followed by a size reduction are also being used to produce nano-particles with the desired size distribution (51).

2.2.1. Bottom up process

The bottom up technologies starts from the molecules which are dissolved and precipitated by adding the solvent (generally organic) phase to a non-solvent one (generally water). In this case the preparation of the nano-particles is done by condensation methods (formation of particles by nucleation and crystal growth).

This process is classified in two categories: solvent diffusion and emulsification

2.2.1.1. Solvent diffusion

The API and lipophilic stabilizer are dissolved in an organic solvent which is miscible to water. The hydrophilic stabilizer is dissolved in water. The two solutions are mixed together in order to form a precipitate by organic solvent diffusion in water. The organic solvent is then removed by evaporation. This process category is illustrated by the flow chart described in the Figure 7.

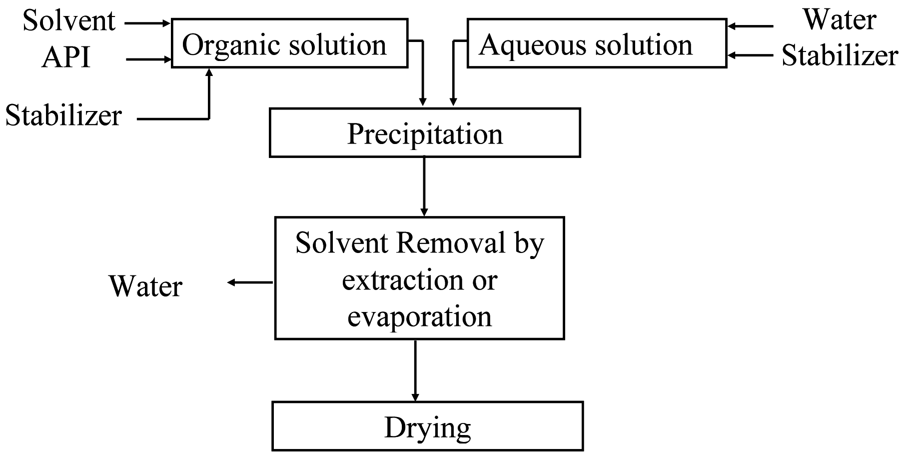

Figure 7 : Flow chart of solvent diffusion method (52).

2.2.1.2. Emulsification

The API and emulsifier are dissolved in an organic solvent which is non-miscible to water. The hydrophilic stabilizer is dissolved in water. The two solutions are mixed together in order to form an emulsion. The size of formed vesicles is then reduced by high pressure homogenization. This step is followed by solvent removal (by evaporation) in order to form the nano-particles. This process category is illustrated by the flow chart described in the Figure 8.

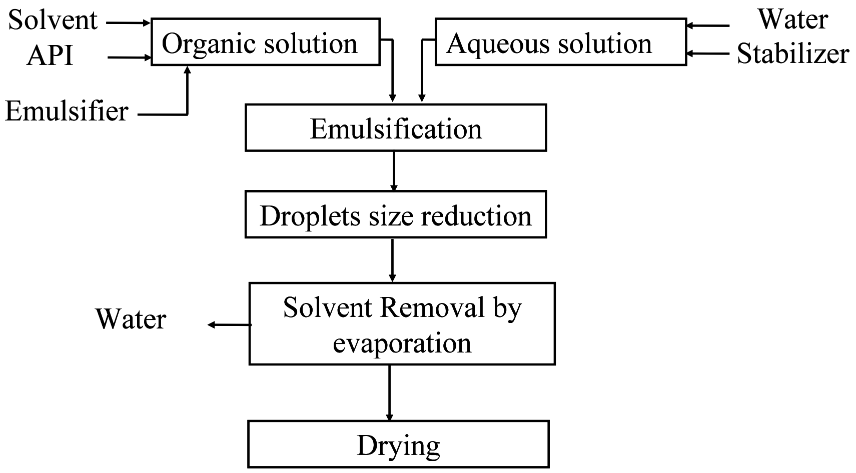

Figure 8 : Flow chart of emulsification method (52).

For both process categories, the achievement of mono-disperse nano-particles or poly-disperse system with narrow particle size distribution requires control of the process of nucleation and particle growth. With most disperse systems where the particles have some finite solubility, the smaller particles have higher solubility than the larger ones. With time, molecular diffusion occurs from the smaller to the larger particles resulting in a shift of the particle size distribution to larger values, a process referred to as Ostwald ripening (53). It is therefore necessary when preparing nano-particles using condensation method to reduce Ostwald ripening to a minimum by producing dispersion with a narrow size distribution. In addition, crystal growth inhibitors such as polymeric surfactants that adsorb very strongly on the particle surface must be used. If a substance becomes less soluble by a change of some parameters, such as temperature decrease or addition of a non-solvent, the solution may enter a metastable state with the formation of some precipitate or nuclei.

The classical theory (54) considers the nucleus to consist of a bulk phase containing N^{s}_{i} molecules and a shell with Ni^{σ} molecules which have a higher free energy per molecule than the bulk. The Gibbs free energy of the nucleus G^{s} is made of a bulk part and a surface part (see (Eq. 3)):

$$\mathbf{G^{S} = \mu_i^{S} \times N_i^{S} + \gamma_{sL} \times SA} \qquad \text{(Eq. 3)}$$

Where μ_i^s is the chemical potential per molecule, γ_{SL} is the solid/liquid interfacial tension and SA is the surface area of the nucleus. In a supersaturated solution the activity a_i is higher than that of a saturated solution $a_i^{(sat)}$. As a result molecules are transferred from the solution to the nucleus surface. The free energy change ΔG^s, upon the transfer of a small number N_i from the solution to the particle, is made of two contributions from the bulk and the surface (see (Eq. 4)):

$$\Delta \mathbf{G^S} = \Delta \mathbf{G^S_{bulk}} + \Delta \mathbf{G^S_{Surface}} \qquad \textbf{(Eq. 4)}$$

The first term on the right hand side of (Eq. 4) is negative (it is the driving force) whereas the second term is positive; work has to be carried out to expand the interface. $\Delta G^s_{(bulk)}$ is determined by the relative super-saturation, whereas $\Delta G^s_{(surface)}$ is determined by the solid/liquid interfacial tension γ_{SL} and the interfacial area SA which is proportional to $(N_i^s)^{2/3}$.

Figure 9 shows a schematic representation of the dependence of ΔG^s on r. This figure shows that ΔG^s reaches a maximum at a critical nucleus size r*; the latter decreases with increase of the relative super-saturation. It also decreases with decrease of the solid/liquid interfacial tension γ_{SL} which shows the importance of effective surfactants in reducing γ_{SL}.

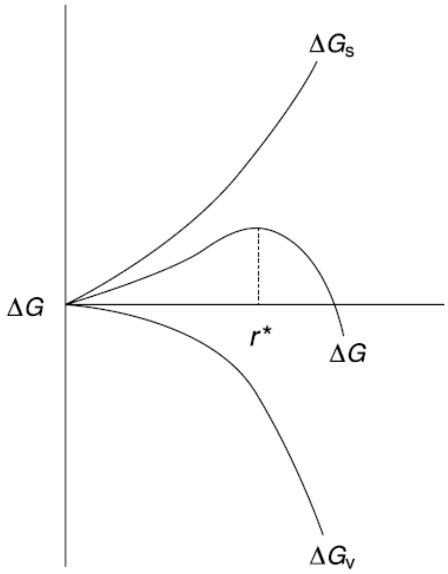

Figure 9: Schematic representation of the effect of super-saturation on particle growth (52).

The bottom up process is much less used than the top-down process for the manufacturing of nano-crystalline suspensions due to the following reasons:

Firstly, it is very difficult to control the crystalline structure of the produced nano-particles. In most cases, nano-particles are in amorphous state and exhibit physical instability. Secondly by using the solvent diffusion method, the spontaneous formation of nano-particles only takes place for very dilute systems (1%) due to Ouzo effect (55).

2.2.2. Top down process

The top down process (particle size reduction method) is the most commonly used method for the preparation of the nano-crystalline suspensions due to the possibility of controlling particle size by a proper choice of wetting / dispersing agent as well as by controlling the milling conditions. The top down process consists of dispersing the powder (in form of aggregates and agglomerates) in the liquid (usually water) into single particles. This is followed by a wet milling process for reduction of particle size. Finally, the nano-crystalline particles must be stabilized against flocculation and crystal growth (Ostwald ripening). The obtained suspension could be kept as it is if it is chemically and physically stable. In the opposite case, the suspension have to be dried by using spray drying or freeze drying or fluid bed granulation. The process principle and its flow chart are illustrated in the Figure 10 and Figure 11.

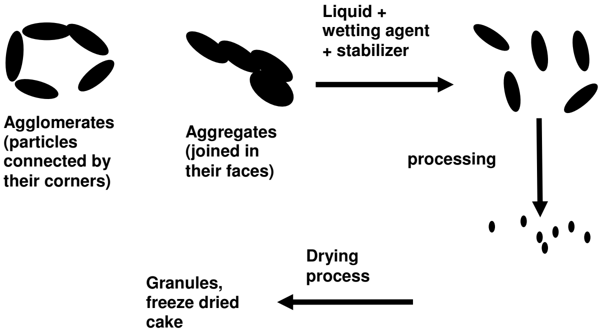

Figure 10 : Principle of manufacturing of nano crystalline suspension (52).

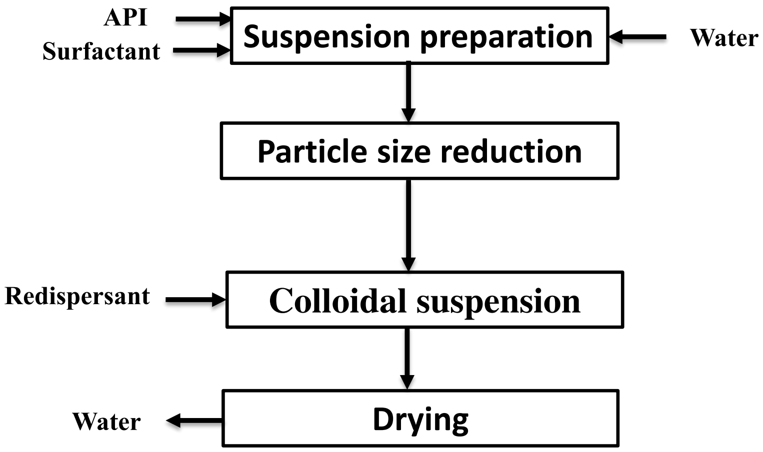

Figure 11 : Process flow chart of top down process (52)**.**

The top down process has several advantages as compared to the bottom up process. In fact, as far as the selected crystalline form of the API is the stable one in the milling vehicle (generally water), the following advantages can be derived:

Firstly, APIs that are poorly soluble in organic and aqueous media can be processed. Secondly, the number of manufacturing steps is significantly reduced (4 versus 6). In addition, the risk to generate amorphous state or polymorphic transition is negligible. In fact, in contrast to dry milling processes, during wet milling of crystalline drugs the water may behave as an inhibitor of the formation of amorphous material due to the reduced glass-transition temperature (56). Furthermore, it is very easy to control the particle size of the suspension. Moreover, it is possible to process very high concentrated suspension (up to 40 % w/w). Finally, the scaling up of the process is very easy and well known.

The purpose of the present thesis will be focused on the formulation and process engineering for the nano-crystalline suspensions from the preclinical evaluation up to commercial batches manufacturing using the top down process. Thus, in the next sections of this chapter, the basic principles of formulation engineering (API powder wetting and nano-particles stabilization) will be reviewed. Then, the particle size reduction step will be reviewed in terms of different applied technologies, scaling up and process modelling. However, the formulation and process engineering of drying steps will not be discussed.

2.3. Formulation engineering considerations for manufacturing of nano-crystalline suspension by top down process

As described in the section 2.2.2 and according to T.Tadros (54), in an API powder of any material the aggregates and agglomerates are held together by very strong attractive forces. When aggregates and agglomerates are dispersed in a liquid medium, the attractive forces are reduced but still sufficient to keep the particles strongly attached together. To separate the particles in such aggregates or agglomerates and to disintegrate them, a combination of milling process and addition of wetting/dispersant agents is required to overcome such attractive forces. The main purpose of dispersing a powder in a liquid is the wetting and separation of primary particles from aggregates and agglomerates and their subsequent stabilization in the liquid medium. This requires an effective wetting agent that adsorbs very rapidly at the solid/liquid interface. The main criteria for an effective dispersant is a strong adsorption or ‘’anchoring’’ to the particle surface. This requires multi-point attachment of the dispersant to the particle surface. The ‘’anchor’’ chain should be insoluble in the medium and should have strong affinity to the surface.

Accordingly, in this section, the formulation engineering will be reviewed in terms of:

i. Basic characteristics of wetting aspects;
ii. Microscopic inter-particles interaction forces (DLVO forces and steric forces);
iii. Mechanisms of destabilization of nano-particles;
iv. Assessment of electrostatic and steric stabilization;
v. Macroscopic forces that could impact the suspension stability.

2.3.1. Wetting phenomena

Wetting is a critical practical application involving mixtures of powders and liquids. Wetting can be defined as the process of displacement at a solid surface of one fluid by another one. In general, the fluids may be a liquid and a gas or two immiscible liquids.

In the case of powders, most pharmaceutical applications are linked to the preparation of a suspension of particles in a liquid. Wetting behaviour is essentially determined by the interaction forces at the different solid-fluid and fluid-fluid interfaces. Characterizing the wetting behaviour is an important component for the suspension preparation.

Three distinct stages in the wetting of a solid surface can be defined (57). The first stage is adhesional wetting which refers to the establishment of a three-phase contact at the solid surface. The second stage is a spreading wetting which involves displacement of one fluid by the other at the solid surface. Finally, the third stage is immersional wetting which represents the complete transfer of a solid particle from one fluid phase to the other. Thermodynamically, the free energy changes involved in the different stages can be expressed as follows:

$$\Delta G_A = \gamma_{SL} - \gamma_{SV} - \gamma_{LV} \qquad \text{(Eq. 5)}$$

$$\Delta G_S = \gamma_{SL} - \gamma_{SV} + \gamma_{LV} \qquad \text{(Eq. 6)}$$

$$\Delta G_L = \gamma_{SL} - \gamma_{SV} \qquad \text{(Eq. 7)}$$

Where ΔG_A, ΔG_s, ΔG_L are the free energy changes (per unit area) corresponding to adhesion, spreading and immersion, respectively. γ_{SL}, γ_{SV} and γ_{LV} are the solid-liquid, solid-vapor and liquid-vapor interfacial tensions, respectively.

The conditions corresponding to three-phase equilibrium (partial wetting) can be conveniently characterized by the means of the contact angle θ defined, through the liquid phase, as shown in Figure 12.

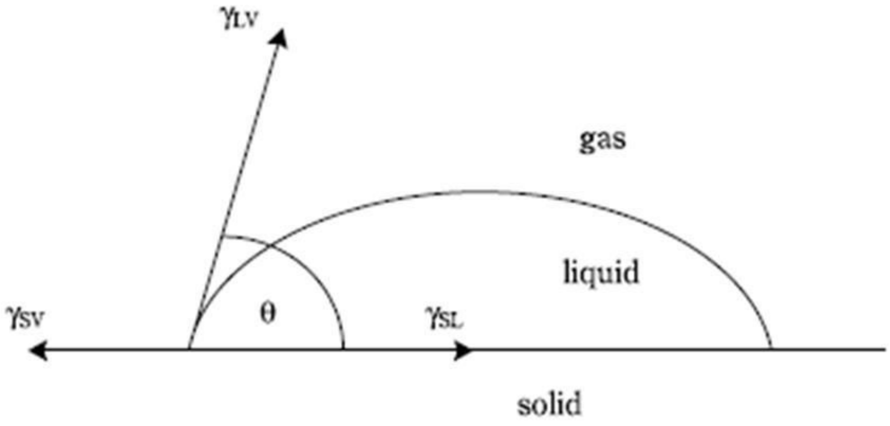

Figure 12 Contact angle at a solid surface as measured through the liquid phase (58)**.**

Thermodynamically, the three-phase equilibrium can be expressed by Young's equation:

$$\boldsymbol{\gamma_{SV} = \gamma_{SL} + \gamma_{LV} \times \cos\theta} \qquad \text{(Eq. 8)}$$

By substitution from (Eq. 8), the free energies given by (Eq. 9), (Eq. 10) and (Eq. 11) can also be expressed in terms of the contact angle as follows:

$$\boldsymbol{\Delta G_A = -\gamma_{LV} \times (1 + \cos\theta)} \qquad \text{(Eq. 9)}$$

$$\boldsymbol{\Delta G_S = -\gamma_{LV} \times (1 - \cos\theta)} \qquad \text{(Eq. 10)}$$

$$\boldsymbol{\Delta G_I = -\gamma_{LV} \times \cos\theta} \qquad \text{(Eq. 11)}$$

Thus the immersion wetting of the external surface of the powder depends on the liquid surface tension and the contact angle. If the contact angle is lower than 90° transfer of a solid particle from the gas to a liquid phase leads to a lowering of the free energy and is, therefore wetting is spontaneous.

The control of the wetting behaviour can be obtained through the addition of surface-active agents to the liquid phase. So-called wetting agents enhance spreading by reducing the liquid-gas or solid-liquid interfacial tensions (or both). In addition, one of the expected added values of wetting agent is to get maximum reduction in the surface energy of the powder. In fact, Rehbinder *et al*. investigated the role of surfactants in the grinding process. It was found that, as a result of surfactant adsorption at the solid/liquid interface, the surface energy at the boundary is reduced, which facilitates the process of deformation or destruction. The adsorption of surfactants at the solid/liquid interface in cracks facilitates their propagation. This mechanism is referred to as the Rehbinder effect (59).

2.3.1.1. Characterization of Wetting Behaviour

The techniques for evaluating wetting characteristics range from sinking time measurement to contact angles measurement.

2.3.1.1.1. Submersion Test – Sinking Time or Immersion Time measurement

This method is by far the simplest (but qualitative) method for assessment of wettability of a powder by a surfactant solution (60). The time for which a powder floats on the surface of a liquid before sinking into the liquid is measured for different surfactant solutions with different concentrations. The immersion time t is plotted versus surfactant concentration as is illustrated in Figure 13. It can be seen that the sinking time starts to decrease sharply above a critical surfactant concentration reaching a minimum above this concentration. This procedure can be used to select the most effective wetting agent. The lower the surfactant concentration above which a rapid decrease in sinking time occurs and the lower the minimum wetting time obtained above this concentration, the more effective is the wetting.

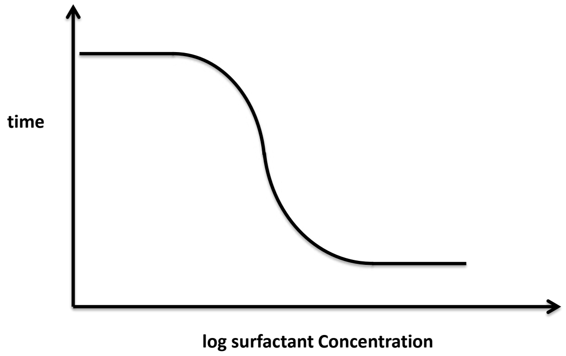

Figure 13 : Sinking time as a function of surfactant concentration.

2.3.1.1.2. Contact angle measurement using direct measurement

The classical technique for determining contact angles is a direct observation of a sessile drop of liquid on a powder compact by using a goniometer. A typical procedure was described by Kossen and Heertjes (61). Interpretation of the results involves some questionable assumptions regarding the structure of the porous surface and the general applicability of the method appears to not have been demonstrated.

2.3.1.1.3. Contact angle measurement using indirect measurement: liquid penetration

While direct measurements of contact angles on fine, micron-size particles are generally non-practical, quantitative estimates can be obtained from studies of the penetration of fluid into (or its expulsion from) a powder bed. If the pores in a packed bed are regarded as a system of fine capillaries, the capillary pressure in the bed can be described by a form of the Laplace equation:

$$\mathbf{\Delta P = \frac{2 \times \gamma_{LV \times \cos\theta}}{r_p}} \qquad \text{(Eq. 12)}$$

Where, r_p is the effective pore radius and ΔP is capillary pressure. The effective mean pore radius can be estimated from (62) the following equation:

$$r_P = \frac{2 \times \varepsilon}{SSA_v \times (1 - \varepsilon)} \qquad \text{(Eq. 13)}$$

Where ε is the porosity of the bed and SSA_v is the volume specific surface area of the powder. Alternatively, the pore radius can be eliminated by measuring the capillary pressure for a wetting liquid ($\theta = 0$), so that:

$$\mathbf{\cos\theta = \frac{\gamma_w \times \Delta P}{\gamma_{LV \times} \Delta P_w}} \qquad \text{(Eq. 14)}$$

Where, γ_w and ΔP_w refer to the wetting liquid.

The use of (Eq. 14) requires a high degree of reproducibility as well as the uniformity in bed preparation, since the measurement with the wetting liquid must be on a separate powder bed. Direct estimation of the pore radius from (Eq. 12) is subject to additional errors due to the involved approximations and the sensitivity of the equation to the bed porosity.

The rate of capillary rise can be used as an alternative to the equilibrium height. In this case, the capillary pressure is substituted into standard expressions for the rate of flow through a porous bed leading to the Washburn equation (63):

$$\mathbf{H^2 = \frac{R_{gf} \times \gamma_{LV \times \cos\theta}}{\eta} \times t} \qquad \text{(Eq. 15)}$$

Where H is the height of liquid in the bed after time t, is the viscosity of the liquid and R_{gf} is a geometric factor related to the effective mean pore radius in the bed. The slope of a plot of h^2 against time is a measurement of the quantity (R_{gf}×cos(θ)).

In this case also, it is common to use measurements with a wetting liquid (cos(θ) = 1) to estimate R_{gf}. It should also be noted that this technique is not suitable for liquids of high viscosity for which bubble entrapment can lead to significant errors and poor reproducibility. The use of gravimetric methods with continuous weighing of a particle bed in contact with a fluid reservoir can substantially improve the accuracy of depth measurement. However, the results are more sensitive to bed porosity and uniformity. The mass of liquid in the bed is given by

$$\mathbf{m = \rho \times \varepsilon \times SA_c \times H} \qquad \text{(Eq. 16)}$$

Where ρ is the liquid density and SA_c is the cross-sectional area of the bed. Thus, the equivalent to (Eq. 16) is:

$$\mathbf{m^2 = \frac{C_{gf} \times \rho^2 \times \gamma_{LV \times \cos\theta}}{\eta} \times t} \qquad \text{(Eq. 17)}$$

Where the geometric factor C_{gf} is given by:

$$\mathbf{C_{gf} = \varepsilon^2 \times SA_c^2 \times R_{gf}} \qquad \text{(Eq. 18)}$$

All in all, the penetration methods can provide a reasonably quantitative comparison of the wetting of a solid by different liquids, but actual estimates of contact angles should probably be regarded as approximate.

2.3.2. Microscopic interaction forces

During and following milling process nano-particles go through very stressing conditions. They need to resist flocculation due to high shear rate applied during the milling process (pumping, going in and out of pipes during the bulking process), concentration during drying process, storage and administration conditions. The whole process requires nano-particles to reach a balance between stability and instability. In order to control these parameters, it is therefore important to understand the forces of interaction between particles and how they affect the stability of the particles. Indeed, the interaction forces between colloidal particles in suspensions play an important role in determining the properties of the materials (shelf life, stability, rheology, injectability) and the behaviour of industrial processes (e.g. mixings, filtrations) as well as the formula of the final pharmaceutical products.

2.3.2.1. DLVO forces

The DLVO theory (64,65) is built on the assumption that the forces between two surfaces in a liquid can be regarded as the sum of two contributions: Van der Waals forces and the electrical double layer forces.

2.3.2.1.1. Van Der Waals forces

The Van der Waals forces are attractive forces between atoms or molecules. They are a part of the most important colloidal interactions. Different types of attraction were separately explained at different times. The dispersion forces were described by London in 1930 (66) and dipole-dipole interactions by Keesom in 1912 (67).

There are two approaches to calculate the van der Waals forces between surfaces, according to Hamaker (1937) (68) or Lifschitz (1956) (69).

The Lifschitz method is based on the properties of the medium in which the interaction takes place. This method requires to know in detail some interactions parameters (dielectric responses of different environments over a wide range of frequency for instance), which leads to some calculation complexity. For calculation simplification the Hamaker approach is more frequently used.

For two spherical atoms separated in vacuum over a distance h, between their centers, the corresponding attractive energy is given by

$$\mathbf{G_A = -\frac{\beta}{h^6}} \qquad \textbf{(Eq. 19)}$$

Where β is the London dispersion constant which depends on the properties of the specific atoms (polarizability of the atom).

However, for colloidal particles which are made from atoms or molecular assemblies, the attractive energies may be additive. This, results in the following expression for two equal spheres of radius r, in vacuum separated at small surface to surface distance h

$$\mathbf{G_A = \frac{-A}{6} \times \left(\frac{2\times r^2}{h^2-4h\times r} + \frac{2\times r^2}{h^2+4\times h\times r+4\times r^2} + \ln\left(\frac{2\times r^2}{h^2+4\times h\times r+4\times r^2}\right)\right)} \qquad \textbf{(Eq. 20)}$$

Where A is the Hamaker constant defined as:

$$\mathbf{A = \pi^2 \times q^2 \times \beta} \qquad \textbf{(Eq. 21)}$$

Where, q is the number of atoms per unit volume in particles. The Hamaker constant depends on the properties of the environment and those of the dispersed particle. Its value is generally between 10^{-19} and 10^{-21} J.

$$\mathbf{A = \left(A_{11}^{1/2} - A_{22}^{1/2}\right)^2} \qquad \textbf{(Eq. 22)}$$

A_{11} is the Hamaker constant between particles in a vacuum and A_{22} Hamaker constant for equivalent volumes of the medium.

When h << r the attractive energy is expressed as:

$$\mathbf{G_A = \frac{-A\times r}{12\times h}} \qquad \textbf{(Eq. 23)}$$

Given a value for A, and surface to surface distance h, the attractive energy G_A can be calculated. G_A decreases with increasing h (see Figure 14); at very short distances, the Born repulsion appears.

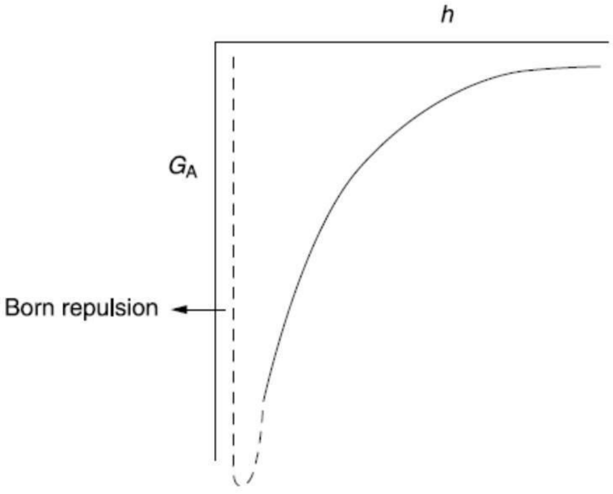

Figure 14 Variation of G_A with h (54).

2.3.2.1.2. Electrostatic forces

Acording to what was observed in colloidal systems, the particles dispersed in water and any liquid of high dielectric constant usually develop a surface charge. The charging of a surface immerging in a liquid result from two charging mechanisms (70):

I) By ionization or dissociation of surface groups, which leaves behind a charged surface (e.g., dissociation of protons from carboxylic groups, which leaves behind a negatively charged surface);

$$COOH \rightarrow -COO^- + H^+$$

II) By adsorption (binding) of ions from solution onto a previously uncharged surface. If we consider an individual particle immersed in the liquid, it is surrounded by an electric double layer. This double layer is formed by the charge at the surface of the particles. Another layer of the electrical double layer is formed by the excess of the opposite charged ions in the solution. As a result of their thermal motion, the electric charge carried by this layer extends over a certain distance from the particle surface, and dies out gradually with increasing the distance (diffuse layer) into the bulk liquid phase.

2.3.2.1.2.1. Distribution of electrical charge and potential in double layer

There are two models describing the theory of the electrical double layer: the Gouy-Chapman model (71,72) and the Stern-Graham model (73).

I) Gouy-Chapman model

Gouy (1910) and Chapman (1913) considered a diffuse distribution of the opposite charged ions with the concentration of the opposite charged ions falling off rapidly with the distance from the charged surface (see Figure 15).

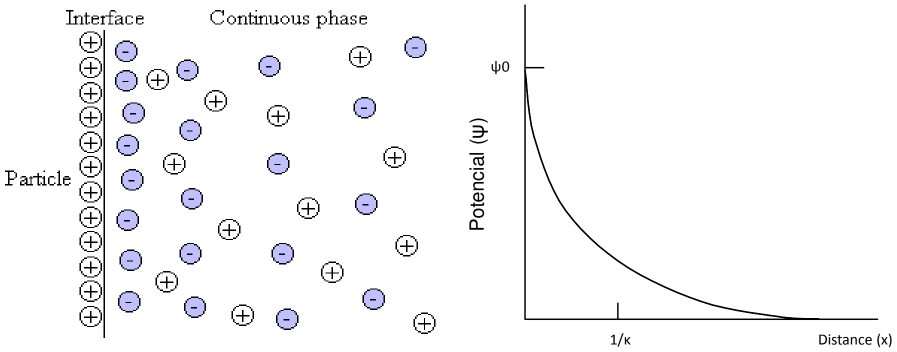

Figure 15: Diffuse double layer according to Gouy and Chapman (74)**.**

As a consequence of the positive charge on the particle surface, negative ions are attracted to the particle surface. Because of the motion of the particles, there are two regions of net negative charge. The region immediately adjacent to the particle surface is strongly negatively charged with very few positive charges and is called the "Stern layer". Outside the Stern layer, there is another region of net negative charge which gradually approaches neutrality as the distance from the particle surface increases. This charge distribution is called the electrical double layer. The properties of the double layer are governed by the Coulomb law and Boltzmann distribution law.

Coulomb law states that the force between two electric charges is inversely proportional to the square of the distance between them. As a result, an electric charge has an electric potential, Ψ which is defined as the work required to bring a unit charge up to a charge of magnitude, q.

The Boltzmann distribution law defines the distribution of energy between particles. It defines the probability of particles having a free energy ΔG being at a given point relative to some reference state where ΔG = 0. If the concentration of particles having free energy ΔG is C_p and that of particles having free energy zero is C_{p0}, the Boltzmann law states:

$$\mathbf{C_p = C_{p0} \times e^{\left(-\frac{\Delta G}{K_B \times T}\right)}} \qquad \textbf{(Eq. 24)}$$

Applied to the case of charged particles, the Boltzmann law gives the concentration of positive and negative ions in the region of a point of electrical potential Ψ. The concentration of positive ions, C_+ will be

$$\mathbf{C_+ = C_{p0} \times e^{\left(-\frac{-z_+ \times e \times \psi}{K_B \times T}\right)}} \qquad \textbf{(Eq. 25)}$$

Where z_+ is the valency of the positive ion, e is elementary (protonic) charge and C_o is the concentration of positive ions in a region where Ψ= 0.

Similarly the concentration of negative ions in the region will be

$$\mathbf{C_- = C_{p0} \times e^{\left(-\frac{+z_{-\times} e \times \psi}{K_B \times T}\right)}} \qquad \textbf{(Eq. 26)}$$

For the case where the valency of both positive and negative ions is 1, the net charge in the region will be given by

$$\mathbf{C_+ + C_- = C_{P0} \times (e^{\left(\frac{-\,e \times \psi}{K_B \times T}\right)} - e^{\left(\frac{+\,e \times \psi}{K_B \times T}\right)})} \qquad \textbf{(Eq. 27)}$$

If the region of electrical potential Ψ is close to a positive ion, Ψ will be positive and $[C_+ - C_-]$ will be negative. In case of a plane surface carrying a uniformly distributed charge (see Figure 15), it can be shown that the charge distribution near the surface is

$$\boldsymbol{\psi = \psi_{0\times} e^{(-\kappa\times x)}} \qquad \textbf{(Eq. 28)}$$

Where, κ is the decay length of potential and 1/κ is a measure of thickness of double layer known as the Debye length. When x= 1/κ; $\Psi=\Psi_0/e$:

$$\boldsymbol{\left(\frac{1}{\kappa}\right) = \left(\frac{\varepsilon_r\times\varepsilon_0\times K_B\times T}{2\times n_{0i\times} z^2\times e^2}\right)^{1/2}} \qquad \textbf{(Eq. 29)}$$

ε_r is the relative permittivity (dielectric constant), equal to 78.6 for water at 25 °C; ε_0 is the permittivity of free space. K_B is the Boltzmann constant and T is the absolute temperature; n_{0i} is the number of ions per unit volume of each type present in bulk solution and z is the valency of the ions and e is the electronic charge.

Thus the electrical potential near the surface is exponentially distributed. For z=1, the electrical potential decreases by a factor of 1/e at a distance of 1/ κ from the charged surface. This leads to a charge distribution near the surface as shown in Figure 16.

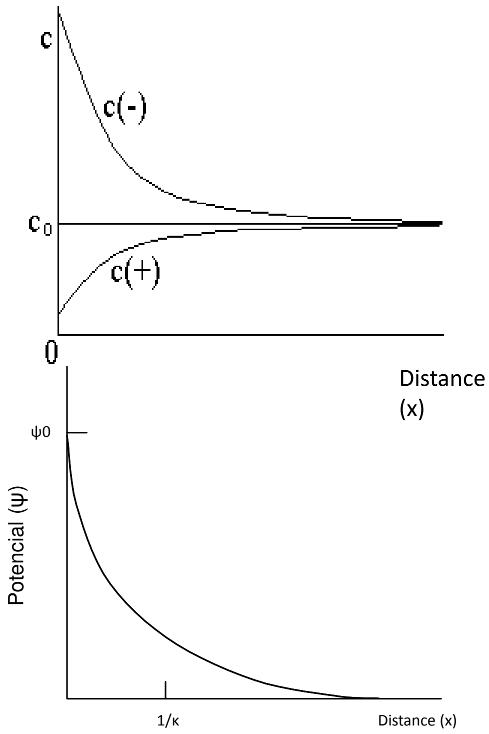

Figure 16 Charges distribution in the electrical double layer (74)**.**

II) Stern and Graham model

Stern (75) introduced the concept of the non-diffuse part of the double layer for specifically adsorbed ions, the rest being diffuse in nature (see Figure 17). The potential drops linearly in the Stern region, and then exponentially. Graham distinguished two types of ions in the Stern plane, physically adsorbed counter ions and chemically adsorbed ions.

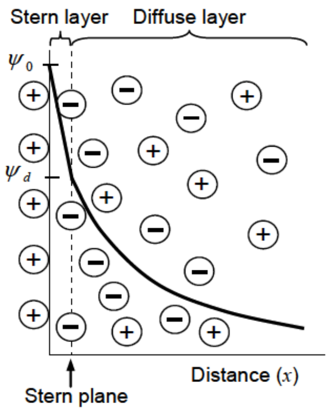

Figure 17: Double layer according to Stern and Graham (76)**.**

2.3.2.1.2.2. Electrical Double Layer Repulsion

When charged colloidal particles in dispersion approach each other such that their double layers begin to overlap (particle separation becomes less than two times the double layer extension), repulsion occurs. The individual double layers cannot be developed without restriction, since the limited space does not allow complete potential diminution (75) (see Figure 18).

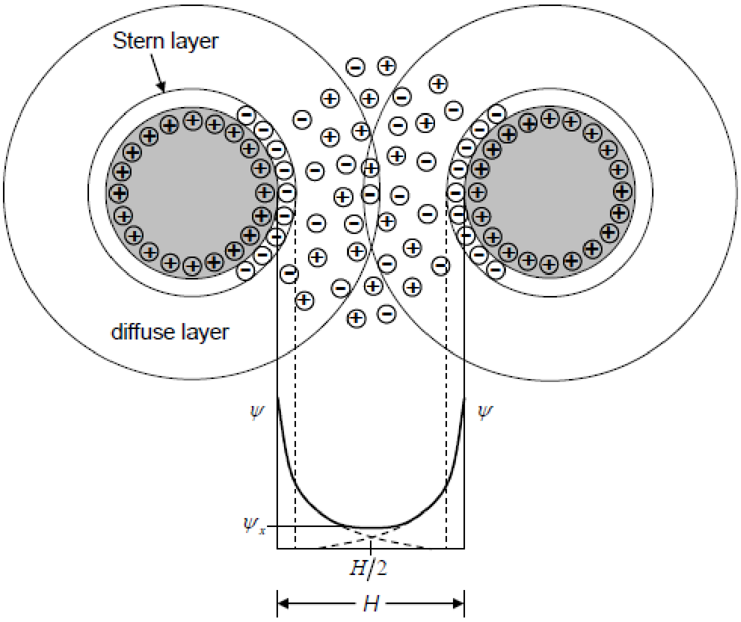

Figure 18 : Schematic of double layer repulsion between two particles (76)

For two spherical particles of radius r and surface potential Ψ_0 and condition κ*r < 3, the expression for the electrical double layer repulsive interaction is given by:

$$\mathbf{G_R} = \frac{4\pi\times\varepsilon_r\times\varepsilon_0\times r^2\times\Psi^2\times e^{-\kappa h}}{2\times r+h} \qquad \textbf{(Eq. 30)}$$

Where h is the closest separation between the surfaces and κ the decay length of potential. The above expression shows the exponential decay of G_R with h. This is illustrated in Figure 19.

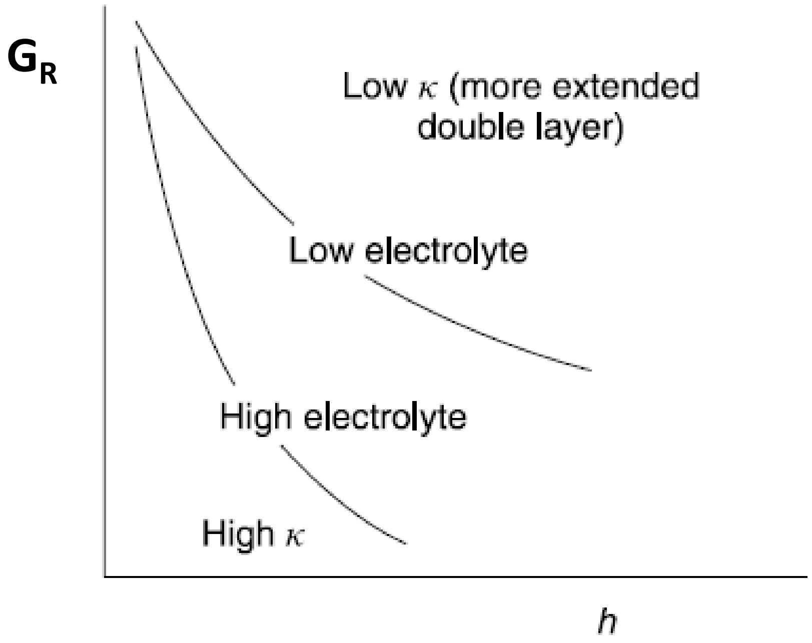

Figure 19: Variation of G_R with h at different electrolyte concentrations (54).

2.3.2.2. Steric repulsion

Steric repulsion results from the adsorption of molecules, often macromolecules on the surface of the colloid particles. In the case of macromolecules, the effect is essentially that of a physical barrier. The particle surface is coated with the macromolecules and the energy to break this layer is greater than the energy of collision between the particles. In such a situation the particles behave as if they were hard spheres with a diameter larger than the diameter of the particles. The slightly larger particle diameter may also reduce inter-particle attraction (77).

The structure of the macromolecules can be linear or branched (containing side chains) and may be cross-linked, linking one chain with another (78). Examples of these three types of macromolecules are shown in Figure 20.

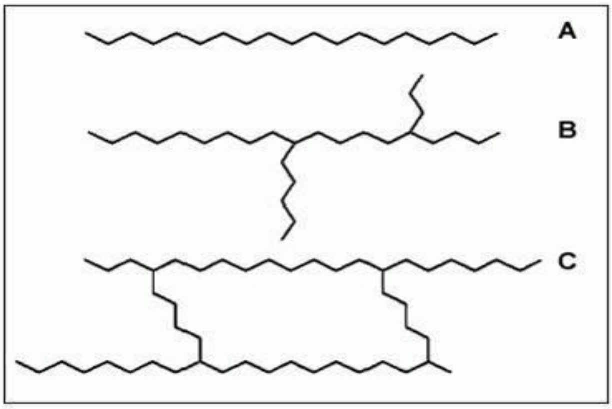

A) Linear polymer

B) branched polymer

C) cross-linked polymer

Figure 20: Basic structures of macromolecules (79).

Polymers can be composed from just one type of monomer (homopolymer) or from different types (copolymer). In the case of a linear copolymer consisting of two different monomers (e.g. A and B), the different monomers can basically be arranged in three different ways:

I) Random copolymer: there is no regularity in the arrangement of the two different monomers in the polymer

II) Block copolymer: blocks of pure A oligomer alternate with blocks of pure B oligomer

III) Alternating copolymer: the monomers A and B alternate within the composition of the polymer.

The composition and arrangement of the different monomers in a copolymer strongly influences its physico-chemical properties. Figure 21 shows the structure of a linear homopolymer and the three types of linear copolymer.

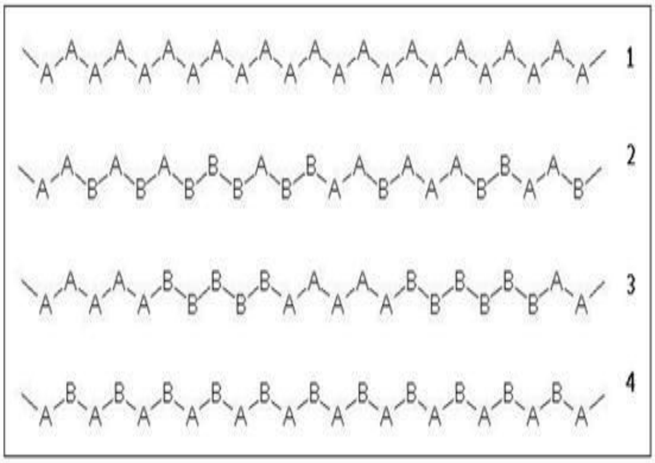

1) Homopolymer

2) Random Copolymer

3) Block Copolymer

4) Alternating copolymer

Figure 21: Chemical composition of linear AB copolymers (79).

The process of polymer adsorption involves a number of interactions (surface/solvent, chain/solvent and chain/surface interactions) and the conformation of the polymer at the interface. The interactions depend on various factors:

I) the nature of the structural groups on the solid surface, whether the surface contains charged sites or nonpolar groups;
II) the molecular structure of the surfactant being adsorbed, whether it is ionic or nonionic, whether the hydrophobic group is long or short, straight-chain or branched, aliphatic or aromatic;
III) the environment of the aqueous phase (“good” or “poor” solvent), pH, temperature, electrolyte content and the presence of any additives such as short-chain polar solutes (alcohol).

The conformations that the polymer takes on a surface depend on:

I) the number of active sites on the solid surface;
II) the number of adsorbable functional groups in the polymer molecule;
III) competitive intermolecular interactions with the solvent and other polymer molecules;
IV) the adsorbability of solvent molecules;
V) the position of the functional groups in the molecule.

The simplest polymer conformation that can be considered is that of a homopolymer (see Figure 22), whereby the molecule attaches itself with some segments (also known as “trains”) leaving loops and tails dangling in solution. According to Tadros (79), the polymer is weakly adsorbed and will not provide effective steric stabilization. The most favorable structures are those of block and graft copolymers, with the A chain highly solvated and the B chain having high affinity for the surface.

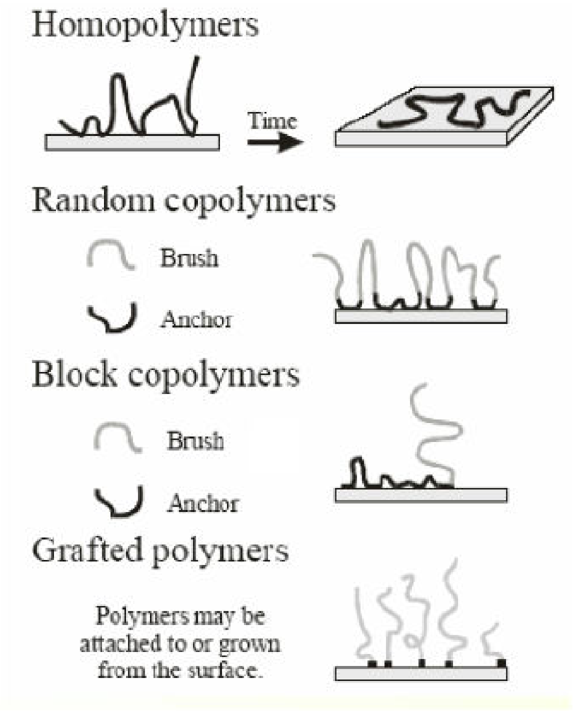

Figure 22 : Polymers conformation (80).

The theory of dispersion stabilization of dispersions using polymeric surfactants is based on this fact: when two particles of radius r containing an adsorbed polymer layer with a hydrodynamic thickness δ, approach each other to a surface-surface separation distance h that is smaller than 2 δ, the polymer layers interact with each other resulting in two main situations:

Either the polymer chains may overlap with each other or the polymer layer may undergo some compression

In both cases, there will be an increase in the local segment density of the polymer chains in the interaction region. This is schematically illustrated in Figure 23. The real situation is perhaps in between the above two cases, i.e. the polymer chains may undergo some interpenetration and some compression.

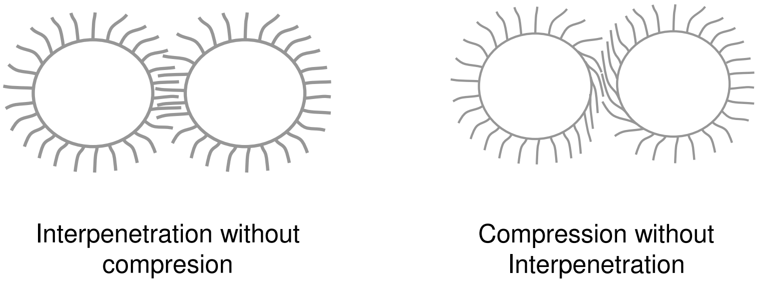

Figure 23: Schematic representation of the interaction between particles containing adsorbed polymer layers (52)**.**

Provided the dangling chains (the A chains in A-B, A-B-A block or BA_n graft copolymers) are in a good solvent, the local increase in segment density in the interaction zone will result in strong repulsion as a result of two main effects: firstly, the increase in the osmotic pressure in the overlap region as a result of the unfavorable mixing of the polymer chains, when these are in good solvent conditions. This phenomenon is referred to as osmotic repulsion or mixing interaction and it is described by a free energy of interaction G_{mix}. Secondly, reduction of the configurational entropy of the chains in the interaction zone, (this entropy reduction) results from the decrease in the volume available for the chains when these are either overlapped or compressed. This is referred to as volume restriction interaction, entropic or elastic interaction and it is described by a free energy of interaction G_{el}.

The combination of mixing interaction (G_{mix}) and elastic interaction (G_{el}) is usually referred to as the steric interaction free energy (G_s), i.e.

$$\mathbf{G_s = G_{mix} + G_{el}} \qquad \textbf{(Eq. 31)}$$

The sign of G_{mix} depends on the solvency of the medium for the chains. If the chains are in a good solvent, i.e. the Flory-Huggins interaction parameter χ is less than 0.5, then G_{mix} is positive and the mixing interaction leads to repulsion. In contrast if $\chi > 0.5$, (i.e. the chains are in a poor solvent condition) G_{mix} is negative and the mixing interaction becomes attractive. G_{el} is always positive and hence in some cases one can produce stable dispersions in a relatively poor solvent (enhanced steric stabilization).

The osmotic effect is also known as the mixing interaction, G_{mix}. The effect is described by Fisher in this theory, which takes into account the enthalpy contribution to steric stabilization. Fisher considered two equal particles with a radius r, each containing an adsorbed polymer layer (with uniform segment density) with a thickness δ, and a chemical potential of the solvent in the adsorbed layer μ_i^α as described in Figure 24. When the particles are apart with a surface to surface distance, h, the system is in an ideal state. However, when the particles approach each other, (h < 2 δ) the polymer chains may undergo some penetration and/or compression. The resulting chemical potential of the solvent in the overlap zone, dV becomes μ_i^β. μ_i^β is lower than μ_i^αas a result of the higher osmotic pressure in the overlap zone. If the polymer chains are in good solvent conditions, solvent will diffuse from the bulk, causing the particles to separate. However, if the polymer chains are in a poor solvent, the interaction becomes attractive resulting in a flocculation of the particles (see Figure 24.

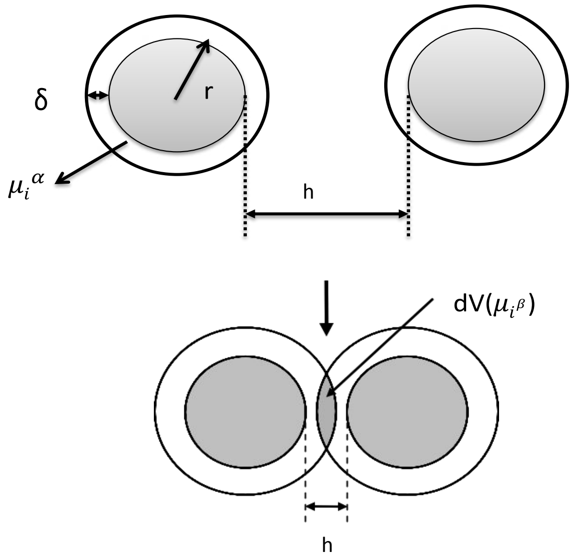

Figure 24: Schematic representation of the overlap of two polymeric layers (81)

The mixing interaction, G_{mix} , can be calculated using the following equation (81),

$$\frac{\mathbf{G_{mix}}}{\mathbf{K_B T}} = (\mathbf{2} \times \frac{\mathbf{V_2^2}}{\mathbf{V_1}}) \times \mathbf{n_{pc}^2} \times (\frac{\mathbf{1}}{\mathbf{2}} - \boldsymbol{\chi}) \times (\boldsymbol{\delta} - \frac{\mathbf{h}}{\mathbf{2}}) \times (\mathbf{3} \times \mathbf{r} + \mathbf{2} \times \boldsymbol{\delta} + \frac{\mathbf{h}}{\mathbf{2}}) \qquad \textbf{(Eq. 32)}$$

Where V_2 is the molar volume of the polymer, V_1 is the molar volume of the solvent and n_{pc} is the number of polymer chains per unit area.

The elastic interaction G_{el} arises from the loss in configurational entropy of the chains on the approach of a second particle. As a result, the volume available for the chains becomes restricted, resulting in a loss of the number of configurations. This can be illustrated by considering a simple molecule, represented by a rod that rotates freely in a hemisphere across a surface. When the two surfaces are separated by an infinite distance h_∞, the number of configurations of the rod is Ω(∞) which is proportional to the volume of the hemisphere. When a second particle approaches to a distance h such that it cuts the hemisphere (loosing some volume), the volume available to the chains is reduced and the number of configurations become Ω (h) which is smaller than Ω(∞) (see Figure 25)

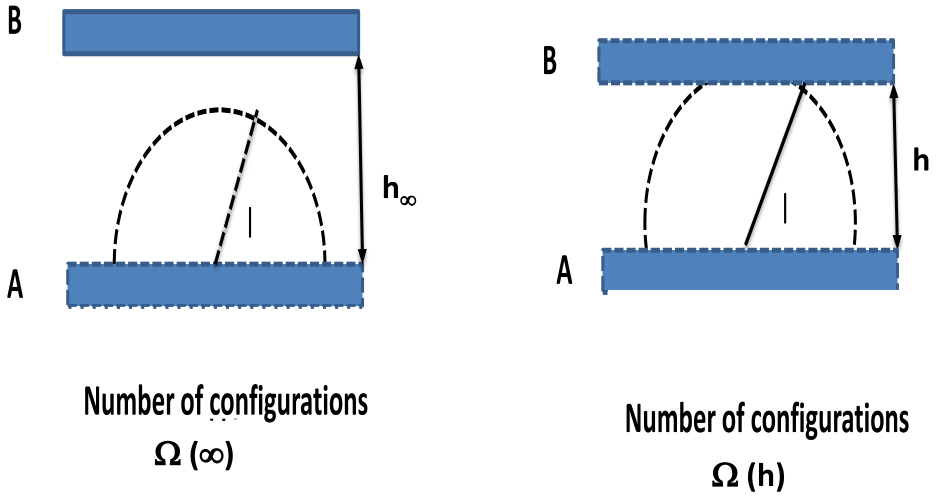

Figure 25 : Schematic representation of the elastic interaction with planes A and B separated at a distance h_∞ , and planes A and B separated at a distance h (76)**.**

For two flat plates, G_{el} is given by the following expression:

$$\frac{G_{el}}{K_B \times T} = -2 \times n_{pc} \times \ln\left(\frac{\Omega(h)}{\Omega(\infty)}\right) = -2 \times n_{pc} \times R_{el}(h)$$ **(Eq. 33)**

Where $R_{el}(h)$ is a geometric function which depends on the segment density.

2.3.2.3. Solvation or hydration forces

Solvation forces appear from the association of molecules of a solvent with molecular, ionic, or particulate solute units. They are referred to as hydration forces when the association involves water molecules. Solvation forces depend not only on the properties of the surrounding medium but also on the chemical and physical properties of the surfaces

These forces can be repulsive, attractive, or even oscillatory in some cases. They can be much stronger than either of the two DLVO forces at small separation distance (70). Usually the liquid structure close to an interface is different from that in the bulk. When two surfaces approach each other, one layer of molecules after another is pressed out of the closing gap. The effect of geometric constraint of the closing wall close on these molecules and the attractive interaction between the surface and the liquid molecules will therefore cause the solvation force between the two surfaces. Solvation forces depend on both chemical and physical properties of the surfaces being considered, such as the wettability, crystal structure, surface morphology and rigidity and on the properties of the intervening medium. Hydration force is expressed as (82,83):

$$\mathbf{F_{solv} = K_f \times e^{-\frac{h}{l_g}}} \qquad \text{(Eq. 34)}$$

Where $K_f>0$ refers to the hydrophilic repulsion forces and $K_f<0$ to the hydrophobic attraction forces and l_g is the correlation length of the orientational ordering of water molecules.

2.3.2.4. Combination of interaction forces

2.3.2.4.1. DLVO theory

The DLVO theory was established by Derjaguin and Landau (64), Verwey and Overbeek (65) who developed it in the 1940s. The theory describes the force between charged surfaces interacting through a liquid medium. It combines the effects of the Van der Waals attraction and the electrostatic repulsion. However it neglects short – range interaction forces such as solvation and steric repulsion.

The concept of the DLVO theory is that the total interaction energy of two surfaces or particles is given by the summation of the attractive and repulsive contributions. This can be written as:

$$\mathbf{G_T = G_A + G_R} \qquad \text{(Eq. 35)}$$

Where the total interaction energy G_T is expressed in terms of the repulsive double layer interaction energy, G_R, and the attractive Van der Waals energy, G_A. Contrary to the repulsive interaction, the Van der Waals interaction energy is mostly non sensitive to variations in electrolyte strength and pH. Additionally, the Van der Waals attraction must always be bigger than the repulsive interaction at extremely small distances. An illustration of G_T is shown in Figure 26.

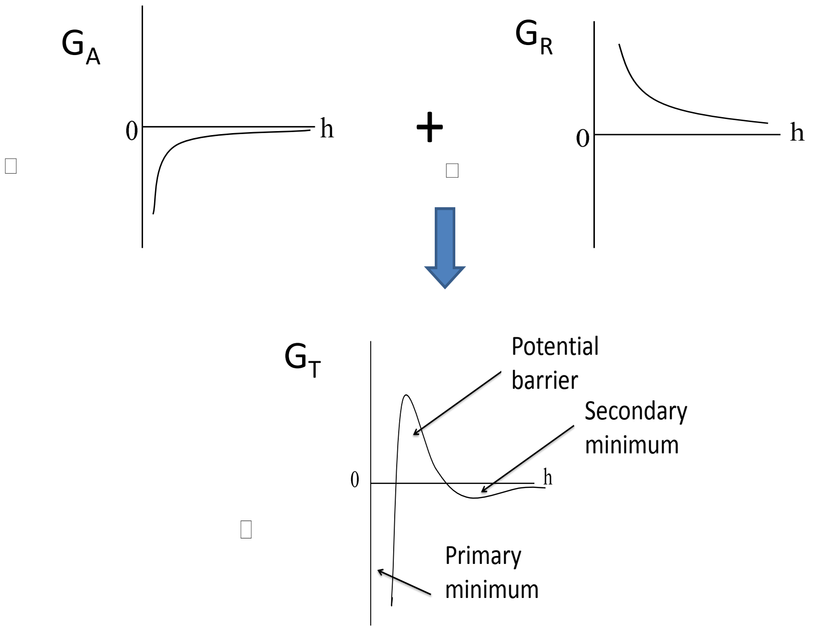

Figure 26 : Potential energy diagram of two electrostatically stabilized particles (84)**.**

The repulsive energy, G_R decays exponentially with distance, h and approaches zero when h is large. At small h, the attractive energy, G_A increases rapidly compared to the repulsive energy as G_A is proportional to 1/h.

At low and large distances where G_A is dominant, a deep primary minimum, $G_{P,min}$ and a secondary minimum, $G_{S,min}$ are observed. In the primary minimum, the particles are in direct contact: they strongly adhere to each other and the process is known as irreversible coagulation. On the other hand, the particles in the secondary minimum are not in direct contact with each other but remain at some distance with the possibility of moving and sliding along each other. As the depth of the secondary minimum is only a few K_BT (85) compared to the primary minimum (several 100 k_BT units), the particles can therefore be redispersed by shaking.

At intermediate distance, the electric double layer interactions give rise to an energy barrier, G_{max}, which depends on electrolyte concentration, valency, and surface or zeta potential.

To ensure adequate colloidal stability, G_{max} has to be greater than 25 k_BT (zeta potential higher than 40 mV, and the electrolyte concentration lower than 10^{-2} mol/dm^3 for 1:1 electrolyte (54)).

In the case where the repulsive force G_R, is negligible and the particles are stabilized only by non-ionic surfactants or polymer, the total potential energy, G_T, is given by (Eq. 36).

$$\mathbf{G_T = G_A + G_{el} + G_{mix}} \qquad \textbf{(Eq. 36)}$$

Where G_{el} represents the elastic interaction, G_{mix} represents the mixing interaction and G_A represents the attractive forces. The different potential energy curves are illustrated in Figure 27.

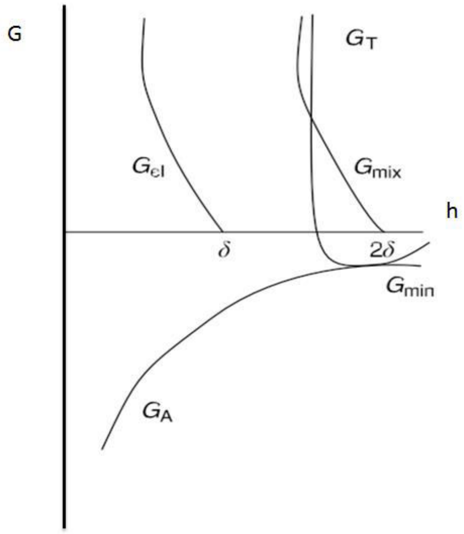

Figure 27 : Potential energy diagram of two sterically stabilized particles (81)**.**

The Figure 27 shows that the potential energy of G_{mix} increases steeply when the distance between particles h, is less than 2δ. Similarly, the elastic interaction, G_{el}, also increases sharply when the distance h, is less than δ. The total potential energy, G_T, presents a minimum, G_{min}, at separation distance comparable to 2δ followed by a rapid increase with a decrease of distance h.

In a case where ionic and non-ionic stabilizers are used, or when polyelectrolytes are used, the present forces are the electrostatic repulsion, G_R, the Van der Waals attraction, G_A, and the steric repulsion, G_S. The combination of these forces is known as “electro-steric interaction” and the resulting total potential energy, G_T, is illustrated in Figure 28. The potential energy –

distance curve shows two minima and one maximum due to the DLVO forces and a rapid increase at small distance as a result of steric repulsion.

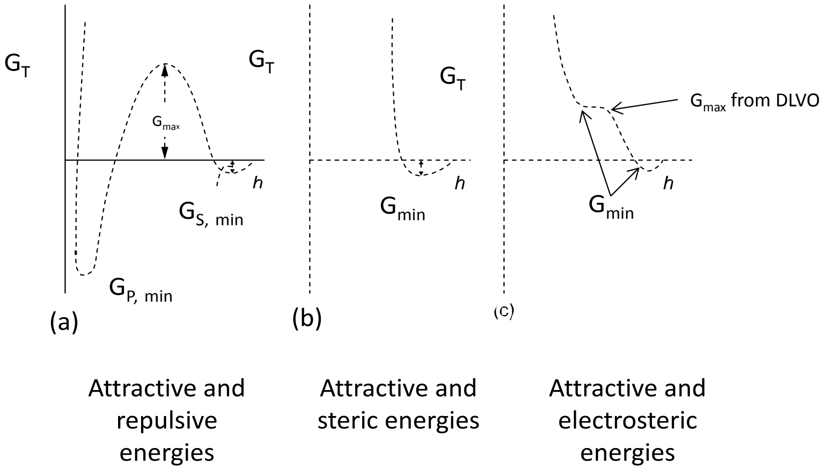

Figure 28 : Potential energy diagram of two electrosterically stabilized particles (81)**.**

Summary

Colloids are thermodynamically unstable; an important element of colloid stability is related to the surface free energy of the particles. Colloidal particles are inherently attracted to each other as a consequence of Van der Waal's forces acting between the molecules on the particle surface. This attractive force results in a negative surface free energy. On the other hand, there are a number of factors which may lead to particles being repulsed from one another. The repulsive forces all result in a positive surface free energy. As a consequence, the stability of a colloidal dispersion may be predicted, at least partly, by the net surface free energy which is determined from the following equation:

$$\mathbf{G_T = G_A + G_R + G_{mix} + G_{el}} \qquad \textbf{(Eq. 37)}$$

A summary of all microscopic interaction forces is given in Figure 29.

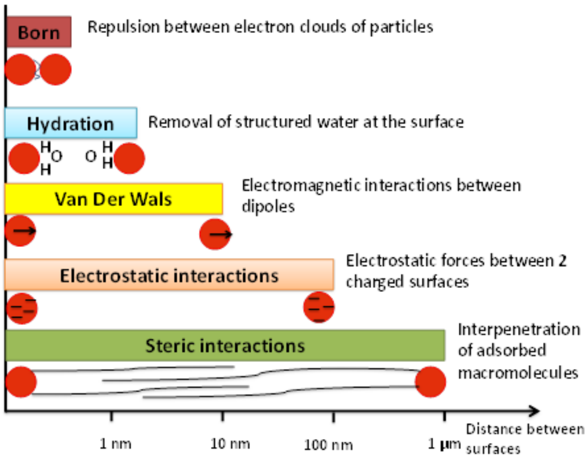

Figure 29 : Summary of microscopic interaction forces (60).

Except G_A, the values of G are repulsive. If the net result is positive the colloidal dispersion will be stable. Even if ΔG is overall negative, the colloidal dispersion may be stabilized by adding macromolecules which act as viscosity modifiers, increasing frictional forces and reducing the rate of approach of particles. Polysaccharides are often used in foods for this purpose.

2.3.3. Mechanisms of destabilization of nano-particles

The small particle size of nano-suspensions, which is inherent to their success, is also responsible for their physical instability. Nano-suspensions consist of hydrophobic particles dispersed in a hydrophilic medium (usually water).The huge surface area associated with the small size of these particle results in high interfacial tension, which leads to an increase in the free energy of the system. Accordingly, nano-suspensions are essentially thermodynamically unstable systems (37). To decrease their free energy, nano-particles tend to reduce their interaction with water via flocculation, aggregation or crystal growth

2.3.3.1. Flocculation (perikenitic aggregation)

In the case of electrostatically stabilized suspensions, flocculation occurs if the energy barrier is small or negligible. According to Sato and Ruch ((84) 1980), an energy barrier of 15 K_BT is sufficient to prevent flocculation since thermal energy is 1 K_BT. Where, K_B is Boltzmann constant and T is the absolute temperature. In real systems where the particles have a distribution of potential energies, some portion of the particles will have enough energy to overcome this barrier and will adhere to each other. Verwey and Overbeek ((65) 1948) stated that the energy barrier should be greater than 25 K_BT to prevent particles from flocculation into the primary minimum. The height of the energy barrier depends on the electrolyte concentration which is directly related to the thickness of the double layer, 1/K (known as Debye length). As the electrolyte concentration increases, the energy barrier decreases resulting in the decrease of 1/K until it is marginal whereby the particles will then be flocculated (see Figure 30).

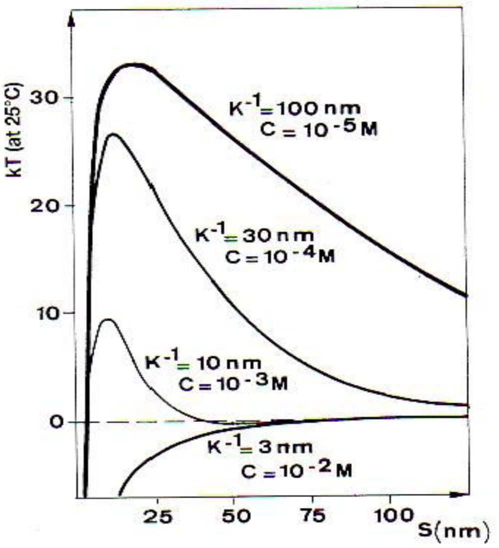

Figure 30: Variation of G_T with distance for various electrolyte concentrations (86).

Coagulation occurs at a critical electrolyte concentration, the critical coagulation concentration (C.C.C), which depends on the electrolyte valency (z). At low surface potentials, C.C.C. is proportional to $1/z^2$ (where, z is the ion valency). This refers to as the Schultze–Hardy rule (87). At large surface potentials, the C.C.C. is proportional to $1/z^6$. As a consequence, multivalent ions are more effective in decreasing the electrostatic repulsion.

The flocculation rate can be monitored by simply following the controlling diffusion rate. Nanoparticle flocculation kinetics have been investigated extensively using light scattering techniques (both dynamic and static) (88,89).

There are two regions of coagulation mechanisms: the diffusion controlled (fast coagulation) and the reaction limited coagulation (slow) (90). This is illustrated in the figure Figure 31.

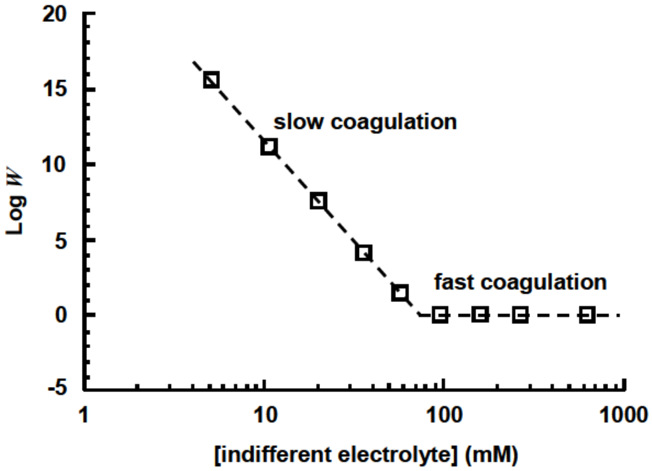

Figure 31 : The stability ratio of silver bromide as a function of the concentration of a 1:1 indifferent electrolyte (76)**.**

For the fast coagulation, each collision is effective in forming an aggregate, the collision efficiency is 1. As a result the flocculation rate constant is the same as the collision rate constant. The rate of change of the k-fold flocculate concentration, where k = i + j are expressed by Smoluchowski equation (91), is the following:

$$\frac{dn_k}{dt} = \frac{1}{2} \times \sum_{i=1,i+J=k}^{k-1} k_{ij} \times n_i \times n_j - n_{k\times} \sum_{i=\&}^{\infty} k_{ik} \times n_i \qquad \textbf{(Eq. 38)}$$

Where, k_{ij} is the second-order coagulation rate constant, t is the time, and n_k is the total particle concentration of n-fold flocculates. The coagulation rate constant can be calculated for diffusion controlled coagulation from the collision rate and expressed as follows:

$$k_{ij} \sim k = \frac{8 \times K_{B\times} T}{3 \times \eta} \qquad \textbf{(Eq. 39)}$$

Where, K_B is the Boltzmann's constant, T the absolute temperature, and η the viscosity of the suspending fluid. For an aqueous dispersion at 25 °C, k_{ij} = 1.23 x 10-17 m^3/s. As indicated in (Eq. 39)**,** the rate constant is nearly independent of particle size. This independence can be explained by the fact that larger particles have lower diffusion coefficients but larger capture radius which effectively cancel each other out. (Eq. 38) can be integrated with the initial condition $n_{total} = n_0$ (n_0 is the initial concentration of particles) to give (Eq. 40)**.**

$$\frac{n_0}{n_{total}} = 1 + \frac{t}{\tau}; \quad \left(\tau = \frac{1}{K_a \times n_0},\ k_a = \frac{1}{2} \times K_{ij}\right) \quad \text{(Eq. 40)}$$

The characteristic time τ is often referred to as the half-life of aggregation. At this time the total number of particles in the dispersion has been reduced by a factor of 2. In the region of reaction limited coagulation, the rate of coagulation is reduced due to the additional repulsive force from electrostatic or steric interaction. In this region not every collision results in coagulation. Only a fraction 1/W of collisions is successful. W is commonly defined as the stability ratio, which is the ratio of the diffusion limited (fast) coagulation rate to the slow coagulation rate. When W = 1, the coagulation is in the diffusion-limited region.

$$W = \frac{k_{ij}(fast)}{k_{ij}(slow)} \text{ or } \frac{\tau(fast)}{\tau(slow)} \quad \text{(Eq. 41)}$$

2.3.3.2. Orthokinetic aggregation

In addition to the Brownian motion, particles movements and their collision rates can be modified by applying an orthokinetic force (shear-influenced aggregation induce by fluid transport). If agitation occurs, the velocity of fluid varies both spatially (from point to point) and temporarily (from time to time). The spatial change in velocity is characterized by a velocity gradient. Particles which follow the fluid motion will also have different velocities, so that opportunities exist for inter-particle contacts. The rate of change in the total concentration of particles with time due to orthokinetic aggregation is expressed as follows (92):

$$\frac{dn_{total}}{dt} = -\frac{2 \times \alpha \times <\dot{\gamma}> \times d^3 \times n_{total}^2}{3} \quad \text{(Eq. 42)}$$

Where, n_{total} is the total concentration of particles in suspension at time t, α is the collision efficiency factor, $< \dot{\gamma} >$ is the mean shear rate, d is the particle diameter

2.3.3.3. Ostwald ripening

Ostwald ripening is the process through which larger particles grow with time at the expense of the smaller ones (93) due to the well-known Kelvin effect (91). There are two preconditions for Ostwald ripening: the system should be poly-disperse, and the dispersed phase should have finite solubility in the dispersion medium.

Both these conditions are frequently encountered in pharmaceutical nano-suspensions. The driving force of Ostwald ripening is the reduction of excess energy associated with solid liquid interfaces. In addition, most of the stabilizers used in the preparation of nano-suspensions also increase their solubility and hence may increase Ostwald ripening. Ostwald ripening kinetics can be controlled either by the diffusion rate of matter between large and small particles or by the rates of growth or dissolution at solid liquid interfaces (92).

Depending upon the nature of the interface and the crystal growth mechanism three different types of interface coarsening can be identified: continuous growth, surface nucleation and spiral growth.

The kinetics of diffusion controlled growth and two of the interface controlled growth (continuous growth and spiral growth) are given by:

$$\mathbf{d^n - d_0^n = k_r \times t} \qquad \textbf{(Eq. 43)}$$

Where, d is the average diameter at time t, d_0 is the average initial diameter at t = 0 and k_r is the ripening rate. The exponent n is 3 for diffusion controlled process (92,94) and spiral growth controlled and 2 for controlled growth processes (92,95).

The ripening rate is given by:

$$\mathbf{k_r = \frac{64 \times D_f \times S \times V_m \times \gamma}{9 \times R \times T}} \qquad \textbf{(Eq. 44)}$$

Where, D_f is the translational diffusion coefficient of the dissolved solute molecules, S is the bulk solubility of the dispersed phase, γ is the surface tension and V_m is the molar volume of the dispersed phase. R and T are the universal gas constant and the absolute temperature, respectively. The surface nucleation controlled growth of particles follows a logarithmic dependence on time (96) and is given by:

$$\mathbf{d - d_0 = \Pi = \log\left(1 + \frac{t}{\tau'}\right)} \qquad \textbf{(Eq. 45)}$$

Where, τ' and Π are constants with dimensions of length and time, respectively. Although, the importance of Ostwald ripening on the physical stability of nano-suspensions has been reported in a number of literature reports (97–102), its role in stability of suspensions has not yet been published.

2.3.4. Assessment of electrostatic and steric stabilization

2.3.4.1. Electrokinetic phenomena and the zeta potential

The liquid layer surrounding the particle exists as two parts; an inner region (Stern layer) where the ions are strongly bound and an outer (diffuse) region where they are less firmly associated. Within the diffuse layer there is a notional boundary inside which the ions and particles form a stable entity. When a particle moves (e.g. due to gravity), ions within the boundary move from it. Those ions beyond the boundary stay with the bulk dispersant. The potential at this boundary (surface of hydrodynamic shear) is the zeta potential (103) (see the Figure 32).

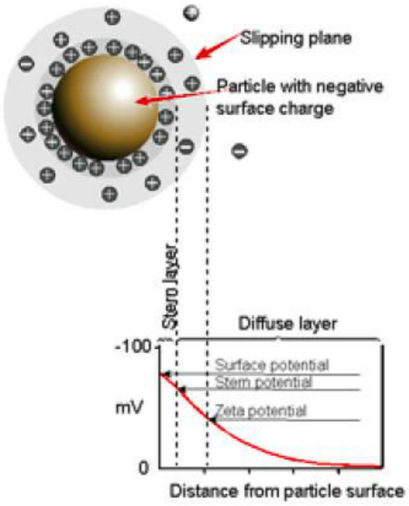

Figure 32: Schematic representation of zeta potential (103).

The magnitude of the zeta potential gives an indication of the potential stability of the colloidal system. If all the particles in suspension have a large negative or positive zeta potential then they will tend to repel each other and therefore will not tend to come together. However, if the particles have low zeta potential values then there will be no force to prevent the particles from coming together and flocculating. The dividing line between stable and unstable suspensions is generally taken at either +15 or -15 mV. Particles suspension with zeta potentials higher than +15 mV or below than -15 mV are usually considered stable. However, if the particles have a different density than the dispersant, they will eventually sediment, forming a close packed bed

2.3.4.1.1. Factors affecting zeta potential

(i) pH: in aqueous media, the pH of the sample is one of the most important factors that affects its zeta potential. A zeta potential value on its own without defining the solution conditions is a virtually meaningless number. Consider particles in suspension with a negative zeta potential; If more alkali is added to this suspension then the particles will tend to acquire a more negative charge; If acid is added to this suspension then a point will be reached where the charge will be neutralised. Further addition of acid will cause a build-up of positive charge. Therefore a zeta potential versus pH curve will be positive at low pH and lower or negative at high pH. There may be a point where the plot passes through zero zeta potential. This point is called the isoelectric point and is very important from a practical consideration. It is normally the point where the colloidal system is least stable;

(ii) Conductivity: the thickness of the double layer (κ-1) depends upon the concentration of ions in solution and can be calculated from the ionic strength of the medium. The higher the ionic strength, the more compressed the double layer becomes. The valency of the ions will also influence double layer thickness. A trivalent ion such as Al^{3+} will compress the double layer to a greater extent in comparison with a monovalent ion such as Na^+. Inorganic ions can interact with charged surfaces in one of two distinct ways: non-specific ion adsorption, where they have no effect on the isoelectric point, or specific ion adsorption, which will lead to a change in the value of the isoelectric point. The specific adsorption of ions onto a particle surface, even at low concentrations, can have a dramatic effect on the zeta potential of the particle dispersion. In some cases, specific ion adsorption can lead to a charge reversal of the surface;

(iii) Concentration of formulation component: The effect of the concentration of a formulation component on the zeta potential can give information for formulating a product to achieve maximum stability. The influence of known contaminants on the zeta potential of a sample can be an asset in formulating the product to prevent flocculation for instance.

2.3.4.2. Surfactant and polymer adsorption

A representative sample of the solid with known mass m and specific surface area SSA is equilibrated with a volume V of surfactant or polymer solution at concentration (C_1). After the equilibrium is reached out (at a given constant temperature), the solid is removed by centrifugation. Then, the equilibrium concentration C_2 is analytically determined. The amount of adsorption Γ (mol/m^2) is given by:

$$\boldsymbol{\Gamma = \frac{(C_1 - C_2)}{m \times SSA} \times V = \frac{\Delta C}{m \times SSA} \times V} \qquad \textbf{(Eq. 46)}$$

In most cases (particularly with surfactants) a plot of Γ versus C_2 gives a Langmuir- type isotherm (see Figure 33).

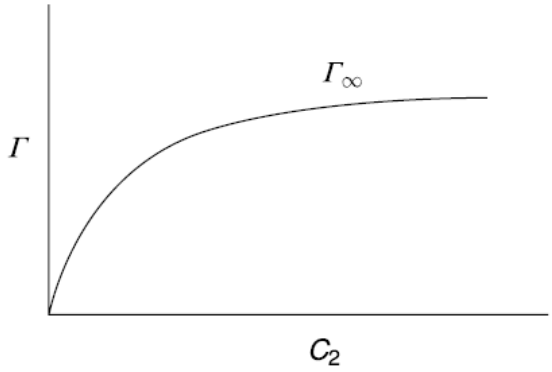

Figure 33: Typical Langmuir isotherm for surfactant adsorption (52)**.**

The data can be fitted using the Langmuir equation,

$$\Gamma = \frac{(\Gamma_{\infty \times} b \times C_2)}{(1 + b \times C_2)} \qquad \textbf{(Eq. 47)}$$

Where b, is a constant that is related to the free energy of adsorption,

$$\mathbf{b} \propto \left(-\frac{\Delta G_{ads}}{R \times T}\right) \quad \text{(Eq. 48)}$$

Most polymers (particularly those with high molecular weight) give a high-affinity isotherm (see the Figure 34).

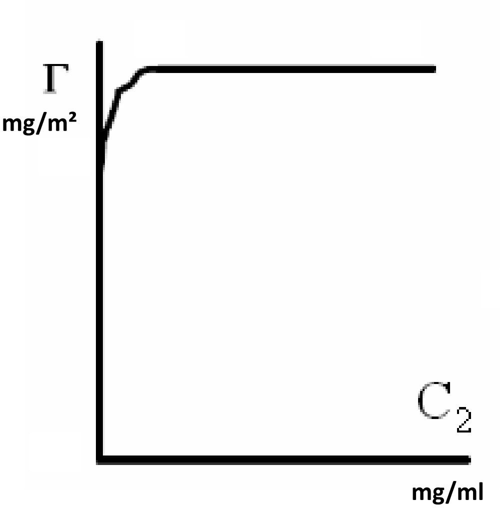

Figure 34: Typical high-affinity isotherm for polymer adsorption (52)**.**

The conditions for efficient steric stabilization are given below (54):

(i) large Γ;

(ii) large δ (layer thickness);

(iii) large G_{ad} (adsorption energy);

(iv) $\chi < 0.5$ (good solvent for the polymer chain);

(v) low C_2 (free polymer concentration).

It is noteworthy that (iii) may conflict with (iv) for homopolymers. This conflict is absent for grafted and block copolymers

2.3.5. Macroscopic interaction forces (hydrodynamic forces)

Hydrodynamic forces can also strongly influence the behaviour of the colloidal dispersion by generating a relative movement of the particles. The term "hydrodynamic forces" combines the dissipation viscous forces in the suspending fluid and the convective forces. Based on the nature of the suspension flow, it is important to calculate some flow parameters as the particle Reynolds number, the stirrer Reynolds number, the power number, the pumping capacity number, the recirculation time and the shear rate.

(i) Particle Reynolds number

The particle Reynolds number is used to estimate the importance of inertial effects compared to viscous effects for a single particle having a diameter d, moving with the velocity u in a fluid having a viscosity η and a density ρ.

$$\mathbf{Re_P} = \frac{\rho \times \mathbf{u} \times \mathbf{d}}{\eta} \qquad \textbf{(Eq. 49)}$$

If $Re_P << 1$, the viscous diffusion is predominant for the movement quantity transportation
If $Re_P >> 1$, the convection is predominant for the movement quantity transportation

(ii) Stirrer Reynolds number

The hydrodynamic forces are the result of the motion of the particles in the suspending fluid. They are linked to the medium where the suspension is contained. That is why a global analysis of the hydrodynamic needs to be considered.

The flow of fluid having a density ρ, a kinematic viscosity ν, in a stirred vessel a stirrer having a diameter D and rotating at speed N, is characterized by the dimensionless Reynolds number as follows:

$$\mathbf{Re} = \frac{\mathbf{N} \times \mathbf{D^2}}{\boldsymbol{\nu}} \qquad \textbf{(Eq. 50)}$$

According the Re number value, 3 different domain of flowing can be distinguished. For a standard vessel, these domains are named the laminar regime ($Re < 10$), the transition regime ($10 < Re < 10^4$) and the turbulent regime for which the maximum Re depends on both the type and the geometrical configuration of the stirrer.

(iii) Power number

The power number characterises the required power to supply to the stirrer in order to rotate the fluid. It is similar to a drag coefficient. It is expressed as follows:

$$\mathbf{N_P} = \frac{\mathbf{P_w}}{\boldsymbol{\rho}\times\mathbf{N^3}\times\mathbf{D^5}} \qquad \textbf{(Eq. 51)}$$

Where, N_P is the power number, P_w is the power draw, ρ is the fluid density, N is the stirrer speed and D is the stirrer diameter. The N_p number, expressed as function of the Reynolds number Re, (see (Eq. 52) and Figure 35) predicts the power draw of the stirrer.

$$\mathbf{N_P} = \boldsymbol{\Xi} \times (\mathbf{Re})^{\boldsymbol{\Upsilon}} \qquad \textbf{(Eq. 52)}$$

Where, Ξ and ϒ are constants.

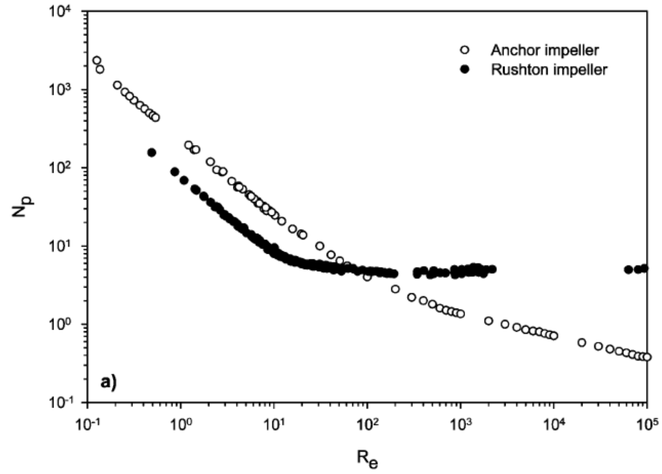

Figure 35: Newtonian power curve for Rushton and anchor impellers (104).

(iv) Pumping capacity number

The pumping capacity number characterises the flow passing through the stirrer. It is expressed as follows:

$$N_Q = \frac{Q}{N\times D^3} \qquad \textbf{(Eq. 53)}$$

Where, Q is the recirculation flow of the stirrer. The typical pumping capacity number is 0.9 for Ruston (radial flow) impeller, 0.79 for 4-blade 45° (axial flow) impeller and 0.56 for 3 blades fluid foil stirrer (axial flow) impeller (105,106)

.

(v) Recirculation time

An estimation of the frequency of particles to the high shear stirrer zone can be obtained from the recirculation time t_c (106), which is expressed as follows:

$$\mathbf{t_c = \frac{V}{N_Q \times N \times D^3}} \qquad \textbf{(Eq. 54)}$$

Where, V is the fluid volume

(vi) Velocity gradient or shear rate

The characterization of the shear rate in the mixing vessel for a suspension is an important parameter for two reasons:

Firstly, the shear rate influences the average apparent viscosity of non-Newtonian fluids and hence affects power absorption, mixing characteristics and mass transfer phenomena (90).

Secondly the suspended solids are susceptible to be damaged, this is dependent on the prevailing shear rate and associated shear stress (107,108).

Most authors have correlated shear rate with the rotational speed of the impeller (109–112), or with power input that depends on the stirrer speed (113,114). The specific energy dissipation rate in a stirred vessel is well known to depend on the shear rate $\dot{\gamma}$ and the shear stress σ, as follows:

$$\mathbf{\frac{P_w}{V} = \boldsymbol{\sigma} \times \dot{\boldsymbol{\gamma}} = \frac{N_{P\times}\boldsymbol{\rho} \times N^3 \times D^5}{V}} \qquad \textbf{(Eq. 55)}$$

Where, P_w is the power input and V is the volume of the fluid in the vessel. Furthermore, for newtonian fluids, the viscosity η is the ratio of shear stress and shear rate, i.e.

$$\boldsymbol{\eta = \frac{\sigma}{\dot{\gamma}}} \qquad \textbf{(Eq. 56)}$$

Therefore, (Eq. 55) can be written as follows:

$$\mathbf{\frac{P_w}{V} = \boldsymbol{\sigma} \times \dot{\boldsymbol{\gamma}} = \boldsymbol{\sigma} \times \dot{\boldsymbol{\gamma}} \times \frac{\dot{\boldsymbol{\gamma}}}{\dot{\boldsymbol{\gamma}}} = \boldsymbol{\eta} \times \dot{\boldsymbol{\gamma}}^2} \qquad \textbf{(Eq. 57)}$$

Finally the shear rate can be expressed as:

$$\dot{\boldsymbol{\gamma}} = \sqrt{\frac{\mathbf{P_w}}{\mathbf{V} \times \eta}} \qquad \textbf{(Eq. 58)}$$

The (Eq. 58) applies to laminar, turbulent and transitional flows. For non-newtonian fluids obeying the power law (90), the viscosity is expressed as:

$$\eta = \mathbf{k}\dot{\boldsymbol{\gamma}}^{\mathbf{n-1}} \qquad \textbf{(Eq. 59)}$$

And therefore:

$$\dot{\boldsymbol{\gamma}} = \left(\frac{\mathbf{P_w}}{\mathbf{k} \times \mathbf{V}}\right)^{(\mathbf{1}/_{\mathbf{n+1}})} \qquad \textbf{(Eq. 60)}$$

(Eq. 60) applies to both laminar and turbulent flow regimes. Note that the shear takes place in the smallest eddies (Kolgomoroff length) defined as follows:

$$\boldsymbol{\lambda}_{\mathbf{k}} = \left(\frac{\mathbf{P_w} \times \boldsymbol{\nu}^{\mathbf{3}}}{\mathbf{V}}\right) \qquad \textbf{(Eq. 61)}$$

Where, $\upsilon=\eta/\rho$ is the kinematic viscosity [m²/s]) leading to a maximum hydrodynamic force acting on a spherical particle (115,116) defined as follows:

$$\mathbf{F_{Hydro}} = \frac{\mathbf{5}}{\mathbf{8}} \times \boldsymbol{\pi} \times \boldsymbol{\eta} \times \mathbf{d^2} \times \dot{\boldsymbol{\gamma}} \qquad \textbf{(Eq. 62)}$$

Where, η is the dynamic viscosity, d is the particle size, and $\dot{\gamma}$ is the characteristic velocity gradient, or shear rate.

(vii) Maximum shear rate

Miroslav Soos, 2007 (116), calculated the shear rate distribution normalized by its volume average value, for a stirring speed equal to 200 rpm (Rushton type impeller). In Figure 36, it is seen that the shear rate distribution is rather broad, covering approximately three orders of magnitude. In agreement with Derksen *et al.*(117), who used a large eddy simulation technique, the largest values of the shear rate (exceeding ten times the volume average values) are located at the tips of the impeller blades.

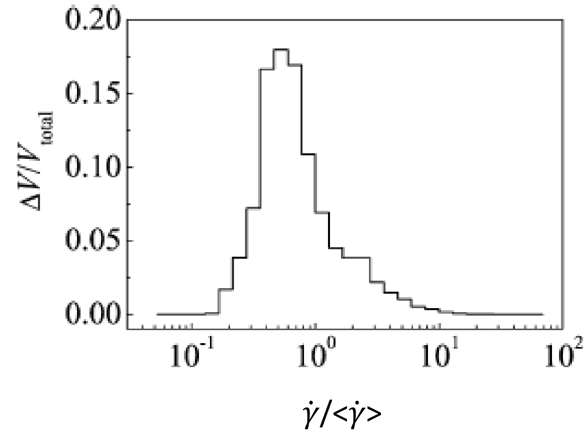

Figure 36: Histogram of the normalized shear rate distribution in the stirred tank calculated for a stirring speed equal to 200 rpm (116)**.**

The maximum turbulent shear rate can be determined by the local energy dissipation, close to the impeller. According to Geissler *et al.* (118), the maximal local energy dissipation can be calculated for cylindrical baffled vessels of diameter D_v and liquid height H by this formula:

$$\frac{P_{wvmax}}{<P_{wv}>} \sim 0.85 \times \left(\frac{D}{D_v}\right)^{-3} \times \frac{H}{D_v} \times {N_p}^{1/3} \qquad \text{(Eq. 63)}$$

2.4. Process engineering considerations for manufacturing of nano-crystalline suspension by top down process

In order to reduce particle size in the sub-micronic domain within reasonable length of time, very high energetic milling is required. The amount of energy required is generally higher than 200 kJ/kg (see Figure 37).

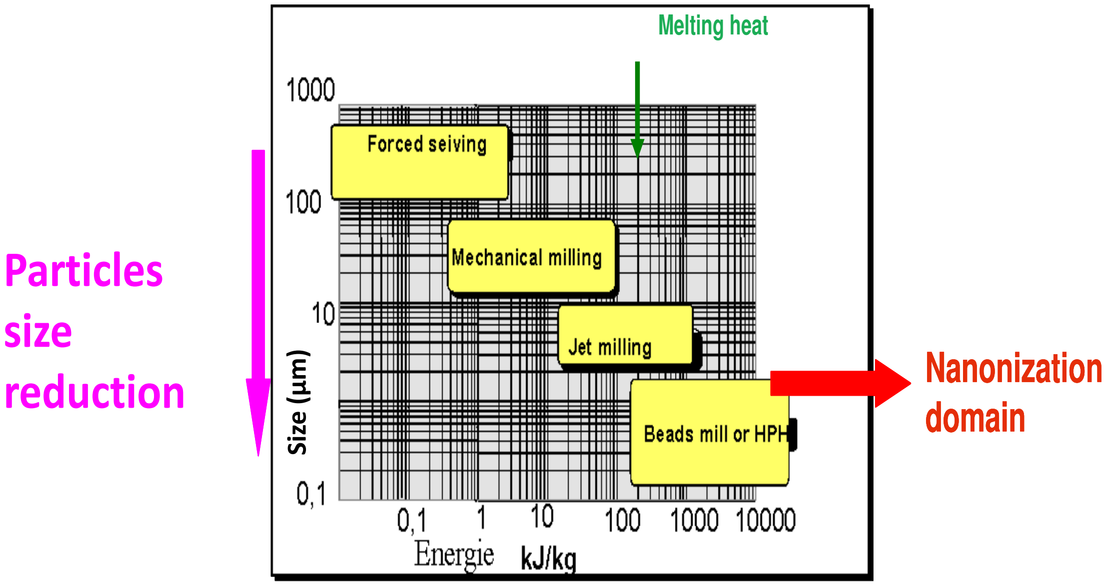

Figure 37 : Energy required for milling according the technology to be used (52)**.**

The technologies commonly used for the production of nano-crystalline suspensions are stirred bead milling or high pressure homogenization.

2.4.1. Principles and mechanisms of milling

2.4.1.1. Milling processes

The changes in particle size and morphology that occur during milling are produced by the following processes (119):

(i) Particles compression and deformation by impact from the milling media: It is the initial and predominant process during milling. This process takes place with little or no net change in individual mass of particles (120,121);

(ii) Fractures: after a period of milling, individual particles deform until cracks are initiated. Then, the cracks propagate until the lead fracture of the particles (120,121);

(iii) Particles agglomeration may occur by bridging, mechanical interlocking of spongy or rough surfaces, or auto-adhesion (Van der Waals forces) (120,121).

2.4.1.2. Mechanism of milling

The milling mechanism consists of an initial stage of compression and deformation. In this stage the particles deform by fracture and by cold welding. As the particles become deformed, they enter a secondary stage caused by fatigue failure and fragmentation. Generated fragments may continue to be reduced in size by alternate compression/deformation and fracture. When fracture dominates, particles continue to become smaller. The degree of size reduction is a function of the milling time (122,123). After a period of time, cold welding and fracturing of the particles attain a steady state equilibrium. The average particle size that can be obtained at this stage depends on the relative ease with which the agglomerates can be formed by welding, fatigue, fracture, and resistance of particles to deformation.

2.4.1.3. Kinetic energy in milling devices

Depending on the way the kinetic energy is transmitted from the motor to the milling media and to the material to be milled, the mills can be divided into three main groups (119):

(i) Kinetic energy is transmitted to the mill body, and then it is transferred to the milling media and material to be milled by friction. The material is subjected to centrifugal and gravitational forces (mills with loose media);

(ii) Kinetic energy is transmitted directly to the particles (various types of peripheral speed and roller mills);

(iii) Kinetic energy is transmitted directly to the material by means of a flowing stream which creates collisions between particles and leads to their impact on a rigid obstacle (fluid energy mills) (121,124,125).

2.4.1.4. Conversion and transfer of energy during milling

Theoretically, there are three main stages of conversion and transfer of energy during milling (121):

(i) Conversion of the drive's kinetic energy to a mechanical action;

(ii) Transfer of the mechanical action to the particles to be milled;

(iii) Use of the stress produced by the mechanical action for the failure stress of the particles.

2.4.2. Stirred bead milling

Stirred bead mills are increasingly used for fine and ultrafine grinding of minerals, ceramic materials, paint, pigments, chemical products, microorganisms, pharmaceutical products and other materials. The stirred bead milling process has led to the successful launch of many products (see section 2.1.3). It was developed it in 1990 by Nanosystems (Kodac group affiliate). Their applications have been widely described in patents and literature (126).

The mill consists of a milling chamber, a milling shaft, a milling media, and a recirculation chamber. The milling chamber is charged with the milling media, water, the product to be milled (i.e. drug) and stabilizer. The milling media or pearls are then rotated at a certain shear rate. They can be made of ceramic (zirconium oxide, alumina oxide, silicon nitride, zirconium silicate, steatite, mulllite, etc….) or polymeric (cross-linked polystyrene). The milling chamber can be made of stainless steel, zirconium oxide or silicon carbide The process can be performed in either batch or recirculation mode. Once the formulation and the process are optimized, a very little batch-to-batch variation is observed in the quality of the dispersion. The principle of milling is based on the high energy and shear forces generated as a result of the impaction of the milling media with the drug that provides the energy input to break the micro-particulate drug into nano-sized particles. Due to the high energy used during milling, the process needs to be performed under controlled temperature.

2.4.2.1. Different mill designs

In the last ten years, different types of closed stirred media mills were developed by the industry. Various mill designs differ mostly in their chamber and stirrer geometry as well as in the separation device, which allows free discharge of the product, but prevents the grinding media from leaving the mill. In general, three different mill designs are used for producing nano-crystalline suspensions (see Figure 38, Figure 39, Figure 40).

(i) Stirred disc mill;
(ii) Stirred pin mill or pin counter pin mill;
(iii) Stirred annular mill.

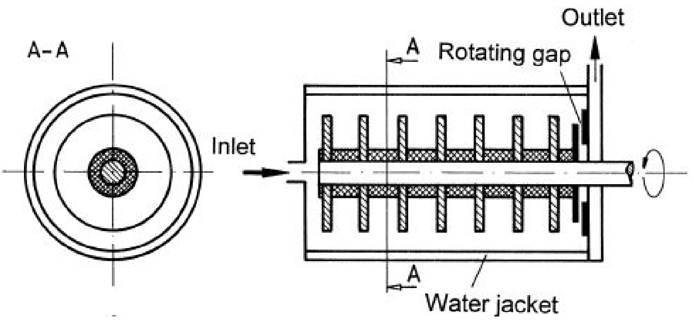

Figure 38 : Stirred disc mill design (127).

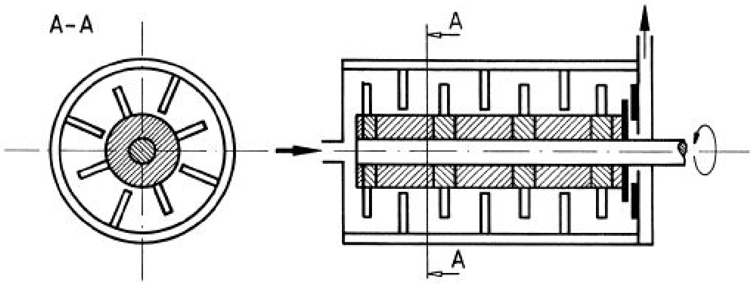

Figure 39 : stirred pin counter pin mill (127).

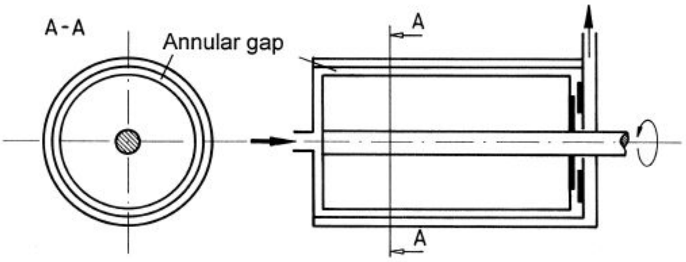

Figure 40 : Stirred annular mill (127).

2.4.2.2. Technological configuration

Three technological configurations are frequently used:

(i) Batch mode which consist of using only the mill itself for manufacturing of nano-crystalline suspensions. The batch mode is usually used at lab scale (from 50 mL to 1 L) for the process development and the manufacturing of small batches for preclinical evaluation;

(ii) Recirculation mode, in which the suspension is recirculated through the mill by using an external vessel. The recirculation mode is generally used for the scaling up and production (in the pharmaceutical industry: from 0.6 to 60 litres);

(iii) Discrete passages mode, in which the suspension is recirculated through the bead mill by using an external vessel. During one passage the first vessel is used as feeding vessel and the second one as milled suspension reception. Generally, the discrete passages mode is more efficient than the recirculation one but needs more complex automations specifically when it has to be used at industrial scale.

Recently Van Eerdenbrugh *et al*. published a nano-suspension scaling-down production study by milling compounds in glass vials in a ball mill which allows for screening stable nano-suspension formulations with very low drug substance amounts of 10 mg (128). They used the planetary mill equipped with a specific holder that could contain up to 10 vials of a few mL. The mill is a low shear one. The related process cannot be scaled up to the high shear mills due to the difference of the hydrodynamic within both mills. Nevertheless, the planetary mill gives a good indication on the milling process of the suspension. Consequently, it is used for the formulation engineering and reduces significantly the API consumption in the early stage development.

Figure 41, Figure 42 and Figure 43 show the schemes of the planetary mill and the three milling modes.

Figure 41 : Planetary mill equipped with stirred media in glass vials (129)**.**

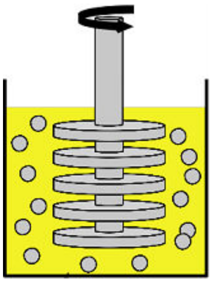

Figure 42 : Stirred bead mill using batch mode (130).

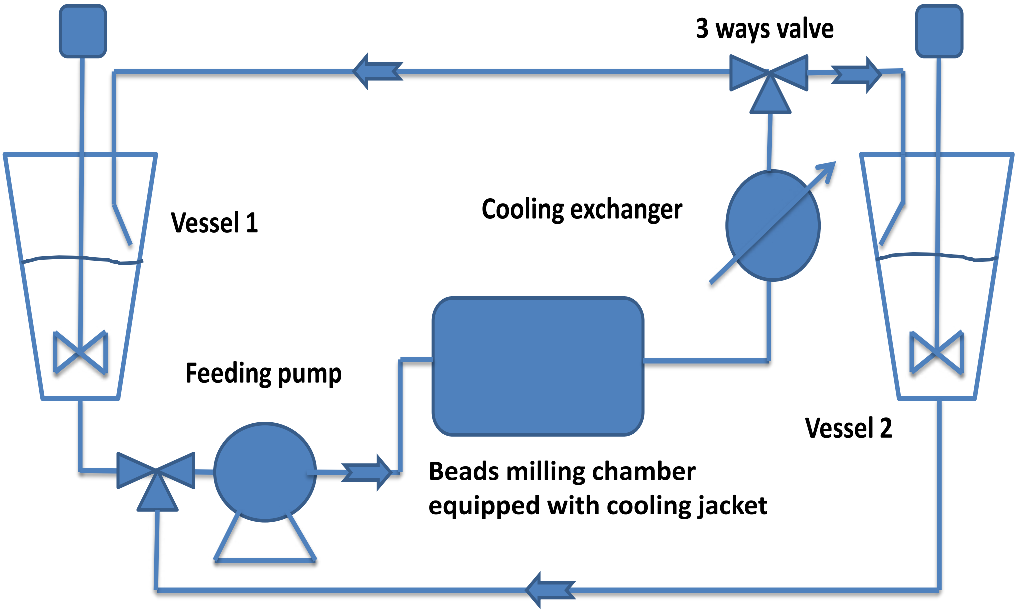

Figure 43 : Stirred bead mill using recycling mode or discrete passages (130).

2.4.2.3. Theoretical considerations

Ultra-fine milling is well established for inorganic material. A large amount of research investigations on stirred bead milling has been carried out at the Institute for Particle Technology in Braunschweig, Germany, where the approach developed by Kwade *et al.* (127) has became the most established in this area. However, for the organic material, an abundant lliterature can be found but it is mainly dedicated to formulation and biopharmaceutical characterization and not to process engineering . Fundamental differences (131–133) between mechanical properties of organic and inorganic materials at small deformations, plastic deformation and deformation to fracture may exist and should impact milling performances.

In the approach developed Kwade *et al.* it was described that two conditions are required to break the particles. Firstly, there must be a direct contact between the milling media and the particles. Secondly, the milling media must apply sufficient stress intensity to the particles. The milling process in a stirred bead mill depends on the stress number and the stress intensity. The stress number is determined by the number of media contacts N_c, by the probability that a particle is caught and sufficiently stressed at a media contact P_s, and by the number of product particles inside the mill N_{part}.

$$\mathbf{SN} = \frac{\mathbf{N_{C} \times P_{S}}}{\mathbf{N_{Part}}} \qquad \textbf{(Eq. 64)}$$

The number of media contacts is assumed to be proportional to the number of revolutions of the stirrer N and to the number of grinding media in the chamber N_{gm}.

$$\mathbf{N_c \propto N \times t \times N_{gm} \propto N \times t \times \frac{V_{ch} \times \emptyset_{gm} \times (1-\varepsilon_{gm})}{\frac{\pi}{6} \times d_{gm}^3}} \qquad \textbf{(Eq. 65)}$$

Where N is the frequency of revolutions of the stirrer per unit time, t is the milling time, V_{ch} the volume of the grinding chamber, ϕ_{gm} the filling ratio of the grinding media, ε_{gm} the porosity of the bulk of grinding media and d_{gm} is the diameter of the grinding media.

The probability that a particle is caught and sufficiently stressed at a media contact, depends on the type of the grinding process and on other parameters. In case of desagglomeration and cell disintegration this probability P_c is proportional to the surface of the grinding media according to Stadler *et al.* (134) and Bunge (135) because the shear stresses acting between the media can be sufficient for desagglomeration and disintegration:

$$\mathbf{P_c \propto d_{gm}^2} \qquad \textbf{(Eq. 66)}$$

In case of grinding of crystalline materials, the probability is proportional to the active volume between two grinding media, which is proportional to the diameter of the grinding media:

$$\mathbf{P_c \propto d_{gm}} \tag{Eq. 67}$$

The number of product particles is proportional to the overall volume of the product particles, which can be written as follows:

$$\mathbf{N_{Part} \propto V_{Part} \propto V_{ch} \times (1 - \emptyset_{gm} \times (1 - \varepsilon_{gm})) \times C_{pv}} \tag{Eq. 68}$$

Where, V_{part} is the total volume of the particles within the chamber and C_{pv} is the volume concentration of solid.

Combining equations above, the following proportionality can be derived for the stress number (grinding of crystalline materials).

$$\mathbf{SN \propto \frac{\emptyset_{gm} \times (1-\varepsilon_{gm})}{(1-\emptyset_{gm} \times (1-\varepsilon_{gm})) \times C_{pv}} \times \frac{N \times t}{d_{gm}^2}} \tag{Eq. 69}$$

The milling stress intensity at each stress event influences the milling result: when grinding crystalline materials, a finer product is obtained with increasing stress intensity for a certain number of stress events

The milling stress intensity SI is proportional to the stress intensity of the grinding media SI_{gm} which is equal to the kinetic energy of the grinding media (127):

$$\mathbf{SI \propto SI_{gm} = d_{gm}^3 \times \rho_{gm} \times v_t^2} \tag{Eq. 70}$$

Where ρ_{gm} is beads density and v_t is the beads tangential velocity.

The stress energy SE is the energy transferred to the product during one stress event. It is known that the specific energy (E_s) is proportional to the product of the number of stress events and the stress energy of the grinding media SE_{gm} (133):

$$\mathbf{E_s = \frac{P_w \times t}{m} \propto SN * SE_{gm}} \tag{Eq. 71}$$

$$\mathbf{E_s = \frac{\int_o^t (P_w(t) - P_w(0))dt}{m}} \tag{Eq. 72}$$

Where P_w is the total power consumed inside the grinding chamber decreased by the no loaded power $P_w(0)$, $P_w(t)$ is the power at time of milling t and m is the solid mass inside the chamber.

The specific energy depends on stirrers' tip speed, solid concentration, beads size and beads filling ratio and time of milling.

The power draw can be determined by a torque measurement or by the relationship between dimensionless numbers: power number (described by (Eq. 51)) and Reynolds number (described by (Eq. 50)).

In analogy to stirring technology, it is assumed that the power number only depends on the Reynolds number. Tests with a newtonian fluid and grinding media were carried out in a stirred media mill with disc-stirrer geometry to obtain a theoretical relationship between the Newton number and the Reynolds number (134,136). The results are shown in the Figure 44**.**

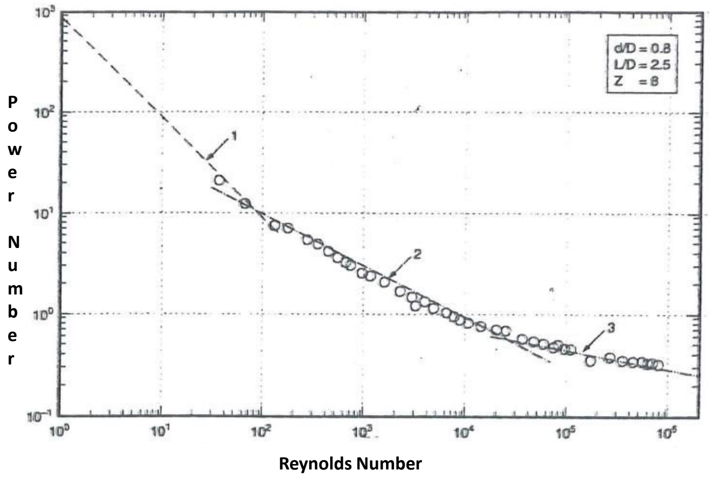

Figure 44 : Relation between power number and Reynolds number without grinding media (137)

In the case of an operation with grinding media, the question is whether the grinding media belong to the mill itself or to the suspension. If the grinding media belong to the suspension, the density and the viscosity, the values of the grinding media-product suspension must be used. In this case the relationship between the power and the Reynolds number is shown in Figure 44 and is also valid if the mill is operated with grinding media. If the grinding media are considered to be part of the mill (like baffles in stirred vessel), the physical quality of the product suspension can be taken for the suspension density and viscosity. In this case, different relationships between the Newton and Reynolds numbers exist for each filling ratio of grinding media, for each grinding media density and for grinding media size. Figure 45 shows the relationship between the Newton and Reynolds numbers for a mill with disc stirrer that was operated without grinding media (continuous line) and with tree different filling ratios of grinding media.

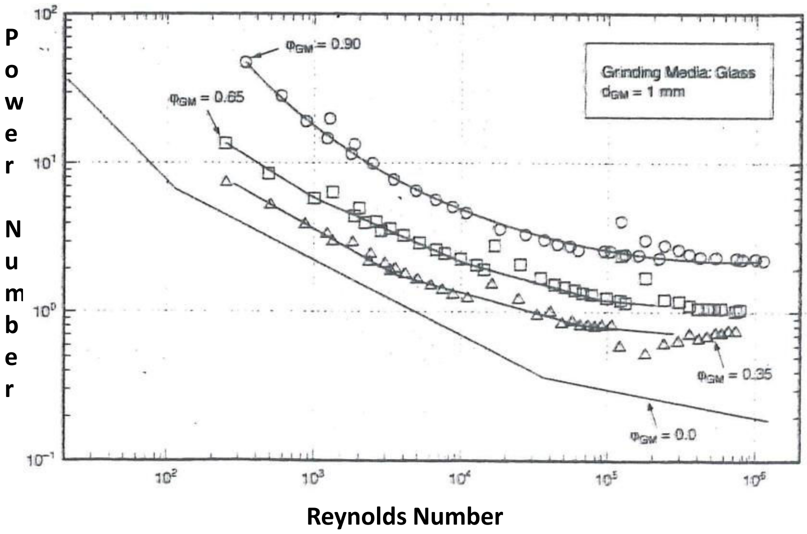

Figure 45 : Relation between Newton number and Reynolds number for the stirrer of different grinding media (137)**.**

For a constant filling rate (Φ_{gm}) and a constant milling media size (d_{gm}), the power number is proportional to the Reynolds number at given power y:

$$\mathbf{N_P = Re^y \text{ then } P_w \propto N^{3+y} \times D^{5+y} \times \rho^{1+y} \times \eta^y} \qquad \text{(Eq. 73)}$$

For a non-constant filling rate (Φ_{gm}) and non-constant milling media size (d_{gm}), the power number is proportional to the Reynolds number at power y, to the filling rate at power x and to milling media size at power o

$$\mathbf{N_P \propto \phi_{gm}^x \times Re^y \times d_{gm}^o \text{ then } P_w \propto \phi_{gm}^x \times N^{3+y} \times D^{5+y} \times \rho^{1+y} \times \eta^y \times d_{gm}^o} \qquad \text{(Eq. 74)}$$

$$\mathbf{V_t \propto N \times D} \qquad \text{(Eq. 75)}$$

For each region of the Reynolds number, a different relationship arises between the power draw and the following parameters: number of revolutions or stirrer tip speed, product density and viscosity, stirrer diameter, beads filling ratio and beads diameter. The typical exponents to determine the power draw are gathered in Table 4 (137):

parameter	Φ_{gm}		**N**	**D**	ρ	η	d_{gm}
Exponent	x	y	3+y	2+y	1+y	-y	o
Reynolds number < 10^5	2.8	-0.5	2.5	1.5	0.5	0.5	≤ 0
Reynolds number > 10^5	2.2	0	3	2	1	0	≥ 0

Table 4: Exponent to determine power draw as function of important parameters.

2.4.3. High pressure homogenization

The first high-pressure homogenizer was developed by Auguste Gaulin in 1899. He introduced his machine for “treating milk” at the Paris World’s Fair in 1900 (138). The technology was then used in pharmaceutical industry, food industry, cosmetic industry, biotechnology industry and environmental technology, for the preparation and for stabilization of emulsions, liposomes and suspensions. It is also used for creating physical changes, such as viscosity changes, in products. Another application is cell disruption of yeasts or bacteria in order to release intracellular products such as recombinant proteins (139). The mechanism of particles or vesicle size reduction is based on cavitation (140), high shear forces, and collision of the vesicles or particles against each other. The dispersion or suspension passes through the high pressure homogenization device with a very high velocity. According to Bernoulli’s equation, the dynamic pressure of the fluid increases, at the same time the static pressure decreases below the pressure of saturation of the dispersion medium (generally water). This leads to the boiling of the milling medium and formation of vapour bubbles which implode when the dispersion or suspension leaves the gap. Considering the schematic representation described in Figure 46, if p_1 is the inlet pressure and p_2 is the outlet pressure, at the entrance, the velocity increases rapidly in the convergence zone, therefore, the pressure decreases and can eventually reach the vapor pressure, p_v, of the liquid causing formation of vapor bubbles (cavities in the liquid). When the cavitation bubbles implode (collapse of the cavities), shock waves are generated in the liquid. These shock waves break apart the dispersion.

Thus, the mechanisms that can lead to breakage of the particles are:

(i) The effects of laminar and turbulent shear in the convergence zone, which are sensitive to the viscosity of the fluid;

(ii) The implosion of vapor bubbles when cavitation takes place;

(iii) The impact of particles on the impact ring is more or less reduced by the fluid viscosity.

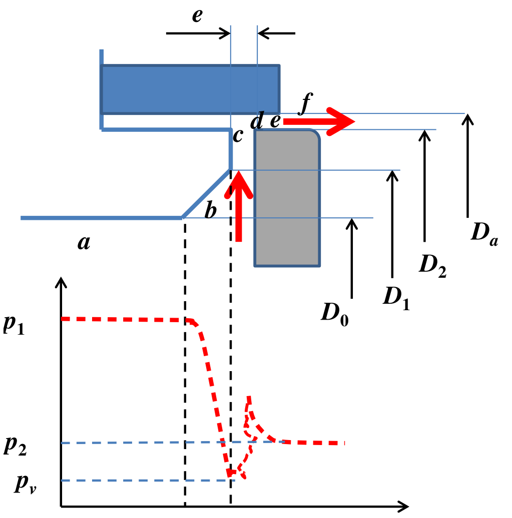

Figure 46: Pressure evolution within the valve (piston gap technology) (141)

2.4.4. Different high pressure homogenizer design

Two technologies are used in the industry: microfluidics technology and piston gap technology

2.4.4.1. Microfluidics technology

Micro-fluidisation works on a jet stream principle where the suspension is accelerated and passes at high velocity through specially designed interaction chambers. Frontal collision of fluid streams under high pressures (up to 1700 bars) inside the interaction chamber generates shear forces, particle collision, and cavitation forces necessary for particle size reduction. The interaction chamber can be made of stainless steel, polycrystalline diamond (PCD) or aluminium oxide. There are two types of interaction chambers: Y-chamber is useful for liquid-liquid emulsions and finds application in preparing liposomes while Z-chamber is typically used for cell disruption and nano-dispersion. A schematic representation of both chambers is shown in Figure 47.

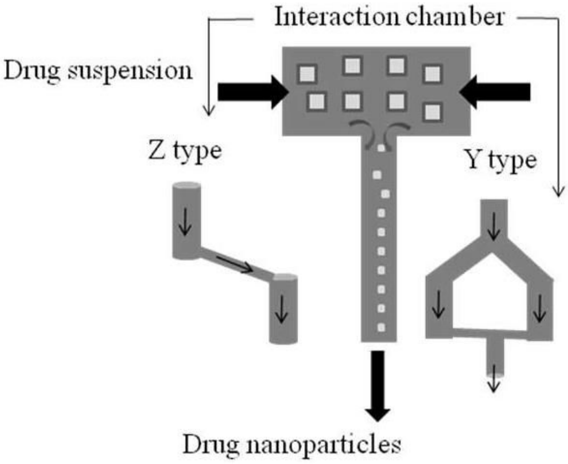

Figure 47: Microfluidization technology (142)

2.4.4.2. Piston gap technology

The high-pressure homogenizer consists in the combination of a high-pressure plunger pump with a homogenization valve (Figure 48). The role of the plunger pump is to provide the energy level required for the homogenization valve. The homogenization valve consists of a fixed valve seat and an adjustable valve. These parts form an adjustable radial precision gap. The gap conditions, the resistance and thus the homogenization pressure vary as a function of the force acting on the valve. An external impact ring forms a defined outlet cross-section and prevents the valve from damaging (Figure 49).

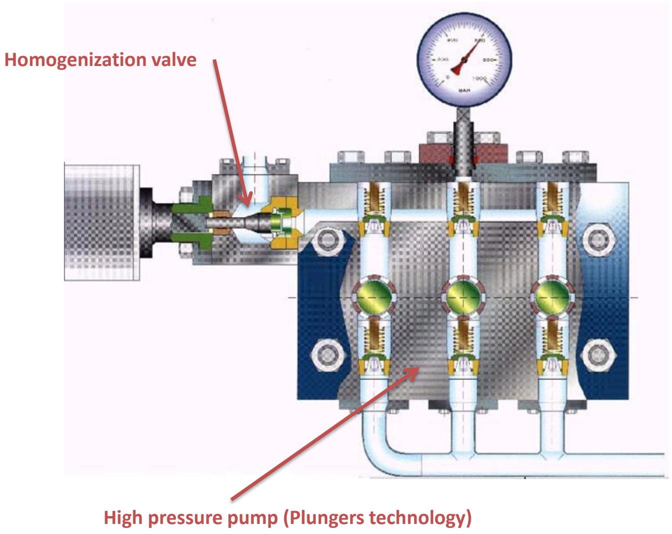

Figure 48: High pressure homogenizer piston gap technology (143)**.**

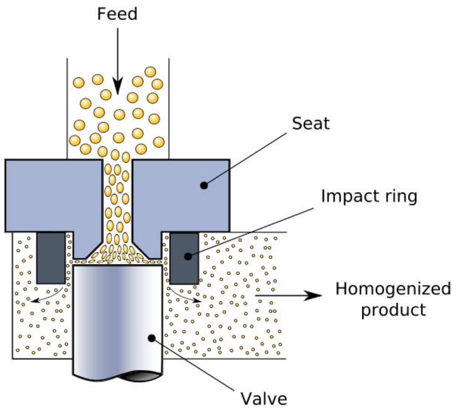

Figure 49: Homogenization valve (144)**.**

High pressure homogenization was developed by R. H. Müller (Müller *et al.*, 1998) (145) and used for the production of crystalline suspensions by Disso Cubes technology. The patent rights of Disso Cubes were initially owned by Drug Delivery Services GmbH (DDS) and are currently owned by SkyePharma plc. Disso Cubes are using piston-gap-type high-pressure homogenizers.

The rest of this bibliographic section will focus on the piston gap technology which was mainly used in the experimental part of this PhD manuscript.

2.4.5. Technological configuration

Two technological configurations are frequently used:

(i) Recirculation mode (Figure 50) in which the suspension is recirculated through the high pressure homogenizer by using an external vessel. The recirculation mode is generally the standard mode used from lab scale (3 L/h) up to industrial scale (few thousands L/h);

(ii) Discrete passages mode (Figure 50) in which the suspension is recirculated through the high pressure homogenizer using two external vessel. During one passage the first vessel is used as feeding vessel and the second one as milled suspension reception. In general the discrete passages mode is more efficient than the recirculation one but it needs more complexes automation, specifically when it has to be used at industrial scale.

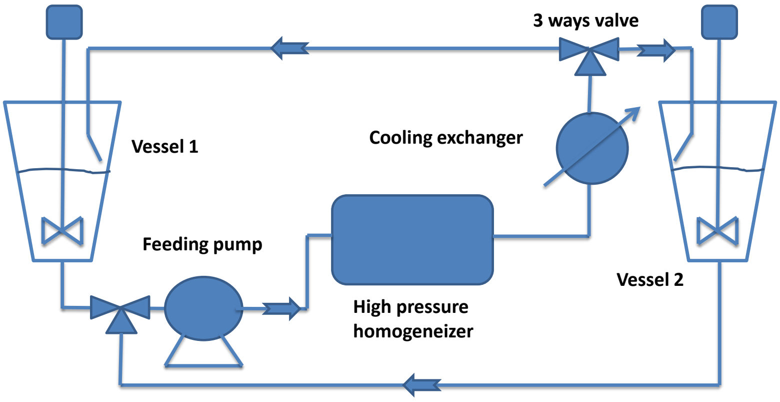

Figure 50: High pressure homogenizer using recycling mode or discrete passages (141)

2.4.6. Theoretical considerations

2.4.6.1. Pressure drop

The key parameters for a given geometry are the inlet and the outlet pressures. During homogenization, the volumetric pump maintains a certain nominal flow rate. The gap (ι) is adjusted in order to reconcile the inlet and outlet pressure-flow rate. The direct access to this important parameter (gap) is not possible. Beyond this basic aspect, the gap can obviously have various shapes and may be larger and smaller, and may even tends to 0 in the case of venturi profiles (see Figure 51, where, D_0 is the inlet diameter of the seat, D_1 is the inlet diameter of the seat outlet (conical part), D_2 is outlet diameter of the seat outlet, D_a is the inlet diameter of the impact ring and D_2-D_1 define the length of the seat edge.

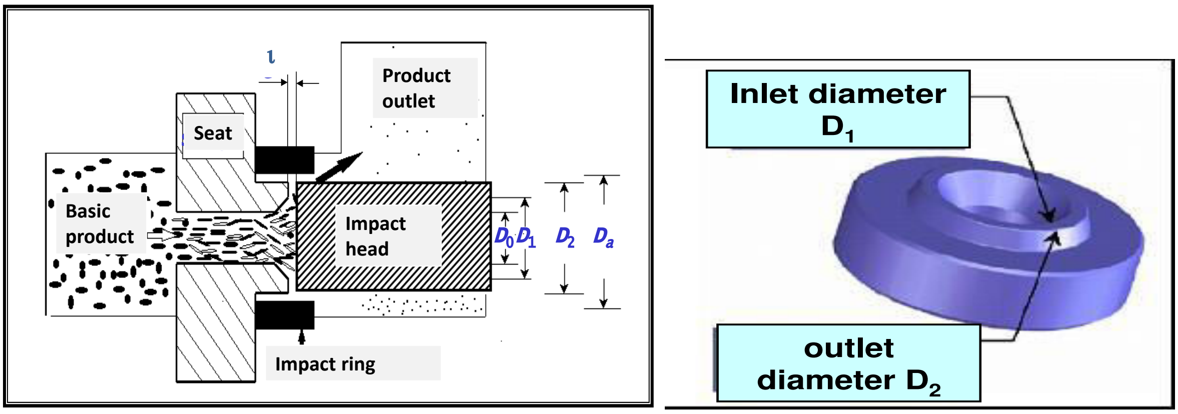

Figure 51: Homogenization valve with various dimensions (141)

Simple models have been proposed by various authors (146–151). These models have been well verified by numerical simulations (152). According to the proposed models, the global pressure loss can be expressed as:

$$\Delta \mathbf{P} = \mathbf{P_1} - \mathbf{P_2} = \Delta \mathbf{P_b} + \Delta \mathbf{P_{bc}} + \Delta \mathbf{P_{cd}} \qquad \textbf{(Eq. 76)}$$

Where, ΔP_b is the pressure loss at the inlet of the valve, ΔP_{bc} is the pressure loss linked to the frictions in the annular gap and ΔP_{cd}, is the pressure loss at the outlet of the valve. These pressure losses are classically explained as singularity (ξ) and friction (C_f) coefficient (see Table 5). It is assumed that, in the other zones, the jet speeds and the pressure losses are negligible.

Håkansson (153) summarized the different expressions:

$$\Delta \mathbf{P_b} = \boldsymbol{\xi_p} \times \frac{1}{2} \times \boldsymbol{\rho} \times \langle \mathbf{u_b} \rangle^2 \qquad \textbf{(Eq. 77)}$$

$$\Delta \mathbf{P_{cd}} = \boldsymbol{\xi_{cd}} \times \frac{1}{2} \times \boldsymbol{\rho} \times \langle \mathbf{u_e} \rangle^2 \qquad \textbf{(Eq. 78)}$$

$$\Delta \mathbf{P_{bc}} = 4 \times \mathbf{C_f} \times \frac{\mathbf{l_{gap}}}{\mathbf{d_h}} \times \boldsymbol{\rho} \times \langle \mathbf{u_{bc}} \rangle^2$$

(Eq. 79)

$$\mathbf{l_{gap}} = \frac{\mathbf{D_2 - D_1}}{\mathbf{2}}$$

(Eq. 80)

Where, l_{gap} is the width of the gap and d_h is the correspondent hydraulic diameter. The Reynolds number that defines the flow within the gap is expressed as follows:

$$\mathbf{Re_i} = \frac{\rho \times Q}{\pi \times D_1 \times \eta} \qquad \mathrm{Re_i} \in [10^3\,;\; 5\,10^3]$$

(Eq. 81)

Where, Q is the instantaneous flow rate, η is the viscosity

Author	ξ_p	ξ_{cd}	Δp_{bc}		regime
Nakayama	0.18	108/70	$\frac{6 \times \eta}{\iota^3} \times \ln\left(\frac{D_2}{D_1}\right) \times \frac{Q}{\pi}$	**(Eq. 82)**	laminar
Kawaguchi	0.18	128/126	$6.15\,10^{-3} \times \frac{\rho \times \nu^{1/4}}{\iota^3} \times \left(\frac{1}{D_1^{3/4}} - \frac{1}{D_2^{3/4}}\right) \times \left(\frac{Q}{\pi}\right)^{7/4}$	**(Eq. 83)**	turbulent
Phipps	0.50	1	$\frac{\rho \times \nu^{3/5}}{\iota^3} \times \left(\frac{1}{D_1^{2/5}} - \frac{1}{D_2^{2/5}}\right) \times \left(\frac{Q}{\pi}\right)^{7/5}$	**(Eq. 84)**	$\mathbf{Re_i} \in [\mathbf{10^3}\,;\; \mathbf{5\,10^3}]$

Table 5: Expression of different pressure losses.

3 correlations can be obtained for ΔP. If ΔP is known, it is possible to deduce ι and therefore the speed of the outlet jet:

$$\mathbf{u_{j0}} = \frac{\mathbf{Q}}{\boldsymbol{\pi} \times \mathbf{D_2} \times \boldsymbol{\iota}}$$

(Eq. 85)

$$\Delta \mathbf{P} = \mathbf{0.18} \times \frac{\rho}{2} \times \left(\frac{Q}{\pi \times D_{1\times}\iota}\right)^2 + \frac{6\times\eta}{\iota^3} \times \ln\left(\frac{D_2}{D_1}\right) \times \frac{Q}{\pi} + \frac{54}{70} \times \rho \times \left(\frac{Q}{\pi \times D_{2\times}\iota}\right)^2 \qquad \text{(Eq. 86)}$$

$$\Delta \mathbf{P} = \mathbf{0.18} \times \frac{\rho}{2} \times \left(\frac{Q}{\pi \times D_1 \times \iota}\right)^2 + \mathbf{6.15\ 10^{-3}}\,\frac{\rho \times \nu^{1/4}}{\iota^3} \times \left(\frac{1}{D_1^{3/4}} - \frac{1}{D_2^{3/4}}\right) \times \left(\frac{Q}{\pi}\right)^{7/4} + \qquad \text{(Eq. 87)}$$

$$\frac{64}{126} \times \rho \times \left(\frac{Q}{\pi \times D_2 \times \iota}\right)^2$$

$$\Delta \mathbf{P} = \mathbf{0.5} \times \frac{\rho}{2} \times \left(\frac{Q}{\pi \times D_{1\times}\iota}\right)^2 + \frac{5}{2} \times \frac{\rho \times \nu^{3/5}}{\iota^3} \times \left(\frac{1}{D_1^{2/5}} - \frac{1}{D_2^{2/5}}\right) \times \left(\frac{Q}{\pi}\right)^{7/5} + \frac{1}{2} \times \rho \times \qquad \text{(Eq. 88)}$$

$$\left(\frac{Q}{\pi \times D_2 \times \iota}\right)^2$$

Thus, if the flow rate, pressure and physical properties of the suspension are known, it is possible to evaluate the thickness of the gap (ι) that drives the hydrodynamic of the valve. Therefore, the power density can be calculated as follows:

$$\mathbf{P_{wv}} = \frac{Q}{\pi \times D \times \iota} \times \left[\frac{12 \times \eta \times Q}{\pi \times D \times \iota^3}\right] \qquad \text{(Eq. 89)}$$

The shear rate within the gap can be defined as follows:

$$\dot{\gamma} = \frac{6 \times Q}{\pi \times D \times i^2} \qquad \text{(Eq. 90)}$$

Or

$$\dot{\gamma} = \sqrt{\frac{3 \times P_{wv}}{\eta}} \qquad \text{(Eq. 91)}$$

2.4.6.2. Cavitation aspects:

The acceleration produced by any flow restriction leads to a local pressure drop. This phenomenon is associated with the geometry of the valve and the flow. In the valve considered here, a first acceleration takes place at the inlet but the critical area is located inside or at the exit of the gap, where the velocity and the pressure drops are maximum, primarily due to the inlet singularity and also due to the friction. It is possible to reach a critical pressure p_C from which cavitation starts due to accelerations and excessive depressurization in the flow. The determination of the threshold for a given valve needs to be done independently from its operating conditions (fluid type and its flow rate). Nowadays, the cavitation events could be detected by various means but cannot be localized. The search of criteria with a certain degree of generality leads to the definition of dimensionless ratio. The first parameter which is widely used by mechanical engineers is the number of cavitation Λ (154):

$$\boldsymbol{\Lambda = \frac{P_{ref} - P_V}{1/2 \times \rho \times u_{ref}^2}} \qquad \textbf{(Eq. 92)}$$

Where P_{ref} and u_{ref} are the values of pressure and velocity at a particular point of the considered flow, P_V is the vapor pressure of the fluid at the flow temperature. ρ is density of the fluid and u is the velocity of the fluid. Frequently, the high speed flow is not isotherm. Therefore, it is necessary to precise the conditions of P_V definition. In the case of high pressure homogenization valve, it is reasonable to define the reference point as the outlet of the gap. Therefore, if P_2 is the outlet pressure, the cavitation equation can be expressed as follows:

$$\boldsymbol{\Lambda = \frac{P_2 + \Delta P_S - P_V}{1/2 \times \rho \times u_{f0}^2}} \qquad \textbf{(Eq. 93)}$$

The combination of (Eq. 86) and (Eq. 93) leads to the following expression of cavitation number:

$$\boldsymbol{\Lambda = \xi + \frac{P_2 - P_V}{1/2 \times \rho \times \left(\frac{Q}{\pi \times D_2 \times \iota}\right)^2}} \qquad \textbf{(Eq. 94)}$$

ζ= 54/35 in the case of laminar regime and ζ= 1 in the case of turbulent regime.

If the second term is negligible Λ is given directly by the singularity coefficient corresponding to the gap outlet. The lower is Λ , the higher is the probability for occurrence of cavitation and higher is the intensity of milling.

The (Eq. 94) shows the importance of applying a counter pressure at the valve outlet.

A number of authors showed (155–158) that it is possible to express the cavitation number by using a simple equation:

$$\boldsymbol{\Lambda} = \frac{\mathbf{P_2}}{(\mathbf{P_1} - \mathbf{P_2})} \qquad \textbf{(Eq. 95)}$$

Where, P_1 and P_2 are the inlet and outlet pressure, respectively.

Others authors simply use the pressure ratio.

$$\boldsymbol{\omega} = \frac{\mathbf{P_2}}{\mathbf{P_1}} \qquad \textbf{(Eq. 96)}$$

The critical value of ω is in the range of 0.2 to 0.50 and often 0.15 to 0.20 depending on experimental results.

Objectives

3. Thesis objectives

Two technologies are currently used in the pharmaceutical industry for the production of nano-crystalline suspensions: bead milling and high pressure homogenization. The suspensions produced are nanosized particles covered with a stabilizer. The milling principles of both technologies are completely different. Bead milling relies on high energy and shear forces generated by the collisions of milling media which stress solid active pharmaceutical ingredients (APIs) and provide the energy necessary to break the APIs. In contrast, the fracture of API particles by high pressure homogenization is brought by cavitation, high-shear forces and collision of the particles against each other. The selection of suitable technology for the production of nano-crystalline suspension depends on a number of questions about the quality of produced nano-suspension by both technologies such as:

(i) How does the technology impact the formation and stability of nano-suspensions, hence their overall performance?
(ii) How does the physical stability of the particles differ when using the same API in both technologies?
(iii) How are the particle size distribution and shape impacted by used technology?
(iv) Which technology is easily scale-able, providing little batch-to-batch variation?
(v) How sensitive is the technology towards generation of residues of the milling media in the final product due to erosion?
(vi) How does the crystal structure or amorphization of the nano-particles change when using both technologies?
(vii) Are the technologies sufficiently reliable, robust and compliant with pharmaceutical regulations for the production of pharmaceutical suspension that can be used for different delivery systems?

The work described in this thesis was designed to address some of these questions, and focused on the following:

(i) Development of Physical/-chemical methodology for stabilizers selection tacking into account the specificities of both technologies;
(ii) Systematic comparison of both technologies and evaluation of the effect of the processing method and stabilizer suitability on nano-suspension preparation and stability. For that purpose a study will be conducted to evaluate the impact of

formulation composition, process parameters, and technology configuration on milling performances in terms of particle size distribution of milled suspension, physical form of milled suspension and wearing of milling media;

(iii) Proposal of modelling tool for process prediction and simulation.

Material & methods

4. Material & methods

4.1. Material

4.1.1. Materials used for formulation engineering

The hydrophobic and non ionisable highly insoluble active pharmaceutical ingredient (API) A was obtained from Sanofi. API A was micronized by jet milling before use. The physico-chemical properties of API A are provided in Table 6

Average particle diameter (µm)	5
Specific surface area (m²g) **	1.5
Molecular weight (g/mol)	497.4
Water solubility (µg/ml)	0.2
pKa	-
Log [P] (*)	6.9
Real density (g/ml)	1.42
Melting point (°C)	156.7

Table 6: Physico-chemical properties of the API used for formulation engineering.

(*) [P] is the partition coefficient between Octanol and water
(**) measurement is performed using Blaine method (159).

The dispersant / wetting agents used for the investigation and their intended use in suspension stabilization are listed in the Appendix A. Several chemical categories were used (Cellulose derivatives, Povidones, Phospholipides, Poloxamers, PolyEthyleneGlycol and derivatives, Fatty Acids and Fatty acid Esters, SDS, sodium ployacrylate).

4.1.2. Materials used for process engineering

The active pharmaceutical ingredients were obtained from Sanofi. Their physico-chemical properties are provided in Table 7.

API Identification	**A**	**B**	**C**	**D**	**E**	**F**	**G**
Molecular weight (g/mol)	497.4	456.4	401.4	411.9	255.3	408.5	405.0
Melting temperature (°C)	156.7	241.6	183.0	240.0	166.0	183.7	92.7
Log P	6.90	4.75	4.1	2.90	2.90	> 5.70	2.50
Water solubility (µg/ml) at neutral pH (6.8)	0.200	0.025	7.100	10.000	5.300	3.500	15.000

Table 7: Physico-chemical properties of the different APIs used for milling evaluation.

The formulation of each API is described in Table 8.

API Identification	A	B	C	D	E	F	G
API content (%)	20	20	15	20	10	10	10
Stabilizer type	PVP K30 (1) SDS (2)	PVP K30 (1) SDS (2)	PVP K25 (1) Sodium docusate (2)	PVP K30 (1) Sodium docusate (2)	Poloxamer 188 (1) mPEG 2000 DSPE (2)	Poloxamer 188 (1) mPEG 2000 DSPE (2)	Poloxamer 188 (1) mPEG 2000 DSPE (2)
Stabilizer content (%)	(1): 0.48 (2): 0.72	(1): 0.48 (2): 0.72	(1): 4 (2): 0.2	(1): 2.5 (2): 0.1	(1): 0.5 (2): 0.2	(1): 0.5 (2): 0.2	(1): 0.5 (2): 0.2
Water content (%)	78.8	78.8	80.8	77.4	89.3	89.3	89.3

Table 8: Associated formulation of each API.

Luvitec® Polyvinylpyrrolidone (PVP K25 and K30) having a molecular weight of 25.000 and 30.000 g/mol, respectively. They were purchased from BASF (France). Sodium dodecyl sulfate (SDS) having molecular weight of 288.4 g/mol was purchased from Univar (France), Dioctyl' sulfosuccinate sodium salt (Sodium docusate) having molecular weight of 444.56 g/mol was purchased from Sigma-Aldrich®, Poloxamer 188 (Pluronic® F 68 NF Prill) having molecular weight of 8400 g/mol was purchased from BASF (France) and Maleimide.

1,2-distearoyl-sn-glycero-3-phosphoethanolamine-N-[maleimide(polyethylene glycol)-2000] (ammonium salt) (mPEG 2000 DSPE) having molecular weight of 2941.605 g/mol was purchased from Avanti® Polar lipids USA.

4.2. Methods

4.2.1. Preparation of nano-suspensions for formulation engineering

For the screening of dispersant / wetting agents using low shear milling, a suspension containing 20 % (w/w) of API, 3 % (w/w) of dispersant / wetting agents, and 77 % (w/w) of water for injection (WFI) was prepared. An aliquot of 10 ml of the suspension and 20 ml of Zirconium oxide beads (700 µm diameter supplied by Netzsch (Germany)) were introduced in 30 ml glass vial. The vial was shaked in orbital roller mill (see Photo 1) for 5 days at 0.03 m/s and at ambient temperature.

Photo 1: Orbital roller mill.

For the assessment of process ability using high shear milling, a suspension containing 20 % (w/w) of API, 3% (w/w) of dispersant / wetting agents and 77 % (w/w) of WFI was prepared. An aliquot of 50 ml suspension and 50 ml of Polymill® Cross-linked Polystyrene bead milling media (500 µm diameter supplied by Alkermes, Inc (Waltham, MA, USA) were introduced in a Nano-mill® 01 milling system (100 ml stirred annular mill purchased from Alkermes, Inc (Waltham, MA, USA), having a stator of 80 mm diameter and a rotor of 73 mm: see Photo 2). The mill was operated during 1 hour at 20°C and 3 m/s.

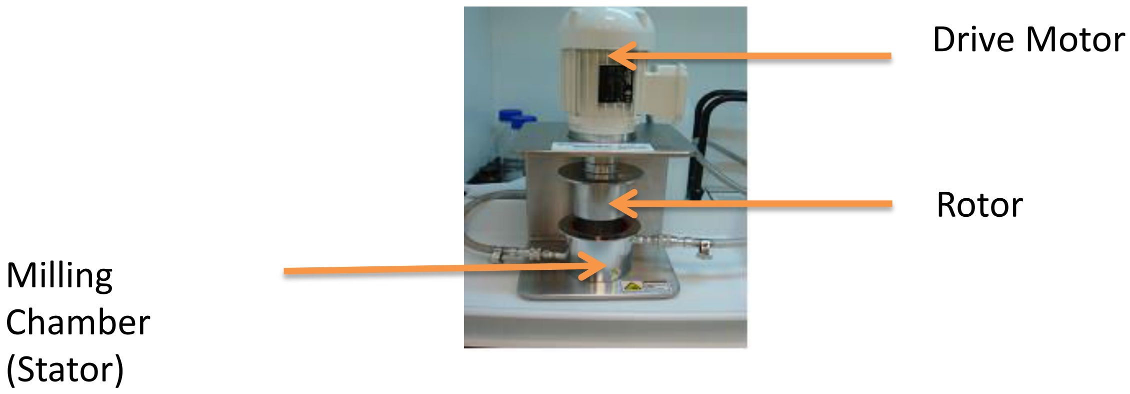

Photo 2: Stirred annular mill.

For the optimization of the % of selected dispersant / wetting agent, suspensions containing 20 % (w/w) of API, the dispersant / wetting agents concentration varying between 0.3 to 3% (w/w) and WFI qs 100% (w/w) were prepared. An aliquot of 50 ml suspension and 50 ml of Polymill® cross-linked polystyrene bead milling media (500 µm diameter supplied by Alkermes, Inc (Waltham, MA, USA) were introduced into a Nano-mill®01 milling system (stirred annular mill purchased from Alkermes, Inc (Waltham, MA, USA), having a stator of 80 mm diameter and a rotor of 73 mm). The mill was operated at 20°C and 3 m/s. The milling operation was performed during 105-240 min.

4.2.2. Milling evaluation for process engineering

4.2.2.1. Bead milling

4.2.2.1.1. Mill used for batch mode

The milling evaluation was performed using stirred annular mill (Nano-mill® 01 milling system). The mill is described in the section 4.2.1.

As the suspension stays within the mill chamber the real time is equal to the effective milling time (mean residence time).

4.2.2.1.2. Mills used for recycling mode

The milling evaluation was performed using 3 mills:

- Stirred disc mill (Dynomill® KDL milling system: The volume, diameter and length of the milling chamber are 618.5 ml, 77 mm and 150 mm, respectively. The rotor is equipped with 4 discs (made of polyamide) of 64 mm diameter (See Photo 3) purchased from WAB (Switzerland);
- Stirred pin mill (Labstar®) milling system: The volume, diameter and length of the milling chamber are 555 ml, 95 mm and 117 mm, respectively. The rotor has a diameter of 72.4 mm diameter (See Photo 4) supplied by Netzsch (Selb Germany);
- Stirred pin mill (LMZ2®) milling system: The volume, diameter and length of the milling chamber are 1600 ml, 128 mm and 194.5 mm, respectively. The rotor has a diameter of 104 mm diameter (See Photo 4) supplied by Netzsch (Selb Germany).

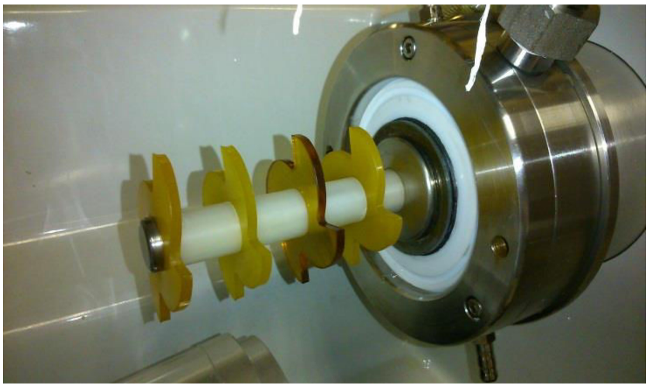

Photo 3: Dynomill® KDL milling system.

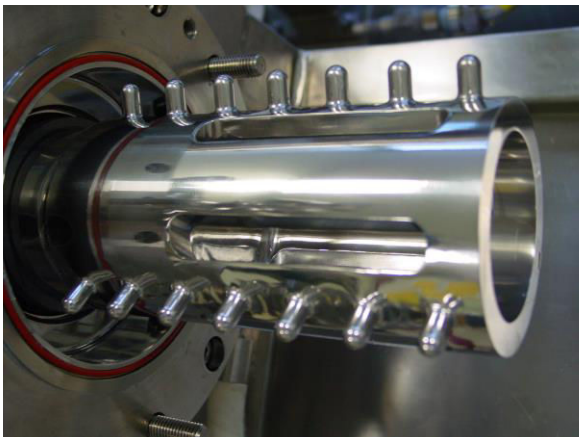

Photo 4: Stirred pin mill system.

For the assessment, a suspension containing the required quantities of API, dispersant / wetting agents and WFI was prepared in the recycling vessel. The required quantity of bead milling media was introduced in the milling chamber. Then, the suspension was fed from the vessel to the milling chamber by means of pump. The suspension enters to the milling chamber and flows back into the recycling vessel continuously. The mill was operated at fixed temperature (15°C) and fixed rotation speed. The generated heat during milling was removed by the cooling jacket of the milling chamber and the cooling exchanger.

For the recycling mode mills, as only a part of suspension resides within the mill chamber the effective milling time (mean residence time) can be defined as follows:

$$\textbf{Effective milling time} = \textbf{real milling time} \times \frac{\textbf{Active volume}}{\textbf{Batch volume}} \qquad \textbf{(Eq. 97)}$$

The active volume is defined as follows:

$$\textbf{Active volume} = (\textbf{Volume of the milling chamber}) - (\textbf{real volume of beads}) \qquad \textbf{(Eq. 98)}$$

The real volume of beads is defined as follows

$$\textbf{Real volume of beads} = (\textbf{apparent volume of beads}) \times \frac{\mathbf{d_{gm-app}}}{\mathbf{d_{gm}}} \qquad \textbf{(Eq. 99)}$$

Where, $d_{gm\text{-}app}$ and d_{gm} are the apparent density and the real density of beads, respectively.

4.2.2.1.3. Beads Material

Beads from two materials were used for milling evaluation:

- Polymill® cross-linked polystyrene bead milling media having bead size of 500 µm diameter supplied by Alkermes, Inc (Waltham, MA, USA) and 200 µm supplied by Netzsch (Selb Germany);
- Zirconium oxide bead milling media having bead size of 500 µm diameter supplied by Netzsch (Selb Germany).

4.2.2.2. High pressure homogenization

The milling evaluation was performed only at recycling mode using 2 types of high pressure homogenizer (HPH): Piston gap and Microfluidics technologies.

For the piston gap technology, 3 different scales were used (see Photo 5):

- Panda homogenizer$^{®}$ (supplied by GEA Niro-Soavi Parma Italy) having homogenization capacity of 10 litres/hour at 1400 bars. The high pressure pump is equipped with 1 plunger made of Zirconium Oxide;
- NS 2006 homogenizer$^{®}$ (supplied by GEA Niro-Soavi Parma Italy) having homogenization capacity of 35 litres/hour at 1400 bars. The high pressure pump is equipped with 2 plungers made of Zirconium Oxide;
- NS3024 homogenizer$^{®}$ (supplied by GEA Niro-Soavi Parma Italy) having homogenization capacity of 300 litres/hour at 1400 bars. The high pressure pump is equipped with 3 plungers made of Zirconium Oxide

Photo 5: High pressure homogenizers Panda, NS2006 and NS3024.

For the capillary technology only 1 scale was used: Microfluidcs$^{®}$ M110EH (supplied by Microfluidics$^{®}$ Inc USA) having a capacity of approximatively 24 Litres/hour at 1200 bars. The HPH was equipped with 2 Z shaped interaction chambers (H30Z and H10Z) made of poly-crystalline diamond and aluminum oxide ceramic, respectively. The two interaction chambers have a diameter of 200 µm and 100 µm, respectively (see Photo 6).

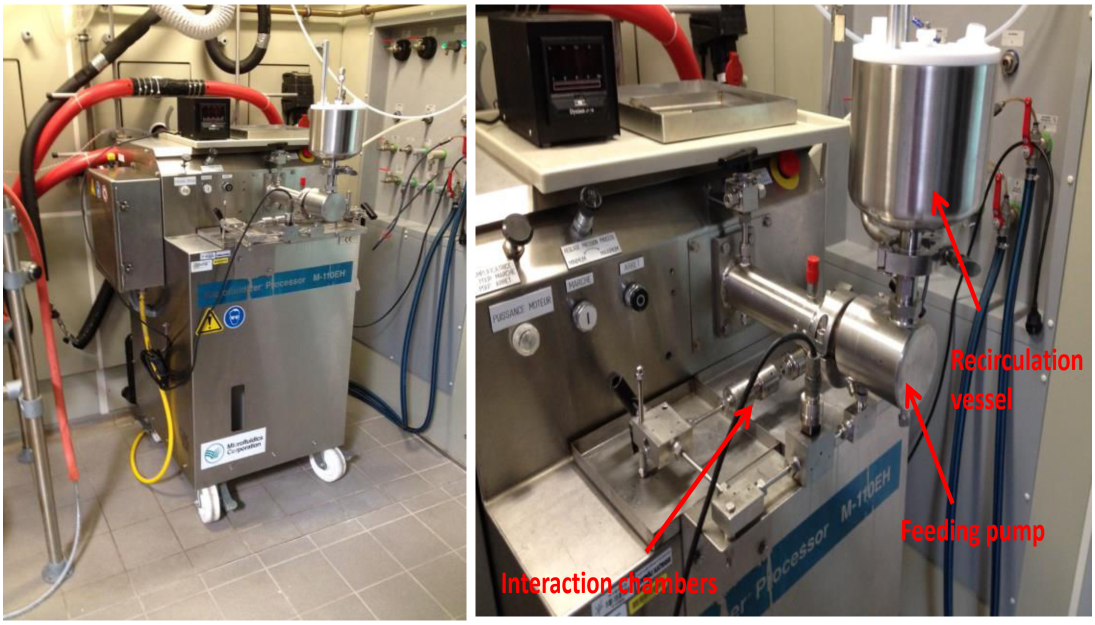

Photo 6: High pressure homogenizers Microfluidics®.

For the assessment, a suspension containing the required quantities of API, dispersant / wetting agents and WFI was prepared in the recycling vessel. Then, the suspension was fed from the vessel to the homogenizer by means of pump. The suspension enters to the homogenizer and flows back into the recycling vessel continuously via cooling exchanger to remove the generated heat during milling. The HPH was operated at fixed temperature (15°C) and fixed homogenization pressure.

For both homogenizers the milling kinetic was monitored by graphing a $6/d_{50}$ as function of recycling number which can be expressed as follows:

$$\mathbf{RN} = \frac{\mathbf{Q}}{\mathbf{V}} \times \mathbf{t} \qquad \textbf{(Eq. 100)}$$

Where, RN is the recycling number, Q is the flow rate (m^3/s) of homogenization, V is batch volume (m^3) and t is the time of homogenization (s).

4.2.3. Characterization

4.2.3.1. Measurement of specific surface area of API powder

The specific surface area (SSA) of API powder is measured using Blaine apparatus BSA1 supplied by ACMEL, France. The measurement was carried out at ambient temperature. The SSA was determined based on Kozeny-Carman theory (160), by measuring the air permeability of compressed powder bed. The relationship between the specific surface area (SSA) and the flow time (t) of a known volume of air in is given by:

$$\mathbf{SSA} = \mathbf{K_{ap}} \times \frac{\varepsilon^{3/2}}{\rho \times (1-\varepsilon)} \times \frac{t^{1/2}}{(0.1 \times \eta)^{1/2}} \qquad \textbf{(Eq. 101)}$$

Where Kap is the apparatus constant [$kg^{1/2}.m^{3/2}.s^{-1}$], ε is porosity of the compressed powder bed, η is air viscosity [Pa.s], ρ is the absolute density of the API [kg/m^3] and t is the flow time [s]

4.2.3.2. Suspension particle size measurement

The particle size measurement was performed using two methods:

(i) Dynamic light scattering (DLS), referred to as photon correlation spectroscopy (PCS), using Coulter N4+® equipment supplied by BECKMAN COULTER (France). The method is based on measuring the intensity fluctuation of scattered light as the particles undergo Brownian diffusion. From the intensity fluctuation, the diffusion coefficient D can be calculated, and from which, the particle radius, r, is estimated using the Stockes-Enstein equation (161). The particle size measurements were carried out using a scattering angle of 90°.The refractive index was fixed at 1.332. The temperature was fixed at 20°C. The suspension was diluted from 20 % (w/w) to 0.1 % (w/w) with purified water. 10 µl of diluted suspension were added to 1 ml of purified water. The resulting suspension was gently mixed in DLS cuvette and then placed into the measuring cell of DLS. The measurement was repeated 3 times. A repeatability study was performed on ten samples. The standard deviation was found about 0.8 %;

(ii) Laser diffraction using Malvern Mastersizer 2000®. This method is based on measurement of angle of light diffracted by the particles, which depends on the particle radius, using Fraunhofer diffraction theory. This method can measure the particle sizes down to 1 µm. For small particles, forward light scattering is measured with the application of Mie Theory of light scattering.

By combining the results obtained with light diffraction and forward light scattering, the particle size distributions in the range 0.02 to 10 µm can be measured (162).

The symmetry of distribution can be evaluated using polydispersity index that is described by the following equation:

$$\mathbf{P.I} = \mathbf{ln}\left(\frac{\mathbf{d_{10} \times d_{90}}}{\mathbf{d_{50}^2}}\right) \qquad \textbf{(Eq. 102)}$$

Where, d_{10}, d_{50}, d_{90} are the characteristic diameters of particle distribution referring to diameter of 10, 50 and 90 % of particles population, respectively.

Three situations may be encountered. They are described below:

(I) P.I = 0 for log-normal distribution;

(II) P.I < 0 for dissymmetric distribution towards small diameters $d_{50}/d_{10} > d_{90}/d_{50}$;

(III) P.I > 0 for dissymmetric distribution towards large diameters.

The Mastersizer is equipped with lens having focal length of 550 mm and cell measurement having thickness of 2.4 mm. The sample was diluted in 100 ml of purified water and introduced in MS1 sampler. The suspension was stirred at 1500 r.p.m and recirculated through the measurement cell. The dilution factor was adjusted in order to ensure an obscuration in the range of 2.5-4.5. The measurements were carried out at ambient temperature. Each measurement was performed during 20 seconds and repeated 3 times. The refractive index of the API and dispersing were fixed at 1.61 and at 1.33, respectively.

Each measurement was repeated 3 times. A repeatability study was performed on ten samples. The standard deviation was found about 1 %

4.2.3.3. Scanning electron microscopy (SEM) evaluation of suspension

The nano-suspension was diluted 10,000 times using WFI. 1 ml of the obtained suspension was filtered through Isopore® (Polycarbonate) filter having diameter of 13 mm and porosity of 0.1µm (supplied by Millipore, France). The filter was then rinsed 3 times with 1 ml of WFI for each rinse. The filter was then bonded to an aluminum pad using conductive adhesive on both sides, and subsequently metalized with gold using metallizer Xenosput XE200 EDWARDS. The gold deposit was approximately 1.5 to 2 nm thickness. For an overview and detailed view, nano-particles were observed at 15 kV using JEOL JSM-6300F® field emission SEM (supplied by SEMtech solution Inc USA), at several magnifications (X 1000, X 5000, X 10 000 X 20 000).

4.2.3.4. Suspension stability assessment

The short-term stability was monitored by measuring the particle size immediately after milling, after 7 days and after 15 days of storage at ambient temperature.

For the selected formulation, the stability was monitored over 8 weeks at ambient temperature.

4.2.3.5. Zeta potential measurement of suspension

A Zetasizer Nano ZS® (Malvern, UK), which applies the M3-PALS technique, a combination of laser Doppler velocimetry (LDV) and phase analysis light scattering (PALS), was used for the zeta potential measurements. The equipment employs a He-Ne laser (red light of 633 nm wavelength) which first splits into two, providing an incident and a reference beam.

From the electrophoretic mobility, μ, zeta potential, ζ, is calculated using the Smoluchowski equation (103), that is valid when

$$\boldsymbol{\kappa \times r >> 1} \qquad \textbf{(Eq. 103)}$$

(Where κ^{-1} is the Debye length and r is the particle radius). In case of small particles and a low electrolyte concentration, the Huckel equation is applicable for the calculation of zeta potential.

The sample to be measured was diluted in purified water to achieve a solid concentration in the range of 0.0001-0.1%. The obtained suspension was introduced in disposable cuvette (DTS1060) and gently mixed. The cuvette was then placed into the measuring cell of the Zetasizer. The dilution factor was checked in order to generate a minimum count rate of 20,000 counts per second. The measurements were performed at ambient temperature and repeated 3 times.

4.2.3.6. Rheological measurement of suspension

4.2.3.6.1. Unmilled suspension

Study state, shear stress versus shear rate curves, were carried out using HAAKE Viscotester® VT550 supplied by HAAKE (Germany). A concentric cylinder device was used for this measurement. The measurement was carried out at 20°C. The shear rate was gradually increased from 0 to 1500 s^{-1} (up curve) for over a period of 2 min and decreased from 1500 to 0 s^{-1} (down curve) over another period of 2 min. The test samples were 25 ml of unmilled suspension containing 20% API (w/w), 3 % (w/w) stabilizer and 77 % (w/w) of WFI. These samples were homogenized by using an ultra-Turrax® T-8 (supplied by IMLAB France) for 10 min at 6000 rpm. The measurements were performed at ambient temperature. When it is a Newtonian system, the shear stress increases linearly with the applied shear rate, and the viscosity of the suspension can be obtained from the slope. In this case, the up and down curves coincide with each other. When, it is a non-Newtonian system, the viscosity of the suspension decreases with the applied shear rate. When, it is a thixotropic system, the down curve is below the up curve showing hysteresis. The latter could be assessed by measuring the area under the loop.

4.2.3.6.2. Milled suspension

The viscosity measurement was conducted on a Thermo Scientific viscometer HAAKE MARS III equipped with coaxial system (double gaps concentric cylinder [CC27DG]) and Peltier temperature control.

2 milliliters of suspension were introduced in the system and were equilibrated for 5 minutes under constant shear rate of 50 s^{-1}. A shear rate ramp where the shear rate was increased from 0 to 7000 s^{-1} at a constant rate of 1400 s^{-1}/min with data collected at every second intervals was performed. Then a shear rate ramp where the shear rate was decreased from maximum shear rate to 0 s^{-1} was initiated in the same conditions.

4.2.3.7. Surface tension measurement of wetting/dispersant solution

The surface tension γ of selected dispersant / wetting agent was measured by using KRÜSS K12® tensiometer supplied by KRÜSS GmbH (Germany). In these measurements, the Wilhelmy plate method (163) was applied under quasi-equilibrium conditions. Therefore, the force required to detach the plate from the interface was accurately determined. From the γ versus log C, where C is the total surfactant concentration curves, the critical micelle concentration (CMC) was determined. The measurements were carried out at ambient temperature and repeated 3 times.

4.2.3.8. Evaluation of wetting

Wetting was assessed using the sinking time test method , as well as by measuring the rate of penetration of wetting/dispersant solution through a powder plug based on Washburn method (58,164). By manual tapping a known weight of powder was placed in glass tube, having inner diameter about 9.8 mm (see Figure 52). To ensure a constant packing of the powder, the tube was always filled to the same weight. The lower end of the tube was closed with a glass filter. The higher end of the tube was hanging on weighing scale platform (precision of ± 0.1 mg). The mass of the liquid penetrating within the powder plug was measured when the lower end of the tube is placed vertically in the wetting liquid. The experiments were performed at 22 ± 1°C. Each experiment was repeated 3 times.

From the slope of the linear relationship between the square penetrated liquid weight and time the wettability factor (K_{wf}) can be calculated using (Eq. 15):

To Calculate H^2, the relationship of the mass (m) and the height of the liquid penetrating within the powder plug was used. It can be expressed by the equation:

$$\frac{d(m^2)}{dt}.\left(\frac{\eta}{\gamma}\right) = K_{wf} = \rho^2.\times C_{gf} \times \cos\theta$$ (Eq. 104)

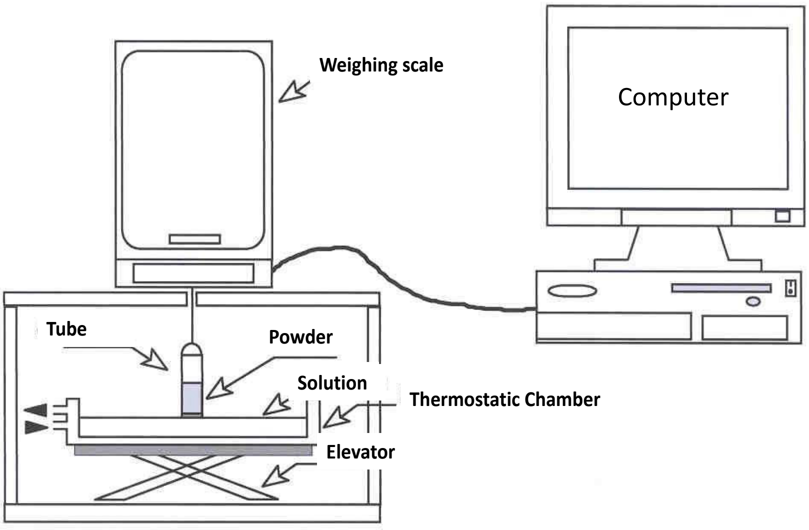

Figure 52: Experimental setup for studying the wetting of powders.

4.2.3.9. Adsorption isotherm measurement of PVP

The adsorption isotherm of the selected dispersant, namely PVP, was measured at ambient temperature. Known amounts of the API were introduced in vials at ambient temperature with various concentrations of PVP solutions. Then, the vials containing the various dispersions were rotated from a few hours to up to 15 hours until equilibrium was achieved. Indeed, it is reported that the intrinsic adsorption kinetic of homopolymer is usually instantaneous (less than 1 hour) (165,166).

Then the particles were removed from the dispersant solution by centrifugation at 3000 rpm during 20 min. The supernatant was then filtered through 0.45 µm PVDF® filter (supplied by Millipore). The dispersant concentration in the supernatant was determined using UV spectrometry by Cary® 50 (UV-Vis spectrophotometer supplied by Varian Australia) at 200 nm wavelength. Each measurement was repeated 3 times. To obtain the amount of adsorption per unit area of the powder (Γ), the specific surface area of the powder (SSA) in m²/g was determined using the gas flow method (Blaine).

4.2.3.10. Desorption measurement

The desorption of the wetting/dispersing agent was carried out using a kinetic experiment by following the particle size as a function of time (up to 45 min) using laser diffraction (Malvern Mastersizer 2000) in recirculation mode at 1800 rpm. The suspension was diluted by factor of 1000.

4.2.3.11. Critical concentration of coagulation measurement (Perikinetic aggregation)

The aggregation rate measurement was carried out by following the particle size as a function of time using dynamic light scattering (DLS). Different solutions of varying ionic strength were prepared by diluting the appropriate 5.0 M sodium chloride (NaCl) standard solution with purified water. The milled suspension was diluted with purified water from 20 % w/w to 0.1 % w/w. 10 µl of this diluted suspension were added to 1 ml NaCl solution covering a wide range of concentration and the resulting suspension was gently mixed by hand in the DLS cuvette and then placed into the measuring cell of the DLS instrument.

4.2.3.12. Impact of the shear rate (orthokinetic aggregation)

The orthokinetic evaluation was assessed using 20% API suspension by measuring the particle size as a function of time on a sheared sample. The milling was performed using stirred annular mill without beads at 3880 rpm (15 m/s), during 7 hours and at 2 ionic strengths of sodium Chloride (0 molar and 0.17 molar corresponding to 0.24 x CCC (according to M.Sommer (167)). The applied shear rate and shear strain were found equal to 26000 s^{-1} and 6.5 10^8, respectively.

4.2.3.13. pH impact on particle size of suspension

The flocculation rate measurement was carried out by monitoring particle size as a function of time using dynamic light scattering. The measurements were carried out using a scattering angle of 90°. Solutions of different pHs were prepared by diluting the appropriate 1.0 Molar solution of hydrochloric acid (HCl) and 1.0 Molar solution of Sodium Hydroxide solution with purified water. The milled suspension was diluted with purified water from 20 % (w/w) to 0.1 % (w/w). 10 µl of this diluted suspension were added to 1 ml of acidic or basic solution covering a wide range of pH and the resulting suspension was gently mixed by hand in the DLS cuvette and then placed into the measuring cell of the DLS instrument.

4.2.3.14. API A solubility in water and in SDS/PVP solution

To assess API solubility an HPLC-UV method was developed. The concentration of API was determined using a HPLC system composed of Varian Prostar® 230 pump (supplied by Varian France), injector Waters® 717 plus (supplied by Waters® France) and UV absorbance detector (supplied by Thermo-Fisher® France) set at 232 nm. The mobile phase was acetonitrile/phosphate buffer pH 3.5 10 mM (60/40, v/v). A XTerra RP18 50 X 2.1mm, 3.5 µm column (supplied by Waters® France) was used with the flow rate set at 1.0 ml/min and the temperature set at 45°C.

For the samples preparation 100 mg of the API were introduced in vial containing the adequate solution. Then, the suspension was agitated using a magnetic stirrer at fixed temperature during 4 hours and left standing to settle for 1 hour. The obtained supernatant was then filtered through 0.22 µm PVDF® filter (supplied by Millipore®). The obtained filtrate was diluted using ethanol. The injected volume of the filtrate and the analysis time were fixed at 5 µl and 2 min, respectively. The chromato-graphs were analyzed using Empower™ chromatography software (supplied by Waters® France).

The limit of quantification of the used method was found equal to 0.1 µg/ml.

Each measurement was done twice. A repeatability study was performed on 6 samples. The standard deviation was found about 1.8 %.

4.2.3.15. Crystal structure (High-Resolution X-ray Powder Diffraction (HR-XRPD))

High-resolution diagrams are recorded at ambient conditions on a Philips Analytical X'Pert Pro MPD powder diffractometer using the Bragg-Brentano (vertical θ-2θ configuration) parafocusing geometry coupled with a X'Celerator detector. A sealed copper anode X-ray tube is used, running at 45 kV and 40 mA levels. An incident beam monochromator

(Johansson type: a symmetrically cut curved germanium (111) crystal) produces pure Cu $K\alpha_1$ radiation (λ= 1.54060 Å). A thin layer of the product is deposited on a single-crystal silicon wafer, cut out according to Si (510) crystallographic orientation that, by systematic extinction, impedes any Bragg reflection. The angular range extends from 2 to 40° in 2θ, with a 0.02° step size in 2θ. A counting time 2500 seconds per step was used.

This specific instrument configuration (reflexion mode) is highly responsive to crystallite preferred orientations effect, which is valuable information for this specific study as explained in the following paragraph.

4.2.3.16. Contaminant residues

4.2.3.16.1. Quantification of Stainless steel, Zirconium oxide and Silicon Nitride elements

Inductively coupled plasma-atomic emission spectroscopy (ICP-AES) was used to evaluate the contaminant content within the milled suspension. The ICP-AES using a multi-channel detection is an instrumental technique of simultaneous analysis to measure the major and trace elements based on the measurement of the photons emitted by atoms. After dissolution of samples, the solutions to be analyzed are introduced into an argon plasma torch in the form of a liquid aerosol using a peristaltic pump, a nebulizer, a nebulization chamber and an injector. The plasma that can reach 10,000 ° C is maintained by an inductive coil providing a high frequency power of about 1200W. This very high temperature dissociates the material into atoms and free ions and then excites them. Their return to a stable state is accompanied by emission of photons in the ultraviolet and visible.

The emitted photons are transmitted through the optical system (mirrors, network, and prism) to the multi-channel detector (charge injection device). This device will allow the acquisition of the complete UV-visible spectrum of each element, the photons will generate photoelectric charges transferred to a read register and then converted into concentrations after calibration of the system (see Figure 53).

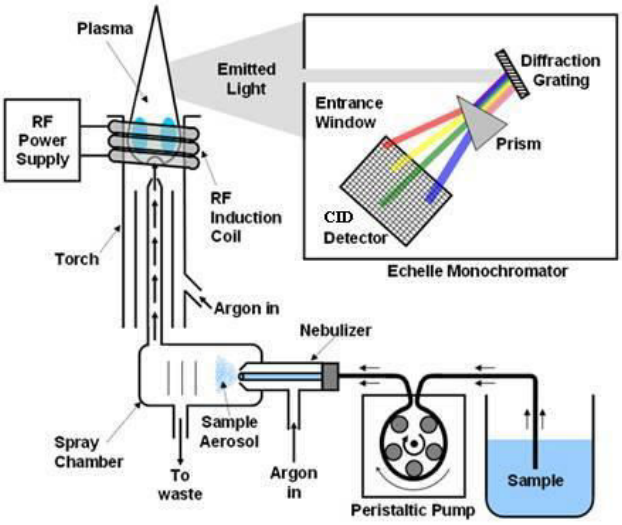

Figure 53: Inductively coupled plasma-atomic emission spectroscopy (ICP-AES)

Prior to samples analysis, the suspension samples were freeze dried to remove water using Usifroid SMH15 (freeze dryer lab scale unit) having surface area of 0.15 m². Then, 100 mg of freeze dried cakes were melted using 200 mg of Sodium hydrogenocarbonate ($NAHCO_3$). The obtained material was dissolved in 9.5 ml of purified water and 0.5mL hydrochloric acid (1 Molar). The obtained solution was then used for the quantification of the following elements: Al,Cr,Fe,Ni,Si,Ti,W,Yand Zr.

4.2.3.16.2. Quantification of cross linked polystyrene

The quantification of cross linked polystyrene residues was limited by the solubility of the fragments in organic solvents. Indeed, no organic solvent was found to be able to dissolve the beads fragments. In addition the available method for the quantification of polystyrene (GPC coupled to light scattering) has a low limit of quantification (1000 ppm). Based on this barrier we decided to quantify beads fragments by weighing. For that purpose, 5 litres of 0.22 µm filtered milling vehicle (Water and stabilizer) were processed in LMZ2 milling system using 480 g (47.8 % of filling ratio) of autoclaved cross linked polystyrene beads. The mill was operated at 10.1 m/s and 15°C during 6 hours using recycling mode. After milling the milling vehicle was filtered through 0.1 µm filter. The filter was weighed before filtration and after drying overnight at 45°C.

Experimental section

5. Experimental section

This section is divided in two parts. In the first part named formulation engineering, the selection of the wetting/dispersant agent methodology was developed. In the second part named process engineering, the impact of process parameters and mill configuration on suspension physical quality was studied for high pressure homogenization and stirred bead milling.

Formulation engineering

5.1. Formulation engineering

5.1.1. Methodology for selection of wetting/dispersant agent

Nowadays , the general strategy ('fast-to-patient') in pharmaceutical industry is to test a new API in a target patient population as quickly as possible (168). The screening methodology, based only on physico-chemistry, would provide a lot of scientific information but would be very time and resources consuming and consequently not aligned with the fast to patient strategy. In contrary, a purely empirical methodology (e.g. design of experiment, trial error approach) may provide a quick solution with poor scientific information. The typical risk of such methodology is that due to the lack of scientific understanding, long term stability or formulation robustness are not anticipated and lead to unfordable formulation development. Our proposal here is to use a compromise between purely scientific and purely empirical methodology in order to achieve both time effectiveness and scientific rationale.

The proposed screening methodology was already published in International journal of Pharmaceutics in 2014 (169). It was derived from the previous theoretical considerations and was divided in two major parts:

(i) Part 1 focused on qualitative screening to select a lead generation: In this part several screening tests were applied to the mentioned list of wetting/dispersant agents (see Appendix 1);

(ii) Part 2 focused on quantitative screening aimed to optimize the selected lead: A customized quantitative optimization of the amount of wetting/dispersant agent, based on wetting, adsorption and process-ability. As in the studied case the SDS/PVP association was chosen after part 1, the PVP and SDS ratio and their amount were optimized.

The tests are summarized in Figure 54

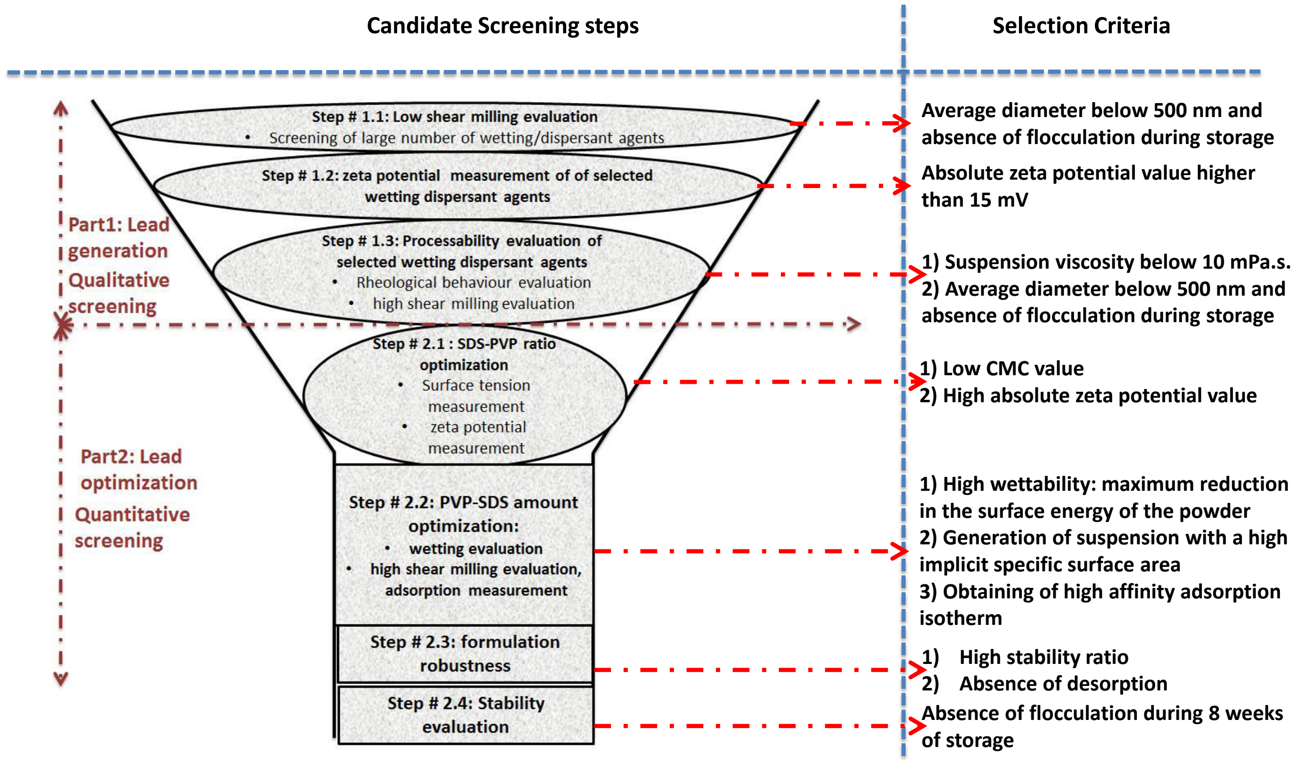

Figure 54: Methodology of wetting/dispersant agents screening.

They are described in more details hereafter.

In Part I all tested suspensions contained 20% of API, which is sufficient from a process productivity point of view, and 3% of wetting/dispersant agent are used (3% of wetting/dispersant agent should be sufficient to meet a full coverage of particles having approximately 80 nm mean diameter assuming a typical adsorption of 3 mg/m² (170)). In this part the selection was performed by the following step by step approach:

(i) Step #1.1: At this step the roller mill is used in order to perform several tests in parallel with a reduced amount of product. Two criteria were used to select the optimum stabilizer. The first criterion is that the API particle mean diameter has to be in the range of 100-500 nm after milling (typical nanocrystals size (126)). The second criterion is that the formulation should be free of flocculation upon at least 2 weeks storage at ambient temperature. The prepared suspensions were assessed by visual observation, particle size measurement and stability of particle size after 2 weeks storage at ambient temperature;

(ii) Step #1.2: At this step the measurement of zeta potential of selected samples from step #1.1 were carried out. To ensure electrostatic repulsion, an absolute value greater than 15 mV was fixed as criterion;

(iii) Step #1.3: At this step, the process ability of selected samples from step #1.2 was assessed. This evaluation was done based on the following tests:

  (a) Step #1.3a: At this step, the viscosity of unmilled suspension was measured as a function of shear rate as well as of thixotropy. The samples that gave viscosity greater than10 mPa.s at shear rate of 1000 s^{-1} were excluded. Indeed our internal observations gave evidence that this criterion is essential to ensure faster milling kinetics as well as manufacturing-ability at industrial scale;

  (b) Step #1.3b: At this step, the milling ability using the high shear mill, namely Nano-mill® 01 milling system of selected samples from step #1.3a was assessed. This step is essential to ensure the preparation of nano-suspension at industrial scale using high speed milling. All the samples that had particle size greater than 500 nm (mean diameter) or that showed instability due to flocculation or Ostwald ripening were excluded;

  (c) Step #1.3c: at this step, two wetting/dispersant agents appear more efficient to others. In order to differentiate them and to evaluate their robustness, both formulations were submitted to a long milling duration at high shear rate.

From the part I, the combination of SDS/PVP appeared as superior to the other tested agents. Therefore, this combination was selected for further evaluation in the part 2 as described below:

(i) Step #2.1: At this step the SDS-PVP ratio was optimized. The synergistic effect of the combination was confirmed by performing the following tests:

  (a) Step #2.1a: At this step, both surface tension and critical micelle concentration (CMC) of solutions made of SDS-PVP at different ratio were measured. Indeed, Cabane *et al.* (171) demonstrated that the Poly(ethy1ene oxide) chains are able to capture SDS monomer and micelles. They have shown the existence of an optimal SDS/PEO ratio which maximizes the interaction of both components. The best association can be easily determined by measuring the surface tension;

  (b) Step #2.1b: At this step the zeta potential of suspensions made of SDS-PVP at different ratio were measured.

(ii) Step #2.2: At this step, the amount of selected SDS-PVP ratio was optimized. This optimization was done based on the following tests:

  (a) Step #2.2a: At this step the wettability of selected SDS-PVP ratio was evaluated in order to select the amount of SDS-PVP allowing a maximum reduction in the surface energy of the powder;

(b) Step #2.2b: At this step, a high shear milling of suspension made of selected SDS-PVP ratio at different amounts was evaluated. From this step an optimal amount that gave suspension with a high implicit specific surface area was selected;

(c) Step #2.2c: At this step, the adsorption isotherm of PVP was measured to ensure the strong adsorption of the dispersant (PVP) on the particles surface.

(iii) Step #2.3: At this step, the perikinetic flocculation was evaluated as well as the desorption of wetting dispersant agent from surface of particles

(iv) Step #2.4: the physical stability of the selected formulation was evaluated. This was assessed by monitoring the particle size distribution during 8 weeks at ambient temperature.

5.1.2. Results and discussion

5.1.2.1. Part 1: Qualitative screening evaluation (lead generation)

5.1.2.1.1. Step # 1.1: Assessment of milling ability using low shear mill (roller mill)

After roller milling, all samples were inspected for API suspendability. HPC, PEG 8000, Montanov® 68 and Sodium polyacrylate® resulted in an obvious flocculation and in appearance of a 'dry' sample. These suspensions were not considered for further tests

The remaining samples were assessed by measuring the particle size at time 0, 7 and 14 days. The results are shown in Figure 55. Suspensions with a particle size greater than 500 nm and/or showing flocculation after 7 days were not evaluated further. Discarded samples were those made with HPMC, Poloxamer 188 and Poloxamer 407 (172).

Figure 55: Low shear milling evaluation using roller mill during 5 days at 0.03 m/s and at ambient temperature.

5.1.2.1.2. Step #1.2: Assessment using surface charges measurement (Zeta potential)

In the present study, the results of the zeta potential measurements of selected wetting/dispersant agents from step #1.1 were collected and compared. Figure 56 shows that all the wetting/dispersant agents, except the Cremophor® RH40, gave an acceptable zeta potential value. One can observe that the charged species (SDS, PVP-SDS) lead to a high absolute value. Therefore, upon this step the Cremophor® RH40 was excluded.

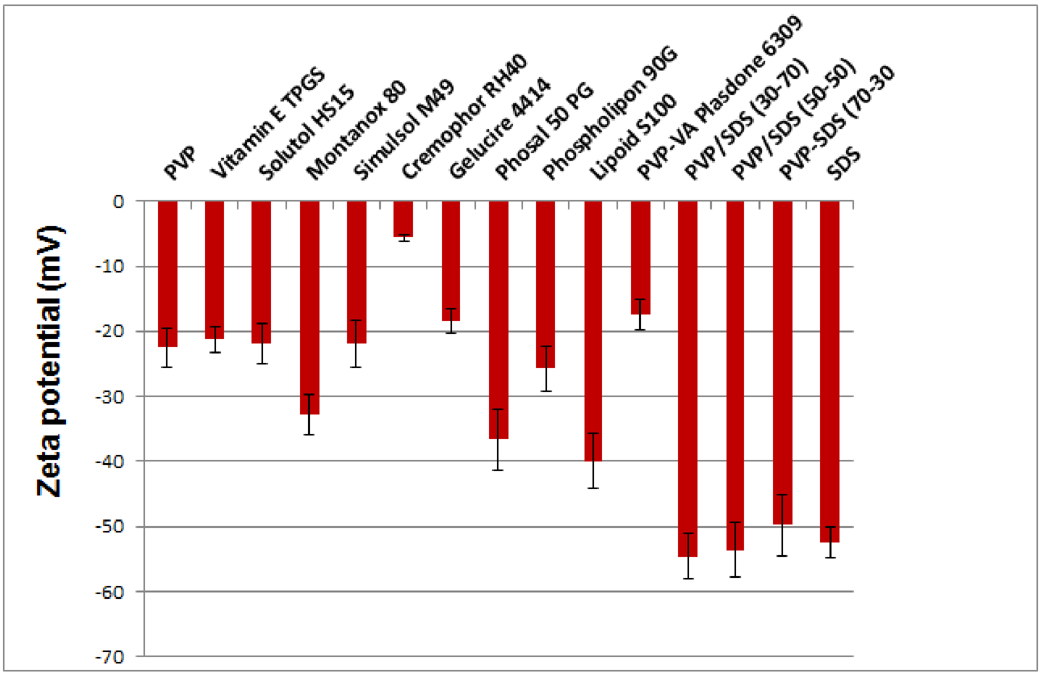

Figure 56: Results of the zeta potential measurements carried out using selected wetting/dispersant agents from step #1.

5.1.2.1.3. Step #1.3 Processability assessment

The evaluation of processability was done in two steps: Rheological evaluation to select the wetting/dispersant agents that will promote the milling process and high shear milling ability of suspensions made from selected wetting/dispersant agents to select those that will lead to stable suspension.

5.1.2.1.3.1. Step #1.3a: Assessment using the rheological behavior of the suspension

Figure 57 shows typical flow curves of unmilled suspensions prepared using Solutol® HS15 and Phosal® 50 PG. The prepared suspension using Solutol® HS15 shows a Newtonian behaviour with a low viscosity of 2.8 mPa.s. In contrast, the suspension using Phosal® 50 PG showed a non-Newtonian behaviour with a clear thixotropy, indicating a flocculation of the suspension.

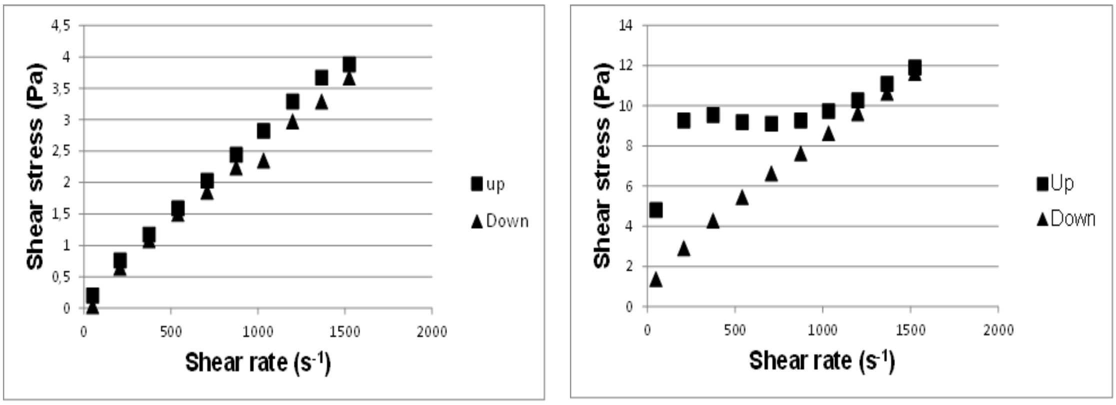

Figure 57: Flow curves (shear stress as function of shear rate) of unmilled suspension prepared using Solutol® HS15 (left) and Phosal® 50PG (right).

Table 9 summarizes the rheology results of various dispersants. Suspensions with viscosity greater than 10 mPas at high shear rate of 1000 s^{-1} were excluded from further evaluation. In fact, we have demonstrated that milling a suspension at different viscosity leads to the following observation: higher the viscosity of the suspension, slower is the milling kinetic (data shown in section 5.2.2.1.1.3). This may impact the productivity at industrial scale.

From this step, the suspensions made of Phosal® 50 PG, Phospholipon® 90 and Lipoid® S100 were excluded.

Dispersant/wetting system	**Viscosity at 1000 s^{-1} (mPas)**
Phosal 50 PG	11
Phospholipon 90G	12
Lipoid S100	15
Solutol HS15	2.8
Vitamine E TPGS	4.5
PVP	4.6
SDS-PVP 30/70	3.6
PVP/VA	4.0
Montanox 80	2.3
Gelucire 44/14	3.4
Simulsol M49	2.8

Table 9: Summary of rheological results for different dispersant / wetting agents.

5.1.2.1.3.2. Step #1.3b: Assessment of milling ability using high shear mill (Nano-mill® 01 milling system)

After high shear milling, the suspensions were assessed by measuring the particle size at time 0, 7 and 14 days. The results are shown in Figure 58.

Two systems, SDS/PVP at a ratio of 70/30 and Vitamin E TPGS® provided the highest stabilization of the nano crystalline formulations. These results were confirmed by SEM measurement as illustrated in Figure 59 for suspensions prepared using SDS/PVP (Figure 59A) and using Montanox® 80 (Figure 59B). These SEM pictures showed significant differences between the 2 formulations. The needles shaped crystals observed with Montanox® 80 formulation depict an anisotropic crystal growth (Ostwald ripening). This is likely related to preferential adsorption of Montanox® 80 on crystal faces which are parallel to the crystal axis. However, the suspension made of SDS/PVP presents a small, but irregular shaped particles. Furthermore, it can be observed that the particle size of the suspension using PVP-VA increased from initial time to 7 days and then decreased at 14 days. This may be due to the relaxation of the suspension. Indeed, it was reported for some formulations that when milling is stopped, nano-particles agglomerated within a few days. The particle size continued to increase until reaching a maximum size. Thereafter, the suspension relaxed spontaneously with an apparent size reduction.

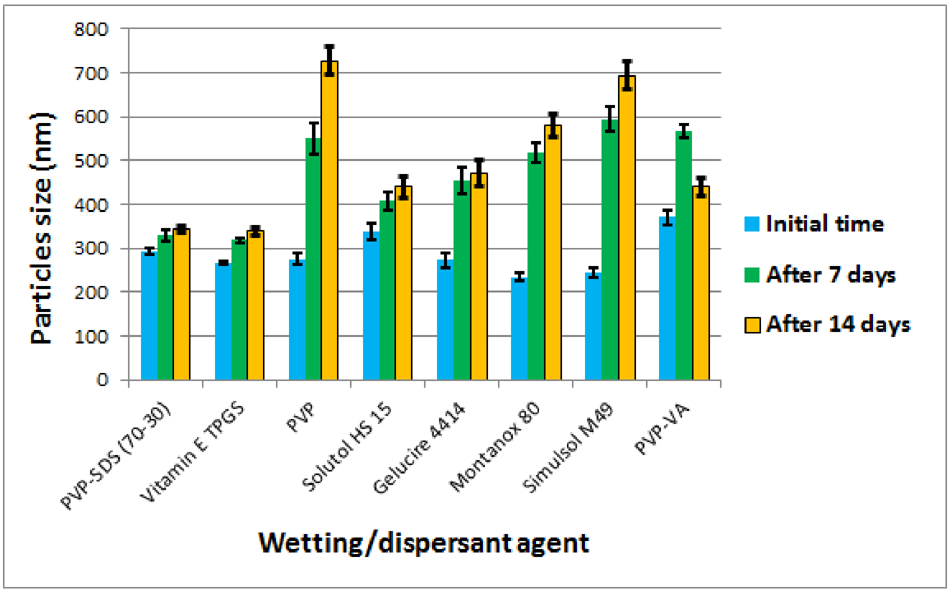

Figure 58: High shear milling evaluation using selected wetting/dispersant agents from step #3a.

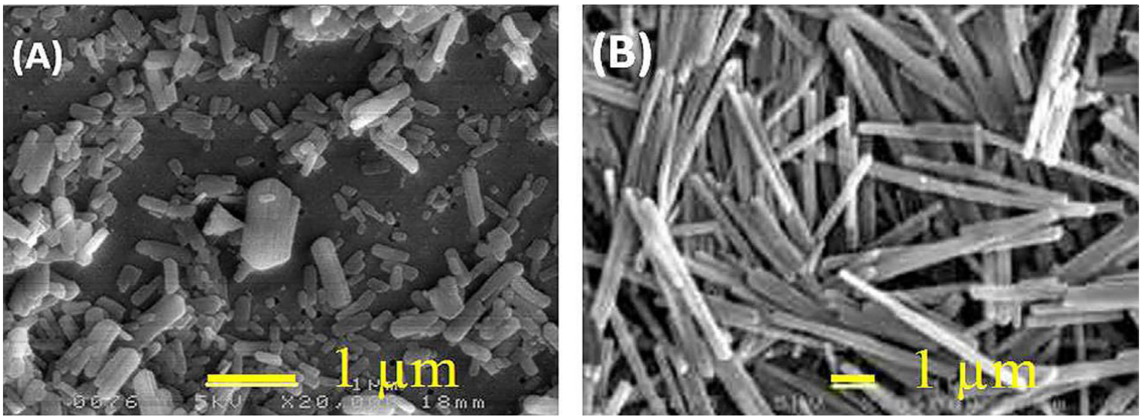

Figure 59: Scanning electro-microscopy pictures of suspensions produced using PVP-SDS (70/30 % w/w) (A) and Montanox® 80 (B).

5.1.2.1.3.3. Step #1.3c: Long milling duration

At the end of this screening, two formulations have been found to be clearly superior: SDS/PVP and Vitamin E TPGS® formulations. In order to differentiate between them, both formulations were submitted to a long milling duration (13 hours) at high shear rate in order to evaluate if the suspension undergoes negative milling phenomenon which is in close relation with aggregation and agglomeration (173). Indeed, during high-energy milling, the size of particles decreases to some critical values. Further energy supply to these particles of limiting size causes further deformation of particles, energy accumulation in the volume or at the surface of particles, and subsequently leads to aggregation.

The mill was operated at 3000 rpm. The mean shear rate generated during milling can be calculated according to (Eq. 58)

The main shear rate was found about 22000 s^{-1}.

The overall shear strain generated during milling can be calculated according to the following equation:

$$\boldsymbol{\Delta = \dot{\gamma} * t = \dot{9}.6\ 10^{8}} \tag{Eq. 105}$$

Where, Δ is the shear strain and t is the milling duration

The results reveal that the SDS/PVP system leads to a suspension with particle size in the nanometric range (see Figure 60) having mono-modal distribution and polydispersity index of 0.003 indicating that the particle size distribution is close to Ln-normal distribution. In contrast, the vitamin E TPGS® led to a suspension with particle size in the micron range exhibiting bi-modal distribution (see Figure 60) with polydispersity index of 1.874 indicating that the particle size distribution is dissymmetric towards large diameters. Furthermore, as illustrated in Photo 7, the milled suspension made from vitamin E TPGS® exhibited a gel aspect after milling. Whereas, the suspensions made of SDS/PVP remained fluid. It is noteworthy that during our previous screening, after 1 hour of milling, the suspension made of vitamin E TPGS® had a mono-modal distribution in nanometric range. We propose the following interpretations to explain the result obtained with vitamin E TPGS® :

- The aggregation can be due to the applied stress during a long period and absence of electrostatic stabilization. In fact in our previous work, we found that SDS/PVP system had a zeta potential of -54 mV and its stabilizing mechanism is electro-steric repulsion, while, vitamin E TPGS® has a zeta potential of -22 mV and its stabilizing mechanism is steric repulsion.
- Another mechanism that can explain the observed result is the gelation of polymer under shear flow (174). We assume that free and adsorbed vitamin E TPGS® on the nano-particles bridge together under shear stress and form gel network that binds the nano-particles together.

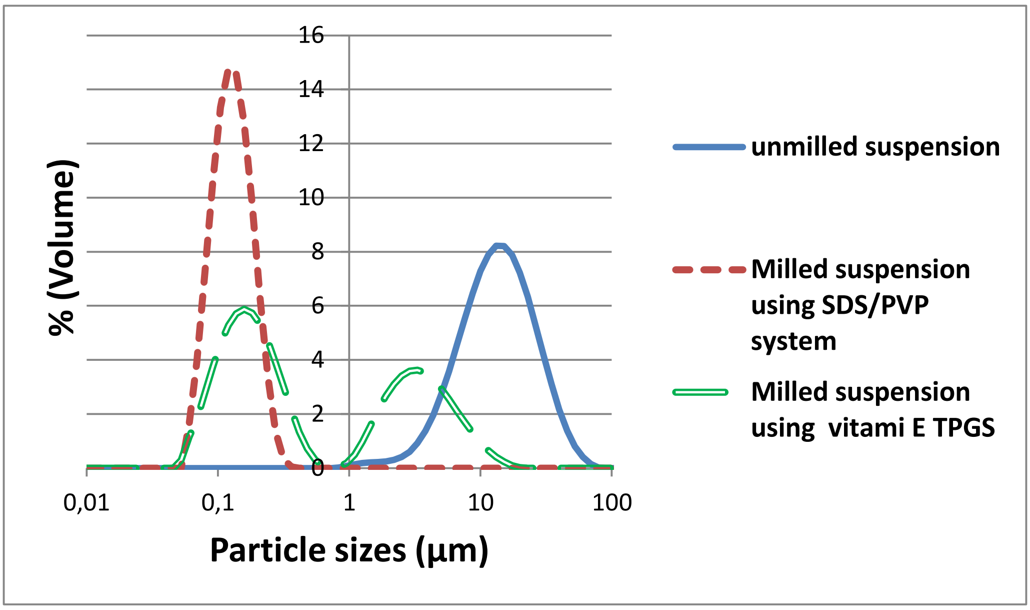

Figure 60: Particle size distribution at initial time and after milling during 13 hours of SDS-PVP sytem (left) and Vitamin E TPGS (right).

Photo 7: Milled suspension of Vitamin E TPGS.

From this evaluation the Vitamin E TPGS was discarded. The SDS/PVP made from ionic surfactant (SDS) and polymer (PVP) association was considered more relevant. Therefore, it was selected for the second part of the methodology.

.

5.1.2.2. Part 2: Quantitative screening evaluation (lead optimization)

In this part, the SDS-PVP ratio is firstly optimized based on both wettability and zeta potential. The amount of SDS-PVP of selected ratio is then optimized to ensure the milling processability and long term stability under storage conditions.

5.1.2.2.1. Step #2.1: Optimization of PVP-SDS ratio

5.1.2.2.1.1. Step #2.1a: Surface tension measurements

Figure 61 shows the γ-log C curve for a typical SDS/PVP mixture (20-80 %). This graph shows a typical behaviour with γ decreasing with log C increase until the CMC is reached after which γ shows only a small decrease with increase of log C. A plot of CMC versus % of

PVP (Figure 62) in the binary mixture shows a minimum at 60 % of PVP. This result implies a maximum of surface activity at 60 % of PVP in the binary mixture.

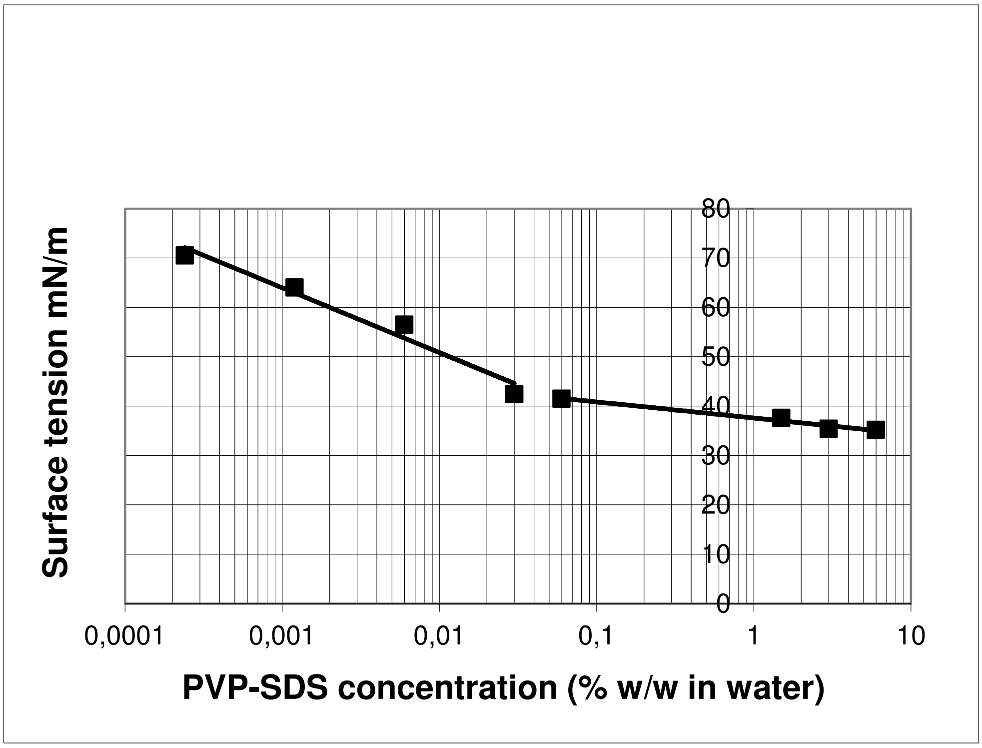

Figure 61: Surface tension as function of PVP/SDS (20-80 % w/w) concentration (ɣ-log C curve) obtained using Wilhelmy plate method.

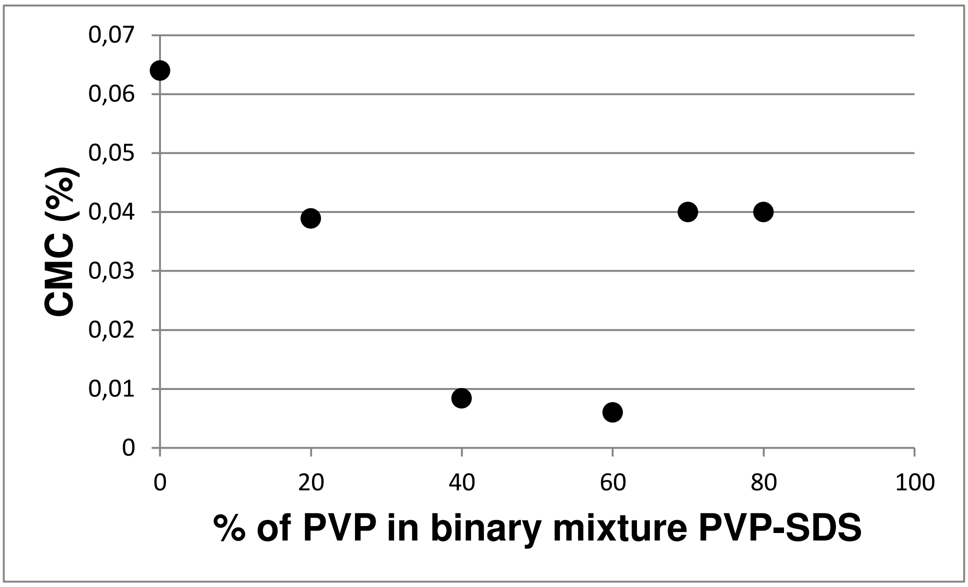

Figure 62: Critical micelle concentration as function of PVP % in the binary mixture PVP-SDS.

5.1.2.2.1.2. Step #2.1b: Zeta potential measurements

Figure 63 outlines that in the absence of SDS, PVP alone results in a low negative zeta potential of -20 mV. However, PVP is not sufficient to induce electrostatic stabilization. In this case, the main stability is obtained from a steric repulsion as a result of the adsorbed loops and tails of PVP molecules. Upon addition of SDS, the zeta potential decreased sharply to -50 mV, which likely contributes to the stability through electrostatic repulsion. With further increase of SDS concentration to 40 % (40-60 SDS-PVP), the zeta potential decreased down to -54 mV and remains almost constant. Thus when using a mixture of SDS and PVP the stabilizing mechanism is a combination of electrostatic repulsion, which shows a maximum energy at intermediate separation distance, and steric repulsion that occurs at shorter distances of separation that is comparable to twice of the adsorbed layer thickness. This combination stabilization mechanism is referred to as electrosteric stabilization (79,175,176).

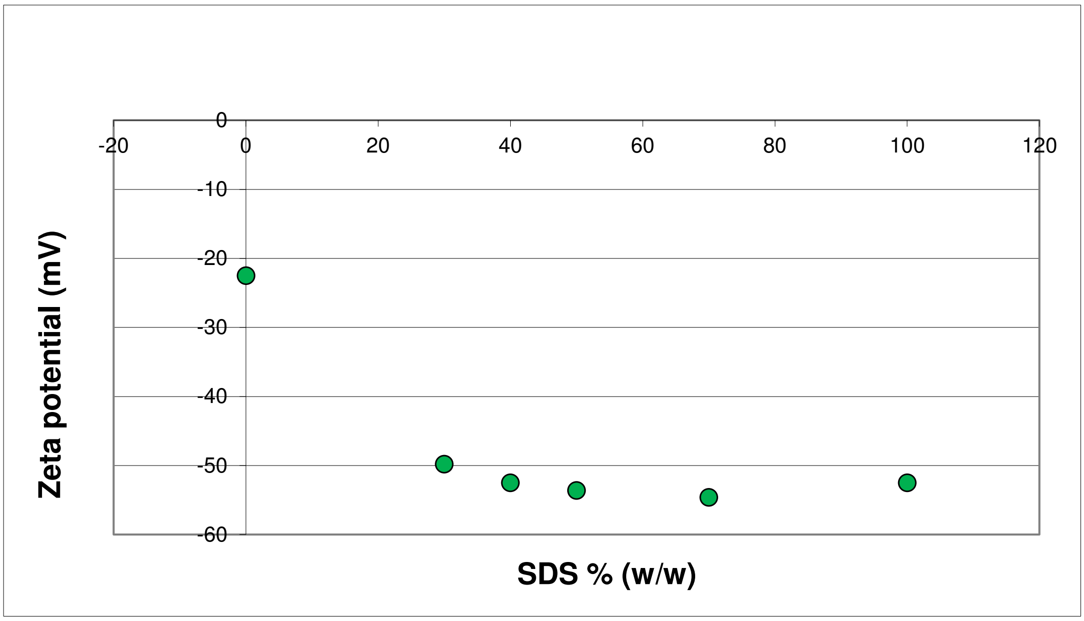

Figure 63: Zeta potential of the PVP-SDS system as a function of SDS concentration.

Based on these two evaluations, the SDS-PVP at a ratio of 40-60 % appears to provide the best association of the two components. Therefore, it was selected for the quantitative optimization.

5.1.2.2.2. Step #2.2: Amount optimization of PVP-SDS at ratio of 40-60 % w/w.

5.1.2.2.2.1. Step #2.2a: Wettability measurements

Figure 64 shows the variation of the square of penetrated liquid weight vs time for the 40-60% (w/w) SDS-PVP system at a total concentration of 1.2 %. Figure 65 shows a plot of wettability factor K_{wf} versus SDS-PVP concentration. For comparison, the results obtained using SDS alone are shown in the same graph (triangle scatter). It can be seen on Figure 65 that K_{wf} increases with increase of surfactant concentration, reaching a plateau at a certain surfactant concentration. For the SDS-PVP system, this plateau is reached at 1.2 % consisting of 0.72% (w/w) of PVP and 0.48 % (w/w) of SDS. Using the same concentration of SDS alone (0.48 % w/w), the K_{wf} value was found to be much lower than that obtained with the combination system. This clearly demonstrates the synergistic effect obtained when a polymer surfactant mixture is used. The latter is much more effective wetting system as compared to individual components. By using 1.2 % of SDS-PVP at the ratio of 40-60 %, maximum reduction in surface energy can be expected for the powder-liquid interface, which will lead to an enhanced cracks propagation (Rehbinder effect), and an enhanced breakage of the particles upon wet milling process.

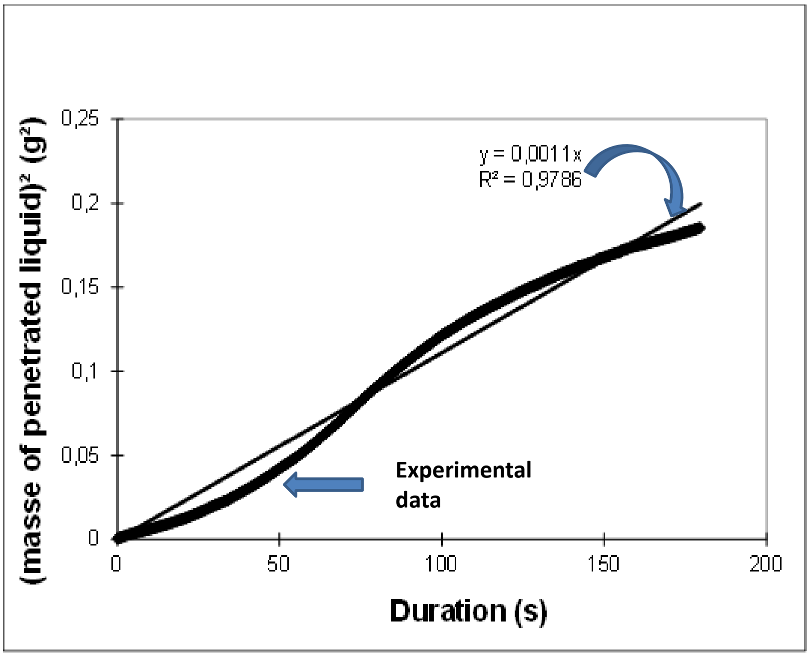

Figure 64: Liquid penetration rate of SDS-PVP mixture at total concentration of 1.2 %.

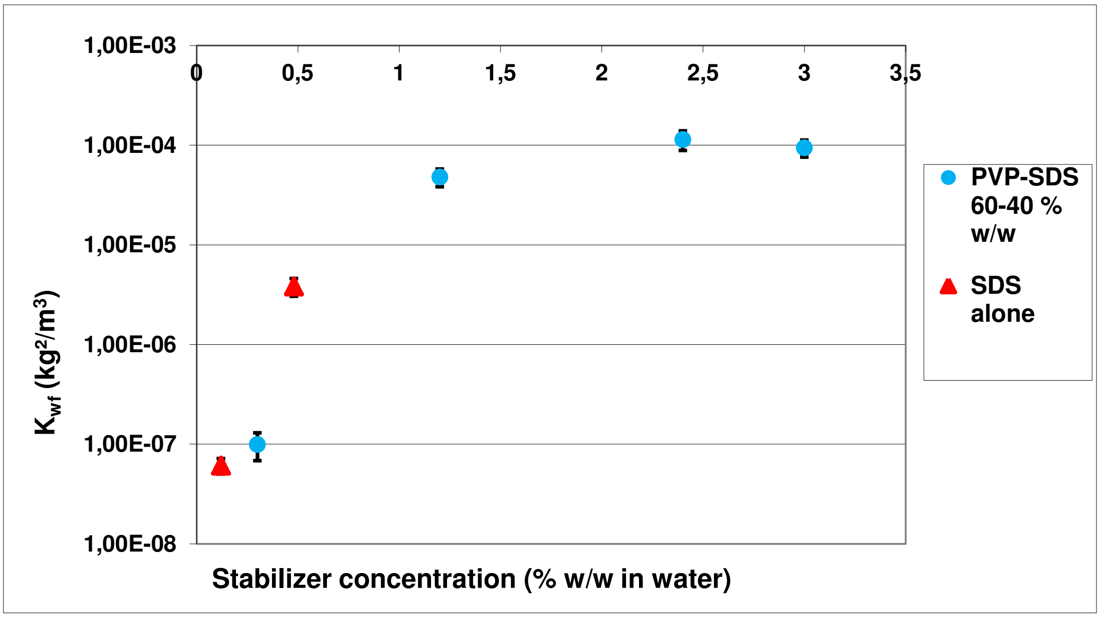

Figure 65: Wet-ability factor as function of stabilizer concentration of SDS-PVP binary mixture and SDS alone.

5.1.2.2.2.2. Step #2.2b: Milling ability as function of % of PVP-SDS at ratio of 60-40 % (w/w)

The milling ability was investigated using a kinetic experiment where the reduction in particle size, or the equivalent increase in implicit specific surface area, was measured as function of milling time. A typical result is illustrated in Figure 66 using 1.2 % w/w SDS-PVP at the ratio of 40-60 %. The results obtained show an exponential increase in the implicit specific surface area (or decrease in particle sizes) reaching a steady state value at 100 min of milling. The results can be represented by the equation:

$$\frac{6}{d_{50}} = \left(\frac{6}{d_{50}}\right)_{\infty} \times \left(1 - e^{\frac{-t}{\tau}}\right) \qquad \text{(Eq. 106)}$$

Where, $6/d_{50}$ is the implicit specific surface area, d_{50} is the mean particles diameter at time t, $(d_{50})_{\infty}$ is the mean particles diameter steady state value over time, $(6/d_{50})_{\infty}$ is the implicit specific surface area steady state value over time and τ is the characteristic time known as the duration to reach 63 % of the maximum specific surface area. Values for $(6/d_{50})_{\infty}$ were generated at various stabilizer concentrations and the results are shown in Figure 67. These results show an initial increase in $(6/d_{50})_\infty$ with increasing stabilizer concentration reaching a plateau at 1-1.2 %, and are consistent with those obtained from the wettability evaluation. One can observe, that, the results show the existence of two distinct regimes. Below 1-1.2 %, the $(6/d_{50})_\infty$ increases dramatically when the concentration of SDS-PVP is increased. In contrast, above 1-1.2 %, a plateau ((($(6/d_{50})_\infty = 50$ corresponding to d_{50} of 120 nm) is reached. A similar behavior was observed when manufacturing submicron emulsion using high pressure homogenization (177). The proposed mechanism is that at low stabilizer concentration “poor regime”, the particle size is limited by the stabilizer amount corresponding to full coverage. At high stabilizer concentration “rich regime”, the particle size is limited by the mechanical energy of milling system. The excess of stabilizer will accumulate in the supernatant phase. This demonstrates that 1-1.2 % is sufficient to ensure the suspension stabilization. Any excess is undesired as it may increase micellar solubility and therefore promote Ostwald ripening

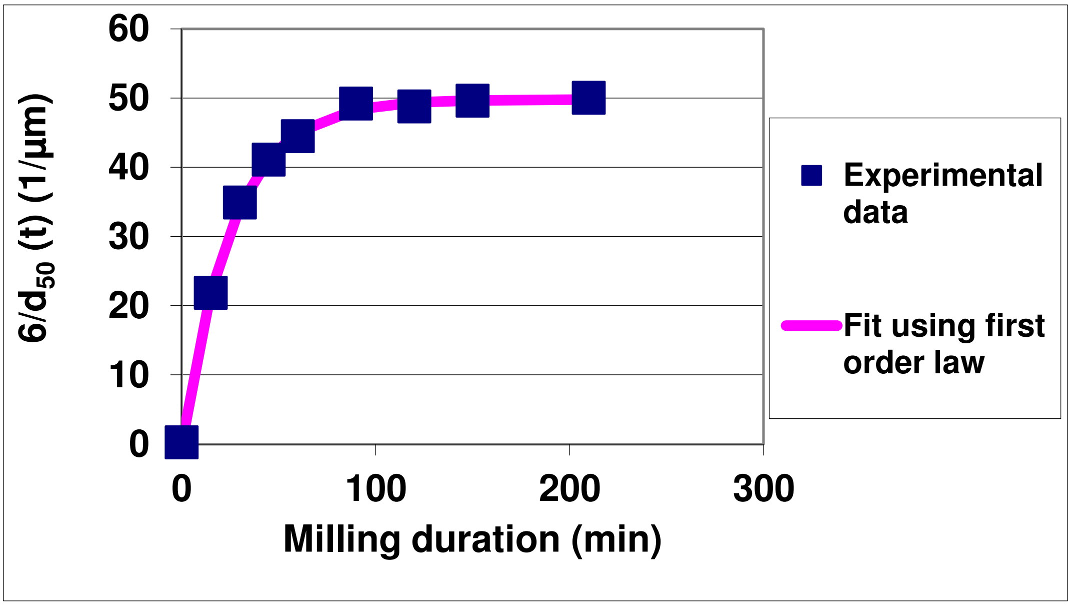

Figure 66: milling kinetic of suspension using PVP-SDS system (60-40 % w/w) at total concentration of 1.2 %.

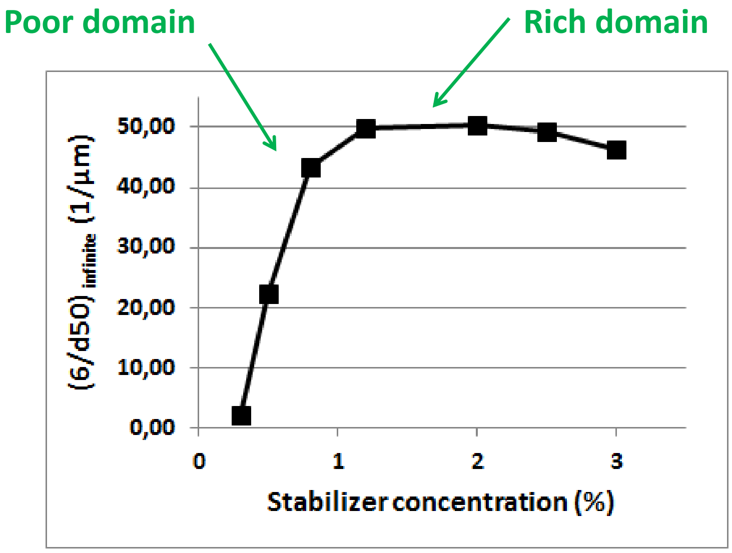

Figure 67: infinite implicit surface specific area $(6/d_{50})_\infty$ as function of stabilizer (SDS-PVP system (40-60 % w/w)) concentration.

5.1.2.2.2.3. Step #2.2c: Adsorption isotherm measurement of PVP.

Figure 68 shows the adsorption isotherm of PVP on the API powder surface. As indicated by the complete adsorption of the first added PVP molecules, the results show a high affinity type isotherm. The great deal of scatter obtained at high PVP concentration is likely due to the variability of the UV method used for determining the remaining PVP concentration. At high PVP concentration, the instrument measures the difference between large quantities, and any uncertainty in the estimated concentration using the UV method can therefore result in a large error in the amount of adsorbed PVP. Hence it is difficult to ascertain an exact plateau value of the isotherm which appeared as between 0.6 and 0.9 mg/m². Assuming a plateau value of 0.7 mg/m², the required concentration of PVP to completely saturate the particles can be roughly estimated. From Figure 14 the smallest particles diameter obtained is about 120 nm. This gives a specific surface area of 35.2 m²/g. For a 20 % suspension the total surface area was calculated by using the following equation and estimated as 704 m²:

$$\mathrm{SSA} = \frac{6\times 20}{\rho\times d_{50}} \qquad \text{(Eq. 107)}$$

The total surface area coverage requires 493 mg or 0.493 % of PVP which corresponds to 0.82 % of SDS/PVP 40-60 % w/w. These results are within the order of magnitude of the values obtained in milling ability and wettability tests.

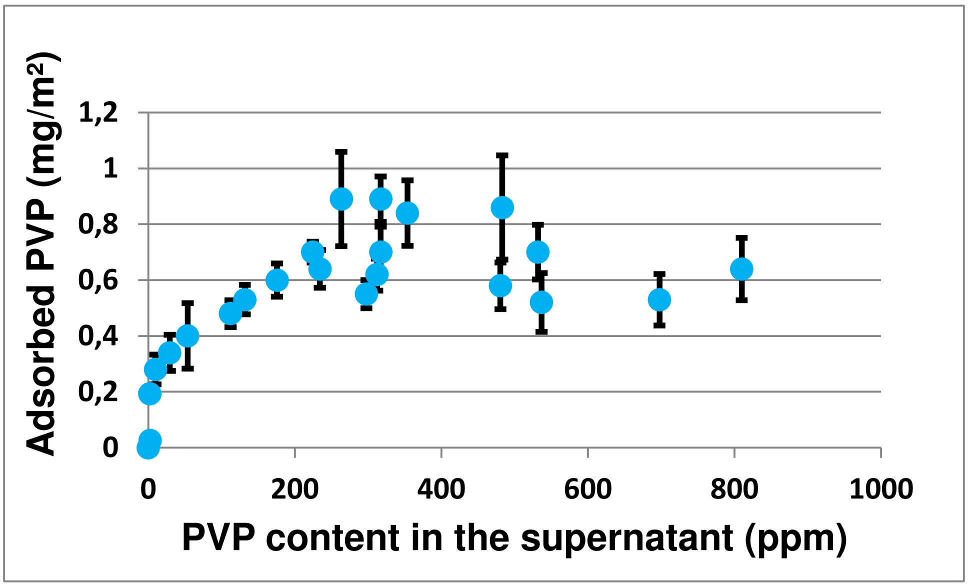

Figure 68: adsorption isotherm of PVP at ambient temperature.

5.1.2.2.3. Step #2.3: formulation robustness

The ability of nano-crystalline suspension to remain in its original state during drug product preparation and administration (processing or in use handling) is critical for since any change could negatively impact its performances. In fact, all suspensions having particle size less than 1 µm are inherently thermodynamically unstable due to the natural tendency decrease the large specific surface area and excess surface energy. For this purpose, wetting / dispersing agents are used to stabilize the suspension against flocculation and crystal growth (Ostwald ripening).

In the section (5.1.1), we described a systematic approach to select a suitable wetting/dispersing agent for the preparation of nano-crystalline suspensions. The objective of this section is to describe the derisking approach implemented for the robustness assessment of the selected formulation with regard to the identified risks that are listed below:

(i) Aggregation during storage or administration due to the lack of electrostatic stabilization: Aggregation occurs if the energy barrier is small or negligible. Basically, when a salt is added to the suspension, the electrical double layer repulsion is screened, and van der Waals attraction becomes dominant and induces fast aggregation of particles (178). At critical electrolyte concentration (CCC) the energy maximum disappears leading to fast aggregation of particles. In our work, the CCC was determined by quantification of aggregation rate as a function of electrolyte addition.

(ii) Shear-induced aggregation (orthokinetic aggregation): Aggregation processes are always carried out under conditions where suspension is subjected to some shear by stirring or by flow leading to increase of collision frequency (179). In our study, Orthokinetic aggregation was evaluated under a fixed shear rate.

(iii) Aggregation by desorption of wetting/dispersing agent from particles surface: Robustness to dilution is important for nano-crystalline suspension to ensure that the particles formed have similar properties at different dilutions to achieve uniform drug release profile and to ensure that the drug will not get aggregation at higher dilutions in vivo which may significantly impact biopharmaceutical attributes of the product. We had previously, demonstrated that the adsorption of polymeric surfactants (PVP K30) led to high affinity isotherm implying that such process is irreversible (see section 5.1.2.2.2.3). To check the irreversibility of adsorbed surfactant, desorption of surfactant from particles surface was investigated by diluting the suspension in water.

(iv) Crystal growth due to Ostwald repining and/or flocculation by depletion at high temperature: During milling or autoclaving (in case of suspension use in parenteral administration), the suspension could be submitted to high temperature. In this case, large particles grow with time at the expense of the smaller ones (93) due to the well-known Kelvin effect (91). Furthermore, high temperature can lead to desorption of polymer molecules which become more soluble (170) or precipitate when the temperature is higher than polymer cloud point (180). Consequently, the non-adsorbing polymer molecules can induce flocculation by depletion interaction between colloidal particles (181). In this section, we evaluated the sensitivity of suspension to Ostwald repining and/or flocculation by depletion at high temperature.

(v) Flocculation due to pH variation: According to the route of administration, an API experiences a wide range of physiological pH. Accordingly, nano-suspension needs to be robustly designed with regards to pH variations which may significantly affect the effectiveness of electrostatic stabilization (182). Indeed, pH is an important parameter to be taken into account because the particle surface is strongly modified by acid-base equilibriums, and the particle charge may vary from negative to zero and to positive values. In fact, by varying the pH, the isoelectric point (IEP) can be reached. The IEP is the pH value at which the zeta potential value is zero, implying no electric charge on the surface of a particle. For that purpose, the sensitivity of our formulation to pH variations was investigated.

The proposed study was already published in International journal of Pharmaceutics in 2016 (183).

5.1.2.2.3.1. Results of perikinetic flocculation evaluation

A common procedure for assessment of the colloidal stability of the dispersant is to measure the rate of flocculation as function of electrolyte addition. The added electrolyte reduces the maximum energy needed for an electrostatically stabilized dispersion, and at critical electrolyte concentration (denoted as the critical coagulation concentration: C.C.C) the energy maximum disappears leading to fast flocculation. One can then compare the rate of fast flocculation (k_0) with that of slow flocculation (k) (167) to obtain the stability ratio ($W = k_0/k$). Clearly the higher W, the more stable is dispersant (167). We used this approach to evaluate the perikinetic flocculation of sodium dodecyl sulphate/ polyvinylpyrrolidone (SDS/PVP).

Figure 69 shows the variation of $Z_{average}$ diameter as function of time. One can see that $Z_{average}$ diameter starts to increase with time when the sodium chloride concentration was higher than 0.25 M.

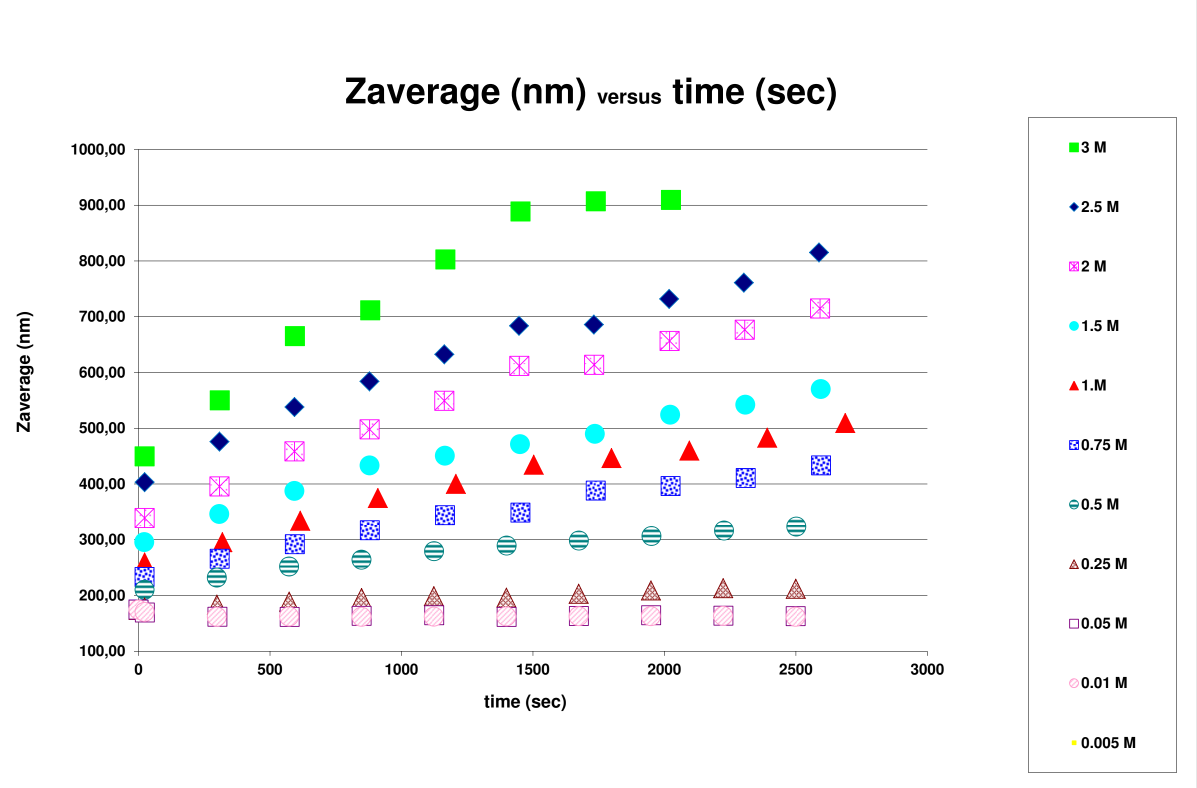

Figure 69: $Z_{average}$ diameter as function of time at different concentration of electrolyte (NaCl).

To calculate the rate of flocculation for each Sodium Chloride concentration, the process was considered to be represented by a second order kinetic as suggested by Smoluchowski (for the fast flocculation rate) and by Fuchs for the slow flocculation rate (88,184). In both cases a plot of n_0/n_t (where n_0 is the initial number of particles, n_t is the number of particles after time (t) versus time (t) should give a straight line with slope equals to the rate constant of flocculation k_0 for the fast rate of flocculation and k for the slow rate of flocculation.

The number of particles at each time can be calculated from the weight-weight % of suspension and the masse of a single particle that can be calculated from its volume and density according to the following equations:

$$\mathbf{m_{total}} = \left(\frac{\textbf{(masse of sample)}\times\textbf{(\% of solid)}}{\textbf{100}}\right) \qquad \textbf{(Eq. 108)}$$

$$\mathbf{m_{SP}} = \boldsymbol{\rho} \times \mathbf{V} = \boldsymbol{\rho} \times \frac{\mathbf{4}}{\mathbf{3}} \times \boldsymbol{\pi} \times \mathbf{r^3} \qquad \textbf{(Eq. 109)}$$

$$\mathbf{n_t} = \frac{\mathbf{m_{total}}}{\mathbf{m_{sp}}} \qquad \textbf{(Eq. 110)}$$

Where, m_{total}, m_{sp}, ρ, V and r are the total mass of the particles, the mass of single particle, the density of particle, the volume of single particle and particle radius, respectively.

Plots of n_0/n_t versus time (t) shown in Figure 70 where n_0 is the number of initial particles and n_t is the number of particles at time t.

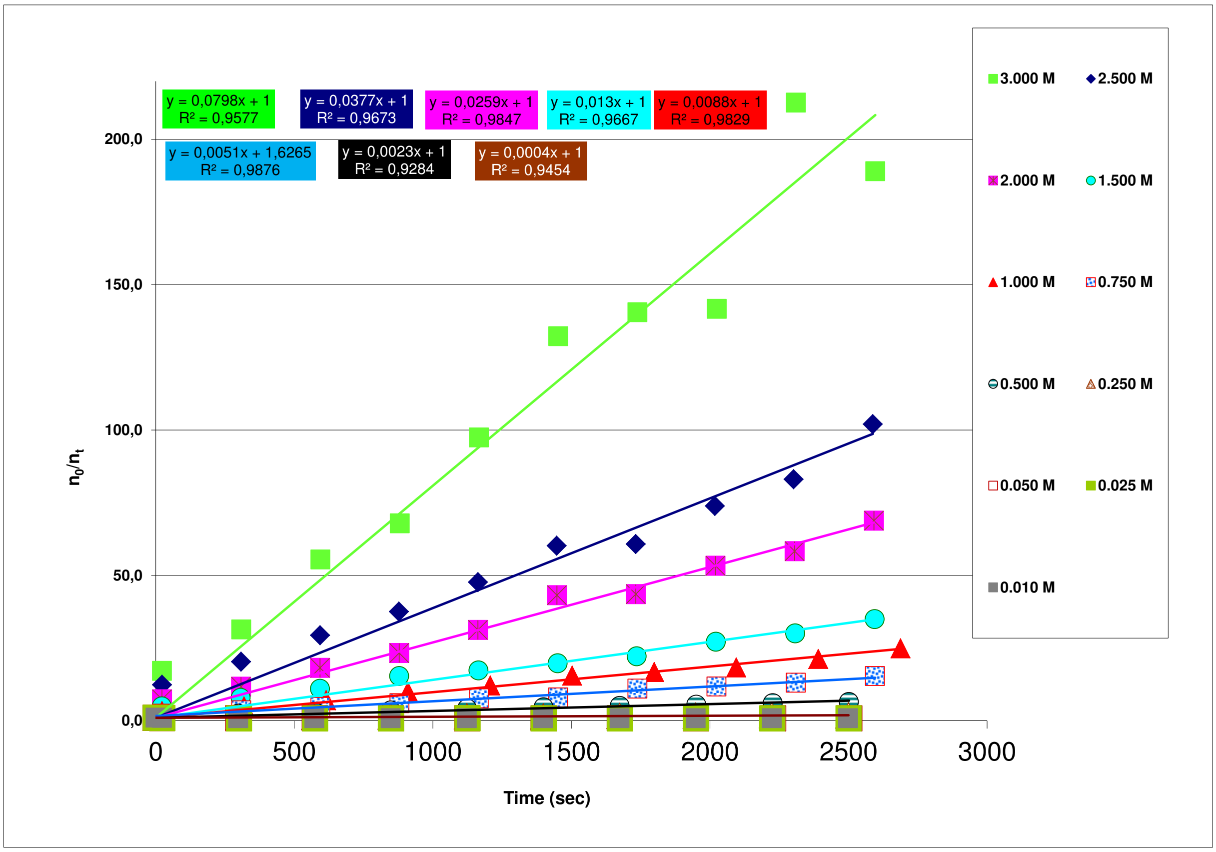

Figure 70 : n_0/n_t versus time at different electrolyte concentration (NaCl).

Plots of n_0/n_t versus time (t) are linear indicating that the process of flocculation follows a second order kinetic.

The value of the rate constant at the highest Sodium Chloride concentration (3 M) was found to be approximately equal to 310^{-11} s^{-1}. It assumed to be that of the fast flocculation rate k_{fast}. From k_{fast} and k_{slow} one can calculate the stability ratio W according the equation:

$$\mathbf{W} = \frac{\mathbf{k_{fast}}}{\mathbf{k_{slow}}} \qquad \textbf{(Eq. 111)}$$

The results for k and W are summarized in Table 10

NaCl concentration (M)	Rate of flocculation; k (s^{-1})	Stability ratio; W
3.03	3.00 10^{-11}	1.00
2.51	1.00 10^{-11}	3.00
2.00	1.00 10^{-11}	3.00
1.50	5.00 10^{-12}	6.00
1.01	3.00 10^{-12}	10.00
0.75	2.00 10^{-12}	15.00
0.50	9.00 10^{-13}	33.00
0.25	1.00 10^{-13}	300.00

Table 10: Rate of flocculation and stability ratio as function of salt concentration.

The plots of W versus log C (electrolyte concentration) gives a rough estimate of the C.C.C of NaCl for the system (see Figure 71

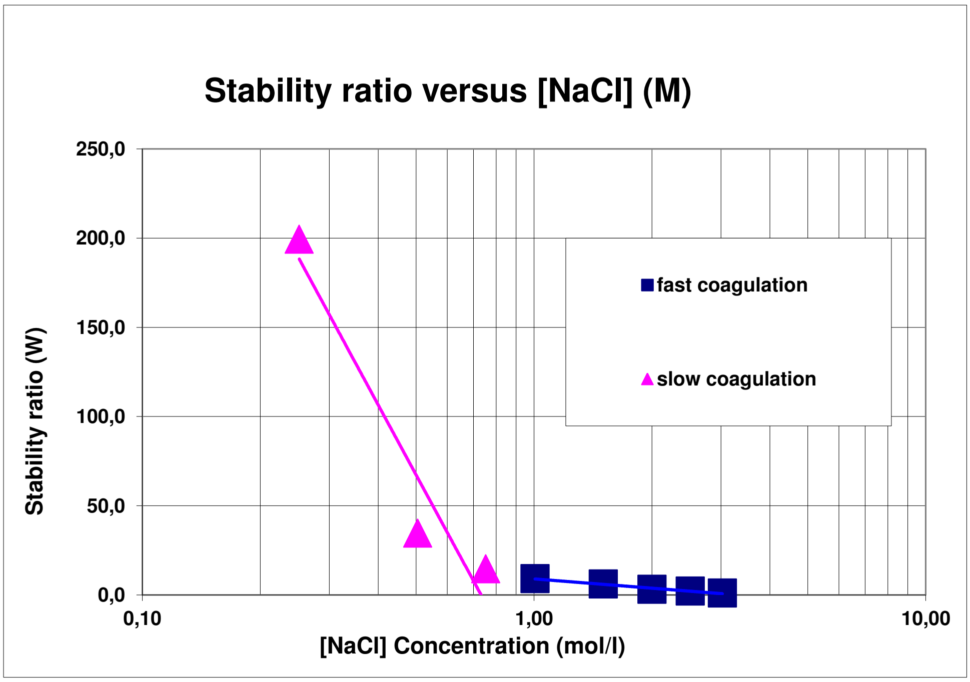

Figure 71 : Stability ratio as function of electrolyte concentration

One can estimate that at a critical electrolyte concentration (~ 0.7 M of NaCl), all the repulsive forces have been effectively screened and coagulation process was purely controlled by diffusion.

The value of measured CCC indicates a high colloidal stability of designed system. In fact, it is about five times higher than that observed in the literature for suspension colloidaly stable at high concentration (185,186).

5.1.2.2.3.2. Ortho-kinetic flocculation evaluation

The results showed that, in the absence of added salt (see Figure 72 left), aggregation and increase of polydispersity index (dissymmetric distribution towards large diameters) (Figure 73) are observed over time. In contrast, in the presence of 0.17 M of NaCl (Figure 72) less aggregation and less increase of polydispersity index (Figure 73) were observed over time. These results may seem counter-intuitive. Indeed, under high shear rate, a high colloidal stability was observed at ionic strength of 0.24xCCC than at very low ionic strength (without salt addition). This observation is in contradiction with results observed during perikinetic evaluation. We propose the following interpretations to explain the obtained results:

At low ionic strength, the PVP molecules are highly soluble in water. Under high shear rate, the polymers chains are may be extracted from nano-particles. Hence, the steric repulsion and a major part of electrostatic repulsion are eliminated. Furthermore, the high shear rate can overcome the electrostatic barrier resulting in orthokinetic aggregation. In contrast, in the presence of 0.17 M NaCl, the low solubility of PVP molecules in the medium leads to a strong adsorption onto the particles. In this case, the shear induced aggregation is prevented. It is noteworthy that one can estimate which mechanism prevails by means of the Peclet number of the particles defined as the ratio of the time scale of convective transport due to shear over the time scale of diffusive transport (see (Eq. 112)) (187). In our case the Peclet's number was found about 77 which is much higher than 1 outlining that the aggregation takes place in orthokinetic regime and the energy used to approach particles between them is likely much higher than DLVO potential barrier.

$$\mathbf{Pe} = \frac{\mathbf{6 \times \pi \times \eta \times r^3 \times \dot{\gamma}}}{\mathbf{K_B \times T}} \qquad \textbf{(Eq. 112)}$$

Where, η is the dynamic viscosity, $\dot{\gamma}$ is the shear rate, r is the characteristic length-scale (particle radius), K_B is the Boltzmann constant, and T is the absolute temperature.

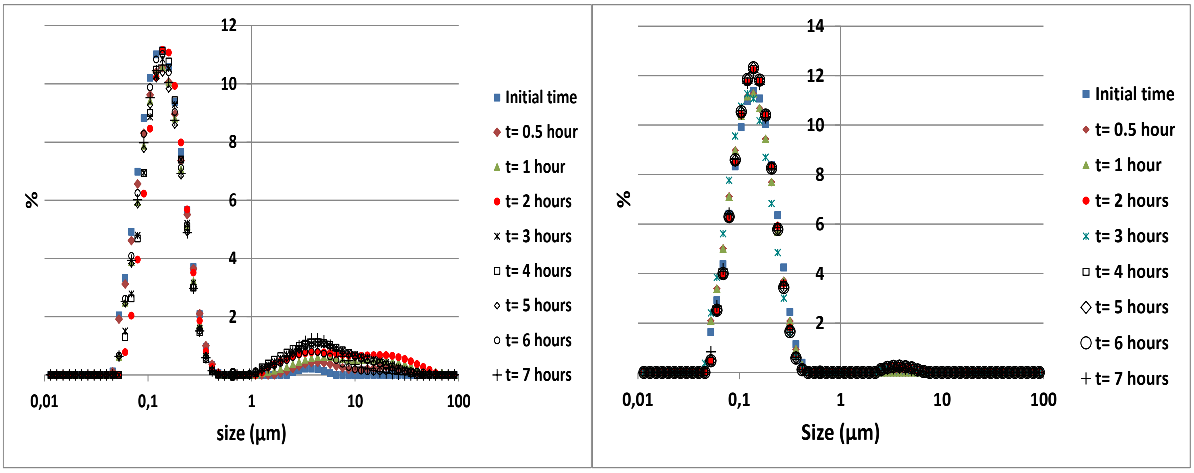

Figure 72: Orthokinetic aggregation at 0 molar (left) and 0.17 molar (right) of sodium chloride.

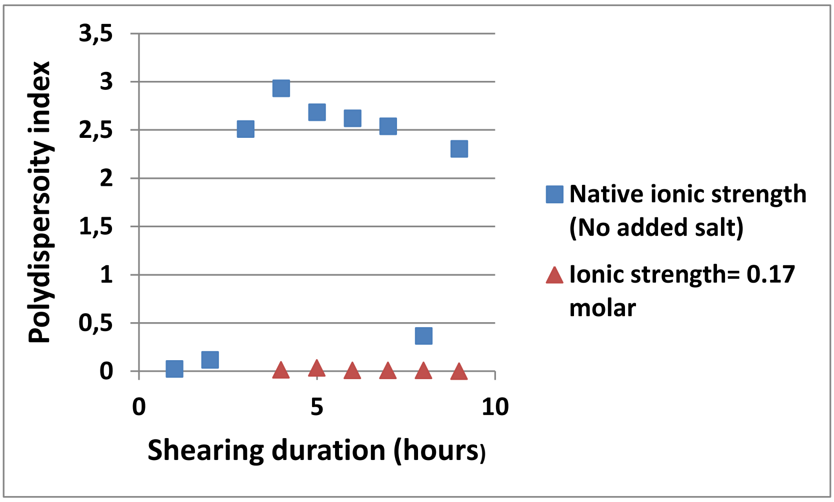

Figure 73 Ortho-kinetic evaluation: polydispersity index as size as function of time for 0.0 and 0.24× C.C.C ionic strength

5.1.2.2.3.3. Desorption evaluation

Figure 74 reveals that the particle size distribution of suspension made of SDS/PVP system is unchanged over time indicating the high colloidal stability of the nano-suspension. In contrast, the results obtained with Solutol® system showed a notable change of particle size distribution as function of time (see Figure 75) indicating the aggregation of the nano-suspension. These results are in agreement with those observed in section 5.1.2.1.3.2 & 5.1.2.2.2.3. In fact, the SDS/PVP system was found to exhibit high affinity adsorption isotherm which is known as irreversible process. In contrast, the Solutol® adsorption is weak and reversible.

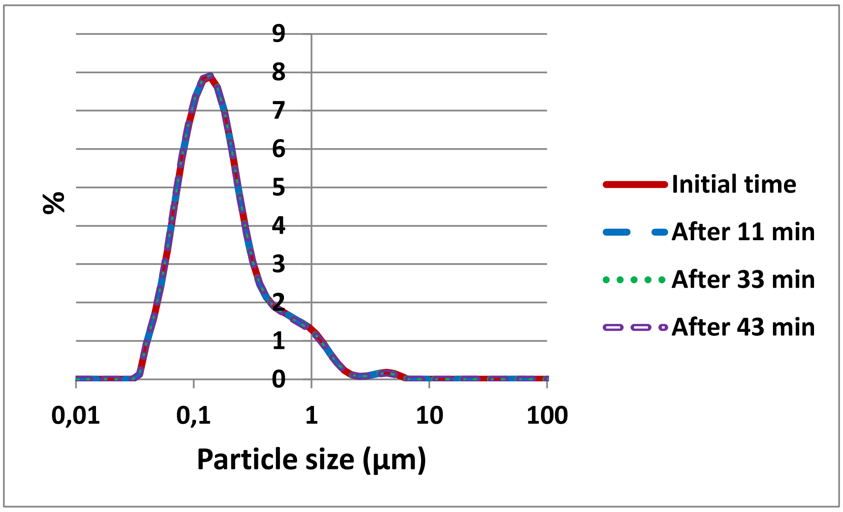

Figure 74: Desorption evaluation of PVP/SDS system.

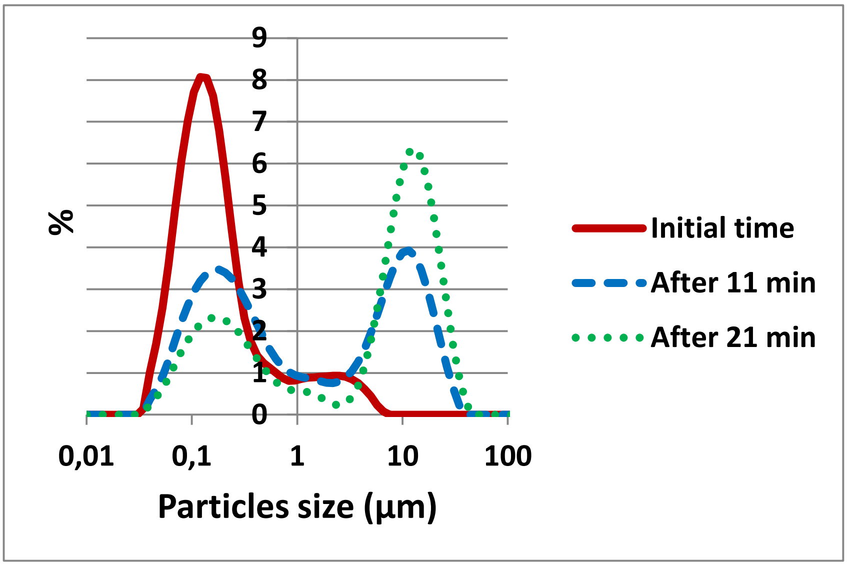

Figure 75: Desorption evaluation of Solutol system.

5.1.2.2.3.4. Sensitivity to Ostwald ripening and flocculation

During milling or autoclaving (in case of suspension use in parenteral administration), the suspension could be submitted to high temperature amplitude. It is important to anticipate the suspension behavior with regard to crystal growth and flocculation. In order to evaluate the sensitivity of the formulation to Ostwald ripening and flocculation, solubility of API was measured as function of concentration of wetting/dispersant agent (SDS/PVP) as well as function of temperature in water. Then, the crystal growth was evaluated during temperature stress test.

5.1.2.2.3.4.1. API solubility as function of wetting/dispersant agent (SDS/PVP) concentration in water

Figure 76 represents the API solubility as function of PVP, SDS and SDS-PVP (at ratio of 40-60 % (w/w)) concentration. It has been observed that:

(i) The API solubility does not change with increase of PVP concentration;
(ii) The API solubility increases with SDS concentration;
(iii) The API solubility increases sharply with SDS-PVP (at ratio of 40-60 % w/w) concentration.

The impact of SDS concentration on API solubility is straightforward. It means, above the critical micellar concentration (CMC), the formed micelles can solubilize 'N' number of API molecules per micelle. The dissolved amount of API by micelle is therefore proportional to formed micelles as described by the following equation:

$$\mathbf{S = S_0 + N_{API} \times M_{API}\left(\frac{C - CMC}{M_{SDS} \times N_{ag}}\right)} \tag{Eq. 113}$$

Where, S, S_0, N_{API}, M_{API}, C, CMC, M_{SDS} and N_{ag} are the API solubility in SDS/PVP solution, API solubility in water, number of API molecules per micelle, API molecular weight, SDS/PVP concentration, critical micellar concentration of SDS, SDS molecular weight and number of micelles aggregation, respectively.

As PVP alone does not solubilize the API, the increase of API solubility when PVP is added to SDS is difficult to understand. This phenomenon in fact can be explained by the subtle mechanism: According to Shirama *et al.* (188) and Cabane (171) at critical aggregation concentration (well below the CMC), polymer chains interact with surfactant to form small micelles of surfactant inside the polymer chain (see Figure 77). Therefore, in presence of polymer much higher number of micelles are formed. The higher number of micelles explains the high solubility.

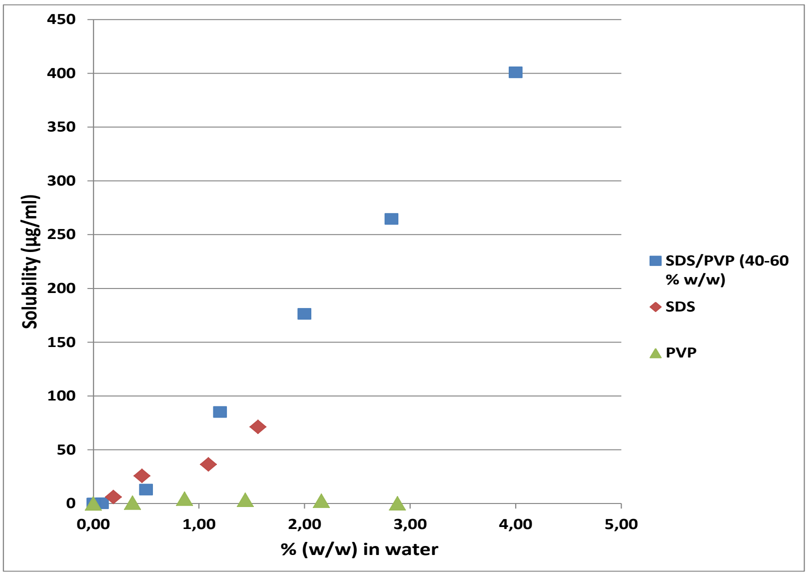

Figure 76: API A solubility in the binary mixture of SDS/PVP, SDS alone and PVP alone.

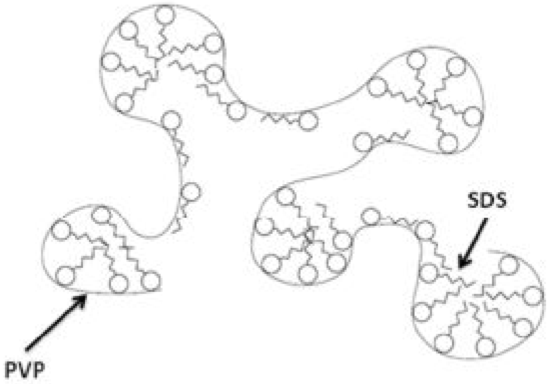

Figure 77: PVP molecules and SDS micelles arrangement.

5.1.2.2.3.4.2. API solubility as function of temperature in (SDS/PVP) solution at concentration of 1.2 %

The obtained results show that the API solubility does not change with increase of temperature when water is used as vehicle. However, when solution containing 1.2 % of

SDS/PVP at ratio of 40-60 % (w/w) is used, the API solubility decreases surprisingly with increase of temperature (see Figure 78). This result can be interpreted by the disaggregation effect of temperature (above room temperature) on SDS micelles. In fact, increase of temperature causes disruption of the structured water surrounding the hydrophobic groups which disfavors micellization (189). Furthermore, this phenomenon can be heightened by solubilisation of PVP molecules at high temperature.

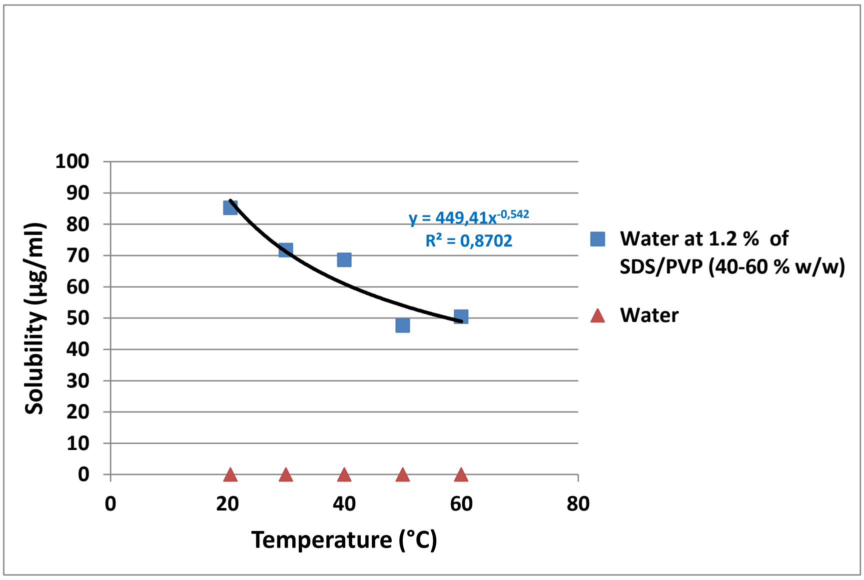

Figure 78: API A solubility in SDS/PVP ((40-60 % w/w) solution at concentration of 1.2 % and in water at different temperatures represented.

Both the observations indicate that the heat induced Ostwald ripening hypothesis can be ruled out. Indeed, the diffusion of dissolved API to solid particles cannot take place from the micellar system as it is attached to the solid particles.

5.1.2.2.3.4.3. Temperature stress test

During milling, the suspension undergoes wide amplitude of temperature. The impact of temperature on particle size of suspension (20 % w/w of API) was evaluated in the range of 20°-60°C. The results show that at 20°C, the dispersion remains stable for more than 600 hours, showing no increase in particle size with time. As the temperature increases to 40°, 50° and 60 °C, significant increase of particle size with time is observed (see Figure 79). Moreover, as can be seen in Figure 80, when the temperature increases, the polydispersity index increases over time indicating a dissymmetric distribution of particles towards large diameters. Hypothetically, this increase could be due to either Ostwald ripening or flocculation. Ostwald ripening can be ruled out since a plot of crystal growth ((r^3(t)-r^3(0)) versus time did not give a linear relationship (see Figure 81) (94,190). In addition, monitoring of particle size distribution showed that the appearance of coarse particles is not due to disappearance of fine particles (see Figure 82). Thus, the increase in particle size with time must be due to flocculation. These results from either desorption of the dispersing agent (PVP molecules) which becomes more soluble at high temperature (170) or degradation of SDS at high temperature. Indeed, prolonged heating of SDS at 40 °C or greater causes decomposition of alkylsulfates into fatty alcohols and sodium sulfate (191,192).

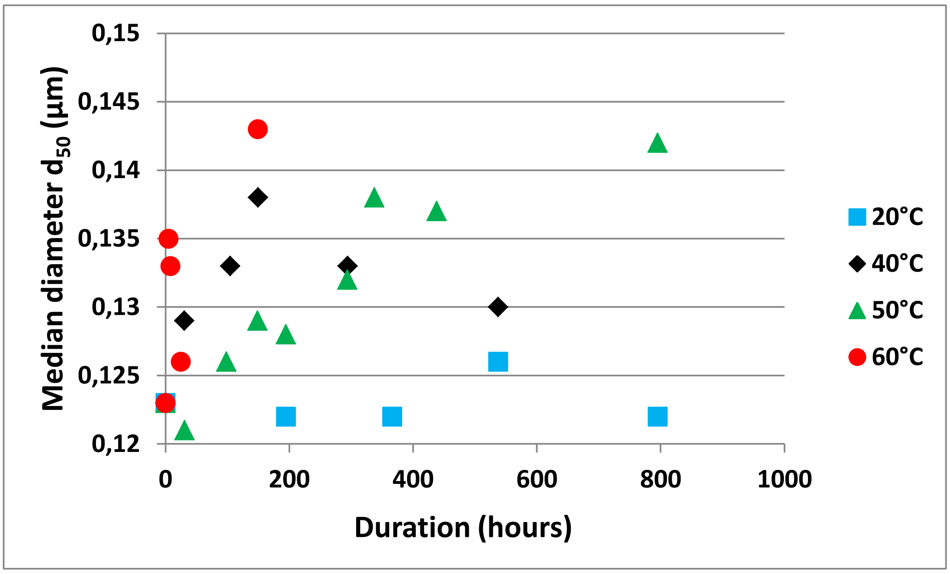

Figure 79: Median diameter (d_{50}) as function of time for different temperatures.

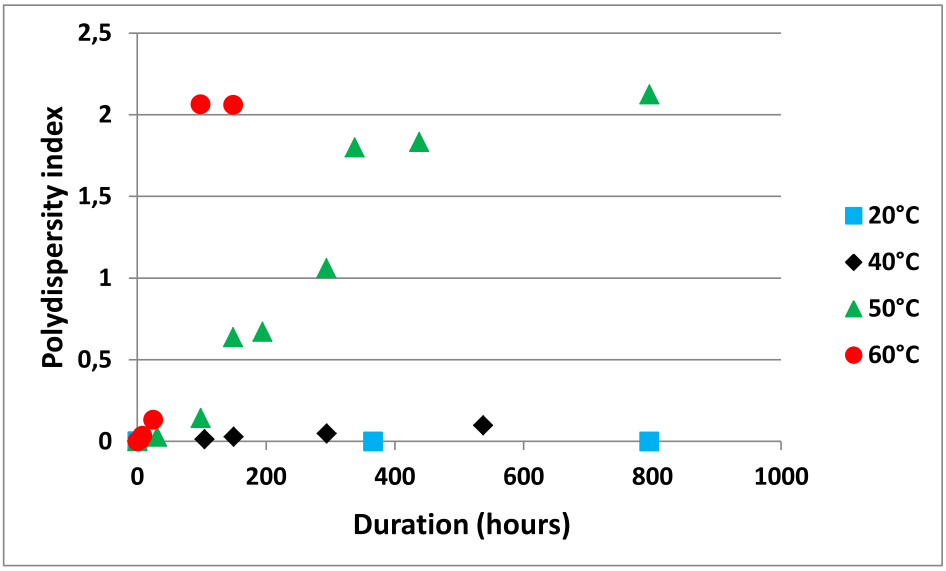

Figure 80: Polydispersity index function of time at different temperatures.

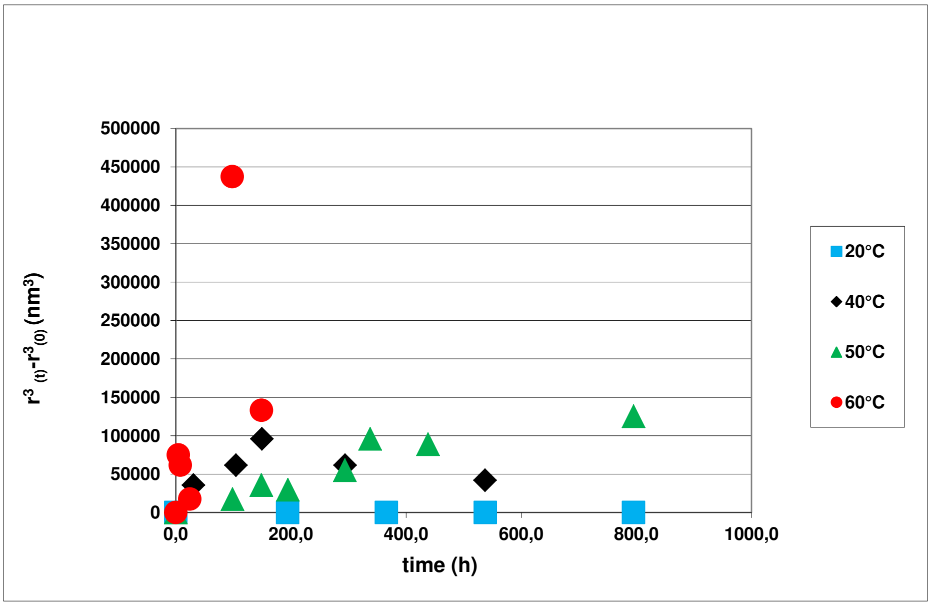

Figure 81: crystal growth ((r3(t)-r3(0)) versus time at different temperature

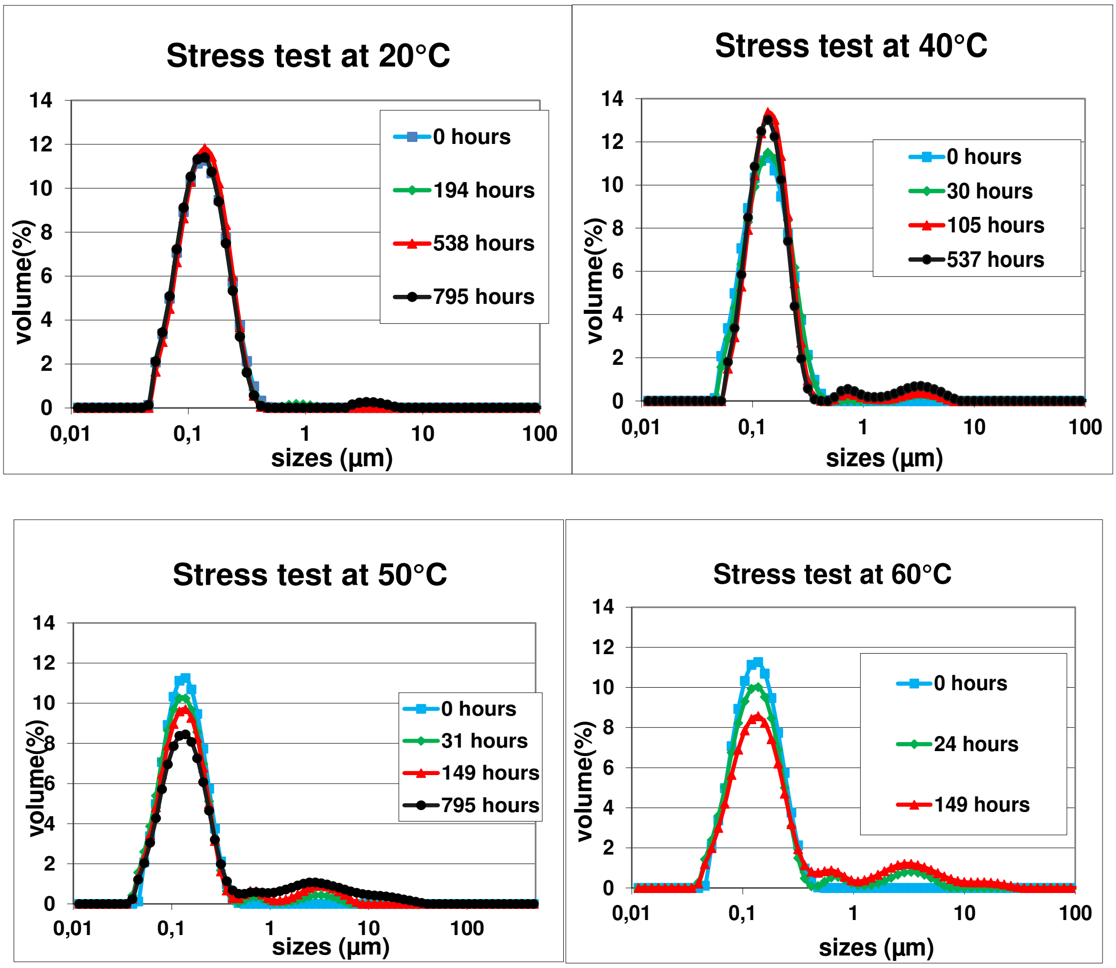

Figure 82: change of particle size distribution over time as function of temperature.

5.1.2.2.3.5. Sensitivity to pH variation

The impact of pH on particle size of suspension (20 % of API) was evaluated in the range of 2.0-9.5 to mimic gastric pH (1.50-5.00), intestinal pH (7.40-7.80) or plasmatic pH (7.35-7.45). The results show (see Figure 83) that particle size did not change over time when the pH was higher than 2 indicating high robustness of the designed formulation. At pH 2, a strong destabilization of suspension was observed. In fact, a spontaneous increase of particle size was observed soon after introduction of the sample within the acidic solution followed by a continuous linear increase of the particle size. This may be due to the contribution of two mechanisms:

(i) pKa of SDS is close to the second acidity of sulfuric acid (1.9). At pH above the pKa, the SDS loses its proton H+ and become negatively charged to ensure electrostatic stabilization. At pH below pKa, the SDS recovers its proton and loses its negative charges and thus its function as electrostatic stabilizer;

(ii) Degradation of SDS. According to the handbook of pharmaceutical excipients SDS (193) under extreme conditions i.e., pH 2.5 or below, it undergoes hydrolysis to lauryl alcohol and sodium bisulfate leading to a lack of electrostatic repulsion between particles.

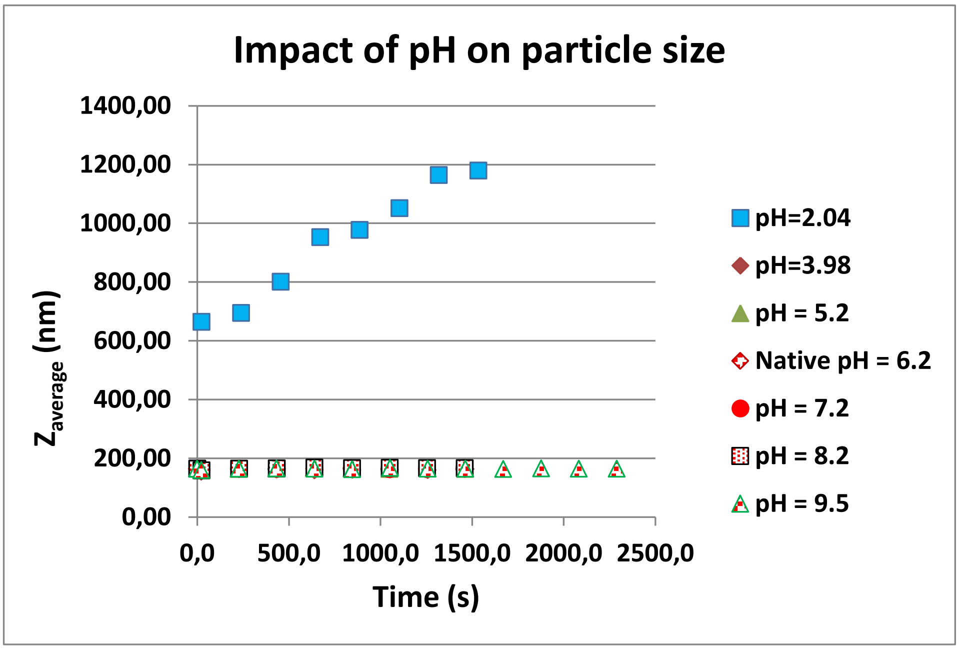

Figure 83 : Sensitivity of particle size to pH variation

5.1.2.2.4. Step #2.4: Stability of selected formulation.

Using the optimum SDS/PVP ratio of 40-60 at a concentration of 1.2 %, the stability data were obtained by assessing the particle size as a function of time at ambient temperature (for the 20 % w/w API nano-suspension). Figure 84 shows the evolution of d_{10}, d_{50} and d_{90} along a storage period of 57 days. It can be seen that no significant change in particle size occurred during the storage period, further confirming the high colloidal stability of the defined nano-suspension following the developed methodology.

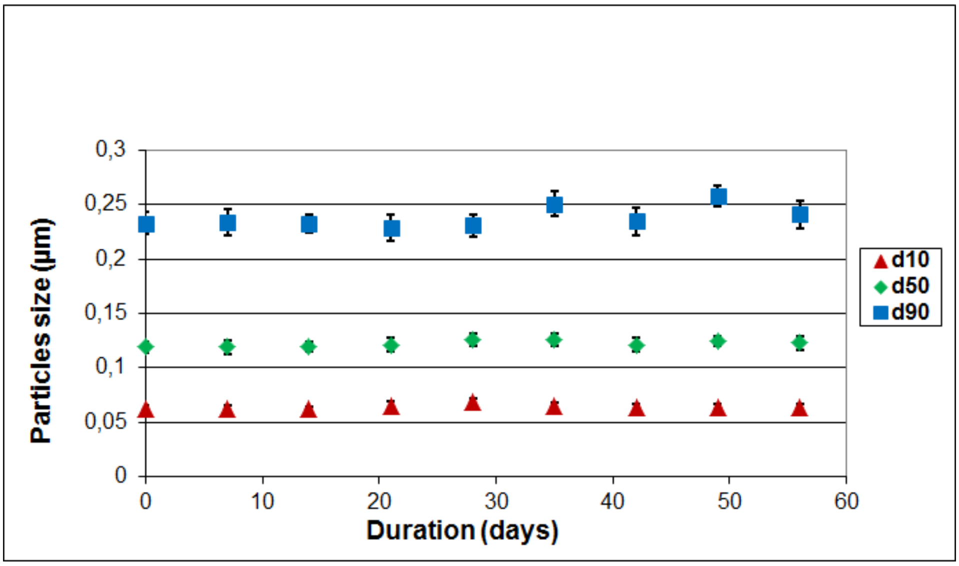

Figure 84: Stability at ambient temperature of nano-crystalline suspension stabilized with PVPV-SDS system (60-40 % w/w) at total concentration of 1.2 % w/w. variation of d10, d50 and d90 with storage duration.

5.1.3. Discussion

It is interesting to observe that the selected formulation is a synergic combination of an ionic surfactant (SDS) and a polymer (PVP). Indeed, it achieves a strong electro-steric protection. The trapped SDS micelles by the PVP chains provide a high electrostatic barrier and furthermore the micelles are placed outside the surface of API as illustrated in Figure 85 (Bernard Cabane, personal communication)

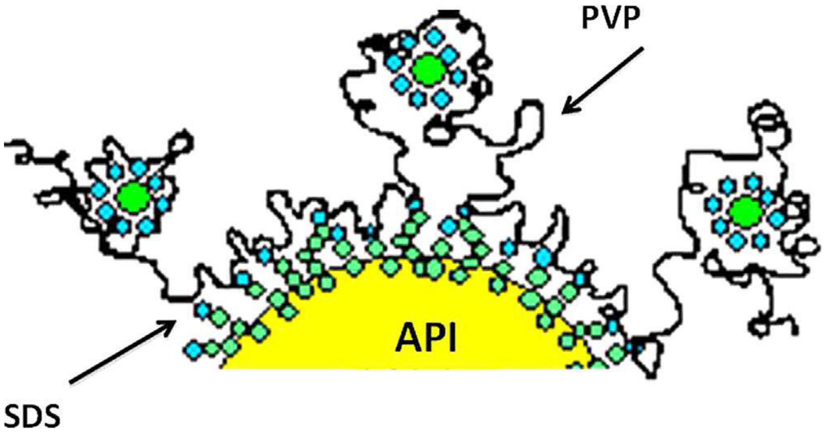

Figure 85 : Schematic conformation of SDS/PVP at surface of API particle.

5.1.4. Conclusion

Using a combination of empirical and colloidal-interfacial fundamental approach, an optimum wetting/dispersant agent was selected for preparing nano-suspensions with a d_{50} lower than 150 nm. Using a systematic approach, a large number of wetting/dispersant agents was investigated. The unsuitable agents were excluded following each step. Using a simple milling procedure, namely roller mill combined with particle size measurement, the agents that resulted in a particle diameter greater than 500 nm or that failed to prevent flocculation were excluded. The remaining agents were further segregated using zeta potential and rheological measurements. Samples that resulted in a low absolute zeta potential value (< 15 mV) and a viscosity higher than 10 mPa.s at a shear rate of $1000s^{-1}$ were also excluded. Among remaining samples, those showing a Newtonian flow were further investigated using high shear milling to select the best wetting/dispersant system. The SDS/PVP mixture was selected for composition optimization using wettability, adsorption isotherm and zeta potential measurement. An optimum stabilizer combination that led to maximum wettability, the best milling results and the maximum stability was identified as SDS/PVP 40-60 % with a total concentration of 1-1.2 %.

Development of a robust formulation stable along the overall value chain (from manufacturing process until administration to patient) is vital. The experimental research methodology described in this thesis represents an efficient approach for evaluating the formulation robustness of nano-crystalline suspension. The assessment of suspension destabilization under various conditions such as, ionic strength, shear rate, temperature, pH and dilution allowed identification of critical parameters whose levels must be tightly controlled to maintain product stability and thus in-vivo performances. A careful attention needs to be paid during down-processing of suspension with regard to the applied shear rate and high temperature mainly during heat based process such as autoclaving where flocculation or aggregation may occur. It would be interesting to determine the limits of shear rate in which variations in the levels have minimal or no effect on product stability or in-vivo performances.

Process engineering

5.2. Process engineering

This section is divided in two parts. The first part is focused on systematic comparison of manufacturing technologies of nano-crystalline suspension by top down process (bead mill versus high pressure homogenization), and the second is dedicated to manufacturing process modeling for simulation and prediction of process parameters to be applied from one scale to another (lab to pilot scale) and from one mill configuration to another (stirred annular mill to stirred pin mill).

5.2.1. Applied methodology

The methodology (parameters to be investigated and data analysis) used in this study was defined based on historical background on wet milling (194,195).

5.2.1.1. Parameters to be investigated

Wet milling is a complex process that involves many parameters to obtain the desired product. Overview of these parameters is provided in Ishikawa's diagram (196) (Figure 86).

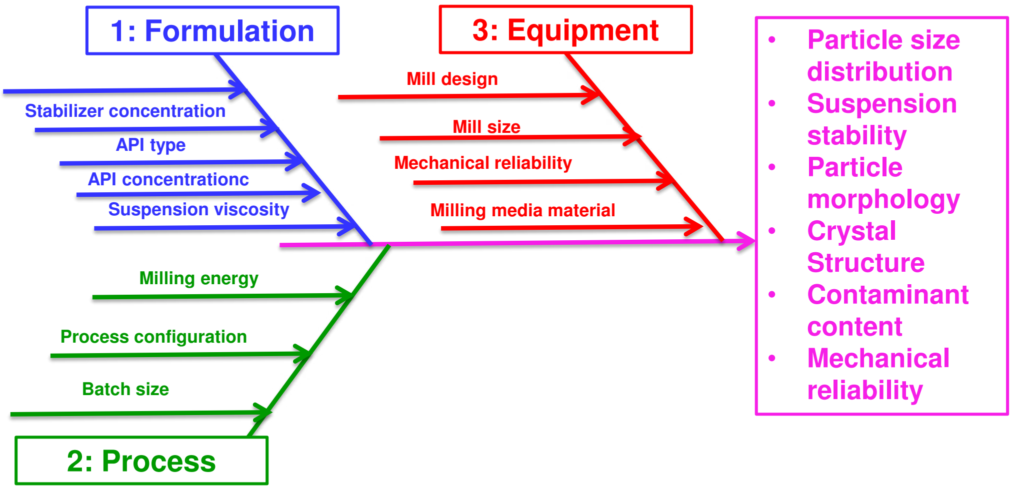

Figure 86 : Ishikawa's diagram of wet milling.

5.2.1.2. Data analysis methodology

Two methodology tools will be presented to analyze the experimental results:

(i) Quantitative tool that will be used to evaluate the increase of created surface during milling;

(ii) Qualitative tool that will be used to evaluate the particle size distribution profile.

5.2.1.2.1. Quantitative tool

Although 5% of all energy is used in size reduction (197), the energetic methodology is still relevant approach to study the milling process.

The required specific energy for physical processes of size reduction E_s is expressed as (194):

$$\mathbf{E_s = \gamma \times \Delta SSA} \quad \text{(Eq. 114)}$$

Where, γ is the surface tension of milling medium and ΔSSA is the created specific surface area.

In 1867, Rittinger proposed that the energy required for particle size reduction was directly proportional to the area of new created surface as described by the following equation (198):

$$\mathbf{E = \varpi \times (\frac{1}{d_2} - \frac{1}{d_1})} \quad \text{(Eq. 115)}$$

Where ϖ is constant, d_1 and d_2 are the starting and final particle size, respectively.

In 1958, Tanaka suggested a first order equation for characterizing the kinetics of milling in batch mode as follows (199):

$$\mathbf{SSA_{(t)} = SSA_{(\infty)} \times (1 - e^{-K' \times E_s})} \quad \text{(Eq. 116)}$$

Where, $SSA_{(t)}$ is specific surface area after time t, E_s is the specific energy input, $SSA_{(\infty)}$ the specific surface area at equilibrium and K' a constant.

Later in 1972 Chodakov improved the previous model by introducing the specific power as described by the equation (200):

$$\mathbf{SSA_{(t)} = SSA_{(\infty)} \times (1 - e^{-K'' \times t})} \quad \text{(Eq. 117)}$$

$$\mathbf{K' = \frac{k''}{P_{wv}}} \quad \text{(Eq. 118)}$$

The constant K'' implies the significance of rate constant of new surface formation and P_{wv} is the specific power of milling.

As the product is made of suspension, it is not easy to measure the specific surface area. Here, the implicit specific surface area ($6/d_{50}$) (see details in Appendix 2) was used. Therefore, (Eq. 118) can be transformed to the following equation:

$$\left(\frac{6}{d_{50}}\right)_{(t)} = \left(\frac{6}{d_{50}}\right)_{(\infty)}\left(1 - e^{(-k'' \times t)}\right) \qquad \textbf{(Eq. 119)}$$

It is noteworthy that it would be more rigorous to use the Sauter's diameter ($d_{[3,2]}$ instead of mean diameter (d_{50}) which is usually used in industrial practices. Nevertheless both diameters are well correlated (see Figure 87)

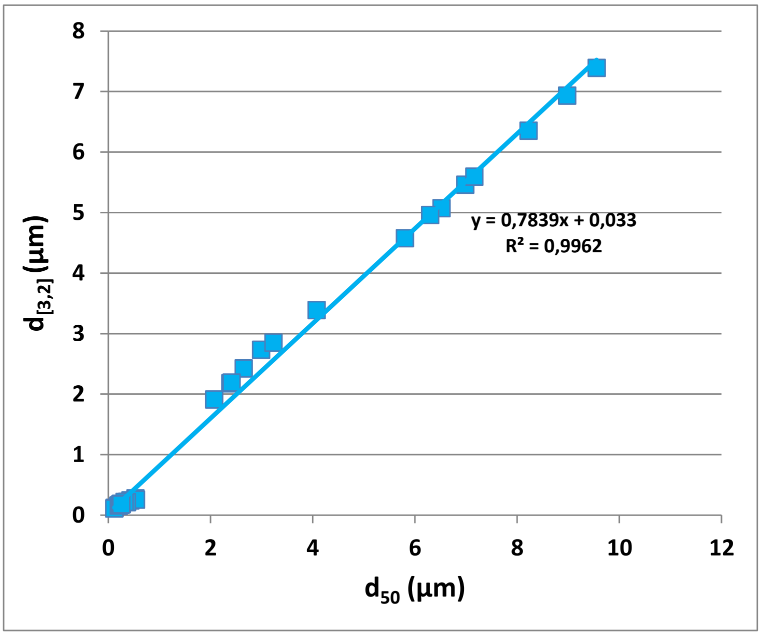

Figure 87: Sauter's diameter versus mean diameter.

Tanaka and Chodakov have made a very successful approach showing that very often particle size reduction follows a first order kinetics, but it cannot be used to fit all milling kinetics. In some cases, we observed that for APIs which are difficult to mill, the milling kinetic does not follow an apparent first order law. Instead it has a sigmoidal shape presenting a period of time where the milling is not very active (see Figure 88 for API E case). This period of time could be assimilated to an induction time.

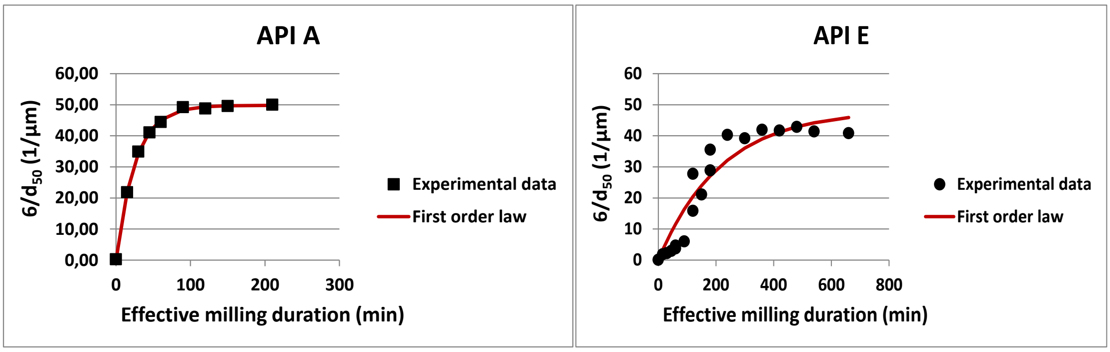

Figure 88: Fit of milling kinetics of API A and API E using first order law.

Mathematically we can find a generalized equation (by introducing an exponent n^* that can be considered as the induction index (see (Eq. 120)) where Tanaka and Chadakov's equations are a particular case. It allows accurate fitting both kinetics of API A and API E (see Figure 89

$$\left(\frac{6}{d_{50}}\right)_{(t)} = \left(\frac{6}{d_{50}}\right)_{(\infty)}\left(1 - e^{-(k''\times t)^{n^*}}\right) \qquad \text{(Eq. 120)}$$

$$K'' = \frac{1}{\tau} \qquad \text{(Eq. 121)}$$

Where τ is the characteristic time (s)

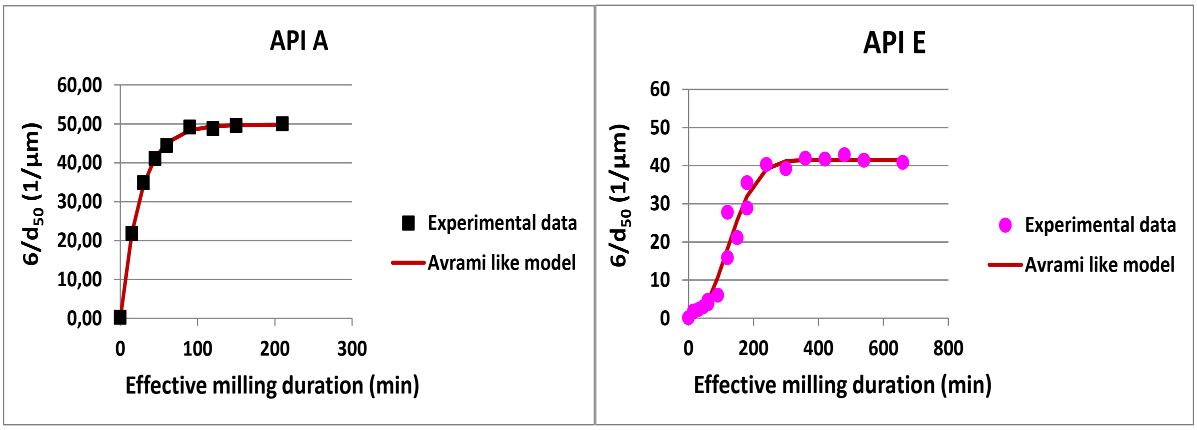

Figure 89: Fit of milling kinetics of API A and API E using Avrami's like model.

The proposed equation was inspired from Avrami's equation (201) which was originally derived to describe solid-solid phase transition at constant temperature, where the original mechanism is nucleation of a new phase followed by growth and then termination. The same analogy was reported to explain the milling mechanism (see section 2.4.1.2).

Three situations may be encountered (Figure 90):

(i) When $n^* < 1$: the kinetic is a stretched exponential exhibiting a vertical tangent at origin indicating that the particle size reduction starts immediately but needs a long time to reach equilibrium;

(ii) When $n^* = 1$: the kinetic is a simple exponential decay having $1/\tau$ as initial tangent. The milling rate follows a first order kinetic;

(iii) When $n^* > 1$: the kinetic is sigmoidal having an horizontal initial tangent (equal to zero). The kinetic is slow at the beginning and at the end of the milling process but rapid in between. The initial milling rate can be attributed to the time required to generate a significant number of defects prior to breakage.

One can observe that regardless n^* value, at $t/\tau = 1$ the value of milling rate is equal to $(1-e^{-1}) \sim 0.63$.

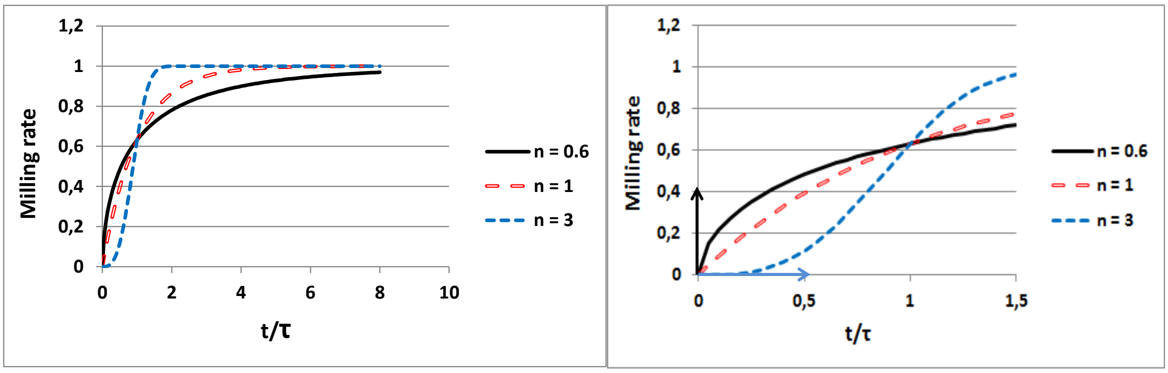

Figure 90: Milling rate as function of induction index (right figure is a zoom of left one).

5.2.1.2.2. Qualitative tool

(Eq. 120) provides information about the change of specific surface area during milling but none about the narrowing of the particle size distribution. In our study we observed that during milling the characteristic diameters d_{90} and d_{50} decrease progressively at the same speed, whereas d_{10} decreases suddenly and stabilizes around 100 nm (see Figure 91). In fact, it can be seen that the particles below 100 nm are not milled. The results suggest that d_{90} and

d_{50} belong to the same category of milling behavior, which allow us to study the profile of d_{90} versus d_{50} as milling pathway.

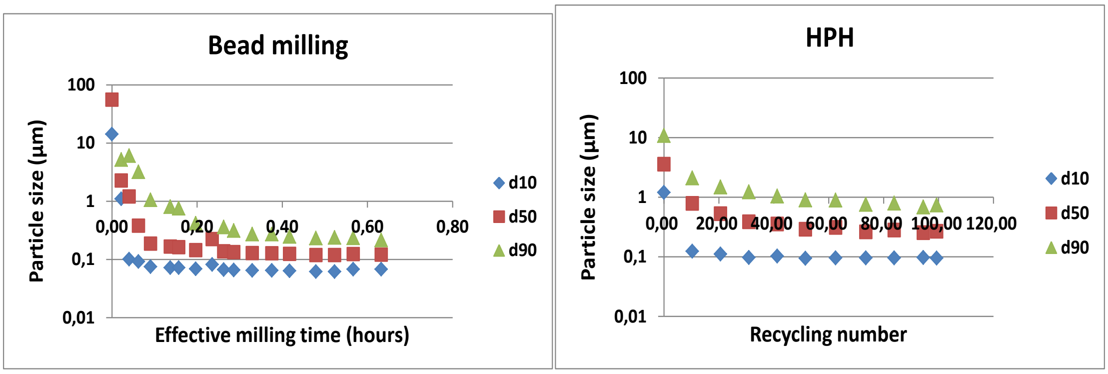

Figure 91: Change of d_{10}, d_{50} and d_{90} during milling for bead milling and HPH.

In order to evaluate the narrowing of the particle size distribution, the Span (see (Eq. 122)): usually supplied by the particle size analyzer provides limited information because the distributions' amplitude is quite large. Moreover, it does not provide any information on the symmetry of the distributions (Figure 92).

$$\mathrm{Span} = \frac{d_{90}-d_{10}}{d_{50}} \qquad \text{(Eq. 122)}$$

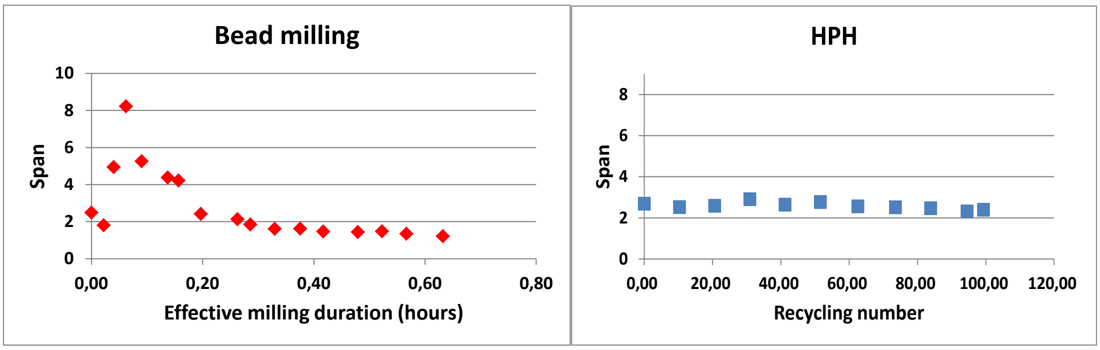

Figure 92: Span change during milling for bead milling and HPH.

We propose to use two qualitative tools in order to evaluate the narrowing of the particle size distribution:

(i) Polydispersity index that will describe the symmetry of the distribution;

(ii) The profile of d_{90} versus d_{50} that will describe the milling pathway

5.2.1.2.2.1. Symmetry of particle size distribution

The symmetry of distribution can be evaluated using polydispersity index which is described by the (Eq. 102).

Figure 93 illustrates the three situations that can be be encountered. They are described below (see section 4.2.3.2)

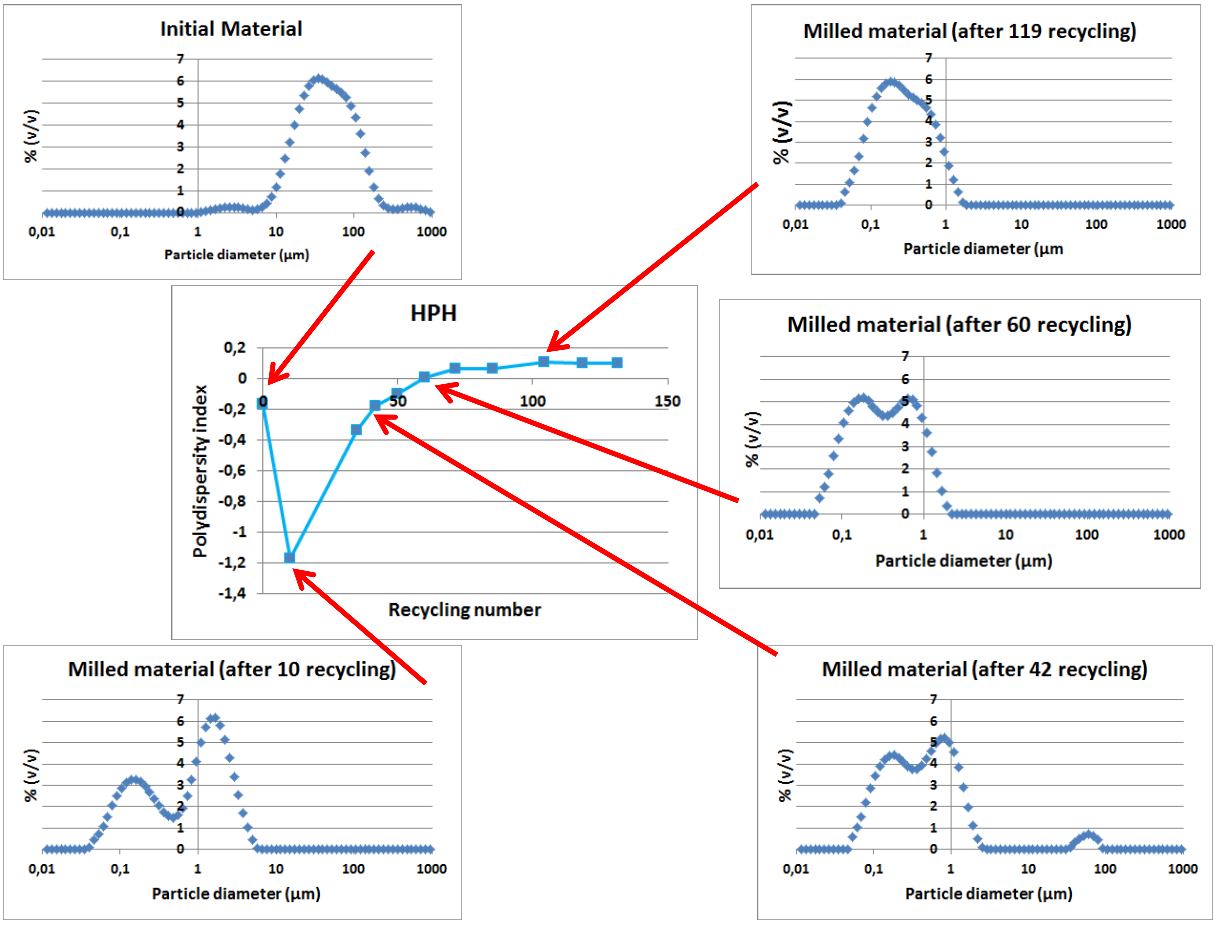

Figure 93: Polydispersity index change during milling.

5.2.1.2.2.2. Milling pathway

As d_{90} and d_{50} evolve similarly during milling, we propose to monitor the d_{90} versus d_{50} as milling pathway (see Figure 94)

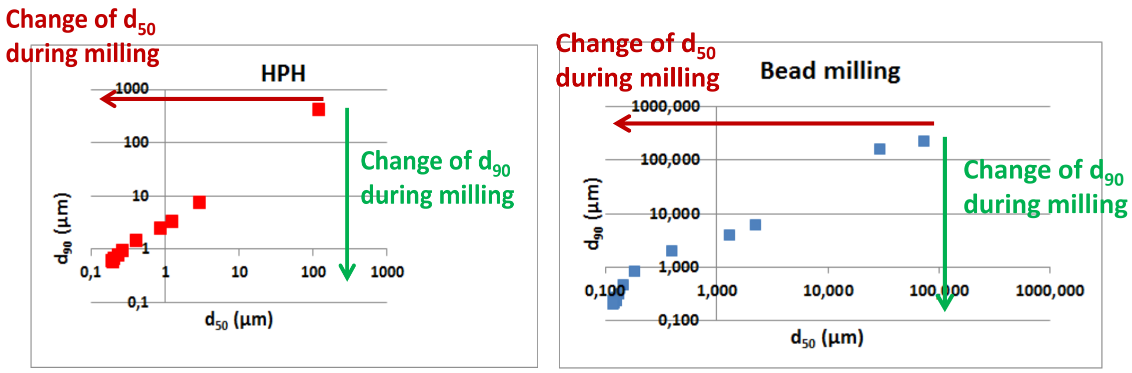

Figure 94: d_{90} versus d_{50} profile (milling pathway)

5.2.2. Results and discussions

5.2.2.1. Comparison of manufacturing technologies of nano-crystalline suspension using top down process.

The comparison of both technologies was carried out by studying the impact of formulation, operating process parameters and mill configuration on milling performances and physical quality of produced suspension. Moreover, the reliability and robustness of both technologies were compared

5.2.2.1.1. Evaluation of formulation impact

The formulation impact on milling performances was assessed by studying the impact of stabilizer content, stabilizer type, viscosity of milling vehicle, API % impact and API type.

5.2.2.1.1.1. Evaluation of stabilizer content

The evaluation of stabilizer content using both technologies (high pressure homogenization and stirred bead milling) was carried out using a kinetic experiment in which the reduction in particle size, or the equivalent increase in implicit specific surface area, was measured as function of milling time. For both technologies the trials were conducted using lab scale equipment (Panda for the high pressure homogenization and Nano-mill$^{®}$ 01 for stirred bead milling). The HPH was operated at 1400 bars and bead mill at 10.8 m/s and 64 % of bead filling rtae. A suspension containing 20 % (w/w) of API A, the SDS/PVP (40-60 % w/w) concentration was varied between 0.25 to 3% (w/w) and WFI q.s 100% (w/w). As explained in the section 5.1.2.2.2 the milling kinetics were represented by the first order law ((Eq.

119)). Values for $(6/d_{50})_\infty$ were generated at various SDS/PVP concentrations. For both technologies, the results shown in Figure 95 highlighted the presence of 3 regimes:

(i) An initial increase in $(6/d_{50})_\infty$ is observed with increasing of SDS/PVP concentration suggesting that at low SDS/PVP concentration "poor regime: % < 0.8 %", the particle size is limited by the stabilizer amount corresponding to a full coverage;

(ii) After the increase in $(6/d_{50})_\infty$, a plateau of $(6/d_{50})_\infty$ is observed "rich regime". The plateau bounds were found in the range of 0.8-2.5 % (w/w) for the HPH and 1-2.5 % (w/w) for the stirred beads media, respectively. The observed plateau was found not dependent on the used mechanical energy of milling system. Indeed, experimental trials performed using bead mill at different rotation speed does not show any impact on the plateau level of $(6/d_{50})_\infty$ (see Figure 96) suggesting that the breakage itself is a limited process for which below a critical size, no fracture of the particles occurs (202). However, this observation has not been encountered when the emulsion is processed using HPH. Indeed it was found that the plateau level is dependent on the used energy $((6/d50)_\infty \sim P^{0.6\text{ to }0.9}$ (177);

(iii) A slight decrease of $(6/d_{50})_\infty$ is initiated starting from 2.5 % w/w, suggesting that the excess of SDS/PVP accumulated in the supernatant phase may promote Ostwald ripening and/or flocculation;

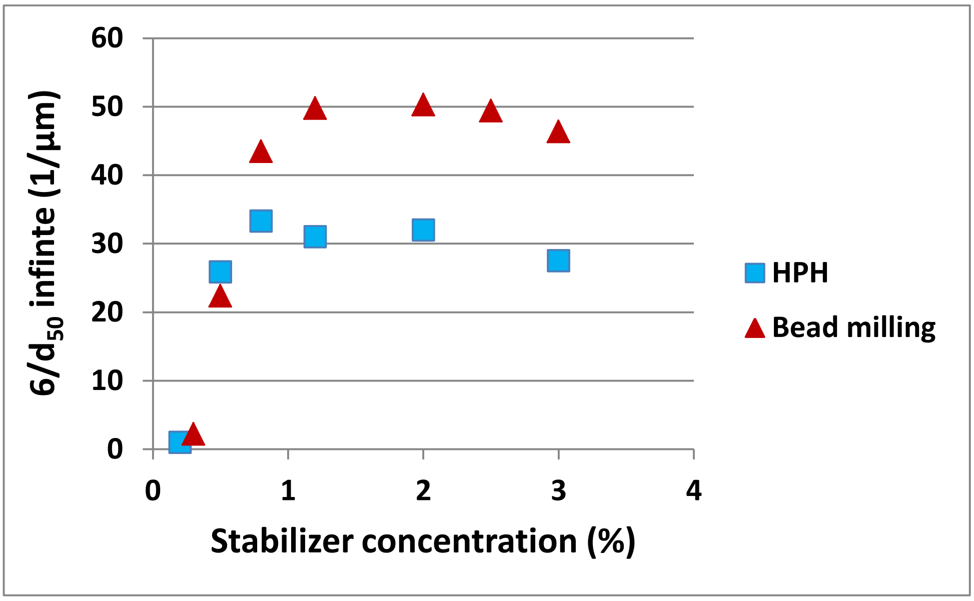

Figure 95: $(6/d_{50})_\infty$ as function of SDS/PVP concentrations.

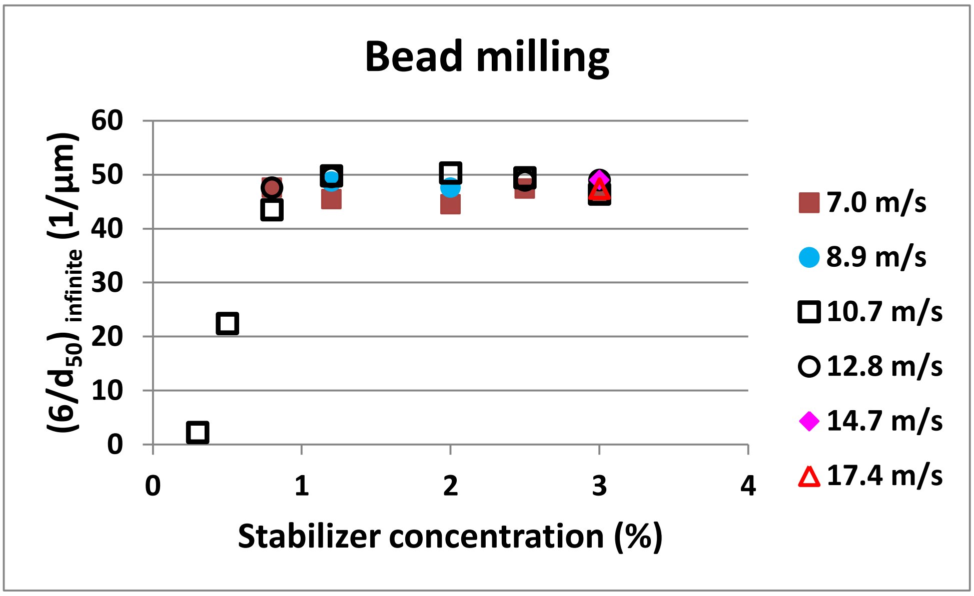

Figure 96 : $(6/d_{50})_\infty$ as function of SDS/PVP concentrations at various bead milling rotation speed.

(iv) As illustrated in Figure 95, The HPH leads to a lower $(6/d_{50})_\infty$ than stirred bead milling (32 versus 50 µm^{-1}). This is may be due to the following reasons:

(a) Difference in terms of application mode of shear strain during milling between HPH and bead mill. Based on experimental data, we found that the shear stress and shear strain for the bead mill are 1.6 10^4 s^{-1} and 9.5 10^7, respectively for a continuous residence time of 100 min. Whereas, for the HPH the shear stress and shear strain are 1.4 10^8 s^{-1} and 1.5 10^5, respectively for an overall residence time of 1 ms (cumulative residence time in discontinuous mode). This observation suggests that when using HPH, the particles reached a strength which cannot be overcome by the supplied stress energy;

(b) Thermal effect: within HPH the product is submitted to high temperature amplitude (± 35°C for HPH versus ± 5°C for bead milling at high energy level see Figure 97), which could lead to flocculation or a low plateau of stabilizer adsorption. Indeed, in stirred bead milling the dissipated heat is removed by the cooling jacket of the milling chamber as well as by the cooling exchanger, whereas in the case of HPH the dissipated heat is removed only by the cooling exchanger;

(c) Flocculation due to SDS degradation. In fact, the SDS undergoes hydrolysis at elevated temperatures especially in acidic medium leading to formation of sulfuric acid (191). However, this hypothesis has been discarded as the pH measurements does not show any significant change of pH value before and after milling for both technologies (see Table 11).

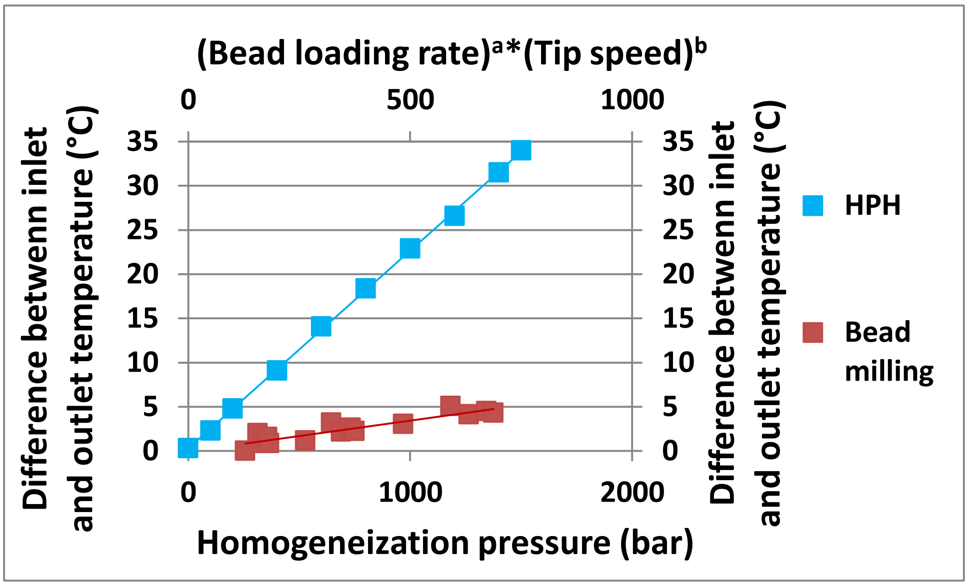

Figure 97: temperature increase during milling for HPH and bead mill.

	Suspension pH before milling	Suspension pH after milling
HPH	6.71	6.67
Stirred bead milling	6.21	6.18

Table 11: pH values before and after milling at ambient temperature.

5.2.2.1.1.2. Evaluation of stabilizer composition impact

The evaluation of stabilizer composition using both technologies (high pressure homogenization and stirred bead milling) was also carried out using a kinetic experiment at lab scale (HPH was operated at 1400 bar and bead mill at 10.8 m/s and 64 % of bead filling rtae). In this part 3 wetting/dispersant systems were investigated using API A at 20 % (w/w) in the suspension. The composition of each system is described in the Table 12. Each composition was selected in the rich regime.

	System 1		System 2		System 3	
	Wetting agent	dispersant Agent	Wetting agent	dispersant Agent	Wetting agent	dispersant Agent
Name	SDS	PVP K30	NaDOC	PVP-VA	None	Vitamin E TPGS
Composition (% w/w) in suspension	0.48	0.72	0.25	6.25	N.A	3.0

Table 12: Composition of wetting/dispersant agent used for studying the impact of formulation composition.

N.A: not applicable

The values of implicit specific area ($6/d_{50}$) were graphed as function of recycling number for HPH and effective milling time for bead mill. The results show that for both technologies, as far as the formulation is designed in rich regime, there is no significant impact on the infinite specific surface area whatever the formulation used (see Figure 98). It can be outlined that the variability is much higher in the case of HPH than with bead mill. This could be explained by the difference in terms of sampling homogeneity. In fact, the HPH is operated using recycling mode whereas the bead milling is operated in batch mode.

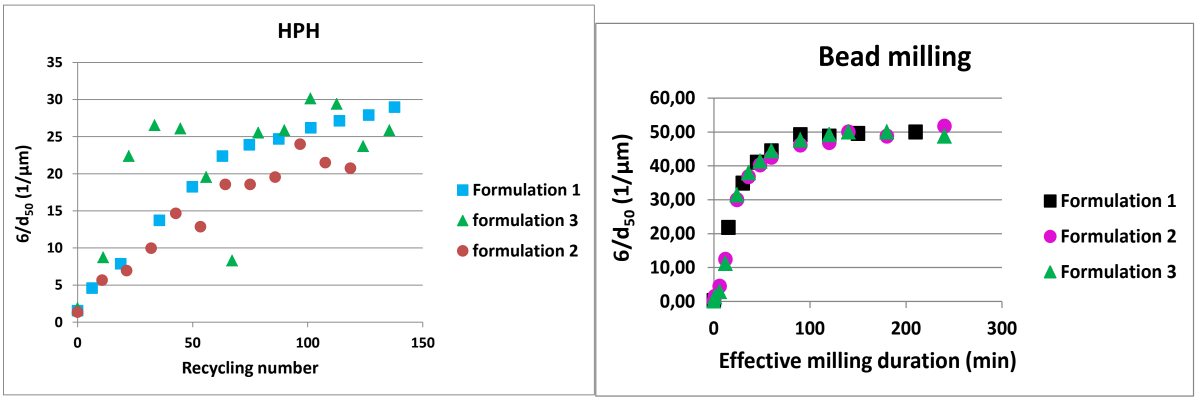

Figure 98: Impact of formulation composition on implicit specific surface area (6/d50).

5.2.2.1.1.3. Evaluation of suspension viscosity impact

The evaluation of suspension viscosity impact using both technologies (high pressure homogenization and stirred bead milling) was also carried out using a kinetic experiment at lab scale. In this part, we used a suspension made of SDS/PVP system as wetting/dispersant agent at concentration of 1.2 % (w/w) in combination of API A at concentration of 20 % (w/w). The native suspension was divided in different aliquots. The viscosity of each aliquot was modified by adding and dispersing carboxylmethyl cellulose in suspension, prior to milling experiments as described in Table 13.

Aliquot	Added carboxylmethyl cellulose (% w/w)	Viscosity (cP)
1	0.00	2.4
2	0.15	10.6
3	0.30	14.8
4	0.5	21.0
5	0.80	46.1
6	1	76.1

Table 13 : Viscosities of aliquot suspensions used for studying the impact of suspension viscosity on implicit specific surface area ($6/d_{50}$).

From the milling investigation the values of implicit specific area ($6/d_{50}$) were graphed as function of recycling number for HPH and effective milling time for bead mill. The results show that:

(i) For the HPH case the increase of viscosity impacts dramatically the milling kinetic. Indeed, the higher is the viscosity the slower is the milling kinetic (see Figure 99). This can be explained by the hydrodynamic calculation (see section 2.4.6), which reveals that the slowing down of the milling kinetic induced by the increase of viscosity (from 2.4 to 46.1 cP) is due to a decrease of milling power density (from $1.5\ 10^{13}$ to $5.5\ 10^{12}$ w/m^3) and therefore to a decrease of several parameters (within the gap of the HPH chamber): mean velocity (from 52 to 20 m/s) and shear rate (from 1.4×10^{8} to 1.9×10^{7} s^{-1}). Furthermore, it can be observed that power density within the HPH gap correlates to suspension viscosity according a power law (power density~viscosity$^{-0,332}$) and when

$6/d_{50}$ is graphed as function of recycling number×viscosity$^{-0,332}$ the kinetic profile is described by one master curve indicating that the power density drives the milling kinetic (see Figure 100);

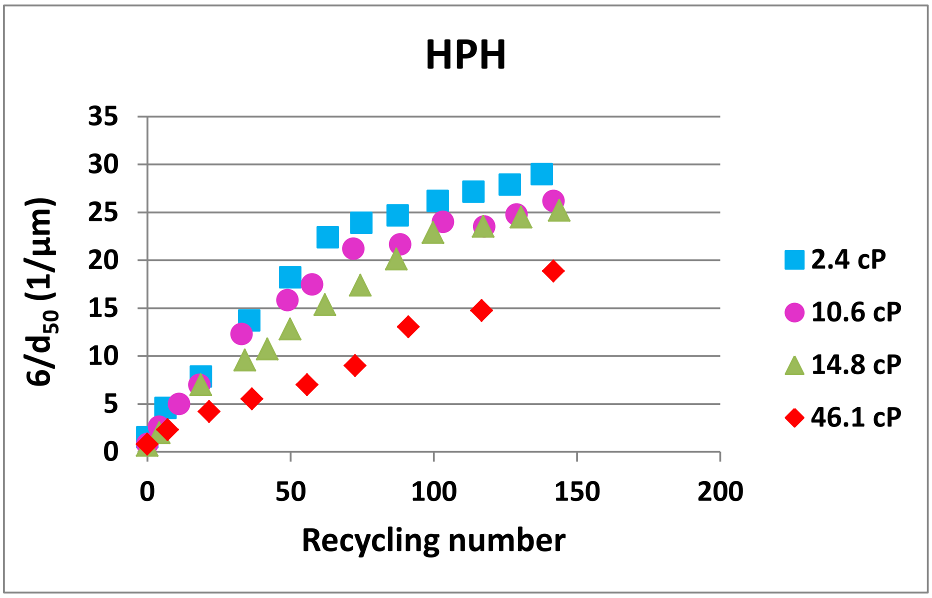

Figure 99: HPH milling kinetic as function of suspension viscosity.

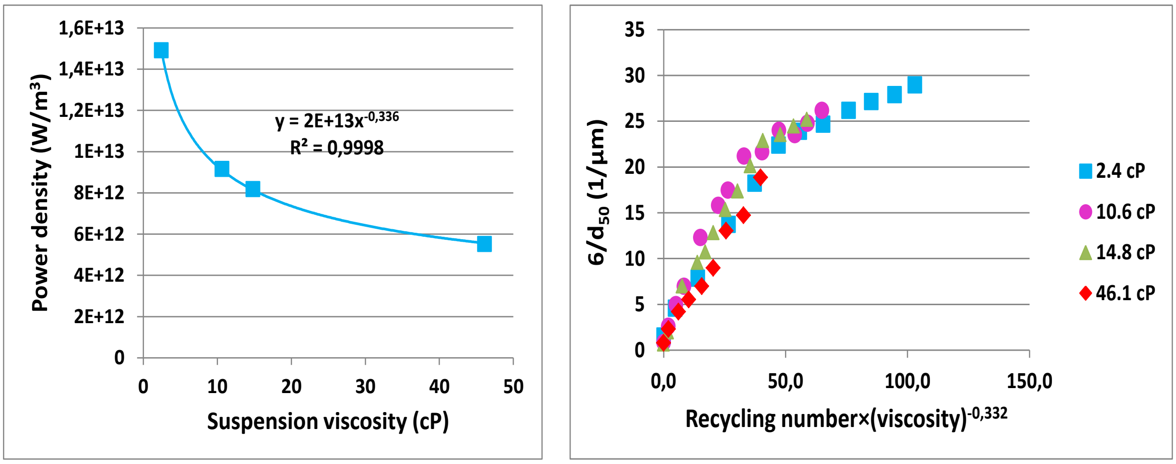

Figure 100 : Power density as function of suspension viscosity (left curve) and $6/d_{50}$ as function of recycling number×viscosity$^{-0,335}$ (right curve) for HPH.

(ii) For the bead mill case, using stirred annular mill, it can be observed that the milling kinetic is not impacted by the increase of viscosity (see Figure 101) while the hydrodynamic regime was switched from turbulent to transient flow (Reynolds number switched from 106000 to 3300). However it is reported in the literature that the stirred disc mill and stirred pin mill react to the change of viscosity. That it is, the increase of viscosity slows down grinding media and reduces energy available for grinding by pressure and impact (true grinding usually uses low viscous liquid carriers) (203). This difference can be attributable to the fact that the annular mill has a significant difference of geometry than the stirred disc mill and stirred pin mill which can lead to different motion and different use of energy;

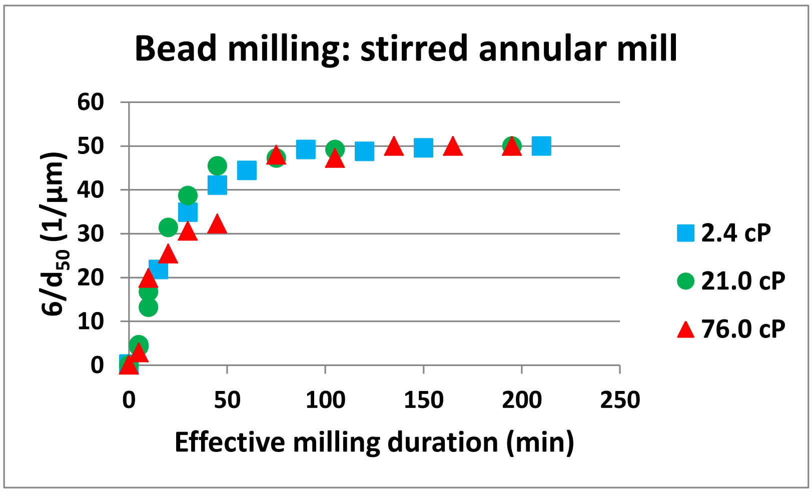

Figure 101 : Bead milling kinetic as function of suspension viscosity for stirred annular mill.

(iii) It can be observed that for both technologies the relationship of d_{90} versus d_{50} is described by a unique master curve showing that the suspension viscosity does not have any impact on the particle size distribution profile (see Figure 102)

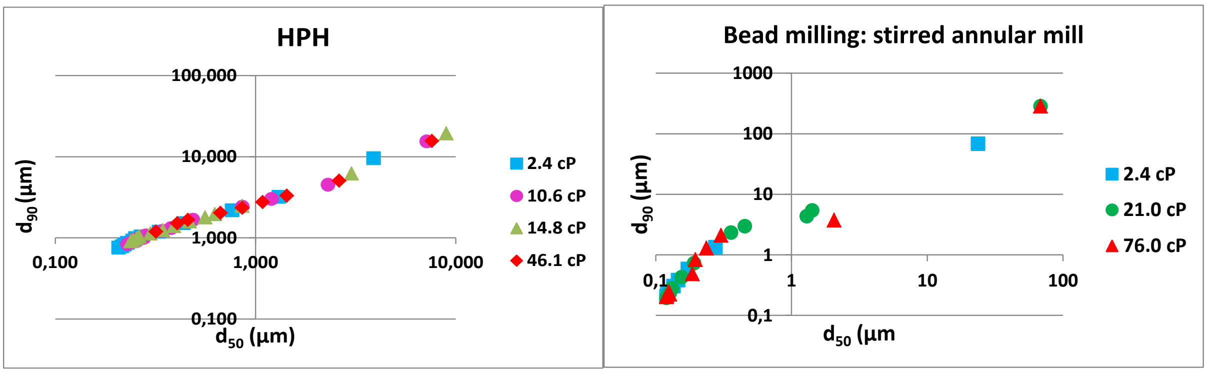

Figure 102 : d_{90} versus d_{50} as function of suspension viscosity for HPH and bead mill

5.2.2.1.1.4. Evaluation of the impact of the API type

The evaluation of the impact of the API type using both technologies (high pressure homogenization and stirred bead milling) was also carried out using a kinetic experiment. The evaluation was performed using NS2006 equipment for HPH at 1400 bar and Nano-mill® for bead mill at 10.8 m/s and 64 % of bead filling rtae. The APIs used in the study and their associated formulation are described in the section 4.1.2

The main observations resulting from this evaluation are summarized below

(i) As shown in Figure 103, for both technologies the milling kinetic profiles and the implicit specific surface area at the equilibrium are dramatically impacted by the API type. This can be explained by difference between different APIs in terms of defect density and grinding limit. Furthermore, as was reported in the section 5.2.2.1.1.1, for different APIs, the HPH leads to a lower $(6/d_{50})_\infty$ than stirred bead milling;

(ii) Provided that the formulation is stable, the milling kinetic profile is the same whatever the technology used. That is, for both technologies, some APIs can be milled easily and others are difficult to mill or cannot be milled. These APIs will require alternative approaches (bottom up process, emulsion, liposomes).

(iv) There is no clear trend on the correlation of milling-ability and APIs physico-chemical characteristics. It could be interesting to study the grind-ability of single-crystals using a nano-indentation technique as reported by Taylor *et al.* (204) in order to investigate the impact of the mechanical properties on milling kinetic profiles and the implicit specific surface areas at the equilibrium.

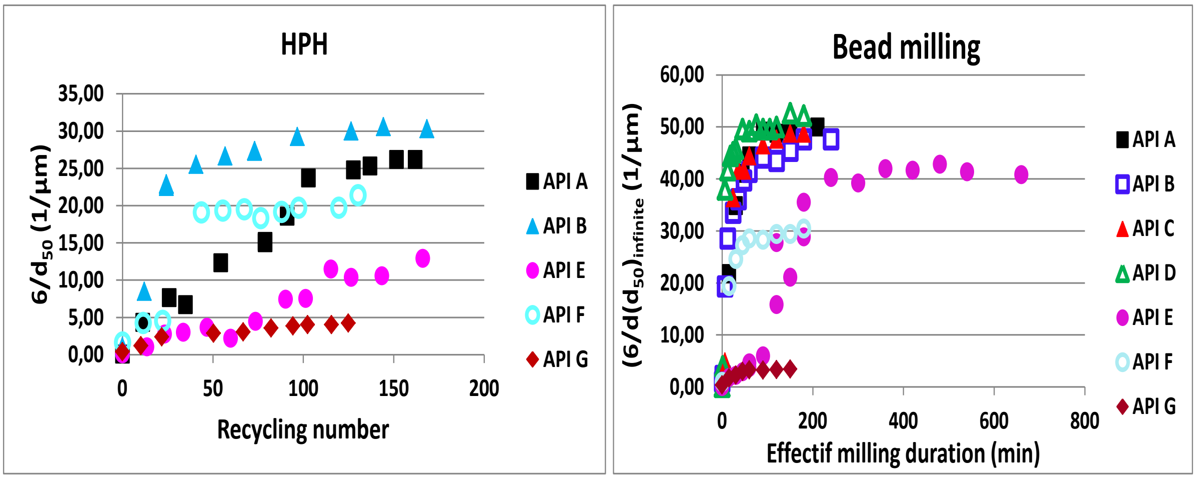

Figure 103 : Milling kinetic profile of different APIs evaluated using HPH and bead milling.

5.2.2.1.1.5. Impact of API concentration

The impact of API loading was studied for both technologies (HPH and bead mill) using a kinetic experiment. The evaluation was performed using NS2006 equipment for HPH at 1400 bar, stirred annular mill (Nano-mill®) and stirred pin mill (Labstar®) for bead mill at 10.8 m/s and 64 % of bead filling rtae.

Prior to this evaluation the rheological behavior of the suspension was investigated as function of API concentration.

The results showed that:

(i) The higher is the API loading, the higher is the viscosity (see Figure 104). The change of viscosity can be accurately fitted using Mooney model described by the following equation;

$$\eta_{susp} = \eta_{liq} \times e^{\left(\frac{B \times C_a}{1 - B' \times C_a}\right)} \qquad \text{(Eq. 123)}$$

Where, η_{susp} is the suspension viscosity, η_{liq} is the carrying liquid viscosity, C_a is the API volume fraction, B is a constant function of maximum attainable solid volume and B' is a constant;

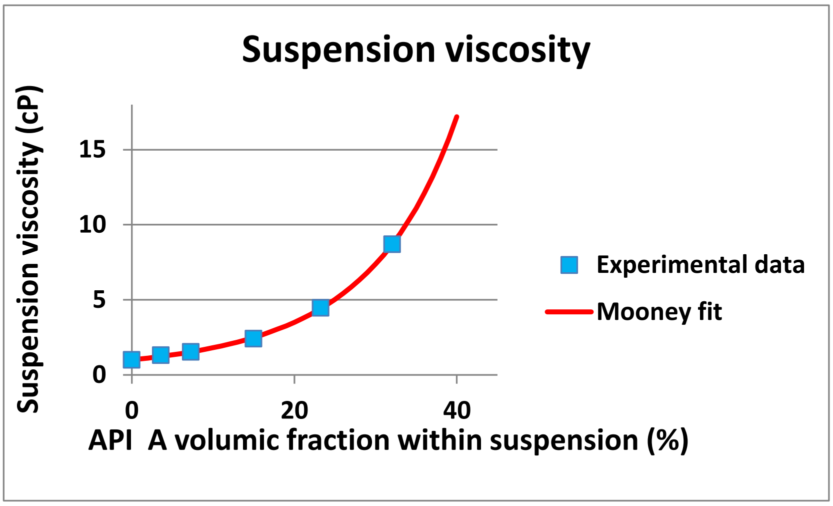

Figure 104 : Suspension viscosity as function of volume fraction of API.

(ii) For the HPH, the API loading has a limited impact on the milling kinetic (see Figure 105). This can be explained by the fact that the increase of concentration in the range of 5-20 % has limited impact on the increase of suspension viscosity (1.3-2.4 cP) which leads to a limited decrease of power density (1.8 10^{13}-1.5 10^{13} W/m3) and shear rate (2.0 10^{8}-1.4 10^{8} s^{-1}) within the HPH valve;

(iii) For the bead mill, although stirred annular mill and stirred pin mill operate in the same hydrodynamic regime (very turbulent flow having Reynolds number in the range of 103000-106000), both mills react differently to the API loading. Indeed, by increasing the API loading no significant impact on the milling kinetic was observed when the stirred annular mill is used (see Figure 106 left). This can be explained by the fact that the annular gap geometry does not react to different viscosities. However, when stirred pin mill is used, the increase of the API loading has a significant impact on milling kinetic. Indeed, we observed that higher is the API loading slower is the milling kinetic (see Figure 106 right). This result is in agreement with already published data as the increase of the API loading decreases the milling specific energy (205);

(iv) For both technologies the API loading does not have any impact on the d_{90} versus d_{50} profile suggesting that the API loading could have an impact on milling kinetic but not on the particle size distribution profile (see Figure 107 and Figure 108).

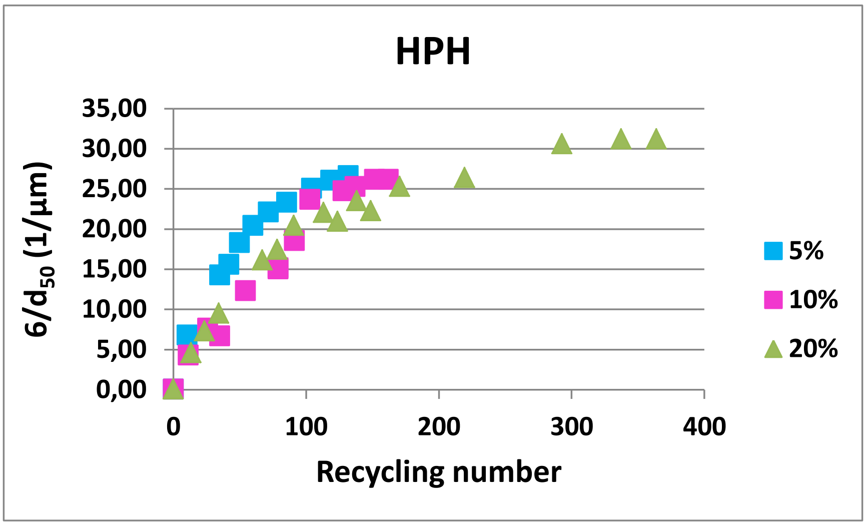

Figure 105 : Impact of API loading on milling kinetic obtained with HPH.

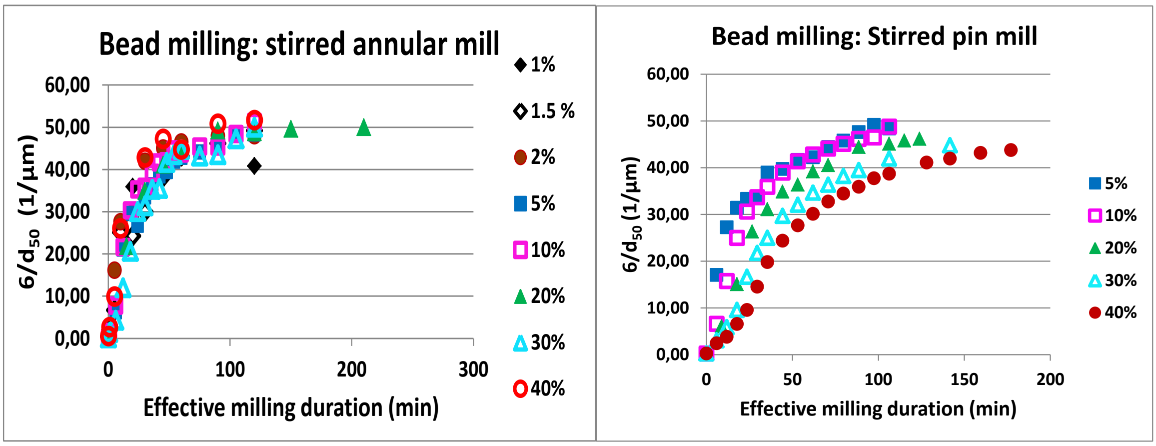

Figure 106 : Impact of API loading on milling kinetic obtained with beads stirred annular mill (left) and stirred pin mill (right).

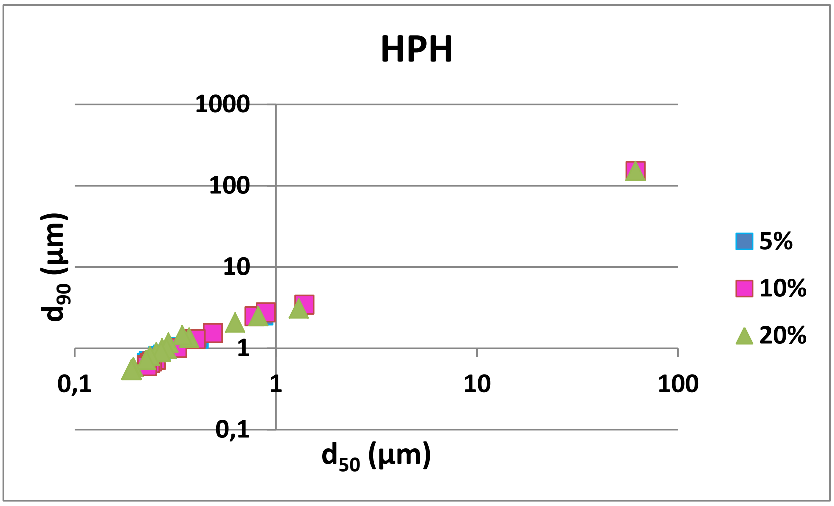

Figure 107 : Impact of API loading on d_{90} versus d_{50} profile obtained with HPH.

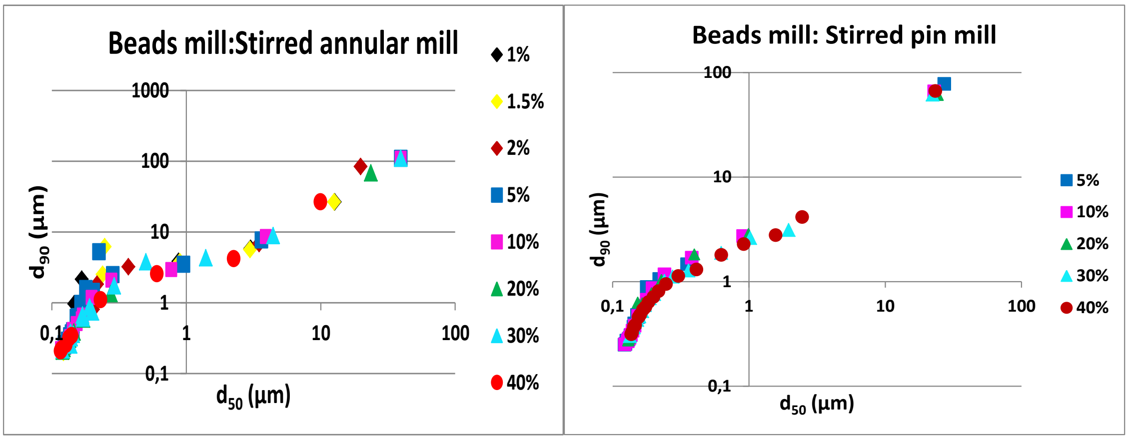

Figure 108: Impact of API loading on d_{90} versus d_{50} profile obtained with beads annular mill (left) and stirred pin mill (right).

5.2.2.1.2. Evaluation of process parameters impact

From methodology stand point three parameters have been investigated: The impact of milling energy, process configuration and manufactured batch size on milling kinetic were studied

5.2.2.1.2.1. Impact of milling energy

For the HPH, the milling energy can be defined as follow:

$$\mathbf{E = P * Q * t} \qquad \text{(Eq. 124)}$$

Where, E is the homogenization energy, P is the milling pressure, Q is the homogenization flow rate and t is the recycling time.

For the bead milling, the milling energy has been reported in section 2.4.2.3, the milling energy is driven for a fixed milling media (size and material of beads) by the mill rotation speed and bead filling rtae.

The evaluation of the impact of the milling energy using both technologies (high pressure homogenization and stirred bead milling) was carried out using a kinetic experiment. The evaluation was performed using intermediate scales (NS2006 equipment for HPH and stirred pin mill (Labstar®) for bead mill.

The assessment was performed using suspension of 20 % of API A and 1.2 % of SDS/PVP as wetting/dispersant agent. The process parameters were varied from 600 to 1400 bars for the homogenization pressure and from 6.9 to 16.4 m/s and from 22 to 90 % v/v, respectively for the bead milling rotation speed and bead filling rtae.

The main findings of this evaluation are the following:

(i) For both technologies the increase of milling energy (Pressure for HPH (see Figure 109), rotation speed and beads filling ratio for bead mill (see Figure 110)) leads to a faster milling kinetic;

(j) For the HPH, when the milling kinetics are graphed in terms of $6/d_{50}$ versus (recycling number)×$(\text{Pressure})^{2.6}$, one master curve is obtained (see Figure 111). This correlation is currently not understood and needs to be investigated in future work;

(k) For bead mill, when the milling kinetics are graphed in terms of $6/d_{50}$ versus (effective milling duration)×$(\text{tip speed})^2$ and (effective milling duration)×$(\text{Beads loading rate})^{3.95}$, one master curve is obtained for each parameter (see Figure 112). The exponent 2 for the rotation speed can be explained by the kinetic energy which is correlated to $(\text{rotation speed})^2$. However, for the time being the exponent 3.95 for bead filling rtae is not explained and needs to be investigated in future work;

(l) As can be seen in Figure 113 for both technologies, the relationship of d_{90} versus d_{50} is described by a unique master curve suggesting that the milling energy has an impact on the milling kinetic but not on the particle size distribution profile.

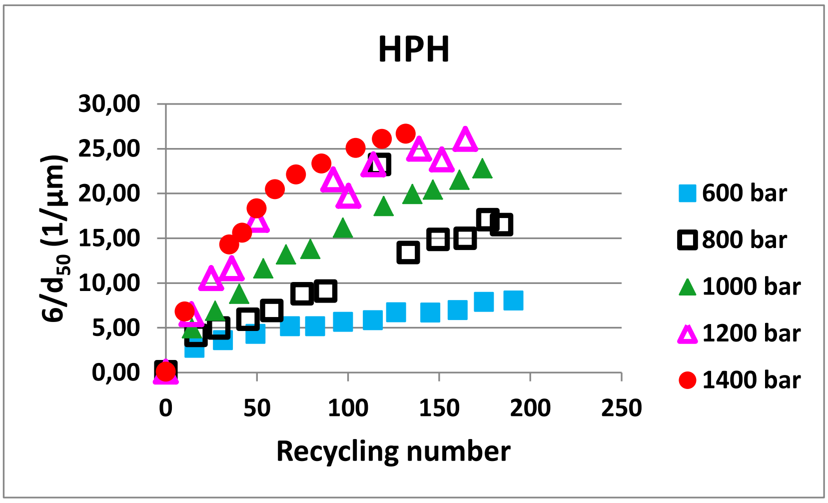

Figure 109 : Impact of homogenization pressure on the milling kinetic.

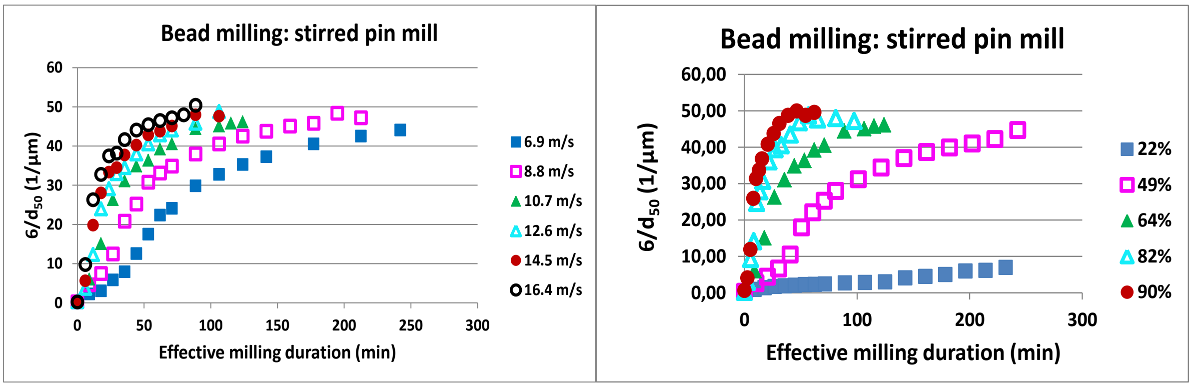

Figure 110 : Impact of rotation speed (left) and bead filling rtae (right) on the milling kinetic.

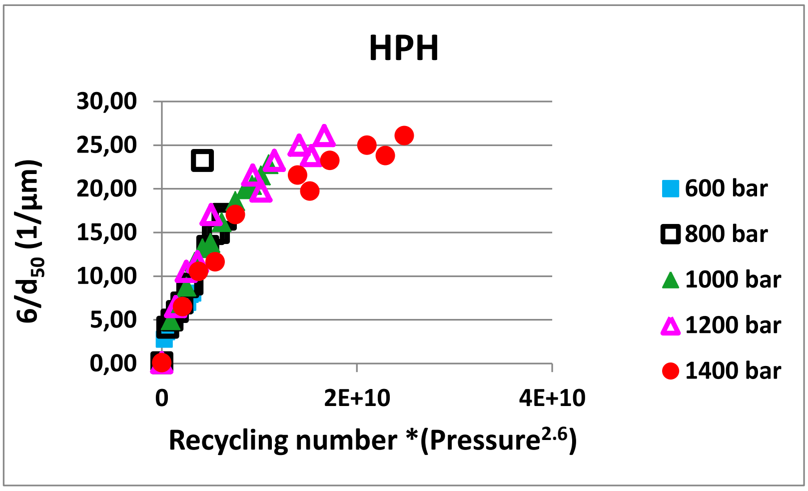

Figure 111 : $6/d_{50}$ as function of recycling number×(pressure$^{2.6}$).

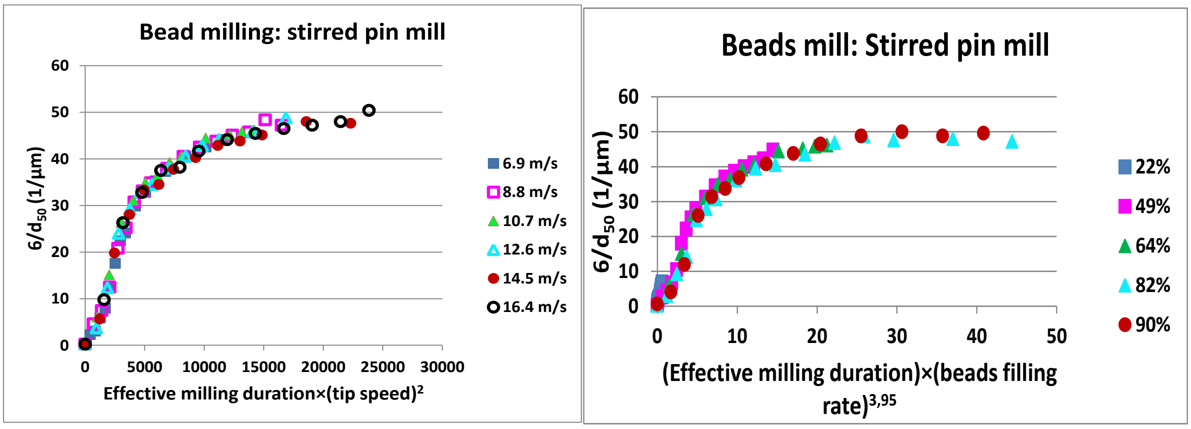

Figure 112 : $6/d_{50}$ as function of (effective milling duration)×(tip speed^2) (left) and $6/d_{50}$ as function of (effective milling duration)×(bead filling rtae$^{3.95}$) (right).

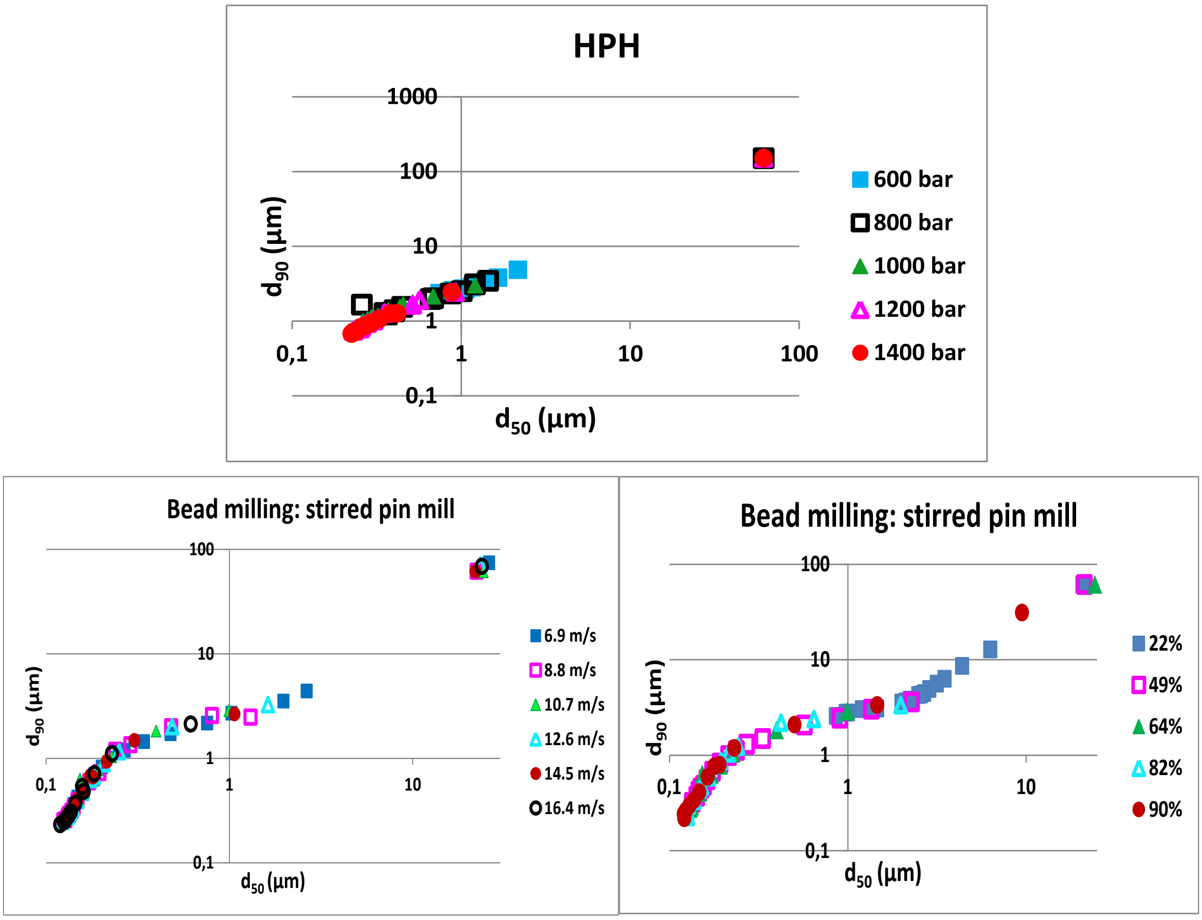

Figure 113 : d_{90} versus d_{50} as function of pressure for HPH (top), of tip speed (bottom left) and of bead filling rtae (bottom right) for bead mill.

5.2.2.1.2.2. Impact of milling process configuration

The process configuration consists of suspension manufacturing in batch mode or recycling mode trough an external vessel. This evaluation was assessed only for bead milling. It was carried out using a kinetic experiment by comparing Nano-mill® for batch mode and stirred disc mill (Dynomill®) for recycling mode. The assessment was performed using suspension of 20 % of API A and 1.2 of SDS/PVP as wetting/dispersant agent. For both mills the rotation speed and the bead filling rtae were fixed at 10.7 m/s and 64 % v/v, respectively.

The main conclusions of this assessment are the following:

(i) If the milling kinetics are plotted versus the real milling time the batch mode is faster than the recirculation mode. However, if they are plotted versus effective milling time the batch mode and recirculation mode are equivalent (see Figure 114). This suggests that the effective milling duration is one of the invariant parameters to be considered in bead milling process;

(ii) The relationship of d_{90} versus d_{50} from both mills is described by a unique master curve (Figure 115) suggesting that the milling process configuration does not have any impact on the particle size distribution profile

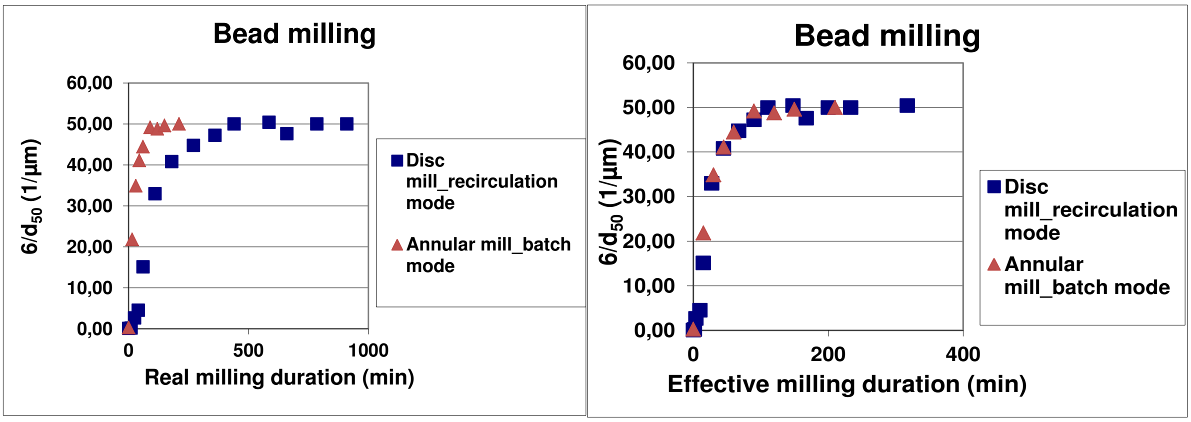

Figure 114 : Milling kinetics comparison using batch and recirculation modes.

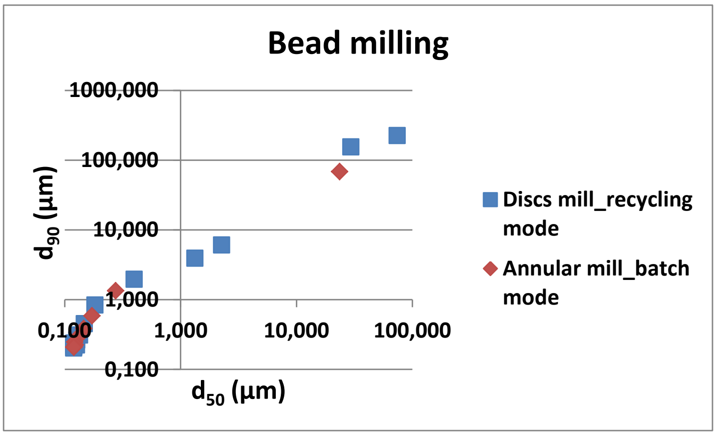

Figure 115 : d_{90} versus d_{50} from batch and recirculation modes.

5.2.2.1.2.3. Impact of manufactured batch size

The evaluation of the batch size using both technologies (high pressure homogenization and stirred bead milling) was also carried out using a kinetic experiment. The evaluation was performed using NS3024 equipment for HPH at 1400 bar and Labstar® for bead mill at 10.8 m/s and 64 % of bead filling rtae. For the high pressure homogenization, 2 batches were manufactured at 15 and 60 litres using suspension having 20 % (w/w) of API A and 1.2 % of SDS/PVP as wetting/dispersant agent. For the bead milling 3 batches were manufactured at 0.58, 1.16 and 1.78 litres, respectively using the same suspension composition as for the HPH.

As shown in the Figure 116 and Figure 117, for both technologies, when the milling kinetics are plotted as function of milling duration, the batch size has a significant impact on the milling kinetic. More precisely, the higher is the batch size, the slower is the milling kinetic. However, when the milling kinetics are graphed as function of recycling number for the HPH and effective milling duration for bead milling, the milling kinetics are described by 1 master curve for each technology. This suggests that the recycling number for the HPH and the effective milling duration for bead milling are the invariant parameters when the batch size needs to be changed.

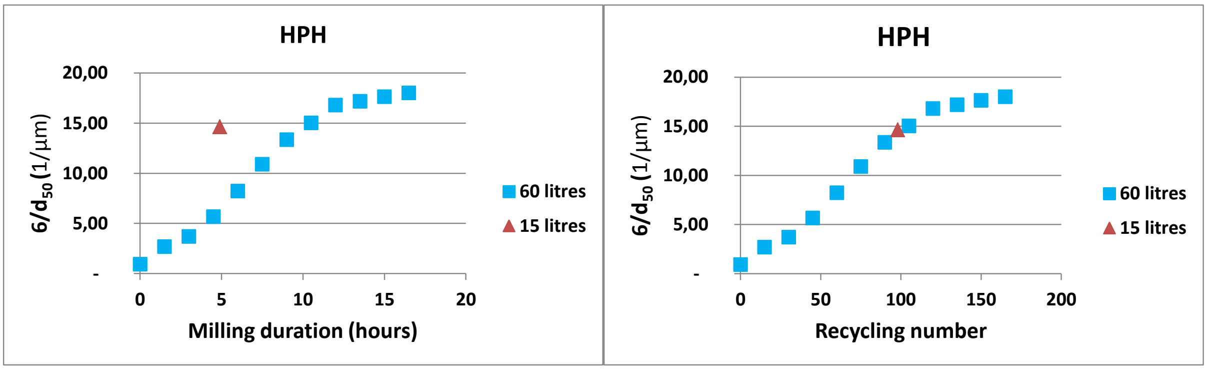

Figure 116: HPH milling kinetic for different batch size as function of milling duration (left) and recycling number (right).

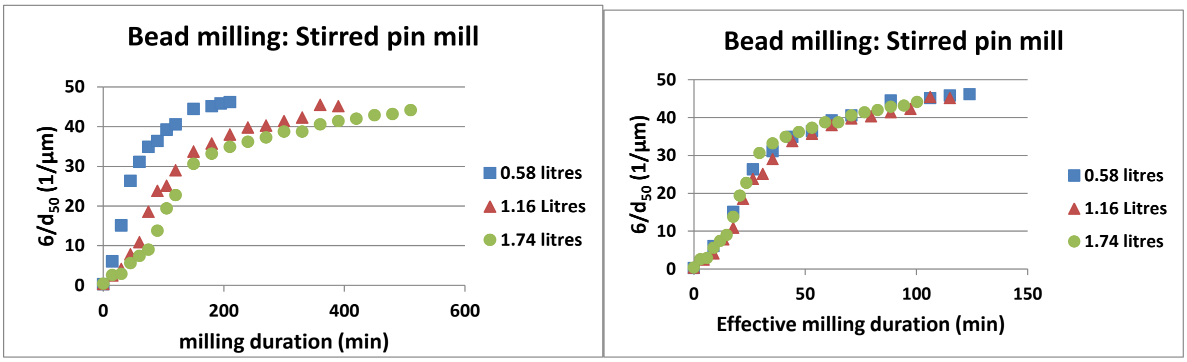

Figure 117: Bead milling kinetic for different batch size as function of milling duration (left) and effective milling duration (right).

It is worth to notice that the recycling number is not relevant parameter for bead milling. Indeed, the impact of the flow rate in bead milling was evaluated using a Labstar® mill at 10.8 m/s and 64 % of bead filling rtae. The milling flow rate was varied from 6.1 to 25.5 litres/hours using suspension having 20 % (w/w) of API A and 1.2 % of SDS/PVP as wetting/dispersant agent. The obtained results showed (see Figure 118) that when the milling kinetics are graphed as function of recycling number, the milling flow rate has a significant impact on the milling kinetic. That it is, the higher is milling flow rate, the slower is the milling kinetic. However, when the milling kinetics are plotted as function of milling time, the milling kinetics are described by one master curve. This suggests that the milling flow rate for bead milling does not have any impact on bead milling kinetic.

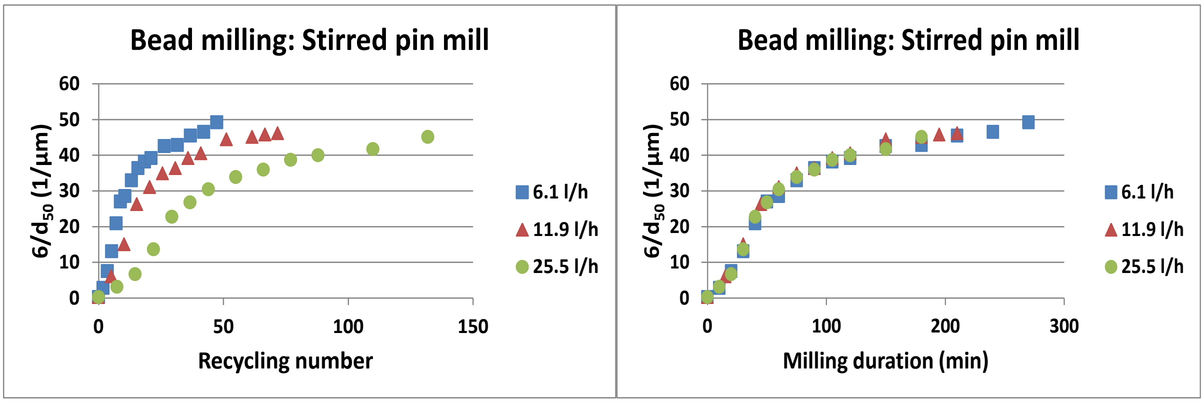

Figure 118: Bead milling kinetic for different flow rate as function of recycling number (left) and milling duration (right).

5.2.2.1.3. Impact of milling equipment

As illustrated in Ishikawa diagram (Figure 86) the impact of milling equipment was evaluated in terms of influence of milling media, mill configuration, mill scale, mechanical robustness and proneness of mill to wearing

5.2.2.1.3.1. Impact of milling media

Two aspects of milling media were assessed: Geometrical configuration and milling media material

5.2.2.1.3.1.1. Impact of geometrical configuration

The evaluation of geometrical configuration using both technologies (high pressure homogenization and stirred bead milling) was carried out using a kinetic experiment. The evaluation was performed using NS2006 equipment for HPH at 1400 bar and Nanomill® for bead mill at 10.8 m/s and 64 % of bead filling rtae. For the high pressure homogenization, three geometrical configurations of high pressure homogenization chamber (made from silicon Nitride) were used by varying the difference between the outlet and inlet diameter (D_2-

D_1; see Figure 51). For the bead mill two diameters of Polystyrene beads were used: 200 and 500 µm.

The results of this evaluation showed that:

(i) For HPH, the lower is the difference between the outlet and inlet diameter (D_2-D_1) of the chamber, the faster is the milling kinetic (see Figure 119). This can be explained by the hydrodynamic calculation (see section 2.4.6) which reveals that the slowing down of the milling kinetic induced by the increase of D_2-D_1 from (0.7 to 6 mm) is due to increase of the gap of the HPH valve (from 3.2 to 6.7 µm) and therefore to decrease of several parameters (within the gap of the HPH chamber): mean velocity (from 103 to 57 m/s), power density (9.4×10^{7} to 1.4×10^{7} w/m3) and shear rate (from 3.2×10^{7} to 8.5×10^{6});

ii) For bead mill, we did not found any significant impact of beads size on the milling kinetic profile by using Polystyrene material (see Figure 119). However, it is reported in the literature that using Zirconium Oxide the beads size has a significant impact on the milling kinetic profile. That it is, the lower is the beads size, the faster is the milling kinetic (206). This can be explained by the fact that when beads size is small the number of used beads is higher leading to high stress frequency and therefore to high milling energy;

iii) The relationship of d_{90} versus d_{50} from both mills is described by a unique master curve (Figure 120) suggesting that the geometrical configuration of milling media could impact the milling kinetic profile but not the particle size distribution profile.

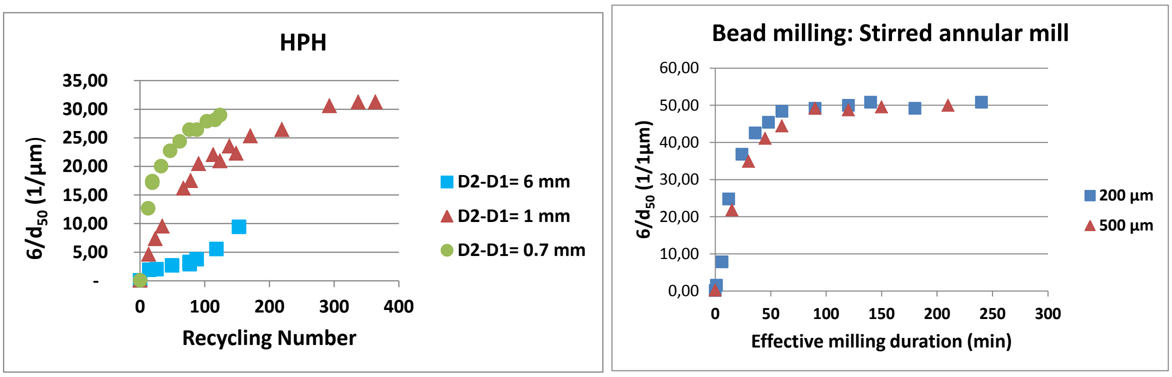

Figure 119: Impact of geometrical configuration of milling media on the milling kinetic of HPH (left) and beds mill (right).

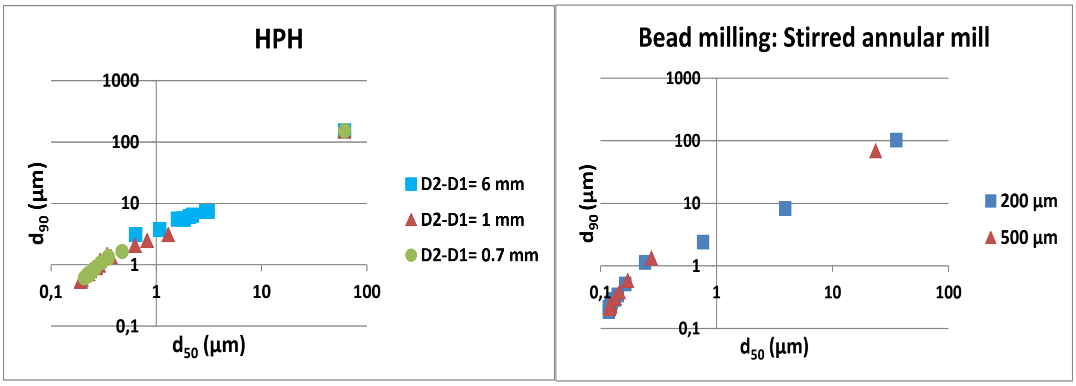

Figure 120: d_{90} versus d_{50} HPH (left) and beds mill (right)

5.2.2.1.3.1.2. Impact of milling media material

The evaluation of the impact of milling media material using both technologies (high pressure homogenization and stirred bead milling) was carried out using a kinetic experiment. The evaluation was performed using NS2006 equipment for HPH at 1400 bar and Nanomill® for bead mill at 10.8 m/s and 64 % of bead filling rtae. For the high pressure homogenization, 3 materials of high pressure homogenization chamber (having D_2-D_1 of 1 mm) were used: Tungsten Carbide, Zirconium oxide and Silicon Nitride). For the bead mill, two beads material (Polystyrene and Zirconium oxide having diameter of 500 µm) were tested.

The main findings of this assessment are summarized below:

(i) For the HPH, despite of mechanical difference between used materials, no significant impact milling media material was observed (see Figure 121). This suggests that the milling within the HPH is mainly driven by the hydrodynamic within the chamber gap which is fixed by D_2-D_1.

(ii) However, for the bead mill, the milling media material impacts dramatically the milling kinetic Figure 122. That it is, the milling kinetic is faster when the Zirconium oxide is used. This can be explained by the high density of zirconium oxide (6.1 g/ml versus 1.1 g/ml) which confers to beads high stress intensity as described by (Eq. 70). Moreover, when $6/d_{50}$ obtained using Polystyrene beads is graphed as a function of reduced effective milling duration (as defined by the (Eq. 125)) and compared to the milling kinetic obtained using Zirconium oxide, only one master curve is obtained (Figure 122) confirming that the material density drives the milling kinetic.

$$\mathbf{t_{eff\_r}} = \mathbf{t_{eff}} \times \frac{\rho_{gm\_PS}}{\rho_{gm\_zr}} \qquad \textbf{(Eq. 125)}$$

Where t_{eff_r} is the reduced effective milling duration, t_{eff} is the effective milling duration, d_{gm_PS} is the polystyrene density and d_{gm_Zr} is the Zirconium oxide density;

(iii) When, using zirconium oxide, further increase of milling time, decreases the implicit specific surface area (see Figure 123). This phenomenon was described in the literature by Jimbo *et al.* (207) and named “negative grinding phenomenon”. It has been explained as follow: the more energy is supplied to the crystals of a limiting size, the further deformation of crystals, energy accumulation within or at the surface of the crystals and subsequently amorphization occurs. However, this phenomenon was not observed with polystyrene beads;

(iv) When d_{90} is graphed as function of d_{50}, no significant impact of milling media material on milling pathway was observed for the case of HPH. However, for the bead mill, the milling media material impacts the milling pathway more precisely when d_{50} is below 1 µm (see Figure 124) suggesting that the milling media material impacts the particle size distribution profile.

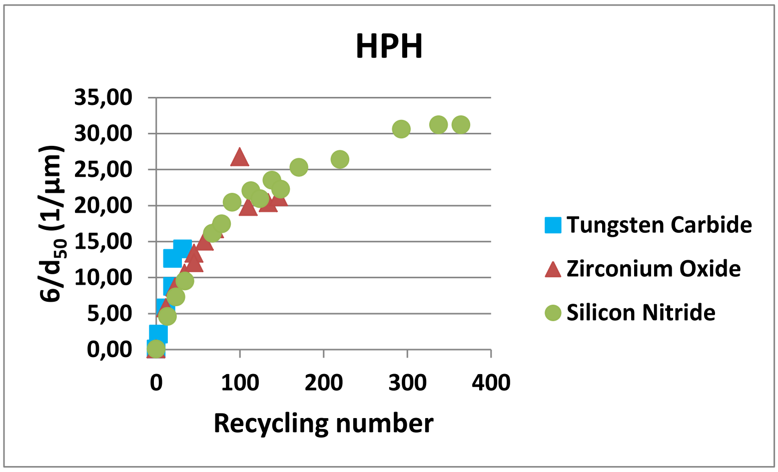

Figure 121 : Impact of milling media material in HPH.

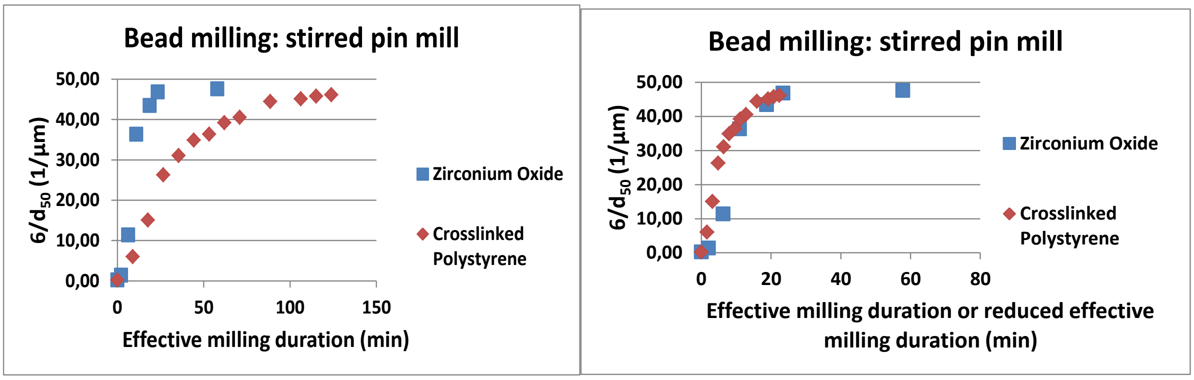

Figure 122 : Impact of milling media material in bead mill right.

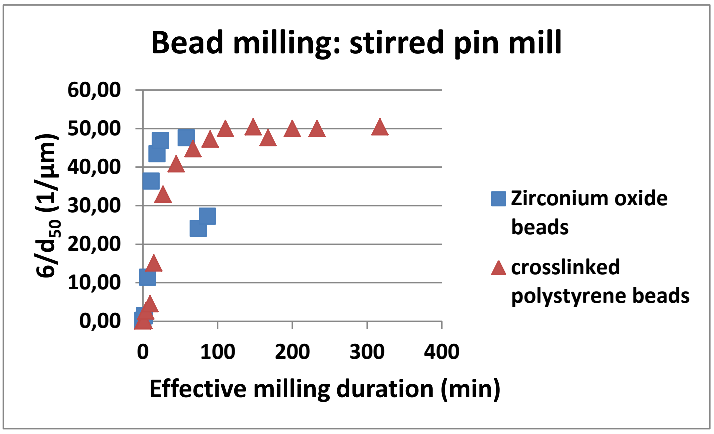

Figure 123 : bead milling kinetic using Zirconium Oxide outlining flocculation or agglomeration.

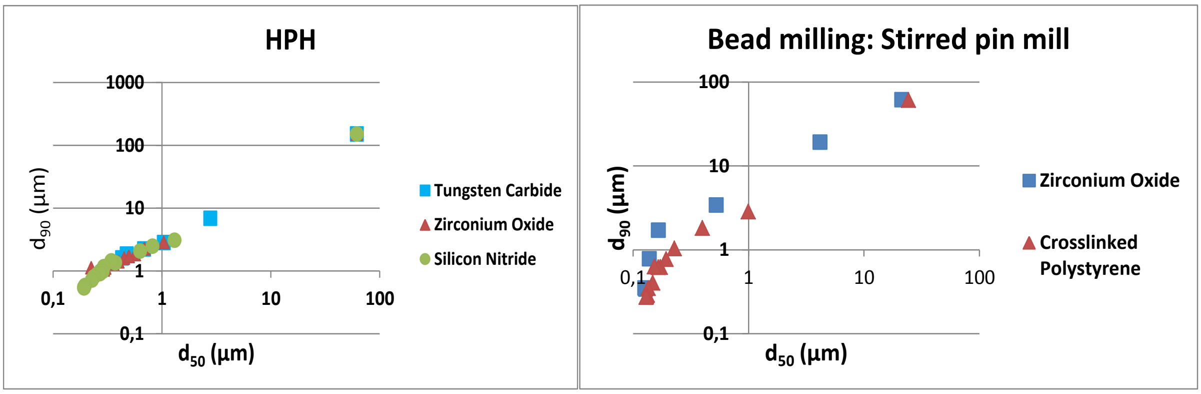

Figure 124 : d_{90} versus d_{50} for HPH and bead mill.

5.2.2.1.3.2. Impact of mill design

The evaluation of the impact of mill design using both technologies (high pressure homogenization and stirred bead milling) was carried out using a kinetic experiment. The evaluation was performed using piston gap technology (NS2006 equipped with Silicon nitride valve having D$_2$-D$_1$ of 1 mm) and Capillary technology (Microfluidics® M110EH) for HPH at 1200 bar. For bead mill stirred annular mill technology (Nanomill®), Stirred disc mill technology (Dynomill®) and stirred pin mill technology (Labstar®) were used at 10.8 m/s and 64 % of bead filling rtae (Polystyrene beads having 500 µm diameter).

The main observations of this evaluation are described below:

(i) For the HPH, even if both equipment are not based on the same hydrodynamic principles, no significant differences are observed between milling kinetics of the both homogenizers for the tested conditions;

(ii) For bead milling, no significant differences are observed between milling kinetics of the three mills for the tested conditions (Figure 125);

(iii) For HPH, capillary and piston gap technology lead to same profile of d_{90} versus d_{50} (Figure 126), suggesting that the mill technology does not have any impact on the particle size distribution profile;

(iv) For the bead mill, stirred disc mill, stirred annular mill and stirred pin lead to same profile of d_{90} versus d_{50} (Figure 126), suggesting that the mill technology does not have any impact on the particle size distribution profile.

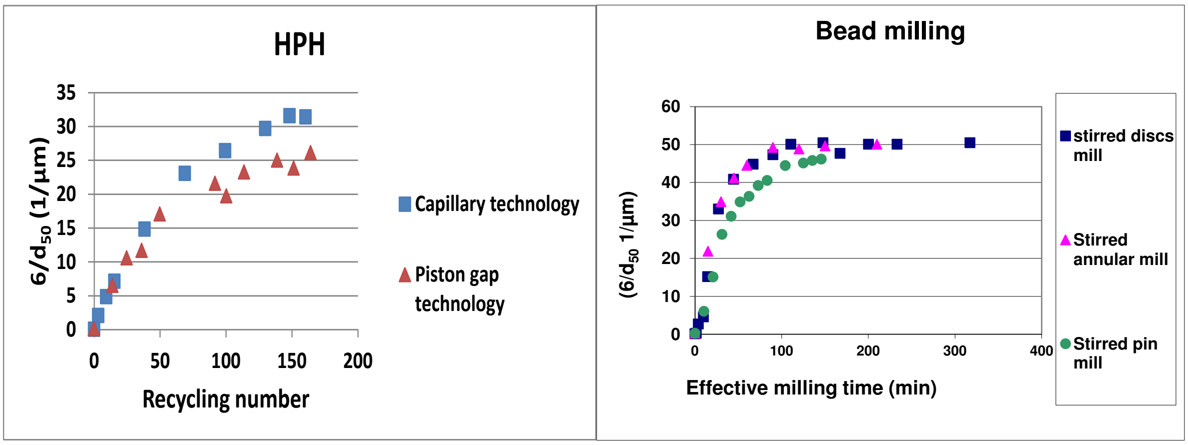

Figure 125: Comparison of milling kinetic of Capillary and piston gap technologies for HPH (left) and of Stirred disc mill, stirred annular mill and stirred pin mill for bead mill.

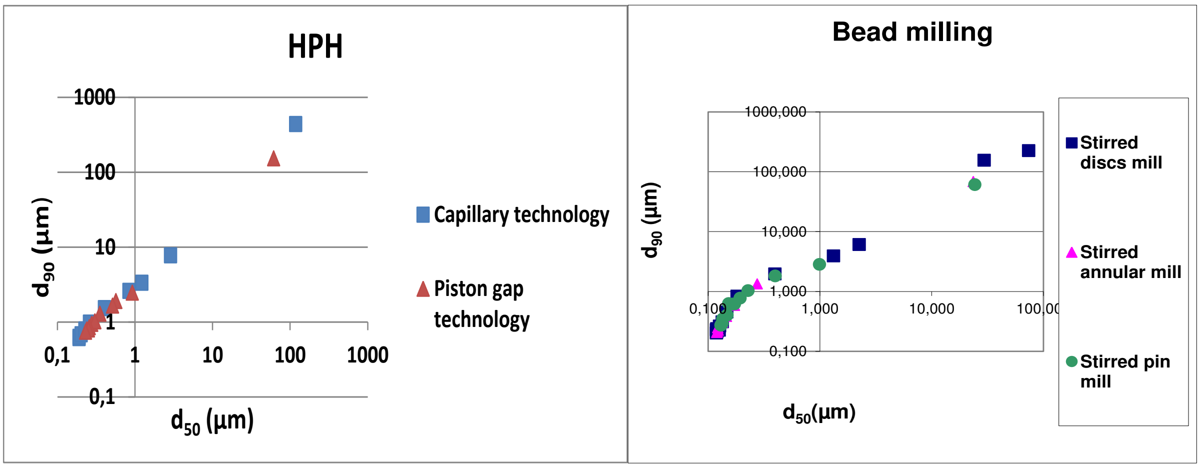

Figure 126: Comparison of d_{90} versus d_{50} of Capillary and piston gap technologies for HPH (left) and of Stirred disc mill, stirred annular mill and stirred pin mill for bead mill.

5.2.2.1.3.3. Impact of mill scale

The evaluation of the impact of mill scale using both technologies (high pressure homogenization and stirred bead milling) was carried out using a kinetic experiment. The evaluation was performed using piston gap technology (Panda, NS2006 and NS3024) equipped with Silicon nitride valves for HPH at 1400 bar. For bead mill, LMZ2® and Labstar® were compared.

The acquired results show that:

(i) For the HPH, no significant difference of milling kinetic profile is observed between the 3 scales (see Figure 127 left). This can be understood from the hydrodynamic calculation stand point which is summarized in Table 14. It outlines that the three scales were operated in laminar regime (Reynolds number < 2000). Moreover, although the average velocity, gap width and time of one recirculation are different, the power density and the shear rate within the gap are not significantly different suggesting that the scaling up rule is to keep the power density and recycling number constant between different scale;

ii) The same profile of d_{90} versus d_{50} (see Figure 127 right) is observed when the 3 scales of HPH are used suggesting that the HPH scale does not have any impact on the particle size distribution profile.

Scale	**Panda**	**NS2006**	**NS3004**
D1 (mm)	6.5	11.2	11.2
D2 (mm)	7	12.2	12.2
Pressure (bar)	1400	1400	1400
Flow rate (l/h)	10	45	300
Batch size (kg)	0.25	2.01	15.00
Reynolds number within the gap	63,2	152	1020
Time of 1 recirculation	90	161	180
Average velocity within the gap (m/s)	52	98	266
Gap width (µm)	2.4	3.3	8.0
Shear rate within the gap (s^{-1})	1.4×10^{8}	1.8×10^{8}	1.9×10^{8}
Power density within the gap w/m^3	1.5×10^{13}	2.5×10^{13}	2.8×10^{13}
ΔPe (bar)	3	11	80
ΔPf (bar)	1375	1314	764
ΔPs (bar)	21	75	556
Cavitation number	1.54	1.54	1.54

Table 14: Hydrodynamic calculation for HPH using different scales.

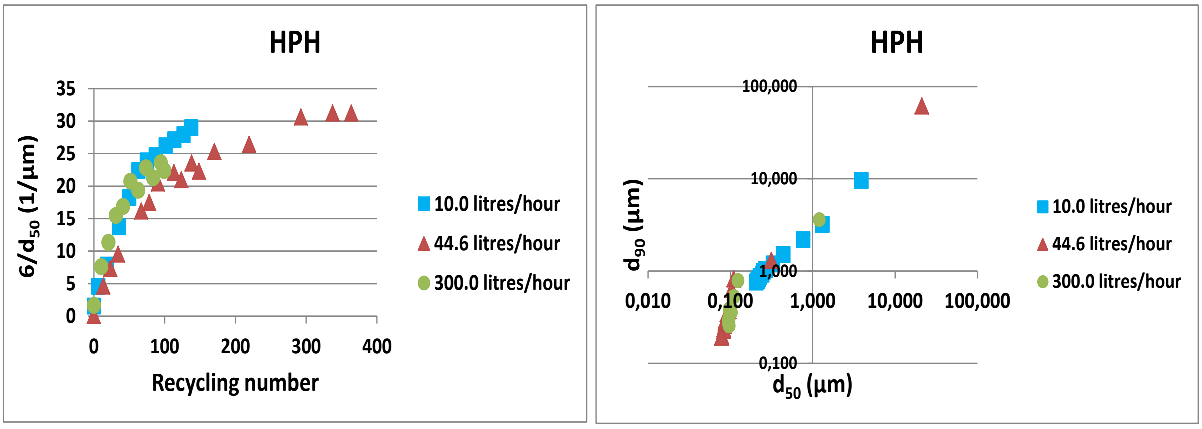

Figure 127 : Impact of equipment scale on milling kinetic for HPH (left) and d_{90} versus d_{50} profile (right).

For the bead mill, the impact of the scale was evaluated by comparing experimental data from LMZ2® and those predicted using Labstar® model (see section 4.2.2.1) for two different milling conditions. It was found that when the same API loading, the same beads material and filling ratio are used, the scale up rule can be established by keeping the same stress intensity or the power density as described by the following equations:

$$\mathbf{N^2 \times D^2 = Cte} \qquad \text{(Eq. 126)}$$

$$\mathbf{\frac{\rho \times N^3 \times D^5}{V} = cte} \qquad \text{(Eq. 127)}$$

Indeed the experimental data are well fitted by simulated data using rotation speed calculated either by keeping stress intensity constant or power density constant (see Figure 128)

The more appropriate rule of scaling-up should be considered as keeping the same stress intensity to generate the same defects and the same particle size reduction.

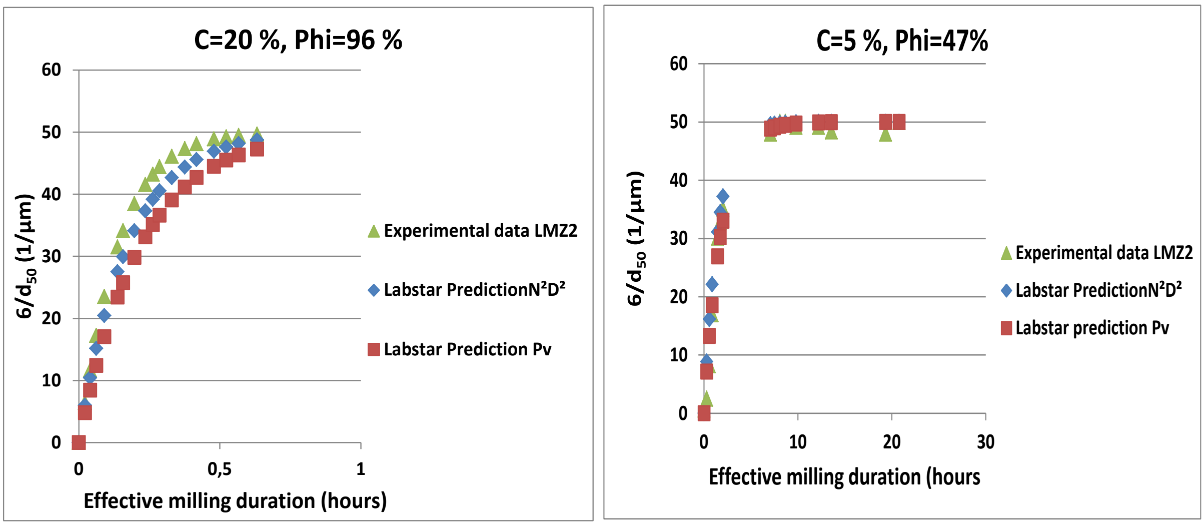

Figure 128 : Impact of bead milling scale by keeping stress intensity or power density constant

5.2.3. Comparison of high pressure homogenization and bead milling

The objective of this comparison is to provide some clue points on the suitability of each technology for pharmaceutical applications mainly for parenteral route where the suspension needs to be persevered from any microbial or foreign particles contamination during processing. For that purpose, the comparison of both technologies (piston gap versus bead mill) was performed based upon the particle size distribution profile generated at the same mean diameter (d_{50}), morphology of the obtained particles, proneness of the technology to wearing and mechanical reliability of the technology.

5.2.3.1. Mean particle size

The comparison of both technologies in terms of particle size was carried out on the basis of manufacturing of 30 litres scale during 12 to 14 hours which correspond to 120 cycles at 1400 bar for HPH and 150 min as effective milling time, respectively for bead milling.

As shown in Figure 129, whatever the processed API, the bead milling leads to a lower d50. As per section 5.2.2.1.1.1, these differences can be explained by either high stress mechanical level that can be generated by bead mill or a low stabilizer adsorption plateau in the case of high pressure homogenization due to high temperature amplitude during milling

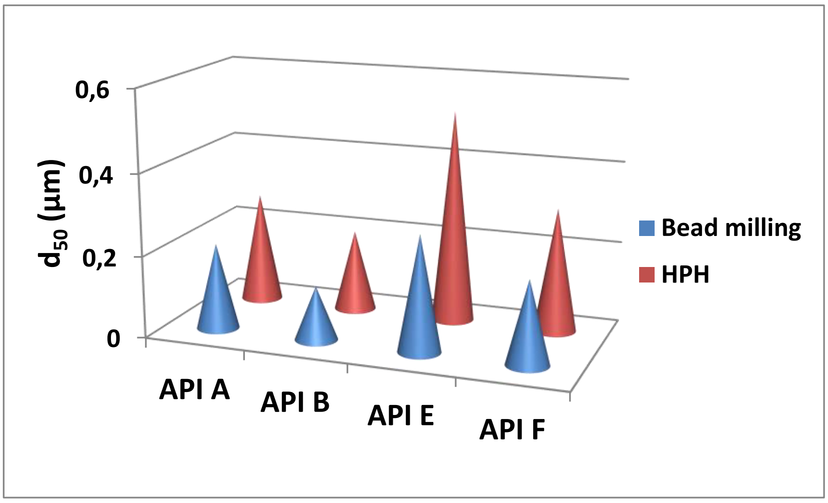

Figure 129 : Comparison of mean diameter obtained by HPH and bead milling.

5.2.3.2. Particle size distribution

For the comparison of the particle size distribution only the API A case study is presented here. The main observations are the following:

(i) The minimum particle size that can be produced by the HPH using the API is around 200 nm;

(ii) At equivalent mean diameter, it can be outlined that 100 % of particles are below 2 µm in the case of HPH, which will not cause any embolism in case of parenteral use. Whereas, in the case of bead milling, particles higher than 5 µm are observed.

Furthermore, in the contrary of bead milling, the particle size distribution generated by HPH is mono-modal which can limit the Ostwald ripening (see Figure 130);

(iii) Even if bead mill is able to produce finer particles, the % of 2 µm particle in the manufactured suspension is high when it compared to HPH (see Figure 131);

(iv) In order to show the same benefit as the HPH, the bead milling time needs to be extended to go down to 130 nm (see Figure 132).

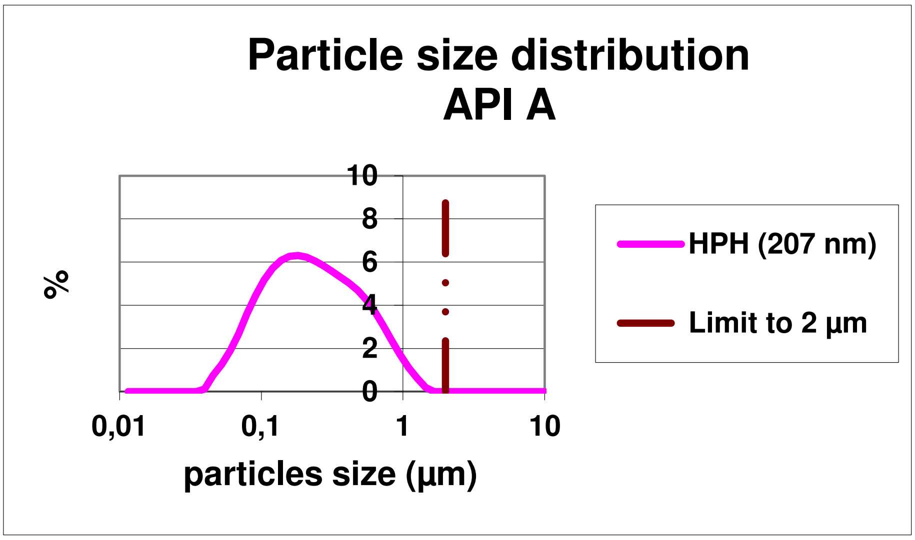

Figure 130 : Comparison of particle size distribution from HPH and bead milling with average diameter of 190-200 nm.

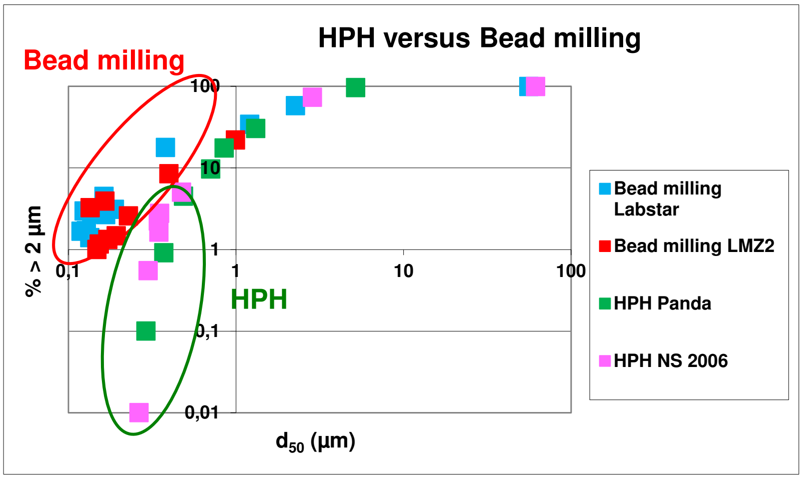

Figure 131 : Comparison of 2 µm % as function of d_{50} for HPH and bead milling.

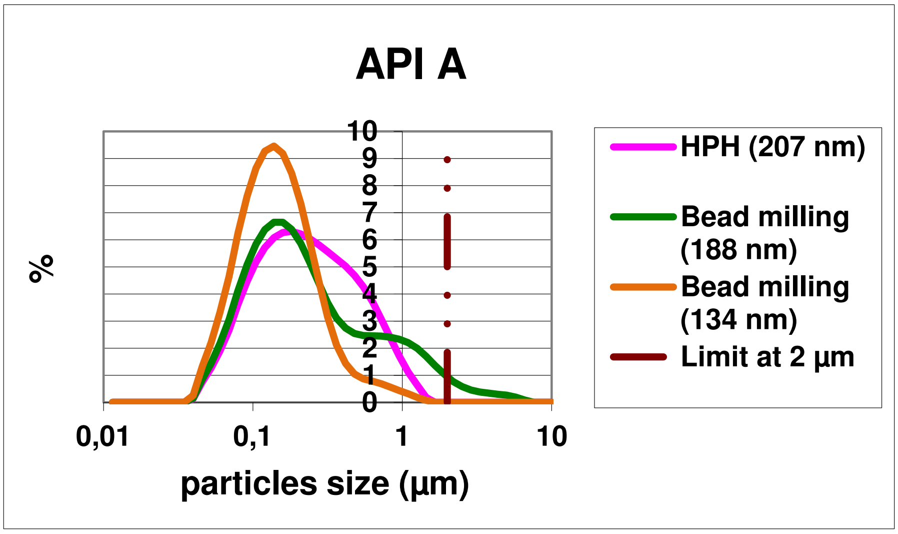

Figure 132 : Comparison of particle size distribution from HPH and bead mill with average diameters of 190-200 and 130 nm

5.2.3.3. Narrowing of the particle size distribution

The narrowing of the particle size distribution was evaluated by comparing at once the profiles of d_{90} vs d_{50} and the polydispersity index of suspensions produced by both technologies.

The main findings are the following:

(i) For both technologies, whatever mill configuration used, mill scale and milling process parameters, the d_{90} versus d_{50} profiles are described by one master curve for each technology (see Figure 133). This suggests that mill configuration, mill scale, milling process parameters have an impact on the milling kinetic profiles but not on the particle size distribution;

(ii) The comparison of d_{90} versus d_{50} from the HPH to that of bead mill leads to a different curve (technology signature) outlining that at the same mean diameter (d_{50}) the HPH generates a narrowed particle size distribution (see Figure 134). Indeed, the d_{90} of 1.5 µm is obtained with HPH when the d_{50} is around 0.5 µm, whereas, the bead mill needs to go down to d_{50} of 0.2 µm to get d_{90} of 1.5 µm. In addition, it can be seen that for the HPH the d_{90} is always between twice and five times the d_{50}. Whereas, in the case of bead milling, when d_{50} is higher than 180 nm the d_{90} is always between five and ten times the d_{50}. Below 200 nm, the d_{90} is between twice and five times the d_{50};

(iii) The impact of mill scales on polydispersity index is not significant. However, it can be observed that the process parameters impact significantly the polydispersity index (see

Figure 135 and Figure 136). Indeed, the higher is the energy, the faster it is to get Ln-normal particle size distribution;

(iv) The comparison of polydispersity index profiles from the HPH to that of bead mill shows that the two mills behave differently in reaching Ln-normal particle size distribution (see Figure 137).

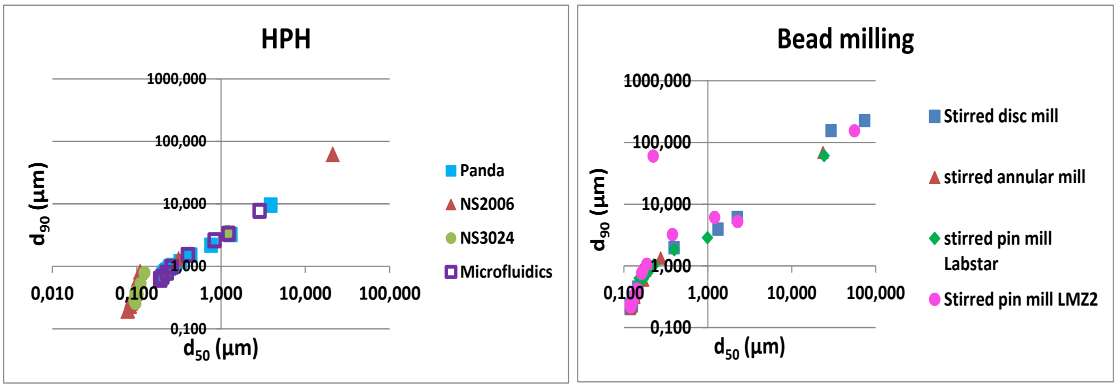

Figure 133: d_{90} versus d_{50} for HPH (left) and bead milling (right).

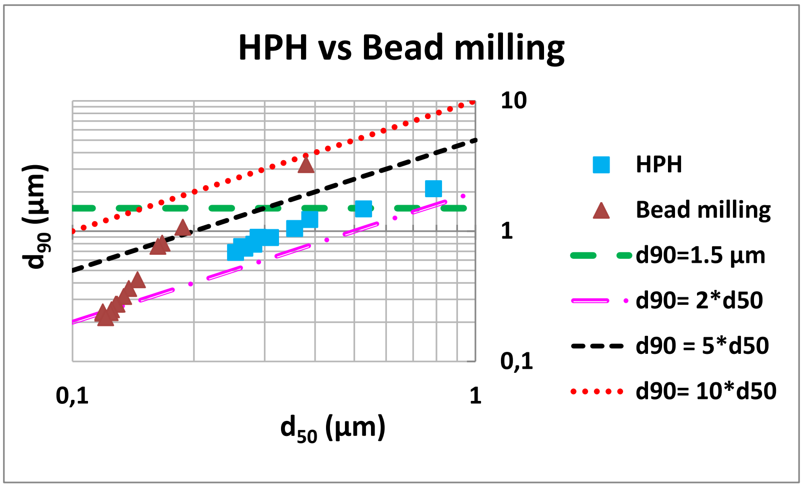

Figure 134: comparison of d_{90} versus d_{50} profiles of HPH and bead milling.

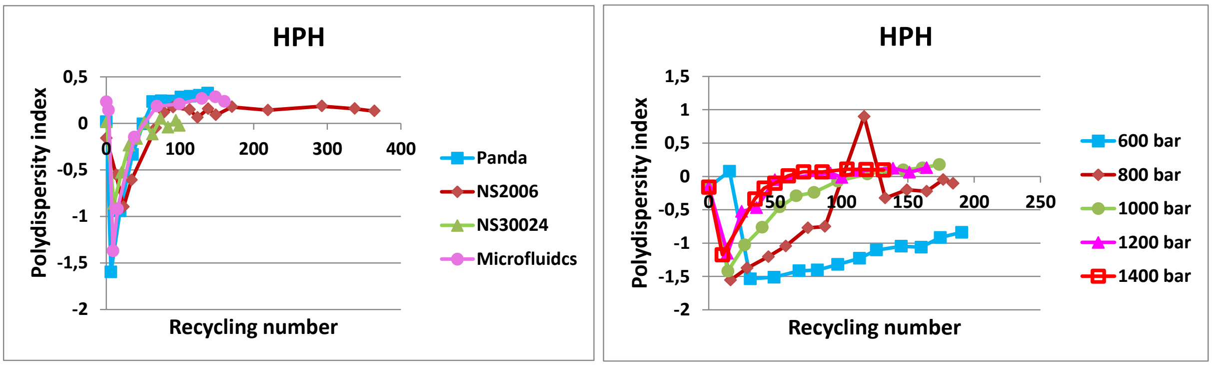

Figure 135: impact of HPH scales and process parameters on polydispersity index.

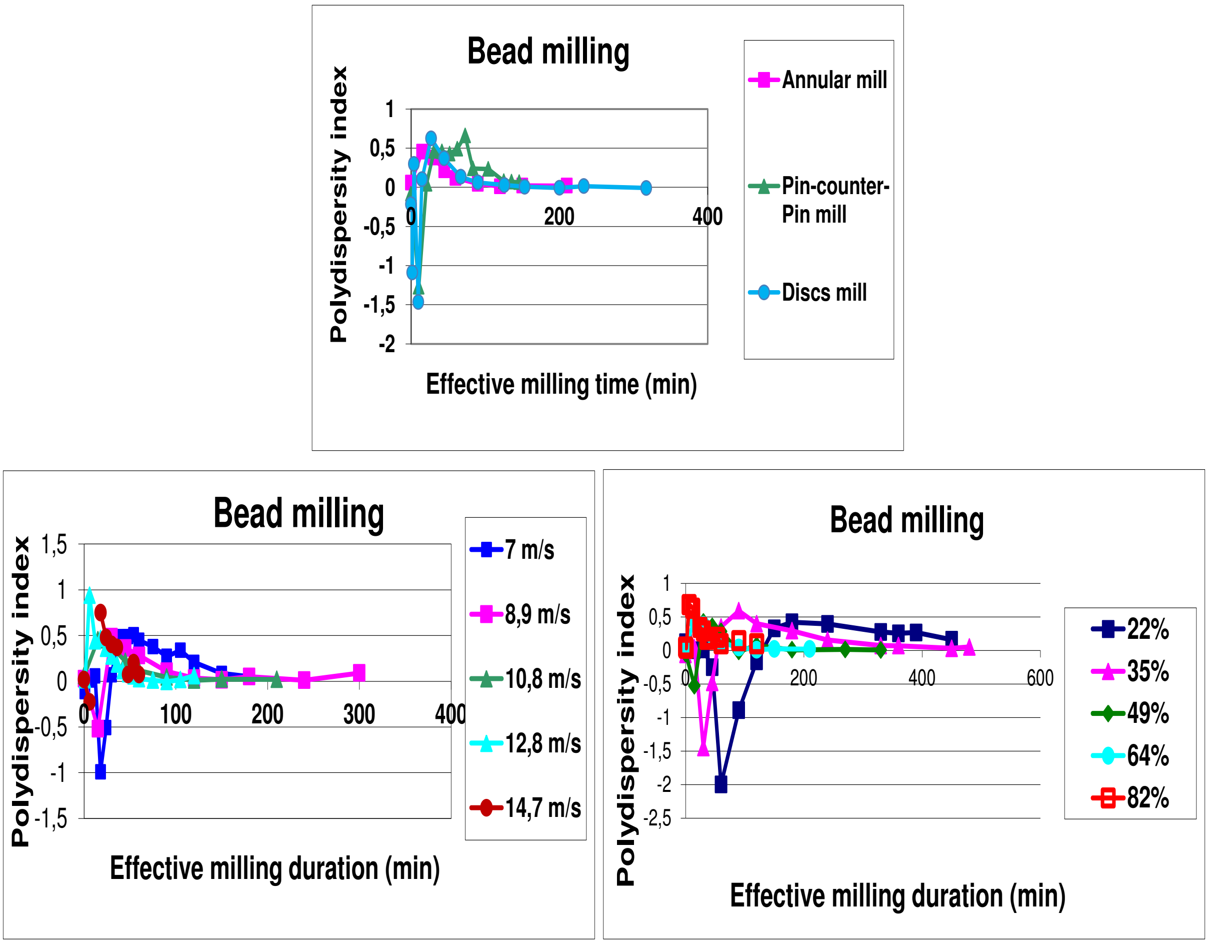

Figure 136: impact of bead mill scales (top) and process parameters: tip speed (bottom left), bead filling rate (bottom right) on polydispersity index.

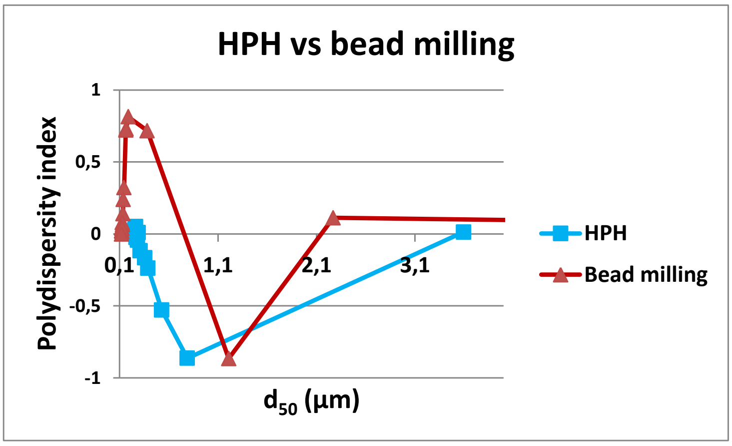

Figure 137: comparison of polydispersity index profiles of HPH and bead mill.

5.2.3.4. Crystal structure

XRPD was used to characterize the crystal structure before and after milling of suspensions obtained using both technologies. The aim of this characterization is to check whether a new phase was generated due to milling by looking for some extra or missing XRPD lines, to detect the eventual presence of a fraction of amorphous phase and to evaluate if there are any morphological modifications after milling.

The evaluation leads to the following observations for all APIs (2 examples of XRPD are provided in Figure 138 and Figure 139):

(i) No modification was observed in the crystalline form due to milling.

(ii) No significant difference was observed due to the technology;

(iii) Slight broadening of XRPD lines (characteristic of milled material) was noticed but no change in the background general profile. We suppose that milling did not induce any amorphization of the API;

(iv) The XRPD pattern of milled products shows similar preferred orientations. Relative intensity of XRPD lines is comparable between milled API and the simulated isotropic pattern. Hence, milled crystals morphology seems to be almost isotropic (opposite to un-milled API for which very important intensity differences is seen).

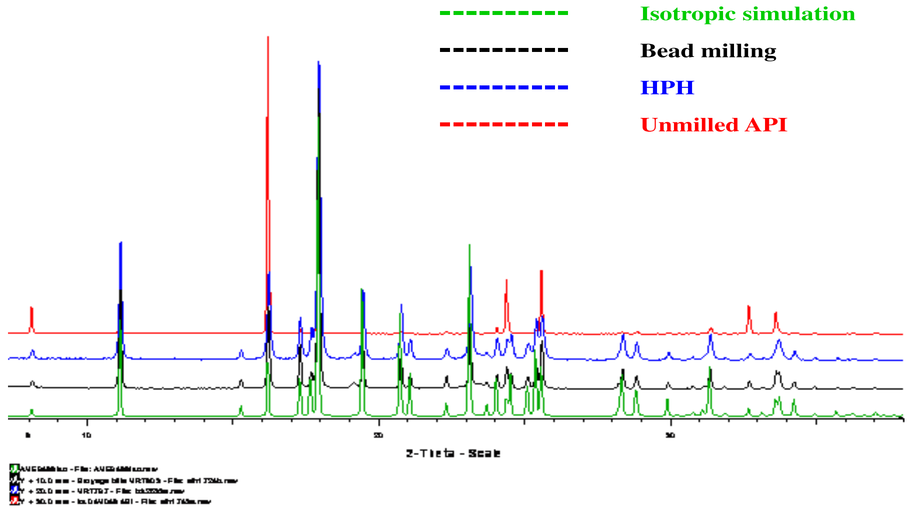

Figure 138: High-resolution XRPD diagram (λ_{Cu} Kα1 = 1,5406 Å) recorded on API E samples at ambient temperature and relative humidity.

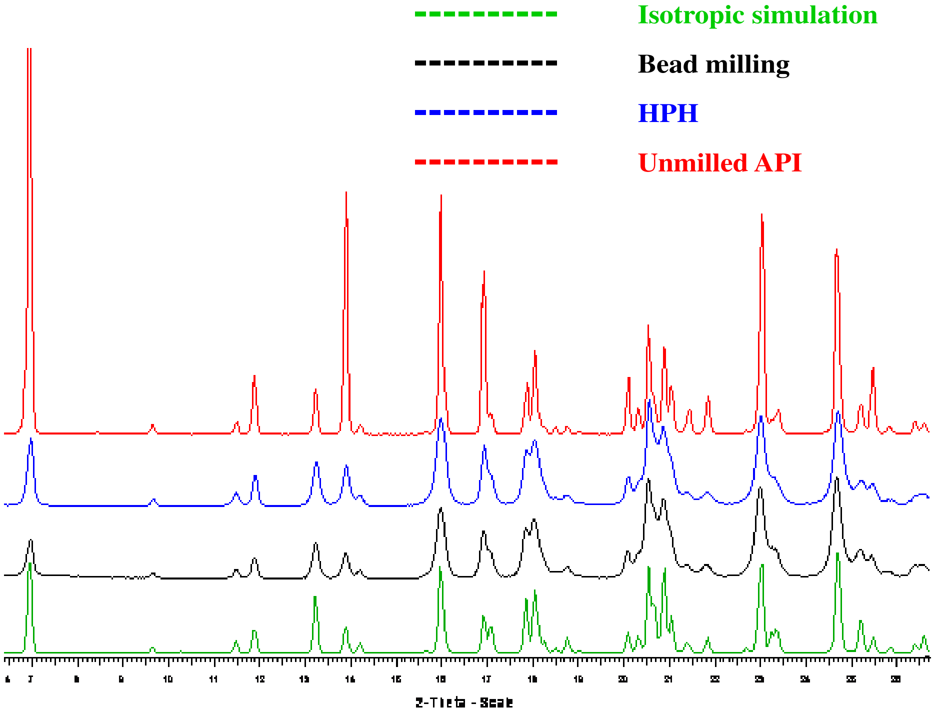

Figure 139: High-resolution XRPD diagram (λ_{Cu} Kα1 = 1,5406 Å) recorded on API A samples at ambient temperature and relative humidity.

5.2.3.5. Particles morphology

The SEM evaluation leads to the following observations:

(i) For the API A, the morphology is significantly impacted by the technology. Indeed, in the case of HPH, the piston gap generated irregular shaped particles (see Figure 140 left) whereas the capillary generated regular shaped particles (see Figure 140 right). In the case of bead mill, the particles have needle shape indicating probably a preferential adsorption of the stabilizer on crystal's faces (see Figure 141). The observed differences may be explained by different 3D distribution of molecular interactions within the crystal, outlining that material fracture preferentially along well-defined cleavage planes may occur when subjected to external stresses that exceed the strength of the crystal across those planes (208);

(ii) For the API F, no significant impact was observed between suspension obtained from HPH and bead mill (see Figure 142). Both technologies generated irregular shaped particle.

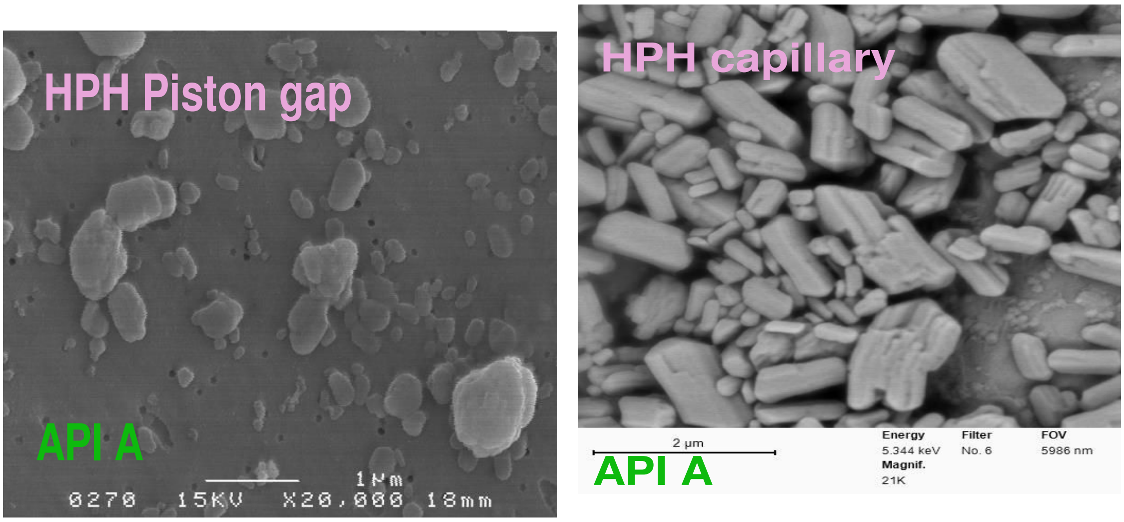

Figure 140: SEM of API A obtained with HPH piston gap (left, d_{50}= 192 nm) and HPH capillary (right, d_{50}= 191 nm).

Figure 141: SEM of API A obtained with bead mill having d_{50}= 125 nm.

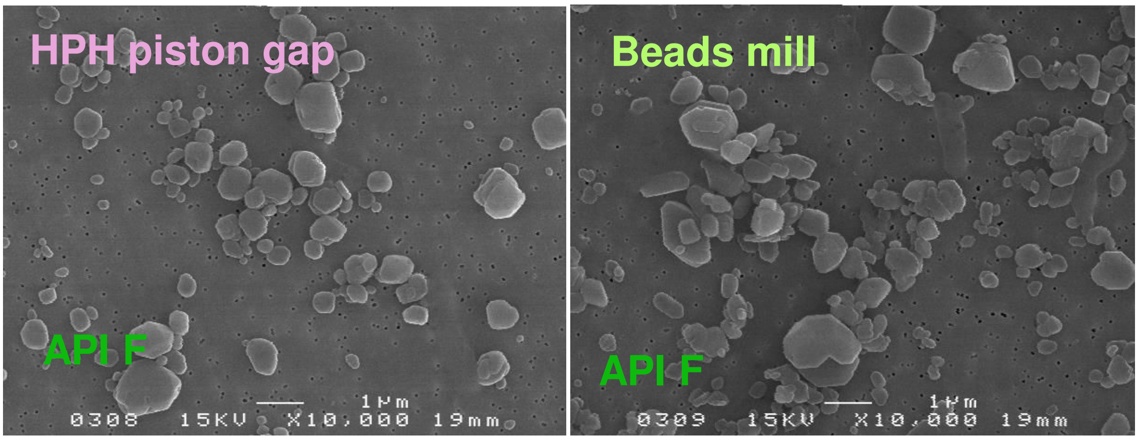

Figure 142: SEM of API F obtained with HPH (left, d_{50}= 465 nm) and bead mill (right, d_{50}= 357 nm).

5.2.3.6. Contaminant content

The contaminant residues from milling media and milling chamber were determined for both technologies (high pressure homogenization and bead milling) using inductively coupled plasma-atomic emission spectroscopy (ICP-AES) for the elements contained in Zirconium oxide, Silicon Nitride and stainless steel. However, the cross-linked polystyrene the contaminant residues were determined by weighing. The results of the analysis are gathered in Table 15 and Table 16. The results show that:

(i) For HPH, whatever the milling media used, no contaminant residues were found. Indeed, the chemical elements contents were found below the limit of quantification;

(ii) For the bead mill case, when cross-linked polystyrene beads are used, no contaminant residues were found including from cross-linked polystyrene itself where it content was found below 5 ppm. However, when Zirconium Oxide is used, the contaminant residue from Stainless steel (Tungsten and Iron) and Zirconium Oxide (Zirconium) level was found very high. This could be an impediment for any application in the pharmaceutical industry.

Suspension Sample	Al (ppm)	Cr (ppm)	Fe (ppm)	Ni (ppm)	Si (ppm)	Ti (ppm)	W (ppm)	Y (ppm)	Zr (ppm)
unmilled material	< 3	< 3	< 3	< 3	25	< 3	< 3	< 3	< 3
Milled using HPH ZrO_2	< 3	< 3	< 3	< 3	30	< 3	< 3	< 3	< 3
Milled using HPH Si_3N_4	< 3	< 3	< 3	< 3	20	< 3	< 3	< 3	< 3

Table 15: Contaminant residues from HPH.

Suspension Sample	Al (ppm)	Cr (ppm)	Fe (ppm)	Ni (ppm)	Si (ppm)	Ti (ppm)	W (ppm)	Y (ppm)	Zr (ppm)
Unmilled material	< 3	< 3	< 3	< 3	25	< 3	< 3	< 3	< 3
Milled using polystyrene beads	5	< 3	< 3	< 3	25	< 3	< 3	< 3	< 3
Milled using $Zr0_2$ beads	25	25	40	5	35	5	100	45	500

Table 16: Contaminant residues from bead mill.

5.2.3.7. Equipment robustness

Both equipment, were found to be reliable and robust. Nevertheless, the risk to lose a batch (leakage or clogging) during processing is not negligible and needs to be mitigated. For that purpose, a risk assessment related to the technology (based on the trial feedback, prior know-how and discussion with suppliers) has to be conducted prior to any technology selection

5.2.4. Comparison conclusion

As conclusion, a global comparison is summarized in Table 17. That it is for the reader to take into account all the comparison aspects to select the suitable technology for any pharmaceutical application.

	HPH	**Bead mill**
Milling performances	**Particle size distribution** d_{50} down to 200 nm $d_{90} < 1.5$ µm All particles are below 2 µm Leads to a narrow particle size distribution **Milling kinetic** Required high milling duration **Crystal structure** No amorphisation observed **Particles morphology** API dependent	**Particle size distribution** d_{50} down to 120 nm $d_{90} < 1.5$ µm All particles are below 2 µm Leads to less narrow particle size distribution than HPH for the same d_{50} **Milling kinetic** Required low milling duration **Crystal structure** No amorphisation observed **Particles morphology** API dependent
Experience as production tool	Daily used for food and cosmetic industry Used for oral application in	Daily used in food, painting, mineral and ceramics industries

	pharmaceutical industry	Used for oral and parenteral application in pharmaceutical industry
Technology versatility	Can be used either for nano-crystalline suspension, nano-polymeric particles, emulsion or liposomes	Can be used only for nano-crystalline suspension
Good manufacturing practices compliance	Compliant: residue from milling media are below 3 ppm	Compliant: residue from milling media are negligible if polymeric milling medias are used

Table 17 : global comparison between HPH and bead mill

5.2.5. Discussion

In the following discussion we will compare our findings to those previously published in the literature.

5.2.5.1. Bead milling

Our bibliography review revealed that the bead milling process is well documented for inorganic materials milled using ceramic beads, as there are many articles emphasizing high level of know-how in this field (127,127,202,209,210). However, no data were found on the use of organic materials with cross-linked polystyrene beads as milling media. Comparison of our results to those published in the literature (Table 18) did not show any significant discrepancy in terms of formulation impact on milling performances. In terms of the impact process parameters, a significant difference was observed. The higher density of ceramic beads (2894- 7550 kg/m3) compared to that of cross-linked polystyrene beads (1075 kg/m^3) may result in different layer packing of beads, different motion and different energy diffusion. One can observe that cross-linked polystyrene beads have similar density as the suspension (d=1030 kg/m^3).Consequently, the beads are little prone to separation by centrifugation. Therefore, they are may better mixed with the suspension when compared to using ceramics beads.

In the case of cross-linked polystyrene, when the change in product particle size (d_{50}) is plotted as function of stress number for similar stress intensity, a range of nonlinear curves is observed (see Figure 143), whereas in the case of inorganic materials a linear master curve is observed. This could be due to the fact that, the limit of grinding was reached during milling with polystyrene beads.

	Finding		**Literature**
	Stirred annular mill	**stirred pin mill**	
Stabilizer content	In poor regime the final diameter is proportional to stabilizer content, while in rich regime the final diameter is independent from stabilizer content and milling energy	Not studied	Published data on Naproxen compound where an optimum working range in terms of stabilizer concentration was found (210) is in agreement with our findings.
Stabilizer type	As the formulation is designed in the rich domain no impact on milling kinetic and final diameter.	Not studied.	No publication was found.
Carrier viscosity	No impact on milling kinetic.	Not studied.	Milling kinetic when using stirred disc mill or stirred pin mill depend on viscosity (202). This could be due to the fact that energy transfer may be impacted by fluid displacement. The stress intensity can be defined as following: $SI \propto SI_{gm} = r_{\eta} \times d_{gm}^{3} \times \rho_{gm} \times v_{t}^{2}$ where r_{η} can be defined as the energy transfer coefficient due to viscosity
API loading	No impact	The higher is the API loading the slower is the milling kinetic	No publication was found for the stirred annular mill. For the stirred pin mill, our results are in agreement with published data. Higher

			solids concentrations negatively affect the grinding results because of higher Viscosity (202)
Rotation speed (N) and Bead filling rtae (Φ_{gm})	Time to reach a certain fineness is proportional to $(N)^{1.75}$ at constant bead filling rtae. Time to reach a certain fineness is proportional to $(\phi_{gm})^{2.4}$ or to $(\frac{\phi_{gm}\times(1-\varepsilon)}{\left(1-\phi_{gm}\times(1-\varepsilon)\right)})^{1.73}$ at constant rotation speed.	Time to reach a certain fineness is proportional to $(N)^{1.95}$ at constant bead filling rtae. Time to reach a certain fineness is proportional to $(\phi_{gm})^{3.95}$ or to $(\frac{\phi_{gm}\times(1-\varepsilon)}{\left(1-\phi_{gm}\times(1-\varepsilon)\right)})^{2.76}$ at constant rotation speed.	The product fineness is driven by the milling specific energy, which is proportional to $(SI \times SN)$ (127)
Flow rate	Not applicable as the mill can be used only on batch mode.	No impact observed.	No impact on milling performances. Only impact on functioning. High flow rate leads to inhomogeneous media distribution over the length of the milling chamber (211).
Bead diameter	No impact is observed in the range of 200-500 µm using crosslinked Polystyrene	Not studied	The lower the beads size the higher the stress frequency and faster is the milling kinetic (206).
Beads material	Not studied.	Impact of material density.	Consistent with published data (206)
Scaling-up	Not studied.	If the bead filling rtae and the formulation are constant, $N^2 \times D^2$ needs to be constant.	The specific energy is the invariant parameter in milling process (211).

Table 18 : Comparison of bead milling results to those published in the literature.

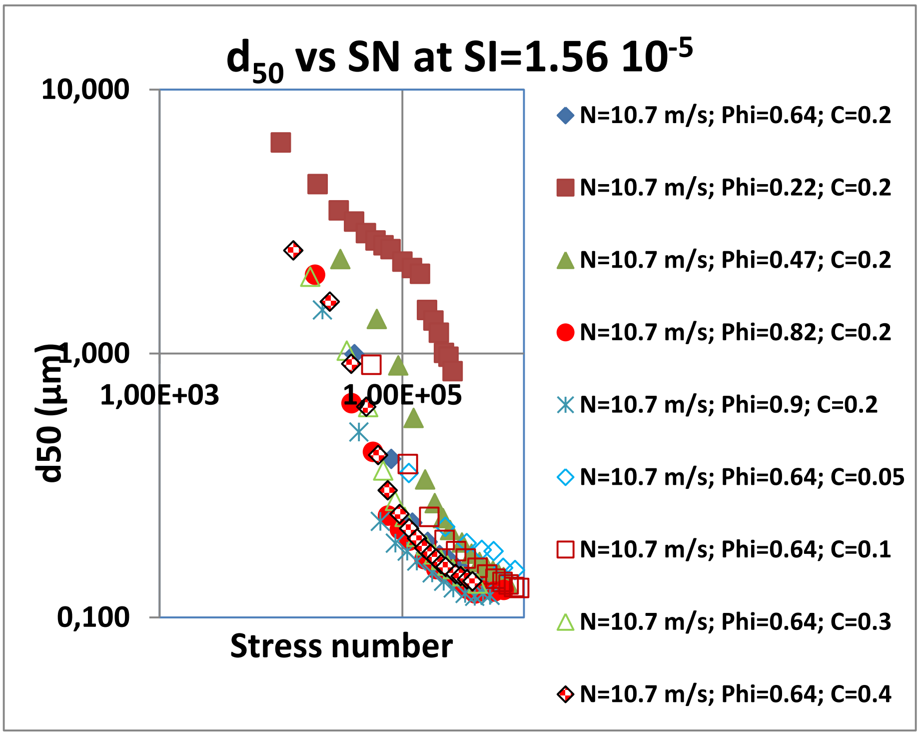

Figure 143 : d_{50} as function of stress number for constant stress intensity (Labstar study).

5.2.5.2. High pressure homogenization

In the case of the HPH, although many articles in the literature are dedicated to parametric study for emulsion manufacturing, only few articles about milling of suspension were found. Furthermore, these articles focused on the formulation aspect and they not discuss manufacturing process aspects (47,212–216). Our main findings were summarized in Table 19.

	HPH	**Literature**
Stabilizer content	In poor regime : final diameter~ stabilizer content In rich regime: final diameter is independent from stabilizer content Increase of energy does not change the final diameter	No published data was found for nano-suspension. For emulsion it was published that in poor regime the final diameter is proportional to stabilizer content, while in rich regime, the final diameter is proportional to $(\text{pressure})^{0.6\text{-}0.9}$
Stabilizer type	As the formulation is designed in the rich domain no impact on the milling kinetic and the final diameter	No published data was found
Carrier viscosity	Gap length$\sim\eta^{-0,33}$ Shear rate$\sim\eta^{-0,7}$ Power density$\sim\eta^{-0,33}$ Milling kinetic$\sim \eta^{0,33}$	No published data was found
Pressure	Gap length $\sim\text{Pressure}^{-0,49}$ Shear rate$\sim\text{Pressure}^{0,6}$ Power density$\sim\text{Pressure}^{1,23}$ Milling kinetic$\sim P^{2,6}$	No published data was found
Valve material	No impact	No published data was found
Valve geometry	Gap length $\sim(D_2\text{-}D_1)^{-0,35}$ Shera rate$\sim(D_2\text{-}D_1)^{-0.89}$ Power density$\sim(D_2\text{-}D_1)^{-1.76}$	No published data was found
Scaling-up	Power density is the invariant parameter in milling process	No published data was found

Table 19: Comparison of HPH results to those published in the literature.

Process modeling and simulation

5.3. Bead milling Process modeling

Nowadays, the general strategy (‘fast-to-patient’) in the pharmaceutical industry is to test a new API in a target patient population as quickly as possible. During the product design stage, the milling process needs to be developed using miniaturized equipment that can allow the use of small amount of API. Furthermore, a typical value chain used from support to candidate selection up to phase III clinical supplies can involve different mill configurations. As an example, this value chain can be composed of the following equipment (see photo 8):

(i) Planetary mill: The Planetary mill can process few mg of API which can be used for support to candidate selection and formulation screening;

(ii) Stirred annular mill (nanomill®): it can process 1-15 g of API according the desirable API loading. This mill can be used for process development and manufacturing of batches for pharmaco-kinetic and toxicological evaluation;

(iii) Stirred pin mill (Labstar®): it can process 10-150 g of API according the desirable API loading. This mill can be used for Process development fine tuning and robustness, and also for production of good laboratory practices batches for toxicology evaluation;

(iv) Stirred pin mill (LMZ2®): it can process 60-1200 g of API according the desirable API loading. This mill can be used for the production of technical and batches for clinical evaluation.

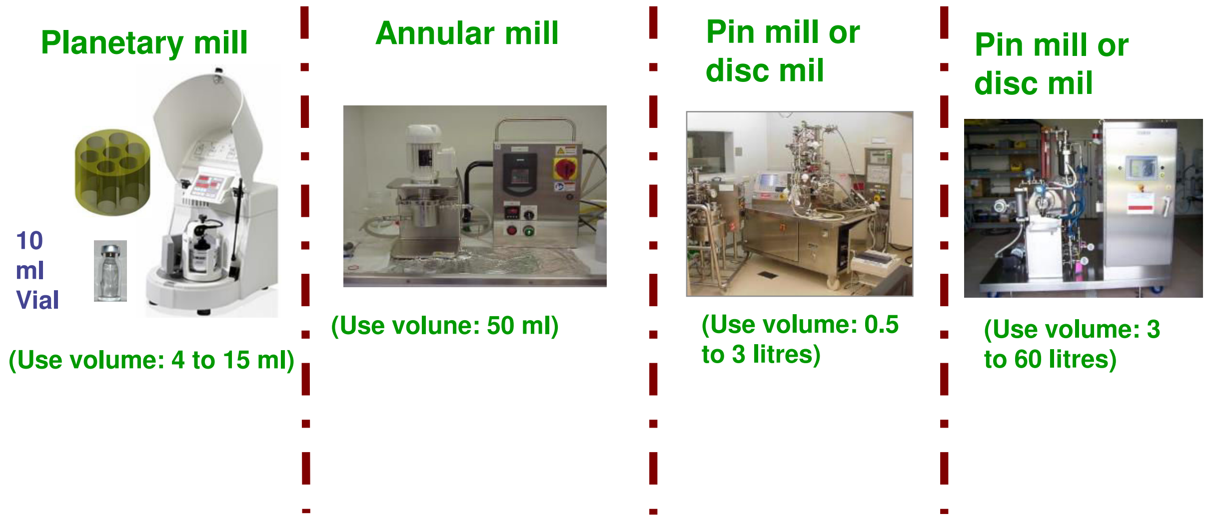

photo 8 : Example of bead mill value chain that can be implemented in research and development

When using this value chain, in order to guarantee the suspension quality, it is important to reproduce the physical quality of suspension from small scale to the large scale. For this purpose, modelling of the milling process can allow switching from one equipment to another by limiting the API consumption. Thus, the scope of the modelling will be as follows:

(i) To verify that the model can accurately fit the milling kinetic from any API and any technology;

(ii) To model the milling process for Nanomill01® and Labstar® in order to predict and simulate it with any process parameters;

(iii) To define a relationship between models obtained from Nanomill01® and Labstar®;

(iv) To define and predict the scale up rule from Labstar® stirred pin mill to the same mill in LMZ2®.

5.3.1. Modelling methodology

The most widely used model for describing the bead milling process is the kinetic model based on mass-balance equations describing the process in different size intervals. This model has been well described in the literature and has been applied successfully in mill circuit design and simulation (217). The approach uses a statistical analysis of collisions between particles, as well as for the breakage functions of the particles. The design of such model is not suitable for the value chain described above due to the difference in its grinding technologies.

In order to achieve the above objectives, we propose to use the analogue to Avrami's equation described in the section 5.2.1.2.1 as follows:

$$\left(\frac{\mathbf{6}}{\mathbf{d_{50}}}\right)_{(\mathbf{t})} = \left(\frac{\mathbf{6}}{\mathbf{d_{50}}}\right)_{(\infty)}\left(\mathbf{1} - \mathbf{e}^{-\left(\frac{\mathbf{t}}{\boldsymbol{\tau}}\right)^{\mathbf{n}^*}}\right)$$

The milling kinetics experimental data generated in the study described in the section 5.2.2.1 will be represented by the analogue to Avrami equation. The equation parameters $(((6/d_{50})_{(\infty)})$, (τ) and $(n^*))$ will be determined using least square method. Then, a correlation will be built between equation parameters $(((6/d_{50})_{\infty})$, (τ) and $(n^*))$ and milling process parameters. The obtained correlation will be used to reflect the changes of milling kinetics as a function of milling operating parameters.

5.3.2. Impact of the API type on the model parameters

It was found that the model is able to fit accurately all the studied APIs (see Figure 144, Figure 145, Figure 146 and Figure 147). From the fit, the implicit specific surface area $(6/d_{50})_\infty$), characteristic time (τ) and the induction index (n^*) can be determined. The results showed that:

(i) The value of implicit specific surface area $(6/d_{50})_\infty$) is API dependent (see Figure 148 left). It is likely that the $(6/d_{50})_\infty$) is driven by the defects density of the initial particle as described by the following equation

$$\mathbf{\emptyset = \frac{n_d}{V} = \frac{n_d}{n \times V_d} \sim \frac{1}{d^3}} \qquad \textbf{(Eq. 128)}$$

Where, ϕ is the defects density, n_d is number of defects within the initial particle, V is the volume of the initial particle, V_d is the volume of a single defect corresponding to the volume of the final particle and d is the diameter of a single defect corresponding to the diameter of the final particle. It is reported in the literature that the grinding limit is reached because the strength of the particles drastically increases for defect-free particles and the required elastic energy for fracture can no longer be supplied by the grinding media (202);

(ii) The value of induction index outlined 2 categories of APIs (see Figure 148 right): The first category requiring induction time to form cracks and generate defects. This API has an induction index higher than 2 (API E). The second category includes those API not requiring induction time to generate defect and start milling immediately (API A, B, C, D and G). These APIs have induction index in the range of 0.6-1.6. This observation is confirmed when the $(6/d_{50})_{(t)}$ is normalized par $(6/d_{50})_\infty$) and plotted as function of time (see Figure 149). In fact, the graph illustrates the presence these 2 categories of APIs. The tentative interpretation is that the induction index may likely give an indication on the hardness of API.

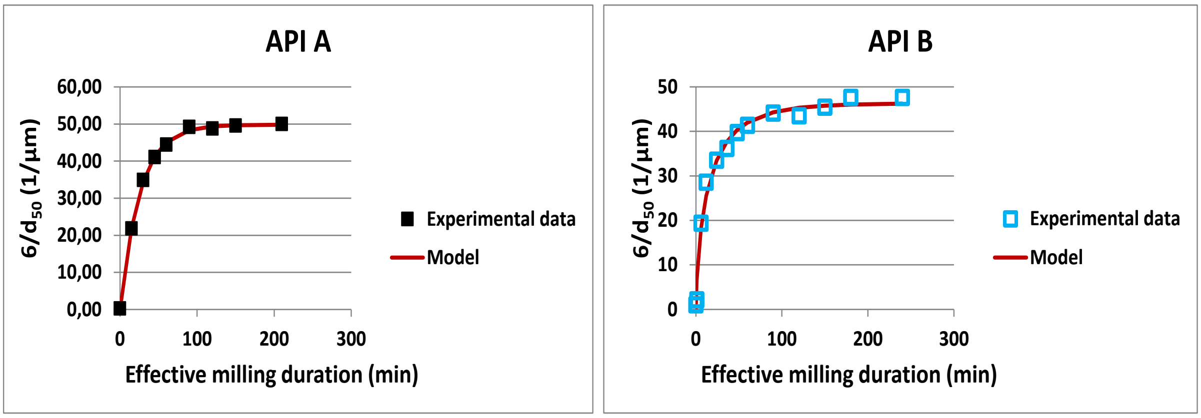

Figure 144: Model fit of milling kinetic from API A (left) and API B (right).

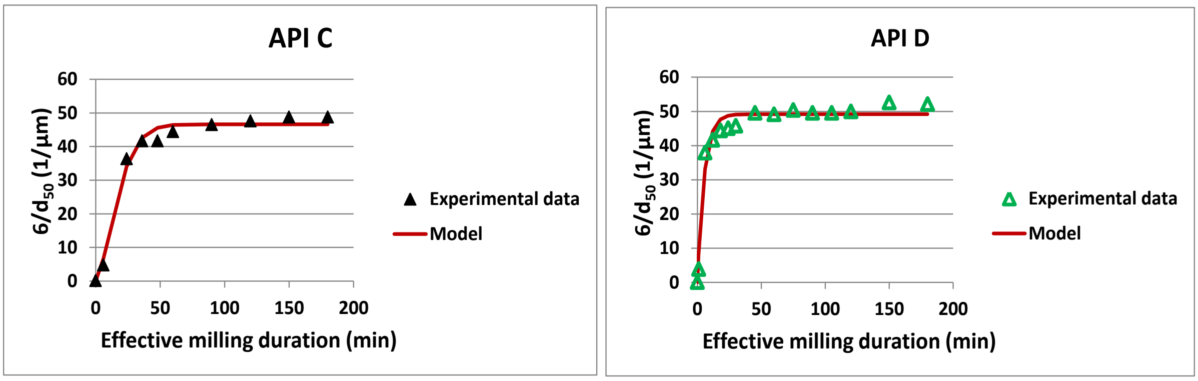

Figure 145: Model fit of milling kinetic from API B (left) and API C (right).

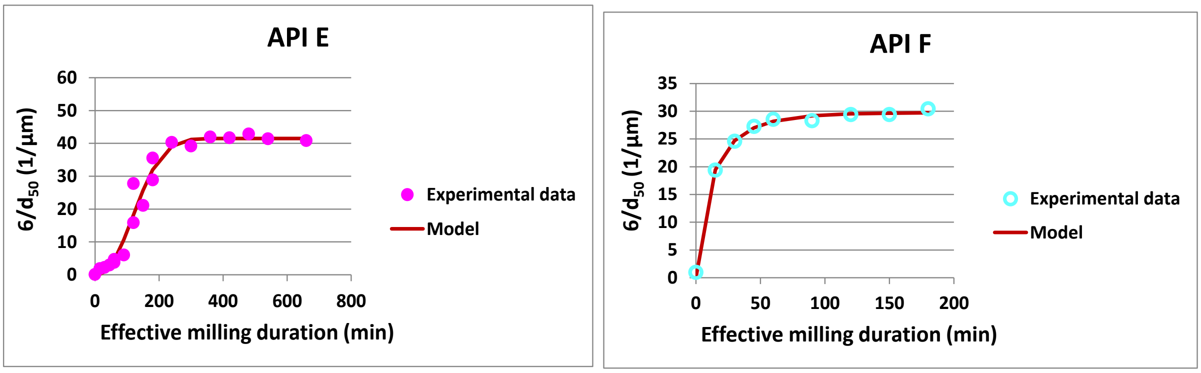

Figure 146: Model fit of milling kinetic from API E (left) and API F (right).

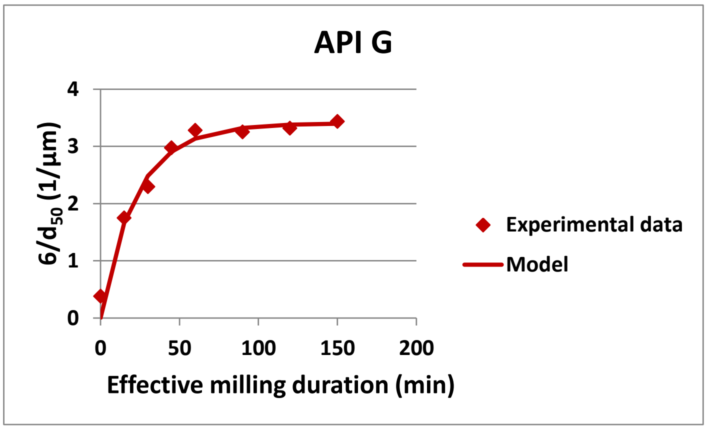

Figure 147: Model fit of milling kinetic from API G.

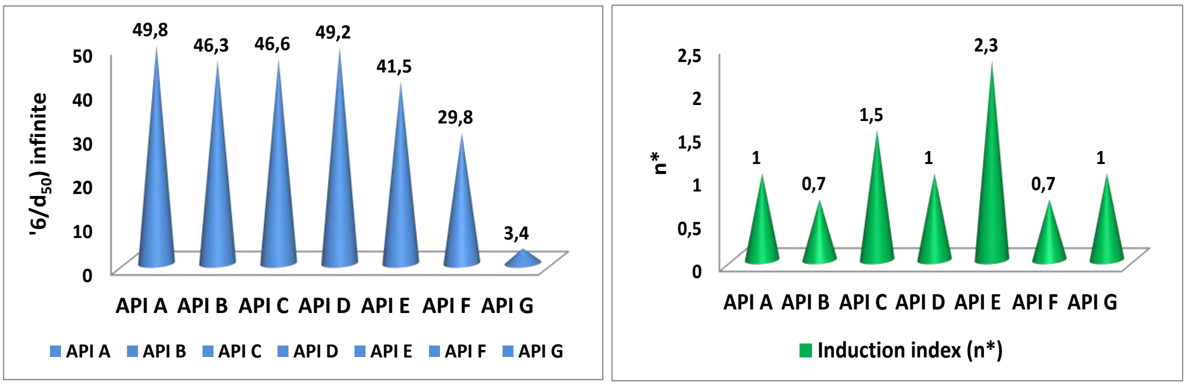

Figure 148: $(6/d_{50})_{\infty}$ (left) and induction index (right) of different APIs.

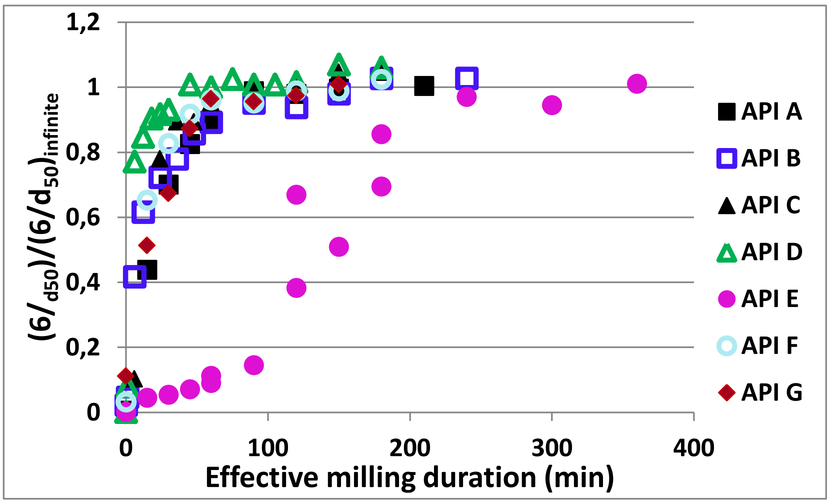

Figure 149 : Normalized milling kinetic of different APIs

5.3.3. Impact of the technology on the on the model parameters

It was found that the model is able to fit accurately all milling kinetics of API A from different mills of value chain (see Figure 150, Figure 151 and Figure 152). Furthermore, one can observe that whatever technology used, the value of implicit specific surface area at the equilibrium $((6/d_{50})(\infty))$ is always equal to $50\ \mu m^{-1}$ Illustrating that the grinding limit is reached due to high particles strength which cannot be overcome by the supplied stress energy.

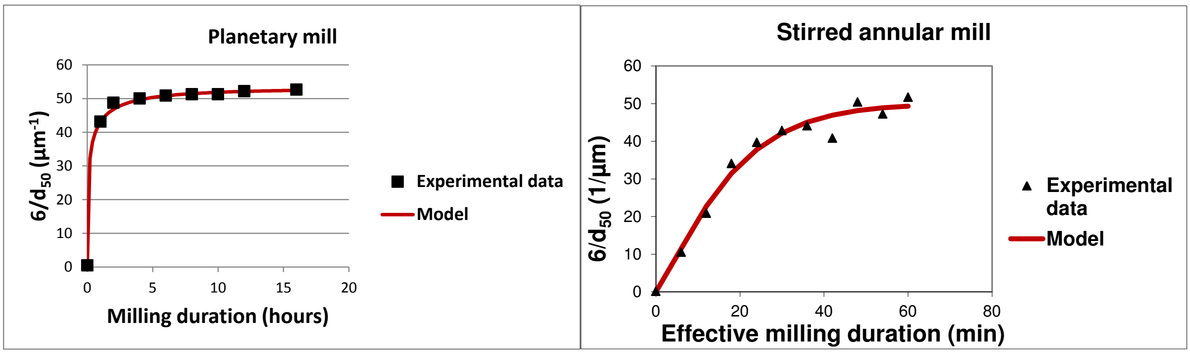

Figure 150 : Model fit of milling kinetic from planetary mill (left) and stirred annular mill (right).

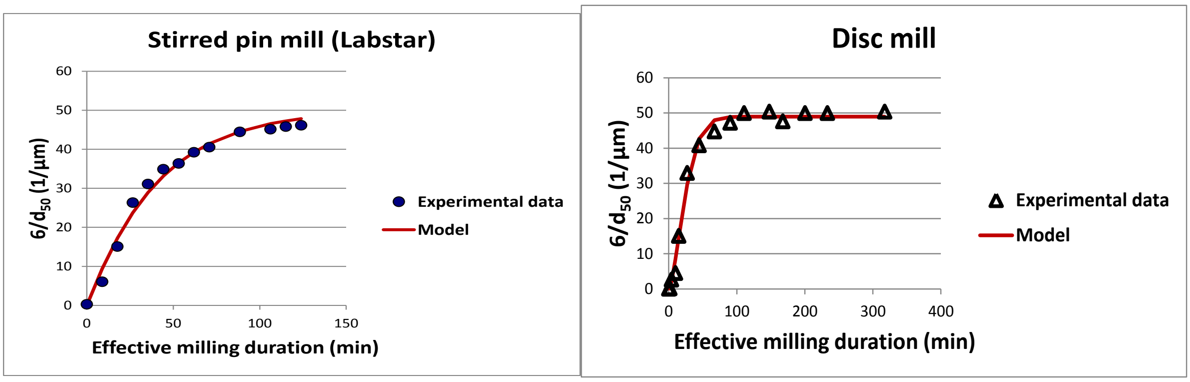

Figure 151 : Model fit of milling kinetic from stirred pin mill Labstar® (left) and stirred disc mill Dynomill® (right)

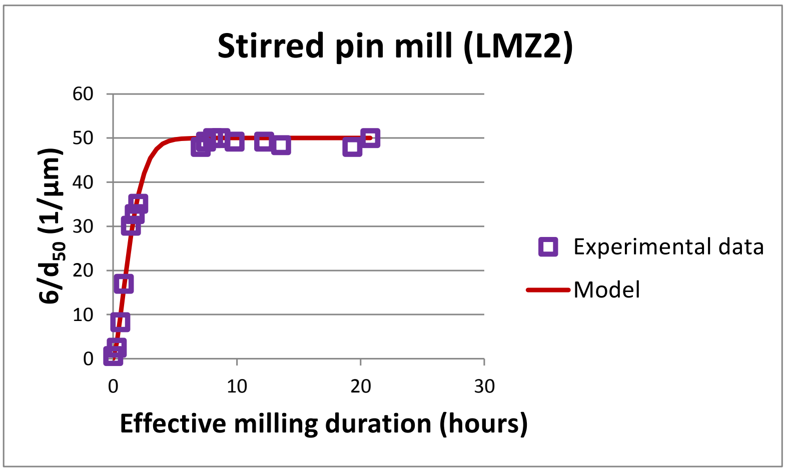

Figure 152 : Model fit of milling kinetic from stirred pin mill LMZ2®

5.3.4. Impact of operating parameters

The impact of operating parameters namely, API loading, rotation speed and bead filling rtae, on the model parameters was assessed using stirred annular mill (Nanomill 01®) and stirred pin mill (Labstar®). It was found that experimental milling kinetics data were well represented by the analogue to Avrami's equation. From the fit, one can determine the characteristic time (τ) and the induction index (n^*). Regarding ($6/d_{50}$) (∞), this parameter was kept constant at 50 μm^{-1} as it was experimentally observed. Consequently, the focus will be put only on the assessment of the impact of operating parameters on τ and n^*.

5.3.4.1. Impact of API loading on τ and n*

The impact of API loading on characteristic time (τ) and the induction index (n^*) leads to the following observations:

(i) Both mills behave differently with regard to API loading. Indeed, in the studied domain, it was found that tau (τ) varies linearly with the API loading for stirred pin mill case. This can be explained by the fact that at high API concentration, the viscosity increases leading to strong slowing down of grinding media velocity and consequently to a reduced milling performances (202). However, in the case of stirred annular mill, as one curve of milling kinetic is obtained regardless of API loading, tau (τ) does not vary significantly with API loading (see Figure 153 left);

(ii) The induction index (n^*) for both mills were found in the range of 0.7 to 1.1 for stirred annular mill and 0.8-1.1 for pin-counter pin mill (see Figure 153 right), respectively.

Both values are close to 1 suggesting that the milling kinetics of API A are well represented by first order law. This is confirmed when milling kinetics time scale is normalized by expressing the implicit specific surface area as function of (effective milling duration /τ), the overall kinetics can be derived from one master curve as illustrated in Figure 154).

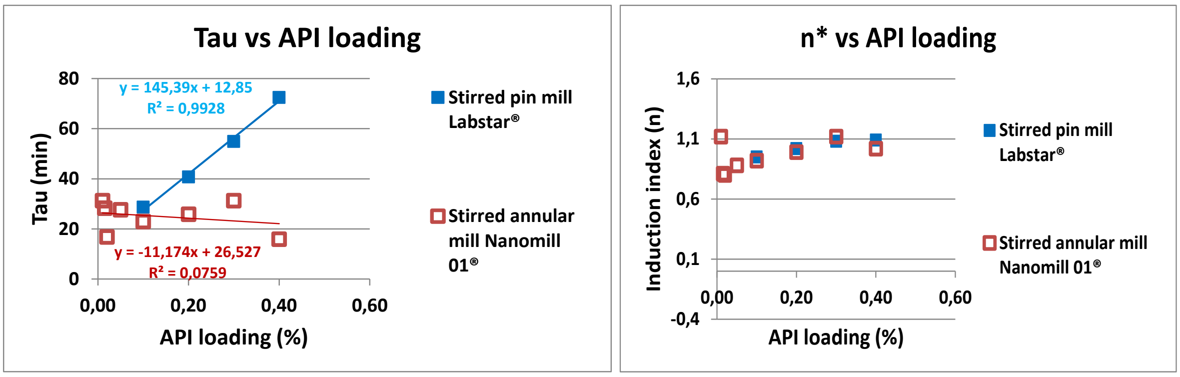

Figure 153: Tau versus API loading (left) and induction index (n*) versus API loading (right) for stirred pin mill labstar® and stirred annular mill Nanomill 01®.

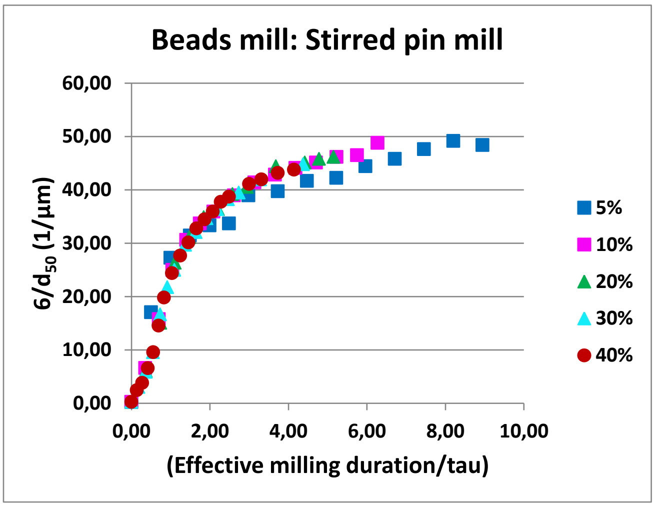

Figure 154 : milling kinetics time scale was normalized by expressing the implicit specific surface area ($6/d_{50}$) as function of (t /τ) for pin-counter pin mill Labstar®.

5.3.4.2. Impact of rotation speed on τ and n*

Studies assessing the impact of rotation speed on characteristic time (τ) and the induction index (n^*) led to the following observations:

(i) In the studied domain, it was found that tau (τ) varies as power law with the rotational speed (see Figure 155 left). The exponent values for both mills were found at -1.75 for stirred annular mill and at -1.95 for pin-counter pin mill, respectively. Both values are close to -2 which can be attributed to the milling kinetic energy. This suggests that higher is the rotation speed, higher is the milling intensity and lower is the time to get 63 % of the final implicit specific surface area;

(ii) The induction index (n^*) for both mills were found in the range of 1.0 to 1.2 for stirred annular mill and 0.9-1.2 for pin-counter pin mill (see Figure 155 right), respectively. Both values are close to 1 suggesting that the milling kinetics of API A are well represented by first order law. This is confirmed when milling kinetics time scale are normalized by expressing the implicit specific surface area as function of (effective milling duration /τ), the overall kinetics can be derived from one master curve as illustrated in Figure 156.

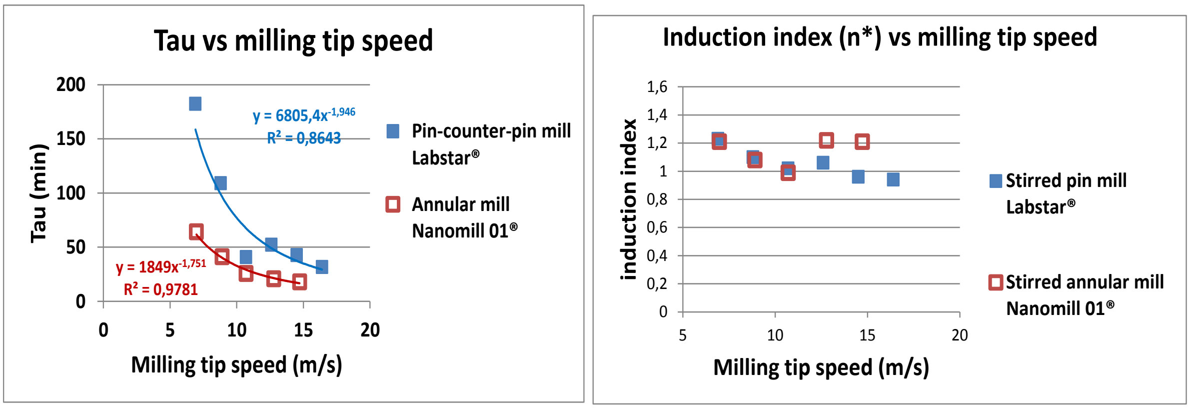

Figure 155: τ versus rotation speed (left) and induction index (n*) versus rotation speed (right) for stirred pin mill labstar® and stirred annular mill Nanomill 01®.

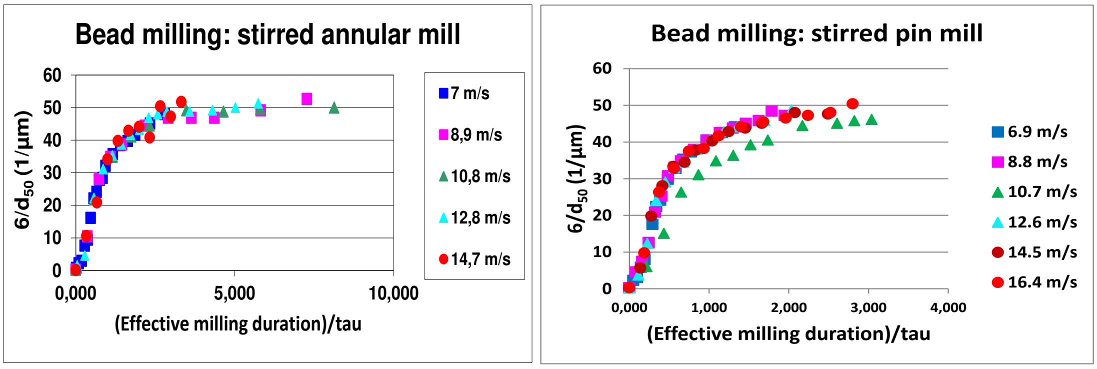

Figure 156 : milling kinetics time scale was normalized by expressing the implicit specific surface area ($6/d_{50}$) as function of (t/τ) for stirred annular mill Nanomill 01® (left) and pin-counter pin mill Labstar® (right)

5.3.4.3. Impact of bead filling rtae on τ and n*

Study of the assessment of the impact of bead filling rtae on (τ) and (n^*) led to the following observations:

(i) In the studied domain, it was found that tau (τ) varies as power law with the bead filling rtae (see Figure 157 left). The exponent values for both mills were found -2.40 for stirred annular mill and -3.95 for pin-counter pin mill, respectively. This illustrate that both mills behave differently with regard to bead filling rtae. This could be explained by the contribution of bead mill to increase of the overall viscosity. Moreover, it was found that tau (τ) varies as power law with stress frequency $[(\emptyset_{gm}\times(1-\varepsilon))/((1-\emptyset_{gm}\times(1-\varepsilon)))]$. The exponent values for both mills were found -1.73 for stirred annular mill and -2.76 for pin-counter pin mill, respectively (see Figure 157 right). These finding are not in agreement with already published data in the literature. In fact, (τ) should vary linearly with stress frequency when using inorganic material combined with ceramic beads;

(ii) The induction index (n^*) for both mills were found in the range of 0.8 to 1.4 for stirred annular mill and 0.8-1.2 for pin-counter pin mill (see Figure 158), respectively. Both values are close to 1 suggesting that the milling kinetics of API A are well represented by first order law. This is confirmed when milling kinetics time scale are normalized by expressing the implicit specific surface area as function of (effective milling duration /τ), the overall kinetics can be derived from one master curve as illustrated in Figure 159.

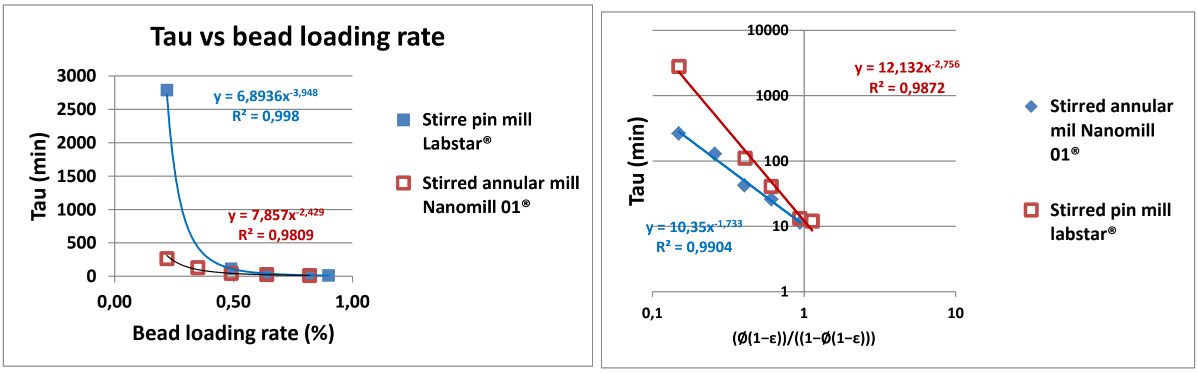

Figure 157: Tau versus bead filling rtae (left) and $(\emptyset_{gm}\times(1-\varepsilon))/((1-\emptyset_{gm}\times(1-\varepsilon)))$(right) for stirred pin mill labstar® and stirred annular mill Nanomill 01®.

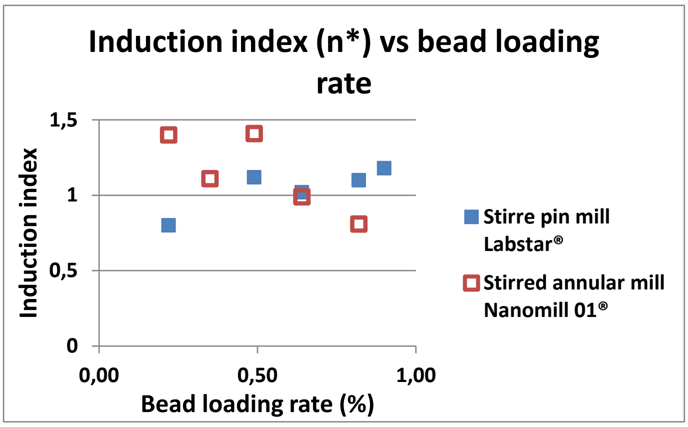

Figure 158: n^* versus bead filling rtae for stirred pin mill labstar® and stirred annular mill Nanomill 01®.

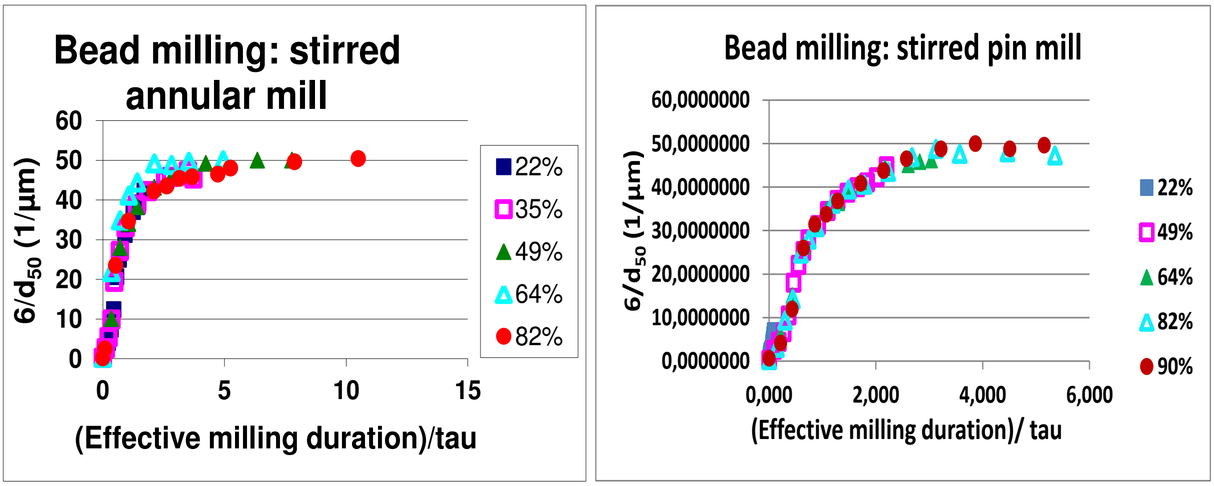

Figure 159 : milling kinetics time scale was normalized by expressing the implicit specific surface area $(6/d_{50})$ as function of (t/τ) for stirred annular mill Nanomill 01® (left) and pin-counter pin mill Labstar®

5.3.5. Design of global model

By studying the impact of the technology and operating parameters, it was found that the implicit specific surface area ($6/d50_{\infty}$) is always around 50 µm^{-1}. The induction index for both mills, stirred annular mill (Nanomill 01®) and stirred pin mill (Labstar®), is close to 1. Indeed, for the stirred annular mill, n^* was found in the range of 0.8-1.4 having a mean value of 1.1 and standard deviation of 0.2. For the stirred pin mill, n^* was found in the range of 0.8-1.2 having a mean value of 1.0 and standard deviation of 0.2. The observed variability of induction index is not significant as can be illustrated by Figure 160. Therefore, it can be considered that the milling kinetic is represented by a first order law.

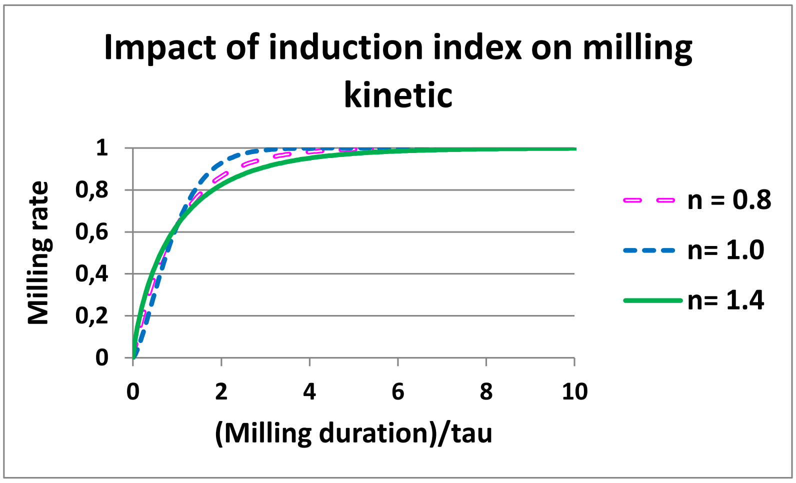

Figure 160: Impact of induction index on milling kinetic.

Consequently, only the parameter characteristic time (τ) is considered for the design of the global model as described in the Table 20

Mill	Impact of API Loading	Impact of rotation speed	Impact of bead filling rtae
Stirred annular mill (Nanomill 01®)	No impact	$\tau_{Na} = k_3 \times V_t^{x'}$	$\tau_{\phi a} = k_5 \times \phi_{gm}^{z'}$
Stirred pin mill (Labstar®)	$\tau_{cp} = (k_1 \times C_l) + k_2$	$\tau_{Np} = k_4 \times V_t^{y'}$	$\tau_{\phi p} = k_6 \times \phi_{gm}^{w'}$

Table 20: equations describing impact of API loading, rotation speed and bead filling rtae on characteristic time for annular and stirred pin mill.

Where, τ_{Na}, τ_{Np}, $\tau_{\Phi a}$, $\tau_{\Phi p}$ and τ_{cp}, are characteristic time as function of rotation speed for stirred annular mill, characteristic time as function of rotation speed for stirred pin mill, characteristic time as function of bead filling rtae for stirred annular mill, characteristic time as function of bead filling rtae for stirred pin mill and characteristic time as function of API loading for stirred annular mill, respectively.

C_l, V_t and Φ_{gm} are API loading, rotation speed and bead filling rtae, respectively.

k_1, k_2, k_3, k_4, k_5, k_6, x', y', z' and w' are constants.

The global models can be designed for each mill as follows:

For stirred annular mill:

$$\boldsymbol{\tau_a = k_{an} \times V_t^{x'} \times \phi_{gm}^{z'}} \quad \text{(Eq. 129)}$$

For stirred pin mill:

$$\boldsymbol{\tau_p = (k_{p1} \times V_t^{y'} \times \phi_{gm}^{w'}) \times (k_{p2} \times C_l + k_{p3})} \quad \text{(Eq. 130)}$$

k_{an}, x, z, k_{p1} ,y, w, k_{p2} and k_{p3} were determined using least square method between observed and calculated values. These values are gathered in **Table 21**

k_{an}	523
x’	-1,8
z’	2.4
k_{p1}	21.3
y’	-2.0
w’	-3.9
k_{p2}	145
k_{p3}	13

Table 21: Model parameters.

As can be seen in Figure 161, the global models of both mills were found to reliably predict the observed characteristic time (τ)

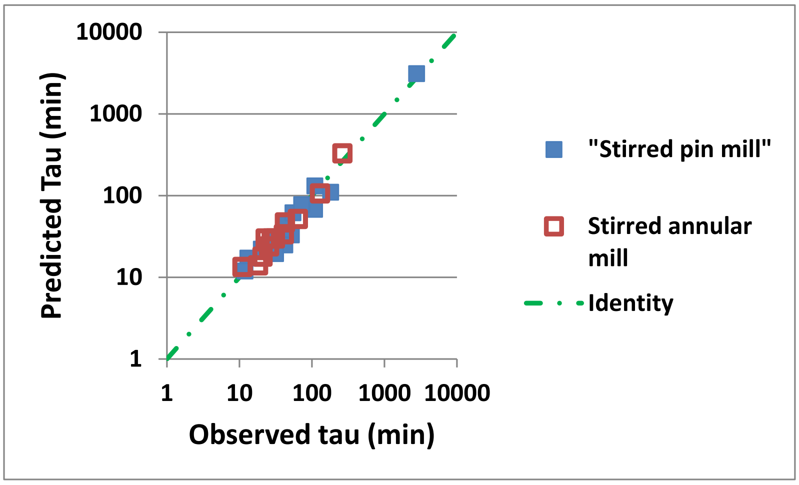

Figure 161: Predicted characteristic time versus observed one.

5.3.6. Validation of the model

In order to validate of the proposed model, a new experimental trial was carried out outside of stirred annular mill experimental space. The operating conditions were fixed at 25 % as API loading, 11.6 m/s as rotation speed and 56 % as bead filling rtae. The value of characteristic time was firstly calculated and found at 29.4 min-1. Then after performing the trial, a fit of the experimental data was done using least square method. The characteristic time value was found equal to 35.5 min^{-1} and in agreement with the established correlation between predicted and observed characteristic time (see Figure 162 left). Furthermore, as illustrated in Figure 162 right side, the predicted milling kinetic and the experimental values are close to each other demonstrating the validation of the model.

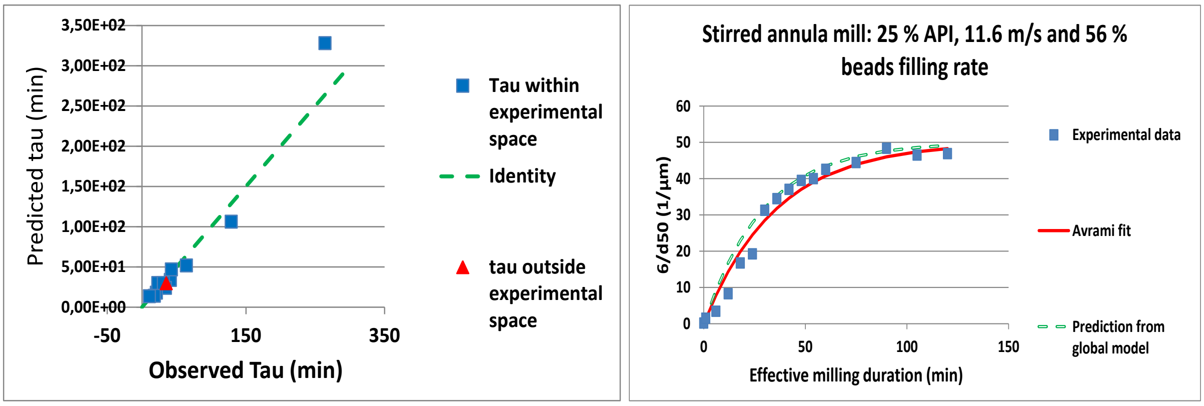

Figure 162: Predicted tau vs observed one (left) and milling kinetic of experiment (right) performed outside of experimental space.

5.3.7. Relationship between models obtained using stirred annular mill (Nanomill 01®) and stirred pin mill (Labstar®)

Both mills can be used in the overall milling value chain. As shown in the section 5.3.5 the model parameters obtained with both mills are different. If there is a need to switch from one type of equipment to another (for example from stirred annular mill to stirred pin mill) in order to achieve the same physical quality of milled suspension, it is required to keep the API loading and bead filling rtae constant. However, as both mills do not behave similarly, a correction factor needs to be applied to a rotation speed according the following equation:

$$V_{tp} = C_{cor} \times V_{ta} \tag{Eq. 131}$$

Where V_{tp} is the rotation speed to be applied with stirred pin mill, C_{cor} is a correction factor and V_{ta} is the rotation speed applied to stirred annular mill.

Therefore, the characteristic time of stirred pin mill can be expressed as follow:

$$\tau_p = (k_{p1} \times (C_{cor} \times V_{ta})^{y'} \times \phi_{gm}^{w'}) \times (k_{p2} \times C_l + k_{p3}) \quad \text{(Eq. 132)}$$

For that purpose, the characteristic time of pin mill was calculated from the experiment performed using stirred annular mill. Then the correction factor was obtained using least square method. The C_{cor} value was found equal to approximately 1.2. The results showed a good correlation between estimated characteristic time using (Eq. 132) and characteristic time obtained from stirred annular mill (see Figure 163 right). As can be seen in the Figure 163 (right), this observation was well supported by performing an experiment based on the relationship between models obtained using stirred annular mill and stirred pin mill. In fact, the milling kinetic of trial experiment performed using stirred annular mill with 20 % API loading, 64 % bead filling rtae and 8.9 m/s as rotation speed was found highly overlap with predicted milling kinetic from pin mill using (Eq. 132) and also to the trial experiment carried at 20 % API loading, 64 % bead filling rtae and 10.7 m/s as the rotation speed (close value to the corrected one (10.4 m/s)).

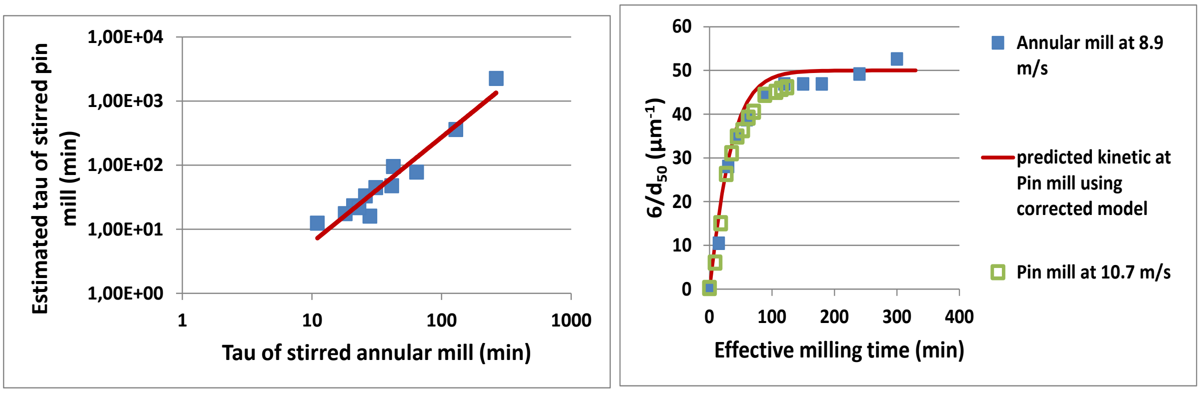

Figure 163: Estimated characteristic time of pin mill versus characteristic time of annular (left) and milling kinetic correspondence between annular and stirred pin mill (right).

5.3.8. Scale up rule

The scale up rule was already described in the section 5.2.2.1.3.3.

5.3.9. Reliability of the model

The reliability of the model was assessed by determining, for both mills (stirred annular mill and stirred pin mill), the difference between observed and calculated values of $(6/d_{50})_t$ obtained from predictive modelling for all milling experiments. The distribution of the differences between the two values was plotted and compared to normal distribution. A statistical analysis was carried out using SAS JMP software v6.10. Table 22 summarizes for stirred annular and stirred pin mill the corresponding quantiles as well as the summary statistics of distribution and Goodness of fit test parameters.

The results show that for both mills the observed values of $(6/d_{50})_t$ are well correlated with those calculated from model prediction (see Figure 164). Indeed, the linear correlation coefficients were found for stirred annular mill and stirred pin mill about 0.9850 and 0.9869, respectively. Furthermore, for both mills, the distributions of the differences were well fitted by normal distribution (see Figure 165). The statistical evaluation outlined that:

(i) Both distributions have a mean value close to zero;

(ii) For the stirred pin mill case, the value of normality test (W = 0.991724) of Wilk-Shapiro (218) on the observed data outlines that the probability of underlying population (p-value = 0.0575) to be normal is higher than 5%. Consequently, the hypothesis distribution normality cannot be rejected;

(iii) For the stirred annular mill case, the value of normality test (W = 0.953563) of Wilk-Shapiro on the observed data outline that the probability of underlying population (p-value < 0.0001) to be normal is low. Therefore, the hypothesis of distribution normality can be rejected (dissymmetric distribution having a tail at the right part).

In both cases the bias of the model is very low and is of the same order of magnitude for the two milling methods therefore the model is considered representative and accurate.

Distribution quantiles		Stirred annular mill	Stirred pin mill
	Maximum value	8.88626	5.4098
	Minimum value	-7.6779	-5.726
	Median value	0.07987	0.24809
	top quartile	1.51881	1.67354
	Bottom quartile	-0.6004	-0.6827
Summary statistics of distribution	Mean value	0.3682411	0.3568941
	Standard deviation	2.1101019	1.8356576
	Standard error mean value	0.1445818	0.1001433
	Upper 95% Mean	0.6532432	0.5538831
	Lower 95% Mean	0.083239	0.159905
	Number of value	213	336
Goodness of fit test parameters	W	0.953563	0.991724
	Prob<W	<0.0001	0.0575

Table 22 : Corresponding quantiles as well as the summary statistics of distribution and goodness of fit test parameters

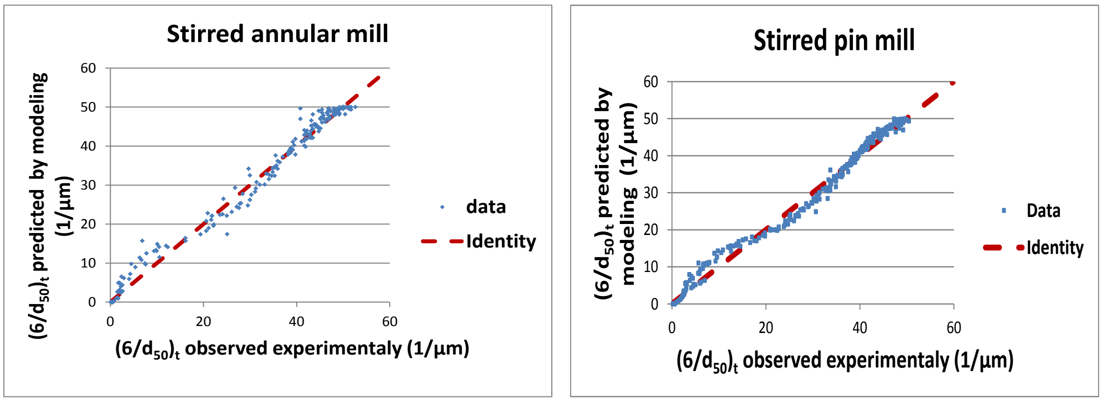

Figure 164 : calculated $(6/d_{50})_t$ from model prediction as function of observed $(6/d_{50})_t$

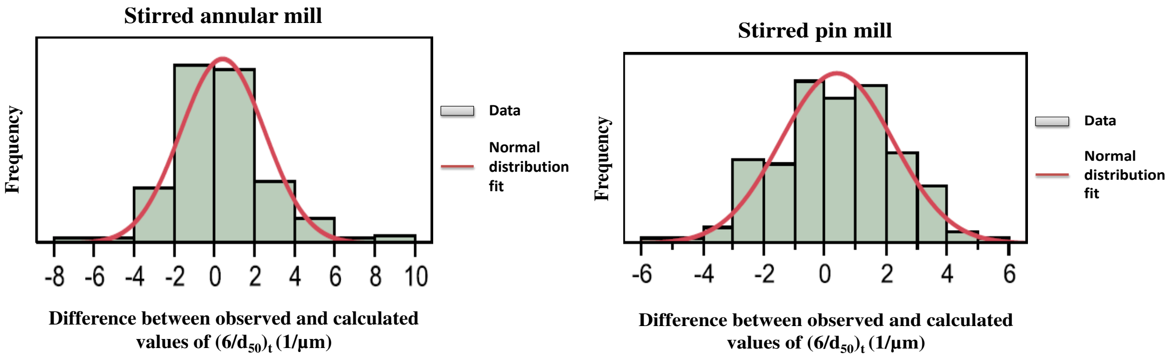

Figure 165 : Distribution of differences between calculated and observed of $(6/d_{50})_t$

General conclusions, future work and perspectives

6. General conclusions

This research work was focused on the formulation and the process engineering of nano-crystalline suspensions. The key conclusions of this work are as follows:

- Formulation engineering
    - Using a combination of empirical and colloidal-interfacial fundamental approach based on milling-ability, wettability and electro-steric repulsion, we were able to select an optimum wetting/dispersant agent achieving high colloidal stability.
    - The designed suspension was found significantly robust under various conditions, such as ionic strength, shear rate, wetting/dispersant agent desorption by dilution, temperature and pH;
    - The developed approach can be considered as useful methodology to be applied in the frame fast to clinical evaluation of any API by achieving both time effectiveness and scientific rationale.
- Process engineering
    - The technological comparison (high pressure homogenization (HPH) versus beads milling) for the manufacturing of nano-crystalline suspension outlined that as far as the formulation is sufficiently robust and stable both technologies are suitable for the production of nano-crystalline suspension;
    - The bead mill is more powerful than the HPH. However, at the same average diameter (d_{50}) of produced nano-suspension, the HPH leads to a tighten particle size distribution;
    - For both technologies, whatever the process parameters used for milling and the scale, the relationship of d_{90} versus d_{50} could be described by a unique master curve. On the other hand, the relationship of d_{90} versus d_{50} of the HPH is different from that of bead mill suggesting that this relationship is a technology signature of milling pathway;
    - Regarding bead milling, the comparison of our results to those published in the literature does not outline any important discrepancy in terms of formulation impact on milling performances. However, in terms of process parameters impact,

  a significant discrepancy was observed between our finding and those published in the literature using ceramic beads;
  - Regarding HPH, we was not able to do any comparison of our finding to those published in the literature as they are focused on the formulation aspect and they not discuss manufacturing process aspects.

This research work can be extended in several directions:

- Formulation engineering:
  - To develop methodology for preliminary screening of wetting/dispersant agent based on characterizing the surface properties of API and excipient and measuring their interaction potential;
  - To investigate and understand the impact of API loading on suspension stability at temperature, shear rate and pH variation in order to define better formulation;
  - To investigate and understand the impact of nano-suspension particle size distribution on the long term stability of suspension.
- Process engineering
  - To better understand why the bead mill is more powerful than the HPH?
  - To understand why the annular bead mill does not react to viscosity change while discs and stirred pin mill react?
  - To understand why the time to reach certain fineness is proportional to $\phi_{gm}^{2.4}$ when using stirred annular mill bead and to $\phi_{gm}^{3.94}$ when using stirred pin mill?
  - To understand why the time to reach certain fineness is proportional to $P^{2.6}$ when using HPH?
  - To investigate the impact of milling energy on chemical quality attributes of milled suspension
  - To build mathematical model for HPH similar to that designed for bead mill.

Appendix

7. Appendix

Appendix 1 : list of wetting/dispersant agents used for formulation engineering

Table 23: list of Witting / dispersant agent used for the investigation

Chemical category	Material	Supplier	Molar mass	Expected added value for stabilization
Cellulose derivatives	**Hydroxypropyl Methylcellulose HPMC (Pharmacoat® 606)**	SEPPIC (France)	Range: 10,000–1,500,000	Steric stabilization
	Klucel® Hydroxypropylcellulose: HPC HF	Hercules (France)	Average: 1,150,000	Steric stabilization
Povidones	**Luvitec® Polyvinylpyrrolidone: PVP (K30)**	BASF (France)	Average : 50,000	Steric stabilization
	PVP-VA (Plasdone™ S-630) Linear random copolymer of N-Vinyl-2-Pyrrolidone and Vinyl Acetate	Ashland (France)	Average: 27,000	Steric stabilization
Phospholipids	**Phosal® 50PG Compound of 50% phosphatidylcholine from soybean with propylenglycol**	Phospholipid GmbH (Germany)	775	Electrostatic Stabilization
	Phospholipon® 90G	Phospholipid	758	Electrostatic

	Pure phosphatidylcholine stabilized with 0.1% ascorbyl palmitate	GmbH (Germany)		Stabilization
	Lipoid® S100 Phosphatidylcholine from soybean	Lipoid (Germany)	787	Electrostatic Stabilization
Poloxamers	**Poloxamer 188 Pluronic® F 68 NF Prill Block copolymers based on ethylene oxide and propylene oxide**	BASF (France)	Range : 7,680-9,510	Steric stabilization
	Poloxamer 407 Pluronic® F 127 NF Prill Block copolymers based on ethylene oxide and propylene oxide	BASF (France)	Range: 9,840-14,800	Steric stabilization
Poly-Ethylene-Glycol & derivatives	Polyethylene Glycol 8000 **PEG 8000**	Sigma-Aldrich (France)	Average: 8,000	Steric Stabilization
	Solutol® HS15 Macrogol 15 HydroxyStearate	BASF (France)	813.2	Steric Stabilization
	Vitamin E TPGS® (d-Alpha Tocopheryl Polyethylene Glycol 1000 Succinate)	Eastman Chemical Company (Netherlands)	1,513	Steric Stabilization
Fatty Acids and Fatty acid Esters	**Cremophor® RH40 Macrogol-**	BASF (France)	Range: 300-6,000	Steric Stabilization

	Glycerolhydroxystearate			
	Montanov® 68 **Cetearyl Alcohol & Cetearyl Glucoside**	SEPPIC (France)	N.A.	Steric Stabilization
	Montanox® 80 **Ethoxylated Sorbitan Ester**	SEPPIC (France)	1,310	Steric Stabilization
	Gelucire® 4414 **Lauroyl macrogol-32 glycerides**	Gattefossé (France)	N.A.	Steric Stabilization
	Simulsol® M49 **Polyethoxylated castor oil (PEG-20 stearate)**	Seppic (France)	1,165	Steric Stabilization
Others	**Soduim Polyacrylate®**	BF Goodrich chemical (USA)	104,400	Electrosteric Stabilization
	Sodium dodecyl sulfate (SDS)	Univar (France)	288.4	Electrostatic Stabilization

Appendix 2 : implicit specific surface area calculation

The specific surface area is proportional to surface unit divided by mass. It can be described by the Eq. A1:

$$\mathbf{SSA} = \frac{\textbf{Surface of the particles}}{\textbf{Particles mass}} \qquad \textbf{Eq. A1}$$

The Eq. A1 can be described by the Eq. A2

$$\mathbf{SSA} = \frac{\textbf{Surface of the particles}}{\textbf{Particles density}*\textbf{Volume of the particles}} \qquad \textbf{Eq. A2}$$

If we assume that the particles are in the shape of spheres, the Eq. A2 can be written as following:

$$\mathbf{SSA} = \frac{\mathbf{4*\pi*r^2}}{\mathbf{\rho*\frac{4}{3}\pi r^3}} = \frac{\mathbf{3}}{\mathbf{\rho*r}} = \frac{\mathbf{6}}{\mathbf{\rho*d}} \qquad \textbf{Eq. A3}$$

Where r is the particles radius, d is the particles diameter and ρ is the particles density.

Therefore, if the main diameter of the particle size distribution is used, the Eq. A3 can be written as following:

$$\mathbf{SSA} = \frac{\mathbf{6}}{\mathbf{\rho*d_{50}}} \sim \frac{\mathbf{6}}{\mathbf{d_{50}}} \qquad \textbf{Eq. A4}$$

Long abstract in French

8. Long abstract in French (Résumé long en français)

La présente thèse a été centrée sur l'application des nanotechnologies dans l'industrie pharmaceutique et plus spécifiquement sur l'utilisation suspensions nanocristallines pour surmonter les obstacles liés aux problèmes de faible solubilité des nouvelles entités chimiques. L'objectif principal de ce travail a été la stabilisation et la comparaison des technologies de fabrication des suspensions nanocristallines à usage pharmaceutique.

Dans un premier temps, nous avons présenté une revue bibliographique ou les sujets suivants ont été décrits:

(i) L'application des nanotechnologies dans le domaine médical. Dance cette section, nous avons rapporté que l'application des nanotechnologies se réfère au diagnostic, au traitement et au contrôle médical. Pour le diagnostic les suspensions colloïdal de particules d'or ou des cristaux d'oxyde de fer sont largement utilisées. Pour le traitement médical, les nanotechnologies sont utilisées pour pallier aux problèmes de solubilité, d'absorption et de distribution en utilisant des systèmes de libération des principes actifs dont la taille particulaire est inférieure à 200 nm ;

(ii) Les différents procédés de fabrication des suspensions nanocristallines. Dans cette section, nous avons souligné qu'il existe plusieurs approches de fabrication des suspensions nanocristallines: l'approche dite « Bottom-Up » qui consiste à solubiliser le principe actif ainsi que les stabilisants nécessaires dans un solvant organique. La phase organique obtenue est ensuite mélangée à un non solvant (généralement de l'eau) pour précipiter le principe actif sous forme de nanoparticules, et l'approche dite « Top-Down » qui consiste à réduire la taille des particules à partir des particules plus grosses en utilisant des systèmes de fragmentation tels que les broyeurs à billes ou les homogénéiseurs haute pression. L'approche dite « Top-Down » est la plus utilisée dans l'industrie pharmaceutique (la majorité des produits commercialisés sont fabriqués en utilisant cette approche) car elle présente les avantages suivants en comparaison avec l'approche dite « Bottom-Up » :

   a. Cette proche est capable de traiter à la fois les principes actifs qui sont peu solubles dans les solvants organiques et dans de l'eau ;
   b. Le contrôle de la taille des particules est plus aisé grâce à un choix approprié des agents de stabilisation ;
   c. Le nombre d'opération unitaire est réduit par rapport à l'approche concurrente (4 au lieu de six);

d. Cette approche peut traiter des suspensions très concentrées (jusqu'à 40 %);

e. Le risque d'amorphiser partiellement ou totalement le produit est très faible ;

f. Cette approche n'utilise pas de solvant organique. Cela rend la conception de l'atelier industriel plus aisée.

C'est pour ces raisons que dans l'ensemble de nos travaux, nous avons considéré d'utiliser l'approche dite « Top-Down » ;

(iii) Les fondements de la conception de la formulation pour la fabrication des suspensions nanocristallines en utilisant l'approche dite « Top-Down ».

L'approche dite « Top-Down » consiste à disperser le principe actif en présence d'excipients dans de l'eau. La suspension obtenue est ensuite broyée pour générer des tailles de particules très fines (< 500 nm). Si la suspension est suffisamment stable, elle est administrée telle quelle au patient. Dans le cas contraire, la suspension est formulée en vue dans son séchage par atomisation ou lyophilisation. Dans ce dernier cas de figure, la suspension est reconstituée avant son administration au patient. La conception de la formulation consiste à choisir les exceptions nécessaires pour faciliter la mise en œuvre du procédé de broyage et pour garantir la stabilité de la suspension pendant le stockage et lors de l'administration au patient. Les excipients utilisés sont en général des tensioactifs chargés qui ont pour rôle de faciliter le mouillage des particules hydrophobes afin de faciliter la mise en œuvre du procédé de broyage et garantir une stabilisation de type électrostatique pendant le stockage. Ces tensioactifs peuvent être combinés avec des polymères qui ont pour rôle de garantir une stabilisation de type stérique. La combinaison des deux types d'excipient apporte une stabilisation plus efficace dite « électro-stérique ». Nous avons rapporté que la conception de la formulation doit reposer sur la prise en compte des fondements suivants :

a. Les caractéristiques de bases du phénomène de mouillage;

b. Les forces d'interaction microscopiques inter-particulaires (forces DLVO et les forces stériques);

c. Les Mécanismes de déstabilisation des nanoparticules;

d. Les forces macroscopiques qui peuvent induire la déstabilisation des nanoparticules.

(iv) Les fondements de la conception des procédés de fabrication des suspensions nanocristallines. Dans cette section, nous avons rapporté que pour réduire la taille des particules des suspensions dans un temps raisonnable, l'utilisation de broyeurs énergétiques est nécessaire. A cet effet, la quantité d'énergie spécifique à utiliser est généralement supérieure à 200 kJ/kg. Le mécanisme de réduction de la taille des particules consiste dans un premier à compresser et à déformer les particules en créant des défauts et à créer des fragments dans un second temps. Ce processus continue en alternant la compression/déformation et fragmentation jusqu'à l'obtention de la taille des particules désirée. Le degré de réduction de la taille des particules dépend du temps de broyage. Au-delà d'un certain temps le processus atteint un état d'équilibre pendant lequel la taille des particules ne varie plus.

L'approche dite « Top-Down » utilise deux principales technologies : le broyage à billes et l'homogénéisation haute pression. Les broyeurs à billes existent avec des rotors à broches ou des rotors à disques ou des rotors annulaires. Ce sont des équipements qui utilisent la technique des impacts pour réduire la taille des particules. Pour cela, des billes de broyage sont projetées les unes contre les autres dans une chambre de broyage. La haute énergie et les forces de cisaillement qui résultent du processus d'impact permettent de réduire la taille des particules. Quant à l'homogénéisation haute pression, elle existe soit sous forme clapet soit sous forme de capillaire. Son principe réside dans le contrôle d'une très forte accélération à travers un orifice très étroit. Le produit est soumis à une puissante turbulence, à un laminage intense, à de la cavitation et un violent impact contre les média de broyage. Les deux technologies peuvent être utilisées soit en mode recyclage soit en mode passages discrets. Les fondements du développement du procédé de broyage réside tout d'abord sur l'acquisition des données de base (cinétique de broyage, impact des différents paramètres de broyage sur la cinétique et sur la qualité de la suspension broyée en terme de taille des particules, de morphologie, de structure cristalline, de stabilité de la suspension etc……) et la définition d'un espace de conception basée sur l'approche « scale-down/scale-up » où le procédé est suffisamment robuste pour produire une suspension avec la qualité requise.

Dans un second temps, nous avons présenté les résultats de notre étude expérimentale en trois parties:

(i) Mise au point d'une méthodologie de criblage des excipients de stabilisation des suspensions nanocristallines. Cette section a été divisée en deux parties. Le première partie a été consacrée au criblage des excipients de stabilisation pour élaborer la formulation nécessaire à la production des nano-particules. La seconde partie a été ensuite consacrée à l'évaluation de la robustesse de la formulation sélectionnée dans la première partie en vue d'anticiper son comportement au stockage et pendant l'administration au patient.

La première partie consacrée au criblage des excipients de stabilisation a été elle-même divisée en deux étapes principales: la première étape a été consacrée à un criblage qualitatif pour sélectionner une formulation potentielle. En effet plus 20 stabilisants candidats (avec un ratio de 3 % de stabilisant et 20 % de principe actif) ont été testés sur la base de plusieurs critères. Le premier test a été de vérifier l'aptitude au broyage en utilisant un broyage basse vitesse (0,03 m/s, broyage permettant de cribler en même un grand nombre de candidats). Les candidats retenus pendant ce test sont ceux qui ont conduit une suspension nanocristalline ayant un diamètre médian d'environ 100-500 nm (taille de particule typique des suspensions nanocristalline) et stable sur une durée de 15 jours. Pour les candidats ayant passé ce premier test nous avons ensuite mesuré le potentiel zêta. Tous les candidats ayant un potentiel zêta inferieur en valeur absolu à 15 mv ont été écartés car ils ne peuvent assurer une protection électrostatique de la suspension produite. Pour les candidats ayant passé ce test nous avons ensuite mesuré la viscosité de la suspension à un taux de cisaillement d'environ 1000 s^{-1}. Tous les candidats ayant une viscosité supérieure à 10 mPas ont été écartés car leur mise en œuvre sera difficile pendant le broyage (ralentissement notable de la cinétique) et éventuellement pendant le remplissage par exemple des seringues si le produit est utilisée pour de la voie parentérale. Les candidats ayant passé le test de rhéologie ont ensuite été testé en broyage à billes haute vitesse (3 m/s, représentatif des conditions industrielle). Les candidats retenus pendant ce test sont ceux qui ont conduit une suspension nanocristalline ayant un diamètre médian d'environ 100-500 nm et stable sur une durée de 15 jours. A ce stade, deux formulations sont apparues supérieures aux autres candidates. Une formulation contenant un polymère (Vitamine E TPGS) dont le mécanisme de stabilisation est basé sur la protection stérique et une formulation contenant un polymère (PVP K30) et un tensioactif (SDS) dont le mécanisme de stabilisation est basé sur la protection électro-stérique. Pour départager ces deux candidats, nous les avons soumis à un broyage très agressif (contrainte de cisaillement d'environ 1.10^9 pendant 13 h). A l'issue de ce test, le système SDS/PVP (30/70 %) a conduit une suspension nanocristalline dans le domaine nanométrique et ayant une distribution monomodale. En revanche, la Vitamine E TPGS a conduit une suspension nanocristalline dans le domaine micrométrique et ayant une distribution bimodale. De plus, la Vitamine E TPGS a conduit à une suspension sous forme de gel après broyage.

Ce résultat, a été expliqué par une possible extraction du polymère de la surface des particules induite par le haut cisaillement appliqué pendant le broyage. Il est à noter que la Vitamine E TPGS ne pouvait pas assurer une protection de type électrostatique. A l’issue de cette première étape, le système SDS/PVP a été utilisé dans la seconde d’étape en vue de l’optimisation de la composition SDS-PVP et de la concentration du mélange. Cette seconde étape a été composée de plusieurs tests. Tout d’abord, nous avons mesuré le potentiel zêta en fonction du pourcentage du SDS pour déterminer la composition optimal au regard de la protection électrostatique. Le résultat de ce test a montré que le potentiel zêta dimuniait avec l’augmentation du pourcentage du SDS jusqu’à 40 %. Au-delà de cette concentration, le potentiel zêta restait stable à environ -52 mV mettant en évidence que l’adsorption du tensioactif à la surface des particules est complète à environ 40 % de SDS. Le second test consistait à évaluer la synergie entre le SDS et la PVP en vue d’assurer une protection électro-stérique. A cet effet, nous avons mesuré la concentration micellaire critique du mélange binaire SDS-PVP. Le résultat de ce test a montré l’existence d’une concentration micellaire critique minimale aux environ de 60 % de PVP qui peut conduire à une activité de surface maximale. A l’issue de ces deux tests la composition du mélange retenue a été 40 % de SDS et 60 % de PVP. Cette composition a été ensuite utilisée pour l’optimisation de la concentration du mélange. A cet effet, nous avons réalisé trois tests. Dans le premier test, nous avons mesuré le facteur de mouillage (en utilisant la méthode Washburn) en fonction la concentration du mélange SDS-PVP (40-60 %). Le résultat a montré que le facteur de mouillage augmente avec la concentration du mélange SDS-PVP (40-60 %) jusqu’à 1,2 %. Au-delà de cette concentration le facteur de mouillage reste inchangé. Il est à noter que plus le facteur de mouillage est élevé plus le l’angle de contact est bas. Sur la base de test, nous avons considéré que la concentration optimale du mélange SDS-PVP (40-60 %) est de 1,2 %. Le second test consistait à mesurer l’isotherme d’adsorption. Le résultat de ce test a mis en évidence un isotherme d’adsorption de type haute affinité ayant un plateau aux environs de 0,7 mg/m2 de PVP correspondant à environ 0,82 % du mélange SDS-PVP (40-60 %). Le dernier test consistait à broyer des suspensions contenants différentes concentrations du mélange SDS-PVP (40-60 %) en utilisant le broyage à billes haute vitesse. Pour chacune des suspensions, nous avons établi la cinétique de broyage en traçant $6/d_{50}$ (surface spécifique implicite) en fonction du temps de broyage. Les cinétiques de broyage ont montré l’existence d’une valeur asymptotique ($(6/d_{50})_\infty$, surface spécifique implicite à l’équilibre) selon une loi de première ordre ayant un temps caractéristique (τ). La valeur asymptotique (($6/d_{50})_{\infty}$ a été ensuite tracée en fonction de la concentration du mélange SDS-PVP (40-60 %). Le résultat a montré l'existence de deux régimes : à haute concentration (régime riche), la valeur asymptotique (($6/d_{50})_{\infty}$ reste inchangée avec la concentration due à la limitation par la technologie de fournir une énergie suffisante pour réduire la taille des particules. A basse concentration (régime pauvre), la concentration en stabilisant n'est pas suffisante pour couvrir les surfaces produites par la technologie. Nous avons noté que la transition entre les deux régimes se situait aux environs de 1,2 % du mélange SDS-PVP (40-60 %). Sur la base de ces 3 trois tests, nous avons considéré que la concentration optimale est de 1,2 % du mélange SDS-PVP (40-60 %). La formulation conçue lors de cette première partie est par définition thermodynamiquement instable. Elle peut être déstabilisée (agrégation ou floculation) sous l'effet des différentes conditions telles que :

(a) le cisaillement induit lors de l'agitation dans les cuves de préparation ou l'écoulement dans les canalisations ou lors d'une variation de force ionique (par exemple pendant la préparation avant administration);

(b) lors d'une variation de pH (par exemple pendant la préparation avant administration ;

(c) lors de la désorption du stabilisant par dilution (par exemple pendant la préparation avant administration)

(d) enfin lors d'une variation de température (par exemple pendant la stérilisation).

La seconde partie a par conséquent été consacrée à l'évaluation de la robustesse de la formulation sélectionnée au regard des risques mentionnée ci-dessus. Chacun des risques a été évalué en mettant en place un test spécifique. Les résultats ont montré que :

A. Le risque lié à la déstabilisation sous l'effet du cisaillement a été évalué sous un cisaillement de 26000 s^{-1} à deux forces ionique différentes (sans ajout de set et avec ajout de 0,17 mole de NaCl). Pendant le cisaillement, nous avons suivi l'évolution de la taille des particules au cours du temps. Le résultat a montré que sans ajout de sel une agglomération de la suspension a été observée alors qu'avec ajout de sel, agglomération de la suspension a été significativement moins importante. Ce résultat s'explique par le fait qu'en présence du sel la solubilité de la PVP dans l'eau est moins importante. De ce fait l'extraction de la PVP de la surface des particules sous cisaillement est plus difficile que dans le cas sans ajout de sel. Sur la base de ce résultat nous avons recommandé soit d'ajouter du sel à la formulation ou de déterminer le niveau de cisaillement à ne pas dépasser pendant la mise en œuvre de la suspension.

B. La déstabilisation sous l'effet de la variation de la force ionique a été évaluée en mesurant la concentration critique de coagulation par ajout de sel. Le résultat a montré que la formulation conçue possède une concentration critique de coagulation très élevée (0,7 mole de NaCl) indiquant une haute stabilité colloïdale.

C. La déstabilisation sous l'effet de la variation du pH a été évaluée en diluant la suspension dans différents milieux à différents pH. Les résultats de ce test n'ont monté aucune déstabilisation lorsque le pH est supérieur à 2. En revanche, nous avons observé une déstabilisation à pH 2 est probablement due à la dégradation du SDS à ce pH.

D. La déstabilisation par désorption a été effectuée en diluant la suspension dans de l'eau par un facteur 1000. La taille des particules a ensuite été suivie sous agitation. Le résultat de ce test n'a montré aucune déstabilisation.

E. Enfin, la déstabilisation sous l'effet de la température a été effectuée en stockant la suspension à différentes températures (20, 40, 50 et 60°C). Pendant le stockage, nous avons suivi l'évolution de la taille des particules au cours du temps. Le résultat de ce test a montré que la suspension est stable à 20°C. Lorsque la température augmente, nous avons enregistré une augmentation de la taille des particules au cours du stockage. Ce résultat peut s'explique par une augmentation de la solubilité de la PVP avec la température. Sur la base de ce résultat nous avons recommandé soit d'ajouter du sel à la formulation ou d'ajouter un agent de protection contre la chaleur si la suspension devra être stérilisée par autoclavage.

(ii) Comparaison systématiques des technologies de fabrication des suspensions nanocristallines (broyage à billes versus homogénéisation haute pression). Les principes de broyage des deux technologies utilisées dans l'approche dite « top-down » (broyage à billes et homogénéisation haute pression) sont totalement différents. Le broyage à billes est basé sur les forces de cisaillement et l'énergie élevée engendrée par les collisions avec les média de broyage. En revanche, la fracture des particules par l'homogénéisation haute pression est provoquée par la cavitation, par des forces de cisaillement élevées et par les collisions des particules les unes contre les autres. Le choix de la technologie appropriée pour la production de suspension nanocristalline dépend d'un certain nombre de questions que l'on peut se poser sur la qualité de la nano-suspension produite par les deux technologies telles que: comment la technologie influence-t-elle la formation et la stabilité des nano-suspensions ?, comment la stabilité physique des particules diffère-t-elle lorsque l'on utilise le même principe actif dans les deux technologies ?, comment la taille des particules est-elle influencée par la technologie utilisée?, Quelle technologie est facilement transposable à l'échelle industrielle, fournissant peu de variation d'un lot à un autre? quelle est la sensibilité de la technologie au regard de l'érosion et la contamination de la suspension produite ?, comment la structure cristalline ou l'amorphisation des nanoparticules changent-elles lorsque l'on utilise les deux technologies? Et enfin, les technologies sont-elles suffisamment fiables, robustes et conformes et conformes à la réglementation pharmaceutique pour la production de suspensions pharmaceutiques qui peuvent être utilisées pour différents voies d'administration? Le travail réalisé dans cette section a été conçu pour aborder certaines de ces questions. A cet effet, nous avons comparé les suspensions produites par les deux technologies en étudiant l'impact de la formulation (Type de stabilisant, concentration de stabilisant, type de principe actif, concentration de principe actif et viscosité de la suspension), énergie de broyage, taille et configuration du broyeur. La comparaison des deux technologies a mis en évidence les points suivants :

a) Les deux technologies se comportent de manière similaire au regard de l'énergie. En effet, plus l'énergie est élevée, plus la cinétique de broyage est rapide. De plus, nous avons observé que le niveau d'énergie impacte considérablement la cinétique de broyage mais pas le profil de distribution granulométrique.
b) Le broyeur à billes conduit à une suspension plus fine que celle obtenue par homogénéisation haute pression. De plus, il a été montré pour les 2 technologies que la relation d_{90} versus d_{50} est décrite par une seule courbe maîtresse indépendamment des paramètres du procédé et de l'échelle utilisée. Ceci a clairement mis en évidence que l'homogénéisation haute pression conduit pour le même diamètre médian à une distribution granulométrique plus resserrée que celle obtenue par broyage à billes. En outre, A même diamètre médian (200 nm), nous avons observé que la distribution granulométrique obtenue par homogénéisation haute pression est dépourvue de particules supérieurs à 2 µm ce qui n'est pas le cas du broyeur à billes.
c) La morphologie des particules broyées est parfois dépendante de la technologie utilisée. En effet, dans certains cas nous avons obtenu des particules de formes irrégulières par homogénéisation haute pression et de formes aiguilles par broyage à

bille. A la date, nous n'avons pas trouvé une rationnel permettant d'expliquer cette différence

d) Aucune différence n'a été observée concernant l'impact de la technologie sur la structure cristalline du principe actif utilisé. En effet, pour les deux technologies, dans la mesure où la forme cristalline la plus stable dans l'eau est utilisée, aucune transition polymorphique n'a été observée pour les principes actifs étudiés.

e) La technologie du broyage à billes est plus sensible à l'érosion que l'homogénéisation haute pression.

f) Les deux technologies sont fiables, robustes et peuvent être utilisées dans un environnement régi par les bonnes pratiques de fabrication.

(iii) Modélisation du procédé de broyage à billes en vue de la prédiction et la simulation des paramètres de fabrication nécessaire à l'obtention d'une suspension nanocristalline avec une taille de particules donnée. Dans l'industrie pharmaceutique en général, la chaîne de de développement du procédé de broyage utilisée pour soutenir les projets de la phase pé-clinique jusqu'à la phase III peut impliquer différentes configurations de broyeur. Lors du développement du procédé de broyage, il est important de reproduire la même qualité physique de la suspension obtenue à petite échelle que celle obtenue 'à grande échelle. C'est à cet effet que dans cette section nous avons proposé un modèle qui permet de réaliser cet objectif. Le but de ce modèle est de simuler et prédire les cinétiques de broyage des différents équipements ainsi que le transfert du procédé de broyage d'un équipement à un autre.

Dans cette section, nous avons rapporté que bien que seulement 5 % de l'énergie est utilisée pour réduire la taille des particules, l'approche énergétique reste pertinente pour étudier et modéliser le procédé de broyage. Une des méthodes utilisée à cet effet est celle développée par Tanaka et Chodakov (cinétique du premier ordre). Cette méthode est capable de décrire les cinétiques de broyage d'une majorité de produits. Cependant, elle n'est pas adaptée pour décrire les cinétiques de broyage des principes actifs qui sont difficiles à broyer. En effet, lors de nos travaux, nous avons observé que les cinétiques de broyage de ces principes actifs ne suivent pas une loi apparente de premier ordre car elles ont une forme sigmoïde présentant une période de temps où le broyage n'est pas très actif. Cette période de temps peut être assimilée à un temps d'induction. Mathématiquement, nous avons trouvé une équation généralisée où l'équation de Tanaka et Chadakov est un cas particulier. Cette équation a été inspirée de l'équation d'Avrami initialement utilisée pour décrire la transition de phase solide-solide à température constante, où le mécanisme original est la nucléation d'une nouvelle phase suivie par la croissance puis la terminaison. L'utilisation de l'équation d'Avrami pour la modélisation du broyage nous semblait pertinente car la même analogie a été rapportée pour expliquer le mécanisme de réduction de la taille des particules (compression suivi de création de défaut puis fragmentation). Cette équation possède trois paramètres : ($(6/d_{50})_\infty$) qui représente la valeur asymptotique de la cinétique de broyage , (τ) qui représente le temps caractéristique de la cinétique de broyage et (n^*) qui représente l'indice d'induction de broyage Les résultats de cette étude ont montré que:

(a) Le modèle proposé est capable de s'agencer parfaitement avec les données expérimentales des cinétiques de broyage issues des différents principes actifs. Le modèle a mis en évidence que ((6/d50)∞) est très dépendant des principes actifs utilisés et probablement de leur taille des cristallites. Par ailleurs, (n*) est très dépendant des principes actifs utilisés et probablement de leur propriétés mécaniques.

(b) Le modèle proposé est capable de s'agencer parfaitement avec les données expérimentales des cinétiques de broyage issues des différentes technologies avec le même principe actif. Le modèle a mis en évidence que ((6/d50)∞) n'est pas impacté par la technologie mise en œuvre

(c) Le modèle proposé est capable de s'agencer parfaitement avec les données expérimentales des cinétiques de broyage issues des différents paramètres de broyages (vitesse de rotation, taux de charges en billes et concentration en principe actif) appliqué au même principe actif sur une même technologie. Le modèle a mis en évidence que ((6/d50)∞) et (n^*) ne sont pas impactés par les paramètres de broyage mis en œuvre. Seul (τ) est impacté par ces paramètres de broyage. A cet effet, nous avons établi une solide corrélation reliant (τ) aux paramètres de broyage pour un même principe et une même technologie

(d) Le modèle établi permet aisément le transfert du procédé d'un broyeur à un autre.

En conclusion, nos travaux ont permis d'établir une méthodologie de conception de la formulation basée sur les principes physico-chimiques des colloïdes. Cela a abouti à une suspension nanocristalline stable et robuste aux conditions des différents procédés mis en œuvre ainsi qu'aux conditions de stockage. Pour la partie conception du procédé, nous avons montré que dans la mesure où la formulation mise en œuvre et robuste les deux technologies de broyages (broyage à billes et homogénéisation haute pression) sont adaptées à la production des suspensions nanocristallines pour usage pharmaceutique. Enfin, le modèle que nous avons proposé pour suivre les cinétiques de broyage s'agence parfaitement avec les données expérimentales et permet de simuler et de prédire les cinétiques de broyage en fonction des paramètres et de la technologie de broyage mis en œuvre

Bibliography references

9. Bibliography references

1. Emerich DF, Thanos CG. The pinpoint promise of nanoparticle-based drug delivery and molecular diagnosis. Biomol Eng. 2006;23(4):171–84.

2. Cahier-ANR-5-nanotechnologies new paradigm. 2012;

3. Gabizon A, Shmeeda H, Barenholz Y. Pharmacokinetics of Pegylated Liposomal Doxorubicin. Clin Pharmacokinet. 2003 Apr 1;42(5):419–36.

4. Klumpp CK Kostas; Prato, Maurizio; Bianco, Alberto. Functionalized carbon nanotubes as emerging nanovectors for the delivery of therapeutics. Biochim Biophys Acta BBA - Biomembr. 2006;1758(3):404–12.

5. Liggins RT, Burt HM. Polyether–polyester diblock copolymers for the preparation of paclitaxel loaded polymeric micelle formulations. Adv Drug Deliv Rev. 2002;54(2):191–202.

6. Paciotti GF, Kingston DGI, Tamarkin L. Colloidal gold nanoparticles: a novel nanoparticle platform for developing multifunctional tumor-targeted drug delivery vectors. Drug Dev Res. 2006;67(1):47–54.

7. Letchford K, Burt H. A review of the formation and classification of amphiphilic block copolymer nanoparticulate structures: micelles, nanospheres, nanocapsules and polymersomes. Eur J Pharm Biopharm. 2007;65(3):259–69.

8. Sutton DN Norased; Blanco, Elvin; Gao, Jinming. Functionalized micellar systems for cancer targeted drug delivery. Pharm Res. 2007;24(6):1029–46.

9. Junghanns J-UA, Müller RH. Nanocrystal technology, drug delivery and clinical applications. Int J Nanomedicine. 2008;3(3):295.

10. Jens-Uwe A H Junghanns RHM. Nanocrystal technology, drug delivery and clinical applications. Int J Nanomedicine. 2008;3(3):295–309.

11. Andeep Singh Chahal* AM SJ Kshirsagar, MR Bhalekar, Amrita Dikpati, Pranjali Gawli. Amorphous Nanoparticles for Solubility Enhancement. J Adv Pharm Sci. 2(1):168–78.

12. Rossi JG Suzanne; Khalid, Mohamed Nabil; Delmas, Pascal; Allen, Christine; Leroux, Jean-Christophe. Long-circulating poly (ethylene glycol)-coated emulsions to target solid tumors. Eur J Pharm Biopharm. 2007;67(2):329–38.

13. Trotta M, Pattarino F, Ignoni T. Stability of drug-carrier emulsions containing phosphatidylcholine mixtures. Eur J Pharm Biopharm. 2002;53(2):203–8.

14. GOYAL PG KUMUD; KUMAR, SENGODAN GURUSAMY VIJAYA; SINGH, AJIT; KATARE, OM PRAKASH; MISHRA, DINA NATH. Liposomal drug delivery systems-clinical applications. Acta Pharm. 2005;55(1):1–25.

15. Immordino ML, Dosio F, Cattel L. Stealth liposomes: review of the basic science, rationale, and clinical applications, existing and potential. Int J Nanomedicine. 2006;1(3):297.

16. Torchilin VP. Recent advances with liposomes as pharmaceutical carriers. Nat Rev Drug Discov. 2005;4(2):145–60.

17. Müller RH, Mäder K, Gohla S. Solid lipid nanoparticles (SLN) for controlled drug delivery–a review of the state of the art. Eur J Pharm Biopharm. 2000;50(1):161–77.

18. Severino PA Tatiana; Macedo, Ana Sofia; Fangueiro, Joana F; Santana, Maria Helena A; Silva, Amélia M; Souto, Eliana B. Current state-of-art and new trends on lipid nanoparticles (SLN and NLC) for oral drug delivery. J Drug Deliv. 2011;2012.

19. Soppimath KS. A Tejraj M.Kulkarni, Anandrao R.Rudzinski, Walter E. Biodegradable polymeric nanoparticles as drug delivery devices. J Controlled Release. 2001;70(1–2):1–20.

20. Kamaly NX Zeyu; Valencia, Pedro M; Radovic-Moreno, Aleksandar F; Farokhzad, Omid C. Targeted polymeric therapeutic nanoparticles: design, development and clinical translation. Chem Soc Rev. 2012;41(7):2971–3010.

21. Ahmed F, Discher DE. Self-porating polymersomes of PEG–PLA and PEG–PCL: hydrolysis-triggered controlled release vesicles. J Controlled Release. 2004;96(1):37–53.

22. Jain JP, Kumar N. Development of amphotericin B loaded polymersomes based on (PEG) 3-PLA co-polymers: factors affecting size and in vitro evaluation: Factors affecting size and in vitro evaluation. Eur J Pharm Sci. 2010;40(5):456–65.

23. Zhang Y, Zhang W, Johnston AH, Newman TA, Pyykkö I, Zou J. Targeted delivery of Tet1 peptide functionalized polymersomes to the rat cochlear nerve. Int J Nanomedicine. 2012;7:1015.

24. Liong M, Lu J, Kovochich M, Xia T, Ruehm SG, Nel AE, et al. Multifunctional inorganic nanoparticles for imaging, targeting, and drug delivery. ACS Nano. 2008;2(5):889–96.

25. Ojea-Jimenez IC Joan; Garcia-Fernandez, Lorena; Megson, Zoe A; Casals, Eudald; Puntes, Victor F. Engineered Inorganic Nanoparticles for Drug Delivery Applications. Curr Drug Metab. 2013;14(5):518–30.

26. Pouton CW. Lipid formulations for oral administration of drugs: non-emulsifying, self-emulsifying and “self-microemulsifying”drug delivery systems. Eur J Pharm Sci. 2000;11:S93–8.

27. Aungst BJ. Novel formulation strategies for improving oral bioavailability of drugs with poor membrane permeation or presystemic metabolism. J Pharm Sci. 1993;82(10):979–87.

28. J AB. Intestinal permeation enhancers. J Pharm Sci. 2000;89(4):429–42.

29. Aungst BJN Nhung H; Rogers, Nancy J; Rowe, Susan M; Hussain, Munir A; White, Susan J; Shum, Linyee. Amphiphilic vehicles improve the oral bioavailability of a poorly soluble HIV protease inhibitor at high doses. Int J Pharm. 1997;156(1):79–88.

30. Schwendener RA, Schott H. Lipophilic 1-β-d-arabinofuranosyl cytosine derivatives in liposomal formulations for oral and parenteral antileukemic therapy in the murine L1210 leukemia model. J Cancer Res Clin Oncol. 1996 Dec 1;122(12):723–6.

31. Floyd AG. Top ten considerations in the development of parenteral emulsions. Pharm Sci Technol Today. 1999;2(4):134–43.

32. Lawrence MJ, Rees GD. Microemulsion-based media as novel drug delivery systems. Adv Drug Deliv Rev. 2012;

33. Leuner C, Dressman J. Improving drug solubility for oral delivery using solid dispersions. Eur J Pharm Biopharm. 2000;50(1):47–60.

34. Serajuddin A. Solid dispersion of poorly water-soluble drugs: early promises, subsequent problems, and recent breakthroughs. J Pharm Sci. 1999;88(10):1058–66.

35. Loftsson T, Brewster ME. Pharmaceutical applications of cyclodextrins. 1. Drug solubilization and stabilization. J Pharm Sci. 1996;85(10):1017–25.

36. Stella VJ, Rajewski RA. Cyclodextrins: their future in drug formulation and delivery. Pharm Res. 1997;14(5):556–67.

37. Rabinow BE. Nanosuspensions in drug delivery. Nat Rev Drug Discov. 2004;3(9):785–96.

38. Shegokar R, Müller R. Nanocrystals: Industrially feasible multifunctional formulation technology for poorly soluble actives. Int J Pharm. 2010;399(1–2):129–39.

39. Kesisoglou F, Panmai S, Wu Y. Nanosizing—oral formulation development and biopharmaceutical evaluation. Adv Drug Deliv Rev. 2007;59(7):631–44.

40. Noyes AA, Whitney WR. The rate of solution of solid substances in their own solutions. J Am Chem Soc. 1897;19(12):930–4.

41. Mosharraf M, Nyström C. The effect of particle size and shape on the surface specific dissolution rate of microsized practically insoluble drugs. Int J Pharm. 1995;122(1):35–47.

42. Müller RH, Gohla S, Keck CM. State of the art of nanocrystals–special features, production, nanotoxicology aspects and intracellular delivery. Eur J Pharm Biopharm. 2011;78(1):1–9.

43. Borm PK Frederick C; Landry, Timothy D; Moudgil, Brij; Pauluhn, Jürgen; Thomas, Karluss; Trottier, Remi; Wood, Stewart. Research strategies for safety evaluation of nanomaterials, part V: role of dissolution in biological fate and effects of nanoscale particles. Toxicol Sci. 2006;90(1):23–32.

44. Kipp JE. The role of solid nanoparticle technology in the parenteral delivery of poorly water-soluble drugs. Int J Pharm. 2004;284(1–2):109–22.

45. Wong JB Andrew; Khare, Atul; Chaubal, Mahesh; Papadopoulos, Pavlos; Rabinow, Barrett; Kipp, James; Ning, John. Suspensions for intravenous (IV) injection: a review of development, preclinical and clinical aspects. Adv Drug Deliv Rev. 2008;60(8):939–54.

46. Bazile D. Nanotechnologies tools in candidate selection for the intravenous route. SMi – 8th Conf Control Release Lond. 2011 Mar;

47. Gao LZ Dianrui; Chen, Minghui; Duan, Cunxian; Dai, Wenting; Jia, Lejiao; Zhao, Wenfa. Studies on pharmacokinetics and tissue distribution of oridonin nanosuspensions. Int J Pharm. 2008;355(1):321–7.

48. Douglas F, Kafilmout K, Patt N. Foreign particle embolism in drug addicts: respiratory pathophysiology. Ann Intern Med. 1971;75(6):865–72.

49. Ward SH LE Reittner, P; Kazerooni, EA Godwin, JD Müller, N. Talcosis Associated with IV Abuse of Oral Medications CT Findings. Am J Roentgenol. 2000;174(3):789–93.

50. Möschwitzer J, Müller RH. New method for the effective production of ultrafine drug nanocrystals. J Nanosci Nanotechnol. 2006;6(9–10):3145–53.

51. Kipp JE, Wong JCT, Doty MJ, Rebbeck CL. Microprecipitation method for preparing submicron suspensions. 2005;

52. Tadros T. Course at sanofi: Nano-dispersion. 2009;

53. Welin-Berger K, Bergenståhl B. Inhibition of Ostwald ripening in local anesthetic emulsions by using hydrophobic excipients in the disperse phase. Int J Pharm. 2000;200(2):249–60.

54. Tadros T. Applied Surfactants: Principles and Applications. 2005.

55. Vitale SA, Katz JL. Liquid droplet dispersions formed by homogeneous liquid-liquid nucleation:“The ouzo effect.” Langmuir. 2003;19(10):4105–10.

56. Puneet S, William A D, Sanjay G. Effect of wet milling process on the solid state of indomethacin and simvastatin. Int J Pharm. 2009;380(1):40–8.

57. Harkins WD, Dahlstrom R. Wetting of pigments and other powders. Ind Eng Chem. 1930;22(8):897–902.

58. Chander S. H R. Characterization of the Wetting and Dewetting Behavior of Powders. Kona. 2007;25:56–75.

59. Monteiro A, Afolabi A, Bilgili E. Continuous production of drug nanoparticle suspensions via wet stirred media milling: a fresh look at the Rehbinder effect. Drug Dev Ind Pharm. 2013;39(2):266–83.

60. Walker P, Petersen E, Wright C. Surface active agent phenomena in dust abatement. Ind Eng Chem. 1952;44(10):2389–93.

61. Kossen N, Heertjes P. The determination of the contact angle for systems with a powder. Chem Eng Sci. 1965;20(6):593–9.

62. White LR. Capillary Rise in Powders,. J Coll Interf Sci. 90:536–8.

63. Siebold A, Nardin M, Schultz J, Walliser A, Oppliger M. Effect of dynamic contact angle on capillary rise phenomena. Colloids Surf Physicochem Eng Asp. 2000;161(1):81–7.

64. Derjaguin BV LL. Theory of the stability of strongly charged lyophobic sols and of the adhesion of strongly charged particles in solutions of electrolytes. Acta Physicochim URSS. 1941;14:633.

65. Verwey EJW OJ. Theory of the stability of lyophobic colloids. Amst Elsevier Publ Co Inc. 1948;

66. London. “The General Theory of Molecular Forces,.” Trans Faraday Soc. 1937;33:8–26.

67. Keesom WH. On the Deduction of the Equation of State from Boltzmann’s Entropy Principle. Commun Phys Lab Univ Leiden. 1912;Supplement 24a to No. 121–132:3–20.

68. Hamaker H. The London—van der Waals attraction between spherical particles. physica. 1937;4(10):1058–72.

69. Lifschitz E.M. Theory of molecular attractive forces. Sov Phys JETP. 1956;2(73–83).

70. Israelachvili J. Intermolecular and surface forces. 1992;London: Academic Press;

71. Gouy LG. Sur la constitution de la charge électrique à la surface d’un électrolyte. J Phys. 1910;4(457 – 467).

72. Chapman DL. A contribution to the theory of electrocapillary. Phil Mag. 1913;6(25):475–81.

73. Grahame DC. The electrical double layer and the theory of electrocapillarity. Chem Rev. 1947;41:441 – 501.

74. Walker G. Interactions between particles. Httpsst-WebteesacukexternalU0000504Notescolloidscolloids04colloids04htmlTop. 1999;

75. Tadros TF. Solid/Liquid Dispersions. Acad Press Lond. 1987;

76. Singh M. Role of Hydrophobically Modified Inulin on Rubber Latex Stability and Film Formation. Thesis Univ Barc CSIC. 2012 Apr;

77. Heller W and P TL. Steric protection of hydrophobic colloidal particles by adsorption of flexible macromolecules. J Chem Phys. 1954;22:1778.

78. Tobolsky AV. Properties and structure of polymers. 1960;

79. Tadros TFB R; Corner, T; Stageman, J. Polymer Colloids. Eds Elsevier Appl Sci Lond. 1985;

80. Fisher EW. Elektronenmikroskopische Untersuchungen zur Stabilität von Suspensionen in makromolekularen Lösungen. Kolloid-Z. 1958;160:120 – 141.

81. Tadros TF. Rheology of Dispersions: Principles and Applications. Wiley-VCH Verl GmbH Co KGaA Weinh Ger. 2010;

82. Churaev NV DB. Inclusion of structural forces in the theory of stability of colloids and films. J Colloid Interface Sci. 1985;103:542–53.

83. Leikin S, Parsegian VA, Rau DC, Rand RP. Hydration forces. Annu Rev Phys Chem. 1993;44(1):369–95.

84. Sato T, Ruch R. Stabilization of colloidal dispersions by polymer adsorption. Marcel Dekker Inc N Y. 1980;

85. Norde WC and I in LS. Colloids and Interfaces in Life Sciences. Book. 2003;Markel Dekker, Inc., New York, USA.

86. Lauten RA, Kjøniksen A-L, Nyström B. Colloid polymer interactions and aggregation in aqueous mixtures of polystyrene latex, sodium dodecyl sulfate, and a hydrophobically modified polymer: A dynamic light scattering study. Langmuir. 2001;17(3):924–30.

87. Heinmenz PC and R R. Principles of Colloid and Surface Chemistry. Marcel Dekker N Y. 1997;3rd ed.,.

88. Schmoluchowski M. Z Phys Chem. 1917;92:129–68.

89. Le Berre F, Chauveteau G, Pefferkorn E. Perikinetic and orthokinetic aggregation of hydrated colloids. J Colloid Interface Sci. 1998;199(1):1–12.

90. M. Elimelech JG X Jia, RA Williams,. Particle Deposition and Aggregation, Measurement, Modelling and Simulation. Woburn,. 1995;Butterworths–Heinemann, Woburn,.

91. Hiemenz PC., Rajagopalan R. Principles of colloid and surface chemistry. 3rd Ed Marcel Dekker Inc NewYork. 1997;255–265.

92. C W. Theorie der Alterung vo Niederschla gen durch Umlosen. Z Elektrochem. 1961;65(581–591).

93. Ostwald W. Uber die vemeintliche Isomerie des roten und gelben Queck-silberoxyds und die Oberflachen-spannung Fester Korper. ZPhysChem. 1901;34(599):495–512.

94. Lifshitz I, Slyozov V. The kinetics of precipitation from supersaturated solid solutions. J Phys Chem Solids. 1961;19:35–50.

95. RT D. Generalized microstructural evolution by interface controlled coarsening. Acta Met Mater. 1984;32:43–47.

96. Solomatov VS SD. Kinetics of crystal growth in a terrestrial magma ocean. J Geophys Res. 1993;(98):5407–5418.

97. Verma S Lan,Y.Gokhale,R.Burgess,DJ. Quality by design approach to understand the process of nanosuspension preparation. 2009;377:185–198.

98. Pace SN Pace,GW.Parikh,I.Mishra,AK. Novel injectable formulations of insoluble drugs. PharmTechnol. 1999;23:116–134.

99. Lindfors L Skantze,P.Skantze,U.Rasmusson,M.Zackrisson,A.Olsson,U. Amorphous drug nanosuspensions Inhibition of Ostwald ripening. Langmuir. 2006;22:906–910.

100. Jacobs C Kayser,O.Muller,RH. Nanosuspensions as a new approach forthe formulation of poorly soluble drug tarapezide. IntJPharm. 2000;196:161–164.

101. Eerdenberg BV Froyen, L ,Humbeeck,JV.Martens,JA.Augustijns, P ,MooterGV. Drying of crystalline nanosuspensions—the importance of surface hydrophobicity on dissolution behavior upon redispersion. EurJPharmSci. 2008;35:127–135.

102. Chaubal MV Popescu,C. Conversion of nanosuspensions into dry powders by spray drying:a case study. PharmRes. 2008;25:2302–2308.

103. Hunter RJ. Zeta Potential In Colloid Science: Principles And Applications. Acad Press UK. 1988;

104. Stephane Foucault GA and Philippe A Tanguy. Power Characteristics in Coaxial Mixing: Newtonian and Non-Newtonian Fluids. Ind Eng Chem Res. 2005;44:5036–43.

105. Holland FA and Chapman, FS. Liquid Mixing and Processing in Stirred Tanks. Reinhold N Y. 1996;78.

106. Oldshue JY. Fluid Mixing Technology. McGraw–Hill N Y. 1984;

107. Woburn 1995. N. Marti F Quattrini, A Butte, M Morbidelli,. Macromol Mater Eng. 2005;290:221–229.

108. V. Oles. J Colloid Interface Sci. 1992;154:351–358.

109. K.A. Kusters. The influence of turbulence on aggregation of small particlesin agitated vessel. PhD Thesis Eindh Univ Technol Neth Eindh. 1991;

110. Spicer PT, Keller W, Partsinis SE. The Effect of Impeller Type on Floc Size and Structure during Shear-Induced Flocculation. J COLLOID INTERFACE Sci. 1996;184:112–122.

111. Spicer PT, Pratsinis SE. Shear-induced flocculation: the evolution of floc structure and the shape of the size distribution at steady state. Water Res. 1996;30(5):1049–56.

112. Kusters KA, Wijers JG, Thoenes D. Aggregation kinetics of small particles in agitated vessels. Chem Eng Sci. 1997;52(1):107–21.

113. Serra TC Jordi; Casamitjana, Xavier. Aggregation and breakup of particles in a shear flow. J Colloid Interface Sci. 1997;187(2):466–73.

114. P.T. Spicer SEP JA Raper, R Amal, G Bushell, G Meesters,. Powder Technol. 1998;97:26–34.

115. Boller M, Blaser S. Particles under stress. Water Sci Technol. 1998;37(10):9–29.

116. Miroslav Soos ASM Lyonel Ehrl ,Jan Sefcik, HuaWu, Massimo Morbidelli. Effect of shear rate on aggregate size and morphology investigated under turbulent conditions in stirred tank. J Colloid Interface Sci. 2008;319:577–589.

117. Sorensen C. Light scattering by fractal aggregates: a review. Aerosol Sci Technol. 2001;35(2):648–87.

118. Geissler R. AM and HV. Macro-and micromixing in stirred tanks. Int Chem Eng. 1991;31:642–53.

119. Ajaol TT. The Development and Characterization of a Bali Mill for Mechanical Alloying. Thesis Queens Univ Kingston Ont Can. 1999;

120. Rose HE Sullivan, RME. A Treastise on the Internal Mechanics of Ball. Tube and Rod Mills. Constable Lond. 1958;35–67.

121. Mishra BK, Rajamani RK. Comminution Theory and Particles,. Book. 1992;Editor S. Komar Kawatra, Soc. for Mining, Metall. and Exploration, Inc. Littleton CO:427–40.

122. George Charles Lowrisen . Crushing and Grinding: The Size Reduction of Solid Materials. Butterworths Lond. 1974;225–54.

123. AMS Committee on Milling,. Met Handb. 7:56–70.

124. Takova K. Developments in Mineral Processing, Mechanical Activation of Minerals. Elsevier. 1989;11:70–108.

125. Austin LG, Luckie PT. Methods for determination of breakage distribution parameters. Powder Technol. 1972;5(4):215–22.

126. Peltonen L, Hirvonen J. Pharmaceutical nanocrystals by nanomilling: critical process parameters, particle fracturing and stabilization methods. J Pharm Pharmacol. 2010;62(11):1569–79.

127. Kwade A. Wet comminution in stirred media mills — research and its practical application. Powder Technol. 1999;105:14–20.

128. Van Eerdenbrugh B, Van den Mooter G, Augustijns P. Top-down production of drug nanocrystals: nanosuspension stabilization, miniaturization and transformation into solid products. Int J Pharm. 2008;364(1):64–75.

129. Eerdenbrugh BV. Nanosuspension stabilization , miniaturization and transformation into solid product. Thesis Katolieke Univ Leuven. 2008;

130. Netzsch. Technical documents. 2015; Available from: www.netzsch-grinding.com

131. Kumar S, Burgess DJ. Wet milling induced physical and chemical instabilities of naproxen nano-crystalline suspensions. Int J Pharm. 2014;466(1):223–32.

132. Bernhardt C, Reinsch E, Husemann K. The influence of suspension properties on ultra-fine grinding in stirred ball mills. Powder Technol. 1999;105(1):357–61.

133. J.Schwedes SM. Mechanical production and stabilization of nanoparticles by wet communition in stirred media mills. Powder Technol. 2006;18(6):366–73.

134. Stadler R, Polke R, Schwedes J, Vock F. Naßmahlung in Rührwerksmühlen. Chem Ing Tech. 1990;62(11):907–15.

135. Bunge F. Dissertation. Braunschweig. 1992;

136. Weit H. PhD Diss Braunscheig Geramany Tech Univ Braunschw. 1987;

137. Kwade A. Advanced in communition. Book. 2006;

138. Innings F. Engineering Aspects of Food Emulsification and Homogenization. Book. 2015;149.

139. Wuytack E., Diels A, Michiels C. Bacterial inactivation by high-pressure homogenisation and high hydrostatic pressure. Int J Food Microbiol. 2002;77(3):205–12.

140. Müller RH, Jacobs C, Kayser O. Nanosuspensions as particulate drug formulations in therapy: Rationale for development and what we can expect for the future. Adv Drug Deliv Rev. 2001;47(1):3–19.

141. Midoux N, Nakach M. High pressure homogeneisation. Sanofi Intern Doc. 2011;

142. Nekkanti V, Vabalaboina V, Pillai R. Drug Nanoparticles – An Overview. Deliv Nanoparticles. 2012;Book:111–32.

143. Niro-Soavi G. Technical documents. 2015; Available from: http://www.gea.com/global/en/productgroups/homogenizers

144. Homogeneising valve. http://en.wikipedia.org/wiki/Homogenization_(chemistry).

145. Timpe C. Drug Solubilization Strategies Applying Nanoparticulate Formulation and Solid Dispersion Approaches in Drug Development. 2010;

146. Kawaguchi T. Entrance loss for turbulent flow without swirl between parallel discs. Bull JSME. 1971;14:335–63.

147. Kleinig AR Ide, BH.Middelberg, APJ. High pressure homogenizer valve mechanics. CHEMECA 95 23rd Aust Chem Eng Conf. 1995;3:50–5.

148. Kleinig AR Middelberg, APJ. Fluid mechanics of high pressure homogenizer. 1996 IChemE Res Event 2nd Euro Conf YoungRes Chem Enh. 1996;1:109–11.

149. Nakayama Y. Action of fluid in the air-mcrometer (3rd report, characterristics of double-disc nozzle no. 1, in the case of compressibility being ignored). Bull JSME. 1964;7:698–607.

150. Phipps LW. The fragmentation of oil drops in emulsion by a high-pressure homogenizer. J Phys Appl Phys. 1975;8:448–62.

151. Phipps LW. Some operating characteristics of a simple homogenizing poppet valve; pressure profile and separation: zone of fat globule dispersion. J Dairy Res. 1974;41:339–47.

152. Stevenson MJ Chen, XD. Visualization of the %ow patterns in a high-pressure homogenising valve using a CFD package. J Food Eng. 1997;33:151–165.

153. Håkansson A, Trägårdh C, Bergenståhl B. Dynamic simulation of emulsion formation in a high pressure homogenizer. Chem Eng Sci. 2009;64(12):2915–25.

154. Brennen CE. Cavitation and bubble dynamics. Oxford University Press; 1995.

155. Franc J-P and M JM. Fundamentals of Cavitation. Springer Sci Berl. 2005;

156. Kurzhals H-A. Untersuchungen über die physikalisch-technischen Vorgänge beim Homogenisieren von Milch in Hochdruck-Homogenisiermaschinen. Dr ThesisTechnischen Univ Hann. 1977;

157. Pearsall IS. Acoustic detection of cavitation. Proceed Inst Mech Eng. 1966;181(1–8).

158. Rus T Dular, M.Sirok, B.Hocevar, M.Kern, I. An investigation of the relationship between acoustic emission, vibration, noise, and cavitation structures on a Kaplan turbine. J Fluids Eng. 2007;129(9):1112–1122.

159. B.H. Kaye. “Permeability Techniques for Characterizing Fine Powders,.” Powder TechnoL. 1967;1(11–22).

160. Rigden P. The specific surface of powders. A modification of the theory of the air-permeability method. J Soc Chem Ind. 1947;66(4):130–6.

161. Pecora R. Dynamic light scattering: applications of photon correlation spectroscopy. Springer; 1985.

162. Swithenbank JB JM; Taylor, DS; Abbot, D; McCreath, GC. A laser diagnostic technique for the measurement of droplet and particle size distribution. In 1976.

163. S. C. Biswas LD and D Marion. Interfacial Behavior of Wheat Puroindolines: Study of Adsorption at the Air–Water Interface from Surface Tension Measurement Using Wilhelmy Plate Method. J Colloid Interface Sci. 2001;244:245–253.

164. Aartsen BHGB and JJ van. The determination of contact angles of aqueous surfactant solutions on powders. Colloid Polym Sci. 1974;252:32–8.

165. P.Somasundara. Encyclopedia of surface and colloid science. Taylor Francis Group. 2006;3:1758–70.

166. Dijit. J.; Cohen Sturat M. F G. Kinetic of polymer adsorption in cappilary flow. macromolecules. 1992;25:5416–23.

167. Sommer MM. Mechanical Production of Nanoparticles in Stirred Media Mills. Thesis Fak Univ Erlangen-N¨urnberg. 2007;

168. Pritchard JF. Fast-to-patient: Creative strategies for quick demonstration of clinical proof-of-concept. Regul Rapp. 2010;7(3):7–10.

169. Nakach MA JR.Tadros, T; Galet, L; Chamayou, A. Engineering of nano-crystalline drug suspension: Employing a physico-chemistry based stabilizer selection methodology or approach. Int J Pharm. 2014;476:277–88.

170. Tadros TF. Dispersion of Powders in Liquids and Stabilization of Suspensions. Book Chapter Struct Solid-Liq Interface Electrost Stab Tharwat. 2012;ISBN: 9783527329410.

171. Cabane B. Structure of Some Polymer-Detergent Aggregates in Water. J Phys Chemlstry. 1977;81(17):1639–45.

172. Deng Z, Xu S, Li S. Understanding a relaxation behavior in a nanoparticle suspension for drug delivery applications. Int J Pharm. 2008;351(1):236–43.

173. Anderson VJ, Lekkerkerker HNW. Insights into phase transition kinetics from colloid science. NATURE. 2002;416:811–5.

174. Omari A, Chauveteau G, Tabary R. Gelation of polymer solutions under shear flow. Colloids Surf Physicochem Eng Asp. 9;225(1–3):37–48.

175. Napper DH. Polymeric stabilization of colloidal dispersion,. Acad Press Lond. 1982;

176. Tadros TF. Effect of polymers on dispersion properties,. Ed Acad Press Lond. 1982;

177. Laurent Taisne PiWABC. Transfer of Oil between Emulsion Droplets. J COLLOID INTERFACE Sci. 1996;184:378–390.

178. Yu Y, von Gottberg F. Coagulation kinetics of surface modified pigment particles. In Society for Imaging Science and Technology; 2002. p. 383–7.

179. Potanin AA. On the mechanism of aggregation in the shear flow of suspensions. J Colloid Interface Sci. 8;145(1):140–57.

180. Corti M, Minero C, Degiorgio V. Cloud point transition in nonionic micellar solutions. J Phys Chem. 1984;88(2):309–17.

181. Jenkins P, Snowden M. Depletion flocculation in colloidal dispersions. Adv Colloid Interface Sci. 11;68:57–96.

182. Kiratzis N, Faers M, Luckham PF. Depletion flocculation of particulate systems induced by hydroxyethylcellulose. Colloids Surf Physicochem Eng Asp. January 7;151(3):461–71.

183. Nakach MA JR.Tadros, T; Galet, L; Chamayou, A. Assessment of formulation robustness for nano-crystalline suspensions using failure mode analysis or derisking approach. Int J Pharm. 2016;506(1):320–31.

184. Fuchs N. ZPhys,. 1936;89:736.

185. He YT, Wan J, Tokunaga T. Kinetic stability of hematite nanoparticles: the effect of particle sizes. J Nanoparticle Res. 2007;10(2):321–32.

186. Serra JP J; Martín, A.Galisteo, F; Gálvez, M; Hidalgo-Alvarez, R. On the adsorption of IgG onto polystyrene particles: electrophoretic mobility and critical coagulation concentration. Colloid Polym Sci. 270(6):574–83.

187. Ehrl LS Miroslav; Morbidelli, Massimo; Bäbler, Matthäus Ulrich. Dependence of initial cluster aggregation kinetics on shear rate for particles of different sizes under turbulence. AIChE J. 2009;55(12):3076–87.

188. Shirahama K, TSUJII K, TAKAGI T. Free-boundary electrophoresis of sodium dodecyl sulfate-protein polypeptide complexes with special reference to SDS-polyacrylamide gel electrophoresis. J Biochem (Tokyo). 1974;75(2):309–19.

189. Sakhawat Shah S, Ejaz-Ur-Rehman. Effect of temperature and aprotic solvents on the CMC of sodium Deodecyl Sulphate. Book Interact Water Ion Nanionic Hydrates. 1987;252–5.

190. Wagner C. Theorie der Alterung von Niederschla gen durch Umlo sen. Z Elektrochem. 1961;65:581–591.

191. Sodium dodecyl sulfate. Chem Abstr. 1970;72:22811d.

192. Specification P. Sodium Dodecyl sulfate. nationalbiochem.com. 2012;2012:1–2.

193. Rowe RC, Sheskey PJ, Cook WG, Fenton ME. Handbook of Pharmaceutical Excipients. book. 2012;Seventh edition.

194. Aliofkhazraei M. handbook of mechanical nanostructuring. Wiley-VCH. 2015;379–410.

195. Balaz P. Mechanochemistry in Nanoscience and Minerals Engineering. Springer-Verl Berl Heidelb Chapter 2. 2008;103–32.

196. Adam S. S D; Radeke, C.Khinast, JG. An integrated quality by design (QbD) approach towards design space definition of a bending unit operation by discret element method (DEM) simulation. Eur J Pharm Sci. 2011;42:106–15.

197. Rhodes M. Introduction to Particle Technology. John Wiley Sons Chichester. 1998;

198. Rittinger PR. Lehrbuch der Aufbereitungskunde. Ernst Korn Berl. 1867;

199. Tanaka T. Staub. 1958;18:157–68.

200. Chodakov GS. Physics of Milling. Nauka Mosc Russ. 1972;

201. Lorenzo AT, Arnal ML, Albuerne J, Müller AJ. DSC isothermal polymer crystallization kinetics measurements and the use of the Avrami equation to fit the data: Guidelines to avoid common problems. Polym Test. 2007;26(2):222–31.

202. Catharina Knieke CS Stefan Romeis, Wolfgang Peukert, Sandra Breitung-Faes, Arno Kwade. Nanoparticle Production with Stirred-Media Mills: Opportunities and Limits. Chem Eng Technol 2. 2010;33(9):1401–1411.

203. Grosse K. Grinding & Dispersion Technologies. Present Part Sci Soc. 2006;

204. Taylor LJ. P DG.Dunn, PJ.Bentham, AC.Dawson, NJ.Mitchell, JC.Snowden, MJ. Predictive milling of pharmaceutical materials using nanoindentation of single crystals. Org Process Res Dev. 2004;8(4):674–9.

205. M. Asif Inam SO Christine Frances. Effects of concentration of dispersions on particle sizing during production of fine particles in wet grinding process. Powder Technol. 2011;208:329–336.

206. Mende S. Grinding and Dispersion in the Field of Nanotechnology. Process Eng. 2005;(9):39–43.

207. Jimbo G Zhao, QQ.Yokoyana, T and Taniyana, Y. The grinding limit and the negative grinding phenomenon. Proc IInd World Congr Part Technol Soc Powder Technol Kyoto Part II. 1990;(305–312).

208. Accelrys Inc. Morphology & Breakage of Crystals: Scale-up Manufacturing during Wet Milling of API. San Diego.

209. Kwade A, Blecher L, Schwedes J. Motion and stress intensity of grinding beads in a stirred media mill. Part 2: Stress intensity and its effect on comminution. Powder Technol. 1996;86(1):69–76.

210. A. Bitterlich CL I Krautstrunk, M Dengler, M Juhnke, A Grandeury, H Bunjes, A Kwade. Process parameter dependent growth phenomena of naproxen nanosuspension manufactured by wet media milling. Eur J Pharm Biopharm. 2015;92:171–179.

211. Jankovic A. A review of regrinding and fine grinding technology: the facts and myths. Metso Miner Process Technol Asia-Pac.

212. J.Hecq MD D fanara H Vranckx K Amigh. Preparation and characterization of nanocrystals for solubilirty and dissolution rate enhancemnt of nifdipine. Int J Pharm. 2005;299:167–77.

213. Srinivas Ganta JWP Bruce C Baguley Sanjay Garg. Formulation and pharmacokinetic evalution of an asulacrine nanocrystalline suspension for intravenous delivery. Int J Pharm. 2009;367:179–86.

214. Rainer H.Müller KP. nanosuspension for the formulation of poorly soluble drugs I. preparation by size-reduction technique. Int J Pharm. 1998;160:229–2237.

215. K.Peters SL JE Diederichs K Borner H Hahn RH Mülle ans S Ehler. Preparation of clofazimine nanosuspension for intravenous use and evaluation of its therapeutic

efficacy in murine Myocobacterium avium infection. J Antimicrob Chemother. 2000;45:77–83.

216. Angelika Maschke nadia C bernhard Appel, Joseph Kiermaier, Torsten Blunk and Achim Göpferich. Micronization of Insilun by high pressure homogenization. Pharm Res. 2006;1–10.

217. Berthiuaux; H, Varinot. C. Approximate Calculation Of Breakage Parameters From Batch Grinding Tests. Chem Eng Sci. 1996;51(19):4509–16.

218. Shapiro; SS, M. B. Wilk. An analysis of variance test for normality (complete samples). Biometrika. 1965;52(3–4):591–611.

Abstract

Stabilization and comparison of manufacturing technologies for production of nano-crystalline suspensions

The small particle size of nano-crystalline suspension increases the bioavailability of water insoluble drug and facilitates their direct injection into the systemic circulation as particles. However, this small particle size can be responsible for their physical instability during storage and/or administration. The main challenges related to the production of nano-crystalline suspensions are to select the best stabilizer agent to ensure process-ability and to stabilize the API. Moreover, it is necessary to select the suitable technology for the suspension manufacturing taken into account the industrial constraints (scale-down/scale-up, process robustness and equipment reliability). The present thesis is focused on the formulation and the process development of nano-crystalline suspension. For the formulation part, we described a systematic approach to select optimum stabilizer for the preparation of nano-suspensions of given drug. The stabilizer can be either a dispersant or a combination of dispersant and wetting agents. The proposed screening method is a fast and efficient way to investigate a large number of stabilizers based on the principles of physical-chemistry and employs a stepwise approach. The methodology has been divided in two main parts; the first part focused on qualitative screening with the objective of selecting the appropriate candidate(s) for further investigations. The second part discussed quantitative screening with the objective of optimizing the ratio and the amount of wetting and dispersing agents. The results clearly showed that SDS/PVP as wetting/dispersing 40/60% (w/w) at a total concentration of 1.2% was the optimum stabilizer composition, at which the resulting nano-suspensions were stable at room temperature. Furthermore, the formulation robustness was assessed by measuring the rate of perikinetic, orthokinetic aggregation rate as a function of ionic strength (using NaCl), temperature and of pH variation. The results show that using the SDS/PVP mixture, the critical coagulation concentration is about five times higher than that observed in the literature for suspension colloidaly stable at high concentration. The nano-suspension was also found to be very stable at different pH conditions. Desorption test confirmed the high affinity between API and wetting/dispersing agent. However, the suspension undergoes aggregation at high temperature due to desorption of the wetting/dispersing agent and disaggregation of SDS micelles. Furthermore, aggregation occurs at very high shear rate by overcoming the energy barrier responsible for colloidal stability of the system. With respect to process engineering, a technological comparison (high pressure homogenization (HPH) versus bead milling) for the manufacturing of nano-suspension was carried out in terms of impact of suspension formulation, process parameters and technological configuration on the physical quality of the produced suspension. In addition both technologies were compared in terms of their robustness and their compliance to pharmaceutical regulations. The main findings are that, insofar the formulation is sufficiently robust and stable, both technologies are suitable for processing nano-crystalline suspensions. Bead milling is more powerful than HPH. It leads to a limit of milling (d_{50}) lower than that obtained with HPH (100 vs 200 nm). In addition, for both technologies, one can observe that regardless, the process parameters used for milling and the scale, the relationship of d_{90} versus d_{50} could be described by a unique master curve (technology signature of milling pathway) outlining that the HPH leads to a tighten particle size distributions. Finally, a modelling approach based on adapted Tanka and Chodakov's equation was proposed for modelling the milling kinetic. The generated model provides an accurate fit of milling kinetic, to predict and to simulate the milling manufacturing process

Key words: Suspension; Nanocrystalline; Milling; Stabilization; Formulation; Homogenisation; Solubility.